

**033259-1-F
FINAL REPORT**

**MICROPACKAGING FOR
MM-WAVE CIRCUITS**

ARO Contract: DAAH04-95-1-0321

Linda P.B. Katehi

May 1998

33259-1-F = RL-2457

Reporting period: May 1995 – April 1998

Students:

Manos Tentzeris (student)

Robert Robertson (student)

Faculty: Linda P.B. Katehi

Other Supporting Research Staff: Michael Krumpholz

Manuscripts Published or Submitted During the Reporting Period.

1. Linda P.B. Katehi, James F. Harvey and Emmanouil Tentzeris, "Time Domain Analysis Using Multiresolution Expansions", Book on Time Domain Techniques, Editor: A. Taflove, Willey.
2. E. Tentzeris, M. Krumpholz and L.P.B. Katehi, "Characterization of Shielded Microwave Circuit Components Using MRTD", submitted to IEEE Transactions on Microwave Theory and Techniques.
3. E. Tentzeris, R. Robertson, J.F. Harvey and L.P.B. Katehi, " Stability and Dispersion Analysis of Battle-Lemarie Based MRTD Schemes," submitted to the to IEEE Transactions on Microwave Theory and Techniques.
4. E. Tentzeris, J.F. Harvey and L.P.B. Katehi, "Time Adaptive, Time Domain Techniques for the Design of Microwave Circuits," submitted in the Microwave and Guided Wave Letters.
5. E. Tentzeris, A. Cangellaris and L.P.B. Katehi, " Space/Time Adaptive Meshing and Multiresolution Time Domain Techniques," presented in the 1997 ACES Conference.
6. E. Tentzeris, R. Robertson, A. Cangellaris and L.P.B. Katehi, "Space and Time Adaptive Gridding Using MRTD" presented in the 1997 International Symposium on Microwave Theory and Techniques.
7. E. Tentzeris, J.F. Harvey and L.P.B. Katehi, "Time Adaptive Time Domain Techniques for the Design of Microwave Circuits," presented in the 1997 International Symposium on Microwave Theory and Techniques.

8. E. Tentzeris, R. Robertson and L.P.B. Katehi, "PML Implementation for the Battle-Lemarie MRTD Schemes, presented in the 1998 ACES Conference.
9. L. Roselli, E. Tentzeris and L.P.B. Katehi, "Nonlinear Circuit Characterization Using a Multiresolution Time Domain Technique," accepted for presentation in the 1998 International Symposium on Microwave Theory and Techniques.
10. E. Tentzeris and L.P.B. Katehi, "Space Adaptive Analysis of Evanescent Waveguide Filters," accepted for presentation in the 1998 International Symposium on Microwave Theory and Techniques.
11. E. Tentzeris, "Time Domain Numerical Techniques for the Analysis and Design of Microwave Circuits," Ph.D. Dissertation, The University of Michigan, April 1998.

Honors and Awards

- 1997 Best Paper Award by the International Microelectronics and Packaging Society (IMAPS)
- First Prize in Symposium Paper Award Contest with Katherine Herrick for the paper "W-Band Micromachined Finite Ground Coplanar (FGC) Line Circuit Elements," IEEE MTT-S, Denver, CO, June 1997

Brief Description of Performed Research

Complex antenna and circuit problems including their package on wafer require very intensive calculations due to the need to accurately simulate the underlying high-frequency effects and account for all the parasitic mechanisms. As part of this project, we have successfully applied a novel frequency domain scheme recently developed at the University of Michigan that allows for the very successful and computationally efficient solution of complex antenna problems. This technique has been applied to a variety of circuit and antenna problems and has demonstrated the capability to provide accurate solutions in a much more efficient ways than the conventional techniques. The whole idea in this approach is the use of wavelets in the expansion of the unknown functions. The use of wavelets allows for the computation of the values of the derivatives of the unknown field quantities in addition to the average values of the field. This allows for the development of novel space-adaptive schemes with unique capabilities.

In previous years the Battle-Lemarie based MRTD Technique has been applied to a variety of homogeneous microwave problems and has exhibited significant savings in memory and

execution time. Nevertheless, the most important advantage of this new technique is its capability to provide space and time adaptive gridding without the problems the conventional FDTD is encountering. This is due to the use of two separate sets of basis functions, the scaling functions and wavelets and the capability to threshold the filed coefficients due to excellent conditioning of the formulated mathematical problem. This year a space/time adaptive gridding algorithm based on the MRTD scheme was proposed and applied to inhomogeneous waveguide problems. As examples, the propagation of a Gabor pulse in partially-filled parallel plate waveguide and a parallel plate filter was simulated and the S-parameters have been calculated for validation of the theory. Wavelets were placed only at locations where the EM fields have significant values, creating a space- and time-adaptive dense mesh in regions of strong field variations, while maintaining a much coarser mesh elsewhere. A mathematically correct way of dielectric modeling has been presented and evaluated. The proposed adaptive gridding offers extra economy in memory by a factor of 30%-40% for the 2-dimensional case. This algorithm has been extended to three dimensions and has been applied to the numerical modeling of evanescent mode waveguide band-pass filters.

To extend the capabilities of the Battle-Lemarie based MRTD scheme, an entire-domain algorithm has been proposed and applied to the numerical analysis of nonlinear circuits including diodes. The frequency spectrum of a mixer diode has been calculated and verified by comparison to reference data. In comparison to Yee's conventional FDTD scheme, the proposed scheme offers memory savings by a factor of 2-6 per dimension maintaining a similar accuracy. Especially in the approximation of time derivatives, the use of entire domain expansion basis would require very high memory resources for the storage of the field values everywhere on the grid for the whole or a large fraction of the simulation time. This problem does not exist in the approximation of the spatial derivatives since the filed values on the neighboring spatial grid points have to be calculated and stored no matter what expansion basis are used. For that reason, Harr basis functions have been utilized and a time-adaptive time-domain technique based on intervalic wavelets has been proposed and applied to various types of circuit problems. The scheme has exhibited significant savings in execution time and memory requirements while maintaining a similar accuracy with conventional circuit simulators. Numerical experiments have shown that the use of an absolute threshold of 10^{-6} and a relative threshold of 5×10^{-4} offered an extra economy of 25%-35% in comparison to MRTD schemes based only on scaling functions.

Another research topic for 1997 was the investigation of the stability and the dispersion performance of entire-domain basis MRTD schemes for different stencil sizes and for 0-resolution wavelets. Analytical expressions for the maximum stable time-step were derived for both scaling only and scaling-wavelet algorithms. It has been observed that larger stencils decrease the numerical phase error making it significantly lower than FDTD for low and medium discretizations. Stencil sizes greater than 10 offer a smaller phase error than FDTD even for high discretizations. The enhancement of wavelets further improves the discretization performance for discretizations closer to the Nyquist limit (2-3 cells/wavelength) making it comparable to that of much denser grids, though it decreases the value of the maximum time-step guaranteeing the stability of the scheme. In the following copies of the submitted/presented papers are included for further information.

Characterization of Shielded Microwave Circuit Components Using the Multiresolution Time Domain Method (MRTD)

Emmanouil Tentzeris, Michael Krumpholz, Linda P.B. Katehi

Radiation Laboratory, Department of Electrical Engineering and Computer Science

University of Michigan, Ann Arbor, MI 48109-2122

Abstract

The recently developed Multiresolution Time Domain (MRTD) technique is applied to the modeling of shielded microwave circuit problems. The technique demonstrates excellent accuracy and efficiency in the calculations with savings of one order in computation times and of two orders of magnitude in memory compared to the conventional. The enhancement of wavelets provides very efficient computations of the characteristic impedance and effective dielectric constant of a variety of printed lines operating in a shielded environment.

I Introduction

Despite the wealth of available codes for analysis and design in microwave frequencies, many problems in electromagnetics and specifically in circuit and antenna problems have been left untreated due to the complexity of the geometries and the inability of the existing techniques to deal with the requirements for large size and high resolution due to the fine but electrically important geometrical details. The straightforward use of existing discretization methods suffers from serious limitations due to the required substantial computer resources and unrealistically long computation times. As a result, during the past thirty years the available techniques are almost incapable of dealing with the needs of technology leading into a quest for fundamentally different modeling approaches.

Recently a new technique has been successfully applied [1, 2, 3] to a variety of microwave problems and has demonstrated unparalleled properties. This technique is derived by the use of multiresolution analysis for the discretization of the time-domain Maxwell's equations. The multiresolution time domain technique (MRTD) based on Battle-Lemarie functions has been applied to linear as well as nonlinear propagation problems and has demonstrated savings in

time and in memory by one and two orders of magnitude respectively. In addition to time and memory, the most important advantage of this new technique is its capability to provide space and time adaptive meshing without the problems encountered by the conventional FDTD [3]. The capability to provide adaptive meshing is connected with the use of two separate sets of basis functions, the scaling and wavelet functions, and the capability to threshold the field coefficients due to the excellent conditioning of the formulated mathematical problem. This advantage and capability of the technique is demonstrated herein by performing a space adaptive meshing.

For the derivation of the MRTD scheme, the electromagnetic fields are represented by an expansion in cubic spline Battle-Lemarie scaling and wavelet functions [4], [5] with respect to space. For this type of basis functions, the evaluation of the moment method integrals is simplified due to the existence of closed form expressions in spectral domain and simple representations in terms of cubic spline functions in space domain. The use of non-localized basis functions cannot accommodate localized boundary conditions. To overcome this difficulty, the image principle is used to model perfect electric and magnetic boundary conditions. Pulse functions are used as expansion and test functions in time-domain. In this paper, a 2.5D MRTD scheme is proposed and applied to a variety of shielded of transmission line problems. Specifically, propagation constant, characteristic impedance and field patterns are derived for shielded and open transmission line structures and compared to FDTD results.

II The 2.5D-MRTD scheme

For simplicity, an overview of the 2.5D-MRTD scheme is presented for a homogeneous medium. The derivation is similar to that of Yee's FDTD scheme [?], which uses the method of moments with pulse functions as expansion and test functions. The magnetic field components are shifted by half a discretization interval in space and time-domain with respect to the electric field components.

Using the approach of [6], Maxwell's curl equations for a homogeneous medium with the permittivity ϵ and the permeability μ can be written in the following form

$$\epsilon \frac{\partial E_x}{\partial t} = \frac{\partial H_z}{\partial y} + \beta H_y \quad (1)$$

$$\epsilon \frac{\partial E_y}{\partial t} = -\beta H_x - \frac{\partial H_z}{\partial x} \quad (2)$$

$$\epsilon \frac{\partial E_z}{\partial t} = \frac{\partial H_y}{\partial x} - \frac{\partial H_x}{\partial y} \quad , \quad (3)$$

where β is the propagation constant and $j = \sqrt{-1}$. The electric and magnetic field components

incorporated in these equations are expanded in a series of Battle-Lemarie scaling and wavelet functions in both x- and y-directions. For example, E_x can be represented as:

$$\begin{aligned}
E_x(x, y, t) = & \sum_{k,l,m=-\infty}^{+\infty} {}_k E_{l+1/2,m}^{x,\phi\phi} h_k(t) \phi_{l+1/2}(x) \phi_m(y) \\
& + \sum_i \sum_{k,l,m=-\infty}^{+\infty} {}_k E_{l+1/2,m}^{x,\phi\psi_i} h_k(t) \phi_{l+1/2}(x) \psi_{i,m}(y) \\
& + \sum_i \sum_{k,l,m=-\infty}^{+\infty} {}_k E_{l+1/2,m}^{x,\psi_i\phi} h_k(t) \psi_{i,l+1/2}(x) \phi_m(y) \\
& + \sum_{i,j} \sum_{k,l,m=-\infty}^{+\infty} {}_k E_{l+1/2,m}^{x,\psi_i\psi_j} h_k(t) \psi_{i,l+1/2}(x) \psi_{j,m}(y) \tag{4}
\end{aligned}$$

where $\phi_m(x) = \phi(\frac{x}{\Delta x} - m)$ and $\psi_{i,m}(x) = \psi_i(\frac{x}{\Delta x} - m)$ represent the Battle-Lemarie scaling and i-th order resolution wavelet function respectively in space and $h_k(t)$ represent rectangular pulses in time. ${}_k E_{l,m}^{\kappa,\mu\nu}$ and ${}_{k+1/2} H_{l,m}^{\kappa,\mu\nu}$ with $\kappa = x, y, z$ and $\mu, \nu = \phi, \psi$ are the coefficients for the field expansions in terms of scaling and wavelet functions. The indices l, m and k are the discrete space and time indices related to the space and time coordinates via $x = l\Delta x, y = m\Delta y$ and $t = k\Delta t$, where $\Delta x, \Delta y$ are the space discretization intervals in x- and y-direction and Δt is the time discretization interval. For an accuracy of 0.1% the above summations are truncated to 18 terms. Upon inserting the field expansions, Maxwell's equations are sampled using pulse functions as time-domain test functions and scaling and wavelet functions as space-domain test-functions. Following the procedure of [1], the 2.5D MRTD scheme is derived. As an example, let's consider the discretization of eq.(1). For simplicity, it is assumed that the fields have been expanded only in scaling functions summations. Wavelets can be added in a straightforward way. Applying the Galerkin's technique, the following difference equation is obtained for a homogeneous medium with the permittivity ϵ ,

$$\frac{\epsilon}{\Delta t} ({}_{k+1} E_{l+1/2,m}^{x,\phi\phi} - {}_k E_{l+1/2,m}^{x,\phi\phi}) = \frac{1}{\Delta y} \left(\sum_{i'=m-9}^{m+8} a(i') {}_{k+1/2} H_{l+1/2,i'+1/2}^{z,\phi\phi} \right) + \beta {}_{k+1/2} H_{l+1/2,m}^{y,\phi\phi} \quad , \tag{5}$$

with the coefficients $a(i')$ defined in [1]. The unit cell of the 2.5D-MRTD scheme is identical to the unit cell of the conventional Yee's FDTD scheme. However, due to the different field expansion functions, the field components in the two techniques have a different physical meaning. Deriving MRTD and FDTD using the method of moments, the field components have to be interpreted as field expansion coefficients. From the different field expressions, it is clear that the field expansion coefficients of the FDTD scheme represent the total field value

at a specific point, while the field expansion coefficients of the 2.5D-MRTD scheme represent a fraction of the total field. To calculate the total field at a space point, the field expansions are sampled with delta test functions in space and time domain. For example, the total electric field $E_x(x_o, y_o, t_o)$ with $(k - 1/2) \Delta t < t_o < (k + 1/2) \Delta t$ is calculated by

$$\begin{aligned} E_x(x_o, y_o, t_o) &= \int \int \int E_x(x, y, t) \delta(x - x_o) \delta(y - y_o) \delta(t - t_o) dx dy dt \\ &= \sum_{l', m' = -\infty}^{\infty} {}_k E_{l'+1/2, m'}^{x, \phi\phi} \phi_{l'+1/2}(x_o) \phi_{m'}(y_o) \quad . \end{aligned} \quad (6)$$

Extending the dispersion analysis of [1] from 3-dimensional to 2.5-dimensional space, the stability condition for the 2.5D-MRTD scheme results in

$$\Delta t \leq \frac{1}{1.568c \sqrt{(\frac{1}{\Delta x})^2 + (\frac{1}{\Delta y})^2 + (\frac{\beta}{2})^2}} \quad (7)$$

with the wave propagation velocity c . It is preferable to choose Δt at least 2.5 time less than the stability limit. In this way, much more linearity of the dispersion characteristics is achieved.

III Applications of the 2.5D-MRTD scheme to Shielded Transmission Lines

In this paper, the 2.5D-MRTD scheme is applied to the analysis of shielded stripline and microstrip lines to investigate propagation and coupling effects. Results for these shielded structures are presented and discussed separately below.

A shielded stripline is a simplified version of a membrane microstrip shown in (Fig.1a). The metallic shield has dimensions $47.6mm \times 22.0mm$ and the central strip has length $11.9mm$. The stripline is filled with air ($\epsilon_r = 1.$). The analysis for the higher order propagating modes is straightforward. For the analysis using Yee's FDTD scheme, a 40×10 mesh was used resulting in a total number of 400 grid points. When the structure was analyzed with the 2.5D-MRTD scheme, a mesh 8×4 (32 grid points) was chosen reducing the total number of grid points by a factor of 12.5. In addition, the execution time for the analysis was reduced by a factor of 3 to 4. The time discretization interval was chosen to be identical for both schemes and equal to the 0.8 of the 2.5D-MRTD maximum Δt . For the analysis $\beta = 30$ was used and 5,000 time-steps were considered.

Mode	TEM	Shield TE_{10}
Analytic values	1.4324 GHz	3.4615 GHz
8x2 MRTD	1.4325 GHz	3.4648 GHz
Rel.Error	0.007%	0.095%
8x4 MRTD	1.4325 GHz	3.4641 GHz
Rel.Error	0.007%	0.075%
16x4 MRTD	1.4325 GHz	3.4633 GHz
Rel.Error	0.007%	0.052%
40x10 FDTD	1.4322 GHz	3.4585 GHz
Rel.Error	-0.014%	-0.087%

Table 1: Mode frequencies for $\beta = 30$

From (Table 1) it can be observed that the calculated frequencies of the two first propagating modes for $\beta = 30$ by use of 2.5D-MRTD scheme are very close to the theoretical values, since the largest error is less than 0.1%. The relative error of the 2.5D-MRTD calculated frequencies is always positive, which corresponds to an overestimation of the resonant frequencies. This is exactly what has to be expected from the dispersion behavior of the MRTD schemes.

The use of non-localized basis functions in the 2.5D-MRTD scheme causes significant effects. Localized boundary conditions are impossible to be implemented, so the perfect electric boundary conditions are modelled by use of the image principle. The perfect electric conductor is replaced by an open structure with electromagnetic fields characterized by even or odd symmetry. Odd symmetry is imposed to the electric field components that are tangential to the conductor in order to ensure zero electric field on the conductor and even symmetry for the magnetic field components that are tangential to the conductor.

The non-localized character of the basis functions offer the opportunity to calculate the field values in any point of the discretization cells. The field values at the neighboring cells can be combined appropriately by adjusting the scaling functions' values and by applying the image principle. For example, the total electric field $E_x(x_o, y_o, t_o)$ with $(k-1/2)\Delta t < t_o < (k+1/2)\Delta t$ is calculated by Eq.(6) by simply truncating the l,m summation from -12 to 12 for each index. That means that the summation based only at the 12 neighboring cells from each side gives the total field component values with good accuracy. In (Fig.2-4), the value of the E_y field has been calculated and plotted for the 4 cells exactly below the strip by use of the 2.5D-MRTD scheme. The relative position of the strip is from 15 to 25. For the TEM mode the pattern obtained by use of the conventional FDTD scheme is plotted for comparison. For the shield

TE_{10} mode, the analytically calculated pattern has been added for reference. All results are normalized to the peak value. It can be observed that the agreement of the MRTD calculated field pattern with the reference data is very good for the shield TE_{10} mode, where the values are changing slowly (sinusoidally) (Fig.2). On the contrary, for the TEM mode where the edge effect is more prominent, the agreement is not good. In this case, wavelets of 0-Resolution are added in both directions to describe the higher spatial frequencies. It can be observed from (Fig.3) that the wavelet coefficients for the 8x4 grid have a significant contribution ($> 10\%$) close to the stripline. Increasing the grid size from 8 to 16 to the strip direction and/or from 4 to 8 to the normal to the strip direction improves more the accuracy of the field representation (Fig.4).

The characteristic impedance Z_o for the TEM mode of the stripline is computed from the equation:

$$Z_o = \frac{V}{I} = \frac{\int_{C_v} E_y dy}{\oint_{C_c} H dl} \quad , \quad (8)$$

where the integration paths C_v and C_c are shown in (Fig.1a). Since both of the schemes used in the analysis are discrete in space-domain, the above integrals are transformed to summations. For the FDTD summations, only one field value per cell is needed, due to the fact that pulse expansion functions which are constant for each cell are utilized. On the contrary, for the 2.5D-MRTD summation the field values for a number of subpoints along the integration path have to be calculated, since the expansion functions are not constant for each cell. It can be observed from Table 2 that the accuracy of the calculation of the characteristic impedance is improved by increasing the number of subpoints per cell, at which the field values are calculated. An accuracy better than 1% is achieved if the field values are computed for more than 9 subpoints per cell along the integration path for the scheme including wavelets of 0-resolution to both directions. On the contrary, the value of Z_o that is calculated from the scheme based only on scaling functions is oscillating, thus indicating that a denser mesh is required. The analytical value of the Z_o is 95.58Ω [7].

The modification of the dimensions of the MRTD mesh (Table 3) shows that the accuracy of the calculation of the Z_o by use of the MRTD is much better than that of the Yee's FDTD scheme with a 40x10 mesh (relative error -3.28%).

A similar procedure is used for the analysis of the shielded coupled-stripline geometry of (Fig.1b) for the first even and odd mode. Both strips have a length of $11.9mm$, the distances between them is $11.9mm$, from the top and bottom PEC's are $11.0mm$ and from the left and right PEC's are $11.9mm$. The structure is filled with air ($\epsilon_r = 1$). For the analysis with the conventional FDTD scheme, a 70×20 mesh resulted in a total number of 1400 grid points. The

Subpoints/cell	Z_o^{sc} (Ω)	Relative error	Z_o^{wa} (Ω)	Relative error
3	80.56	-15.71 %	84.04	-12.07 %
5	94.46	-1.17 %	92.55	-3.17 %
7	99.06	+3.64 %	94.59	-1.04 %
9	101.44	+6.13 %	94.96	-0.65 %
11	97.56	+2.07 %	95.01	-0.60 %

Table 2: Z_o for different number of subpoints/cell (8x4 Grid).

	Z_o (Ω)	Relative error
Analyt. Value	95.58	0.0%
8x4 MRTD	95.01	-0.60%
8x8 MRTD	95.19	-0.41%
16x4 MRTD	95.71	0.14%
40x10 FDTD	92.44	-3.28%

Table 3: Z_o for different mesh sizes (11 subpoints/cell).

same accuracy is achieved by an MRTD mesh 14×4 (56 grid points) resulting in an economy of memory by a factor of 25. The space distribution of the tangential-to-stripline E is plotted in logarithmic scale in (Fig.5) for the even mode.

The 2-D MRTD technique is also used for the analysis of a shielded microstrip (Fig.1c) with width $9.9mm$ on a dielectric substrate with $\epsilon_r = 10.65$ and thickness $11mm$. The microstrip is placed in the center of a rectangular shield $69.3mm \times 44mm$. The same accuracy for the characteristic impedance calculation (Theoretical $Z_o = 50$ Ohms) is achieved by an FDTD mesh 140×80 and an MRTD mesh 28×20 resulting in an economy in memory by a factor of 20.

IV Conclusion

A multiresolution time-domain scheme in 2 dimensions has been applied to the numerical analysis of shielded striplines and microstrips. The field patterns and the characteristic impedance have been calculated and verified by comparison to reference data. In comparison to Yee's conventional FDTD scheme, the proposed 2.5D-MRTD scheme offer memory savings by a

factor of 25 and execution time savings by a factor of about 4-5 maintaining a better accuracy for characteristic impedance calculations. This indicates memory savings of a factor 5 per dimension leading to two orders of memory savings in three dimensions. Compared to 2.5D-FDTD, 25 times less cells in MRTD require about 5 times less running time, thus the computation time per cell is increased by a factor of 5. This leads to computation time savings of more than one order for 3 dimensional structures. For structures, where the edge effect is prominent, additional wavelets have to be introduced to improve the accuracy when using a coarse MRTD mesh.

V Acknowledgments

This work has been made possible by a scholarship of the NATO science committee through the German Academic Exchange Service and by the U.S. Army Research Office.

References

- [1] M.Krumpholz, L.P.B.Katehi, "MRTD: New Time Domain Schemes Based on Multiresolution Analysis", IEEE Trans. Microwave Theory and Techniques, vol. 44, no. 4, pp. 555-561, April 1996.
- [2] E.M.Tentzeris, R.L.Robertson, M.Krumpholz, L.P.B.Katehi, "Application of MRTD to Printed Transmission Lines", Proc. MTT-S 1996, pp. 573-576.
- [3] K.S.Yee, "Numerical solution of initial boundary value problems involving Maxwell's equations in isotropic media", IEEE Trans. Antennas Propagation, pp.302-307, May 1966.
- [4] G.Battle, "A block spin construction of ondelettes", Comm.Math.Phys., vol. 110, pp. 601-615, 1987.
- [5] P.G.Lemarie, "Ondelettes a localisation exponentielle", J.Math.Pures Appl., vol. 67, pp. 227-236, 1988.
- [6] S.Xiao, R.Vahldieck, "An Improved 2D-FDTD Algorithm for Hybrid Mode Analysis of Quasi-planar Transmission Lines", MWSYM 93, vol. 1, pp.421-424.
- [7] B.C.Wadell, "Transmission Line Design Handbook", pp. 136-137, Artech House, 1991.

LIST OF FIGURE CAPTIONS

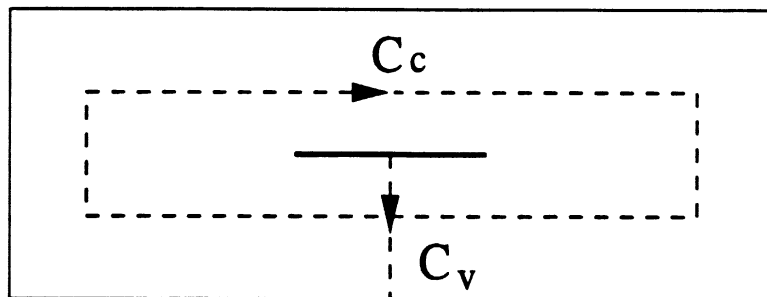
Figure 1: Printed Lines Geometries.

Figure 2: Shield TE_{10} E_y pattern.

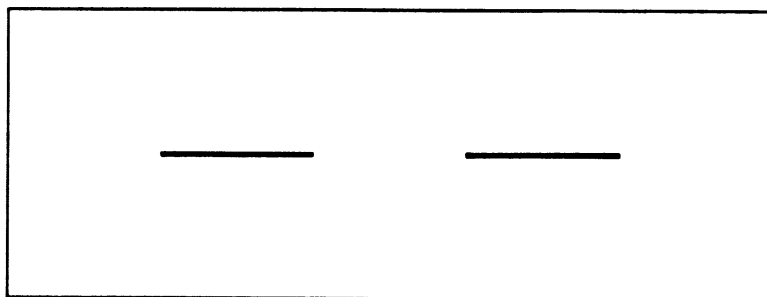
Figure 3: TEM E_y Pattern Components (8x8 Grid).

Figure 4: TEM E_y Pattern Comparison (8x8 Grid).

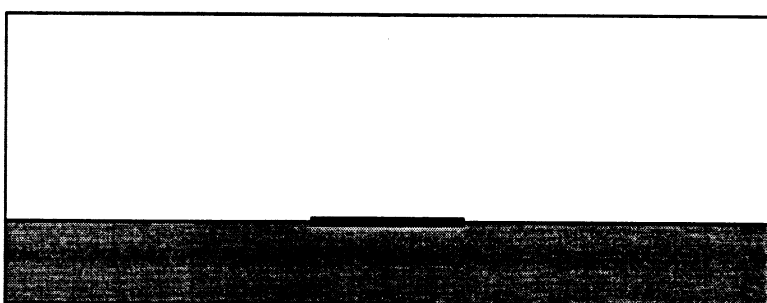
Figure 5: Tangential E-field Distribution (Shielded - Even Mode).



(a)



(b)



(c)

Figure 1: Printed Lines Geometries.

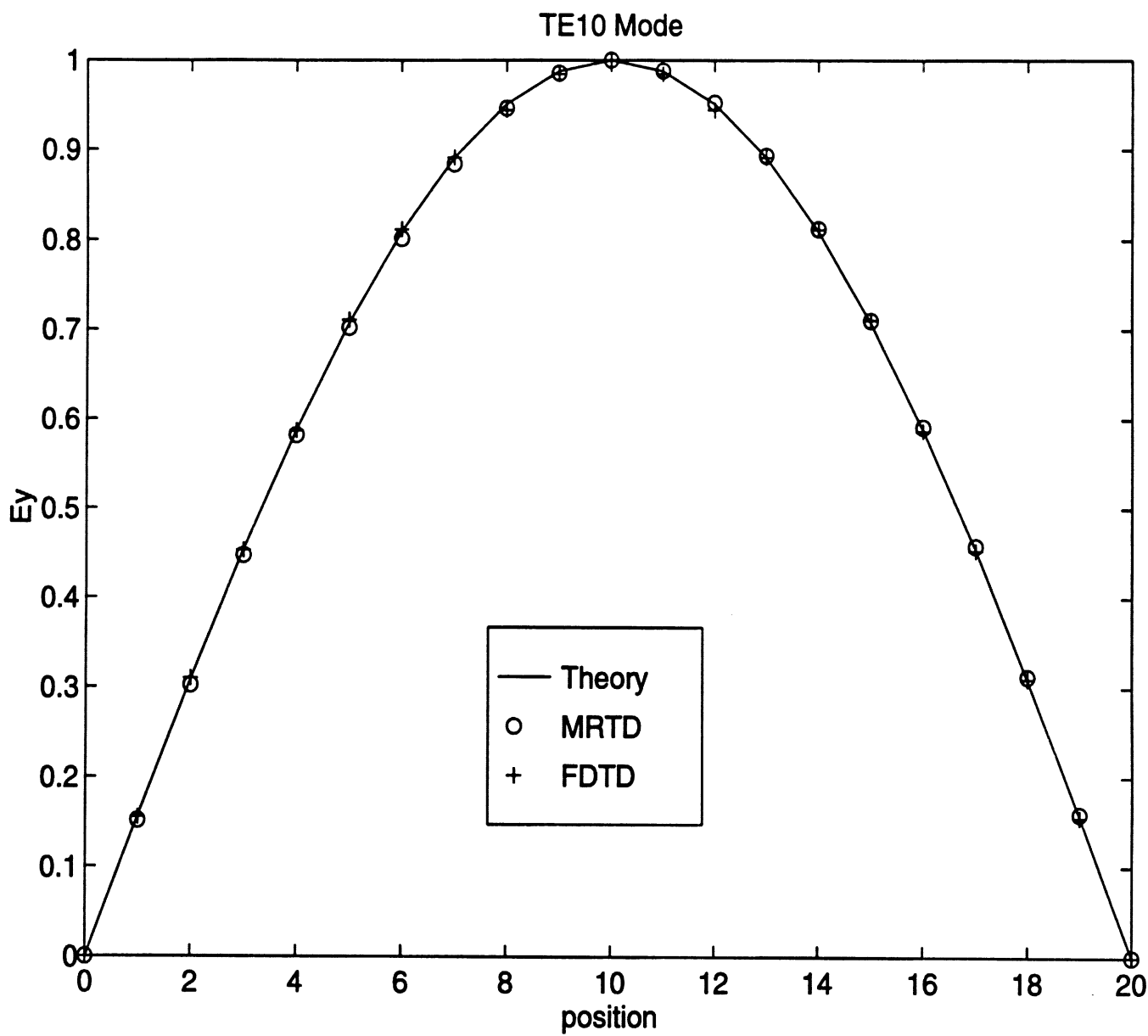


Figure 2: Shield TE_{10} E_y pattern.

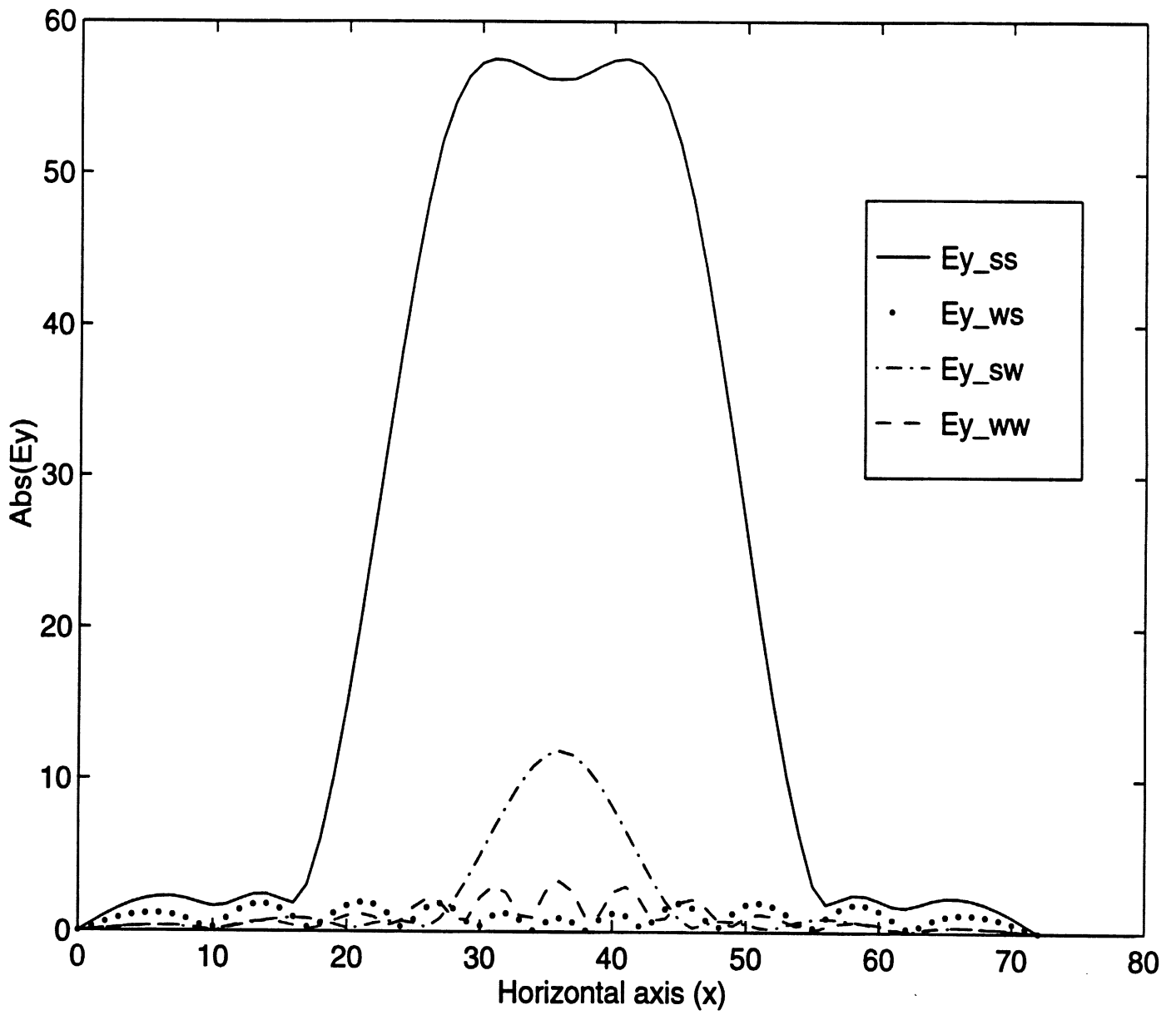


Figure 3: TEM E_y Pattern Components (8x8 Grid).

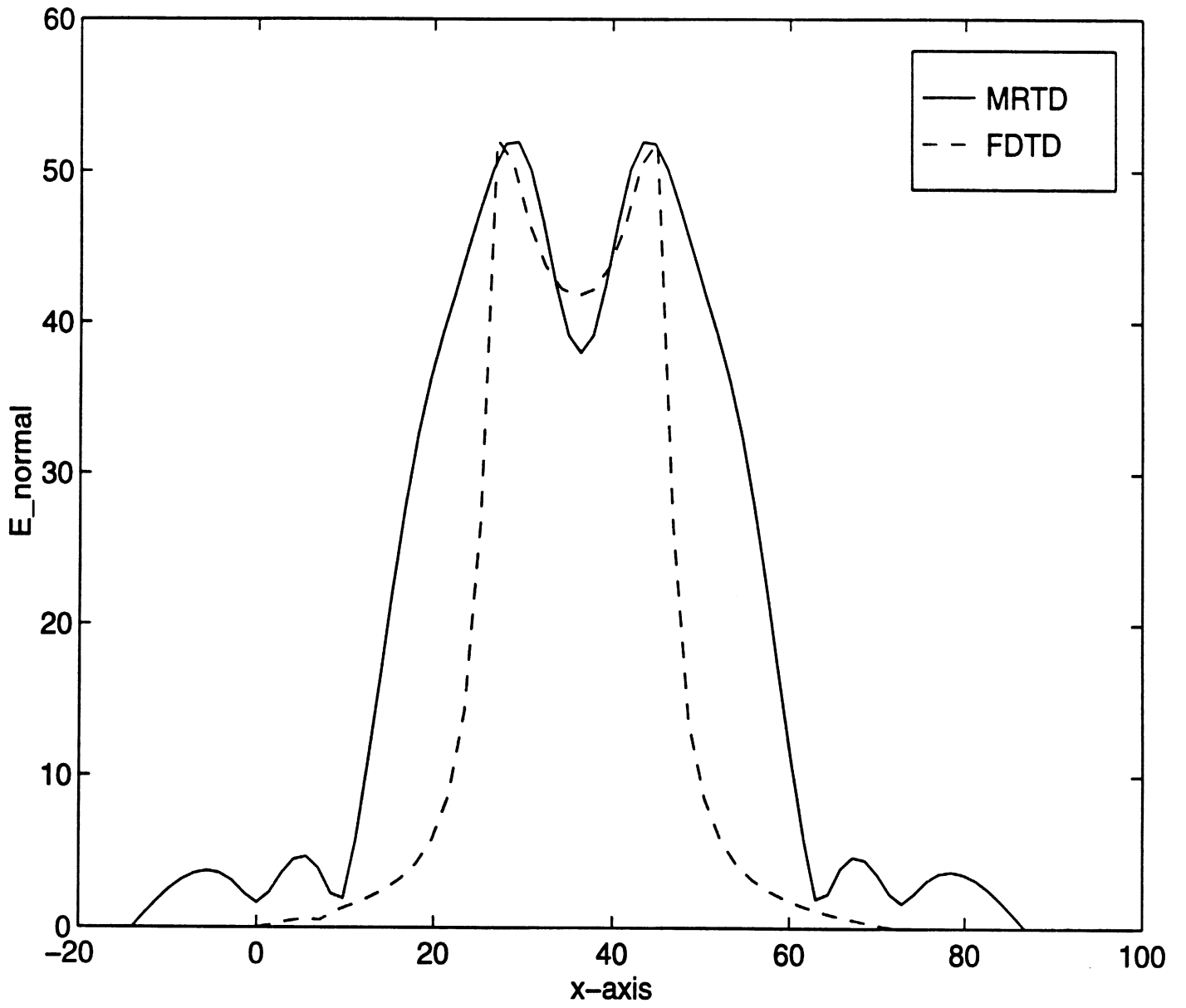


Figure 4: TEM E_y Pattern Comparison (8x8 Grid).

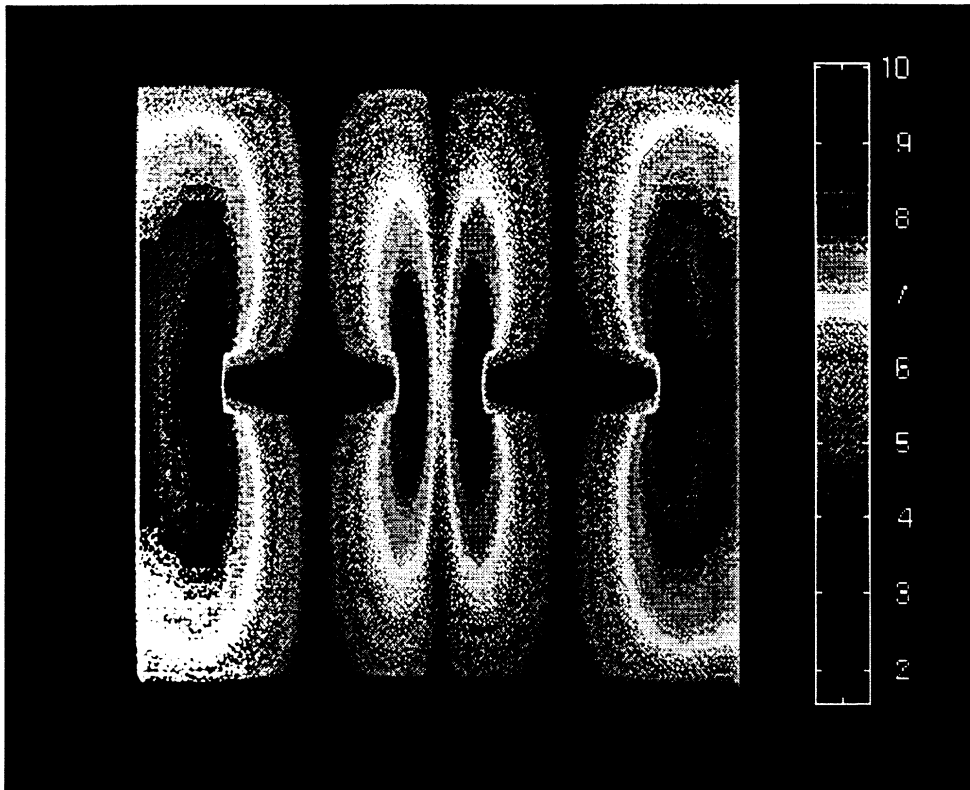


Figure 5: Tangential E-field Distribution (Shielded - Even Mode).

STABILITY AND DISPERSION ANALYSIS OF BATTLE-LEMARIE BASED MRTD SCHEMES

Emmanouil M. Tentzeris¹, Robert L. Robertson¹, James Harvey² and Linda P.B. Katehi¹

¹ Radiation Laboratory, Department of Electrical Engineering and Computer Science
University of Michigan, Ann Arbor, MI 48109-2122

² Army Research Office, NC

I Abstract

The stability and the dispersion performance of the recently developed Battle-Lemarie MRTD schemes is investigated for different stencil sizes. The contribution of wavelets is enhanced and analytical expressions for the maximum allowable time step are derived. It is observed that larger stencils decrease the numerical phase error making it significantly lower than FDTD for low and medium discretizations. The addition of wavelets further improves the dispersion performance for discretizations close to the Nyquist limit, though it decreases the value of the maximum time-step guaranteeing the stability of the scheme.

II Introduction

Finite-Difference Time-Domain numerical techniques are widely used now-a-days for the analysis of various microwave geometries and for the modelling of EM wave propagation. Though many of them are very simple to implement and can be easily applied to different topologies with remarkable accuracy, they cause a numerical phase error during the propagation along the discretized grid. For example, the numerical phase velocity in the FDTD can be different than the velocity of light, depending on the cell size as a fraction of the smallest propagating wavelength and the direction of the grid propagation. Thus, a non-physical dispersion is introduced and affects the accuracy limits of FDTD simulations, especially of large structures.

In addition, it is well-known that the finite-difference schemes in time and space domain require that the used time step should take values within an interval that is a function of the cell size. If the time-step takes a value outside the bounds of this interval, the algorithm will be numerically unstable, leading to a spurious increase of the field values without limit as the time increases.

Though the stability and the dispersion analysis for the conventional Yee's FDTD algorithm has been thoroughly investigated, only a few results have been presented concerning MRTD schemes based on cubic spline Battle-Lemarie scaling and wavelet functions [2]. The functions of this family do not have compact support, thus the finite approximations of the derivatives are finite stencil summations instead of finite differences. In this paper, the effect of these stencils' size as well as of the enhancement of wavelets is investigated and comparison with 2nd-order and higher-order FDTD schemes displays difference in their respective behaviors.

III Stability Analysis

Following the stability analysis described in [1], the MRTD [2] equations are decomposed into separate time and space eigenvalue problems. Assuming an expansion only to scaling functions (S-MRTD), the left-hand side time-differentiation parts can be written as an eigenvalue problem

$$\frac{k+1/2 H_{i,j-1/2}^x - k-1/2 H_{i,j-1/2}^x}{\Delta t} = \Lambda_k H_{i,j-1/2}^x \quad (1)$$

$$\frac{k+1/2 H_{i-1/2,j}^y - k-1/2 H_{i-1/2,j}^y}{\Delta t} = \Lambda_k H_{i,j-1/2}^y \quad (2)$$

$$\frac{k+1 E_{i,j}^z - k E_{i,j}^z}{\Delta t} = \Lambda_{k+1/2} E_{i,j}^z \quad (3)$$

In order to avoid having any spatial mode increasing without limit during normal time-stepping, the imaginary part of Λ , $Imag(\Lambda)$, must satisfy the equation

$$-\frac{2}{\Delta t} \leq Imag(\Lambda) \leq \frac{2}{\Delta t} \quad (4)$$

For each time step k , the instantaneous values of the electric and magnetic fields distributed in space across the grid can be Fourier-transformed with respect to the i - and j - coordinates to provide a spectrum of sinusoidal modes (plane wave eigenmodes of the grid). Assuming an eigenmode of the spatial-frequency domain with k_x and k_y being the x - and y - components of the numerical eigenvector, the field components can be written

$$\begin{aligned} E_{I,J}^z &= E_{z_0} e^{j(k_x I \Delta x + k_y J \Delta y)} \\ H_{I,J-1/2}^x &= H_{x_0} e^{j(k_x I \Delta x + k_y (J-1/2) \Delta y)} \\ H_{I-1/2,J}^y &= H_{y_0} e^{j(k_x (I-1/2) \Delta x + k_y J \Delta y)} \end{aligned}$$

Substituting these expressions to (1)–(3) and applying Euler's identity, we get

$$\Lambda^2 = -\frac{4}{\mu\epsilon} \left[\frac{1}{(\Delta x)^2} \left(\sum_{i'=0}^{n_a-1} a(i') \sin(k_x (i+1/2) \Delta x) \right)^2 + \frac{1}{(\Delta y)^2} \left(\sum_{j'=0}^{n_a-1} a(j') \sin(k_y (j+1/2) \Delta y) \right)^2 \right] \quad (5)$$

Thus, Λ is a pure imaginary, which can be bounded for any wavevector $k = (k_x, k_y)$:

$$\begin{aligned} &- 2c \left(\sum_{i'=0}^{n_a-1} |a(i')| \right) \sqrt{\frac{1}{(\Delta x)^2} + \frac{1}{(\Delta y)^2}} \leq Imag(\Lambda) \\ &\leq 2c \left(\sum_{i'=0}^{n_a-1} |a(i')| \right) \sqrt{\frac{1}{(\Delta x)^2} + \frac{1}{(\Delta y)^2}} \quad (5) \end{aligned}$$

where $c = \frac{1}{\sqrt{\mu\epsilon}}$ is the velocity of the light in the modeled medium.

Numerical stability is maintained for every spatial mode only when the range of eigenvalues given by (5) is contained entirely within the stable range of time-differentiation eigenvalues given by (4). Since both ranges are symmetrical around zero, it is adequate to set the upper bound of (5) to be smaller or equal to (4), giving:

$$\Delta t \leq \frac{1}{c \left(\sum_{i'=0}^{n_a-1} |a(i')| \right) \sqrt{\frac{1}{(\Delta x)^2} + \frac{1}{(\Delta y)^2}}} \quad (6)$$

For $\Delta x = \Delta y = \Delta$, the above stability criterion gives

$$\Delta t_{S-MRTD} \leq \frac{\Delta}{c \sqrt{2} \sum_{i'=0}^{n_a-1} |a(i')|} = s_{SS} \frac{\Delta}{c \sqrt{2}} \quad (7)$$

It is known [3] that

$$\Delta t_{FDTD} \leq \frac{1}{c \sqrt{\frac{1}{(\Delta x)^2} + \frac{1}{(\Delta y)^2}}}, \quad (8)$$

which gives for $\Delta x = \Delta y = \Delta$

$$\Delta t_{FDTD} \leq \frac{\Delta}{c\sqrt{2}}. \quad (9)$$

Equations (7)–(9) show that for same discretization size, the upper bounds of the time-steps of FDTD and S-MRTD are comparable and related through the factor s . The stability analysis can be generalized easily to 3D. The new stability criteria can be derived by the equations (7) and (9) by substituting the term $\sqrt{2}$ with $\sqrt{3}$.

More complicated expressions can be derived for the maximum allowable time-step for schemes containing scaling and wavelet functions. For example, the upper bound of the time-step for the 2D MRTD scheme with 0-resolution wavelets to the one (x-direction) or two directions (x- and y-directions) is given by

$$\Delta t_{W_0S-MRTD} \leq \frac{1}{c \sqrt{\frac{1}{(\Delta x)^2} (\sum_{i'=0}^{n_a-1} |a(i')| \sum_{i'=0}^{n_b-1} |b_0(i')| + 4(\sum_{i'=0}^{n_c-1} |c_0(i')|)^2) + \frac{1}{(\Delta y)^2} (\sum_{j'=0}^{n_a-1} |a(j')|)^2}}$$

and

$$\Delta t_{W_0W_0-MRTD} \leq \frac{1}{c \sqrt{\frac{1}{(\Delta x)^2} + \frac{1}{(\Delta y)^2}} \sqrt{\sum_{i'=0}^{n_a-1} |a(i')| \sum_{i'=0}^{n_b-1} |b_0(i')| + 4(\sum_{i'=0}^{n_c-1} |c_0(i')|)^2}}$$

For $\Delta x = \Delta y = \Delta$, the above equations give

$$\Delta t_{W_0S-MRTD, max} \approx s_{W_0S} \frac{\Delta}{c\sqrt{2}}$$

with

$$s_{W_0S} = \frac{\sqrt{2}}{\sqrt{(\sum_{i'=0}^{n_a-1} |a(i')| \sum_{i'=0}^{n_b-1} |b_0(i')| + 4(\sum_{i'=0}^{n_c-1} |c_0(i')|)^2) + (\sum_{j'=0}^{n_a-1} |a(j')|)^2}}$$

and

$$\Delta t_{W_0W_0-MRTD, max} \approx s_{W_0W_0} \frac{\Delta}{c\sqrt{2}}$$

with

$$s_{W_0W_0} = \sqrt{\sum_{i'=0}^{n_a-1} |a(i')| \sum_{i'=0}^{n_b-1} |b_0(i')| + 4(\sum_{i'=0}^{n_c-1} |c_0(i')|)^2}$$

It can be observed that the upper bound of the time step depends on the stencil size n_a, n_b, n_c . This dependence is expressed through the coefficients $s_{SS}, s_{W_0S}, s_{W_0W_0}$, which decrease as the stencil size increases. Figure 1 shows that s_{SS} practically converges to the value 0.6371 after $n_a \geq 10$ and $s_{W_0S} \approx 0.4872$ and $s_{W_0W_0} \approx 0.4095$ for $n_a = n_b = n_c \geq 10$.

IV Dispersion Analysis

To calculate the numerical dispersion of the S-MRTD scheme, plane monochromatic traveling-wave trial solutions are substituted in the discretized Maxwell's equations. For example, the E_z component for the TM mode has the form

$${}^k E_{I,J}^z = E_{z_0} e^{j(k_x I \Delta x + k_y J \Delta y - \omega k \Delta t)}$$

where k_x and k_y are the x- and y- components of the numerical wavevector and ω is the wave angular frequency. Substituting the above expressions into the Equations (1)–(3), the following numerical dispersion relation is obtained for the TM mode for the S-MRTD Scheme after algebraic manipulation

$$\begin{aligned} \left[\frac{1}{c\Delta t} \sin\left(\frac{\omega\Delta t}{2}\right) \right]^2 &= \left[\frac{1}{\Delta x} \left(\sum_{i'=0}^{n_a-1} a(i') \sin(k_x(i'+1/2)\Delta x) \right) \right]^2 \\ &+ \left[\frac{1}{\Delta y} \left(\sum_{j'=0}^{n_a-1} a(j') \sin(k_y(j'+1/2)\Delta y) \right) \right]^2 \end{aligned} \quad (10)$$

For square unit cells ($\Delta x = \Delta y = \Delta$) and wave propagating at an angle ϕ with respect to x-axis ($k_x = k \cos\phi$ and $k_y = k \sin\phi$), the above expression is simplified to

$$\begin{aligned} \left[\frac{\Delta}{c\Delta t} \sin\left(\frac{\omega\Delta t}{2}\right) \right]^2 &= \left(\sum_{i'=0}^{n_a-1} a(i') \sin(k \cos\phi (i'+1/2) \Delta) \right)^2 \\ &+ \left(\sum_{j'=0}^{n_a-1} a(j') \sin(k \sin\phi (j'+1/2) \Delta) \right)^2 \end{aligned} \quad (11)$$

This equation relates the numerical wavevector, the wave frequency, the cell size and the time-step. Solving this numerically for different angles, time step sizes and frequencies, the dispersion characteristics can be quantified.

Defining the Courant number $q = (c\Delta t)/\Delta$ and the number of cells per wavelength $n_l = \lambda_{REAL}/\Delta$ and using the definition of the wavevector $k = (2\pi)/\lambda_{NUM}$ the dispersion relationship can be written as

$$\begin{aligned} \left[\frac{1}{q} \sin(\pi q / n_l) \right]^2 &= \left[\sum_{i'=0}^{n_a-1} a(i') \sin(\pi u (2i'+1) \cos\phi / n_l) \right]^2 \\ &+ \left[\sum_{j'=0}^{n_a-1} a(j') \sin(\pi u (2j'+1) \sin\phi / n_l) \right]^2 \end{aligned} \quad (12)$$

where $u = \lambda_{REAL}/\lambda_{NUM}$ is the ratio of the theoretically given n to the numerical value of the propagating wavelength and expresses the phase error introduced by the S-MRTD algorithm. To satisfy the stability requirements, q has to be smaller than 0.45 ($= 0.6371/\sqrt{2}$) for the 2D simulations.

The above analysis can be extended to cover the expansion in scaling and 0-resolution wavelet functions in x-, y- or both directions.

The general dispersion relationship is

$$\begin{aligned} \frac{\mu}{\epsilon} (C_1 C_1 + C_2 C_2 + C_4 C_4 + C_5 C_5) + \left(\frac{\mu}{\epsilon}\right)^2 \left[\frac{(C_4 C_5 + C_5 C_6)^2}{A} + \frac{(C_1 C_2 + C_2 C_3)^2}{B} \right] \\ + \left(\frac{\mu}{\epsilon}\right)^4 (C_1 C_2 + C_2 C_3)^2 (C_4 C_5 + C_5 C_6)^2 \left(\frac{1}{A} + \frac{1}{B}\right)^2 \frac{1}{F} = 1 \end{aligned} \quad (13)$$

Scheme	C_1	C_2	C_3	C_4	C_5	C_6
SS	$\neq 0$	0	0	$\neq 0$	0	0
W_0S	$\neq 0$	0	0	$\neq 0$	$\neq 0$	$\neq 0$
SW_0	$\neq 0$	$\neq 0$	$\neq 0$	$\neq 0$	0	0
W_0W_0	$\neq 0$	$\neq 0$	$\neq 0$	$\neq 0$	$\neq 0$	$\neq 0$

Table 1: Coefficients C_i for Different MRTD Schemes

with

$$F = 1 - \left[\frac{\mu}{\epsilon} (C_1 C_2 + C_2 C_3) \right]^2 \frac{1}{A} - \left[\frac{\mu}{\epsilon} (C_4 C_5 + C_5 C_6) \right]^2 \frac{1}{B} - \left[\frac{\mu}{\epsilon} (C_2 C_2 + C_3 C_3 + C_5 C_5 + C_6 C_6) \right] \quad (14)$$

$$A = 1 - \frac{\mu}{\epsilon} (C_1 C_1 + C_2 C_2 + C_5 C_5 + C_6 C_6)$$

$$B = 1 - \frac{\mu}{\epsilon} (C_2 C_2 + C_3 C_3 + C_4 C_4 + C_5 C_5) \quad (15)$$

. The C_i are defined by

$$C_1 = -\frac{\Delta t}{\mu \Delta \sin(\omega \Delta t / 2)} \sum_{j'=0}^{n_a} a(j') \sin(k_y(j' + 1/2)\Delta)$$

$$C_2 = -\frac{\Delta t}{\mu \Delta \sin(\omega \Delta t / 2)} \sum_{j'=0}^{n_c} c_0(j') \sin(k_y j' \Delta)$$

$$C_3 = -\frac{\Delta t}{\mu \Delta \sin(\omega \Delta t / 2)} \sum_{j'=0}^{n_b} b_0(j') \sin(k_y(j' + 1/2)\Delta)$$

$$C_4 = -\frac{\Delta t}{\mu \Delta \sin(\omega \Delta t / 2)} \sum_{i'=0}^{n_a} a(i') \sin(k_x(i' + 1/2)\Delta)$$

$$C_2 = -\frac{\Delta t}{\mu \Delta \sin(\omega \Delta t / 2)} \sum_{i'=0}^{n_c} c_0(i') \sin(k_x i' \Delta)$$

$$C_3 = -\frac{\Delta t}{\mu \Delta \sin(\omega \Delta t / 2)} \sum_{i'=0}^{n_b} b_0(i') \sin(k_x(i' + 1/2)\Delta) \quad (16)$$

Eq.(13) can be applied to the dispersion analysis of SS (only scaling functions), W_0S (0-resolution wavelets only to x-direction), SW_0 (0-resolution wavelets only to y-direction) and W_0W_0 (0-resolution wavelets to both x- and y- directions) following Table 2. In case the $C_i \neq 0$, it can be calculated by Eq.(16).

The above equation is solved numerically by use of Bisection-Newton-Raphson Hybrid Technique for different values of n_a , n_b , n_c , n_l , ϕ and q . Fig.(2)–(5) show the variation of the numerical phase velocity as a function of the inverse of the Courant number $1/s=1/q$ for stencil sizes $n_a = n_b = n_c = 8, 10, 12, 14$. For each figure, three different discretization sizes are used: 10 cells/wavelength (coarse), 20 cells/wavelength (normal) and 40 cells/wavelength (dense). The results are compared to the respective values of conventional FDTD. It can be observed that the phase error for F.D.T.D. decreases quadratically. The variation of the phase error in M.R.T.D. exhibits some unique features. Though for any stencil size the numerical phase error for M.R.T.D. discretization of 10cells/ λ is smaller than that of the F.D.T.D. discretization of 40cells/ λ , the M.R.T.D. error doesn't behave monotonically [4]. It decreases up to a certain discretization value and then it starts increasing. This value depends on the stencil size and takes larger values for larger stencils. For example, this value is

between 10 and 20 $cells/\lambda$ for stencil equal to 10, between 20 and 40 $cells/\lambda$ for stencil=12 and very close to 40 $cells/\lambda$ for stencil=14 and can be used as a criterion to characterize the discretization range that the M.R.T.D. offers significantly better numerical phase performance than the F.D.T.D.

The phase error caused by the dispersion is cumulative and it represents a limitation of the conventional FDTD Yee algorithm for the simulation of electrically large structures. It can be observed that the error of S-MRTD is significantly lower, allowing the modeling of larger structures. FDTD is derived by expanding the fields in pulse basis. As it is well known the Fourier transform of the pulse is a highly oscillating $\text{Si}(x)$. On the contrary, the Fourier transform of the Battle-Lemarie Cubic spline is similar to a low-pass filter. That "smooth" spectral characteristic offers a much lower phase error even for very coarse (close to 3-4 $cells/\lambda$) cells.

By using a larger stencil n_a , the entire-domain oscillating nature of the scaling functions is better represented. Thus, smoother performance for low discretizations (Fig.(6)) and lower phase error for higher discretizations (Fig.(7)) is achieved as n_a increases from 8 to 12. Wavelets contribute to the improvement of the dispersion characteristics for even coarser cells (close to 2.2-2.4 $cells/\lambda$) as it is demonstrated in Fig.(8)-(13). For discretizations above 4 $cells/\lambda$ the effect of the wavelets is negligible. (Fig.(11)) and (Fig.(13)) show clearly that the phase error has a minimum for a specific discretization (17 for $n_a = 10$ and 25 for $n_a = 12$).

Fig.(14)-(17) show that for discretizations smaller than $30cells/\lambda$ the choice of the Courant number affects significantly the dispersion performance which starts converging to the minimum numerical phase error (0.8 deg/λ for $n_a = n_b = n_c = 10$ and 0.2 deg/λ for $n_a = n_b = n_c = 12$) for $1/q$ close to 10. On the contrary, the F.D.T.D. dispersion is almost independent of the Courant number (Fig.(18)-(19)).

It has been claimed in [5] that the S-MRTD Scheme is slightly oscillating and its performance is only comparable with the 14th order accuracy Yee's scheme. Though this is true for the S-MRTD schemes with stencil size of 8, the comparison of the dispersion diagrams of Yee's FDTD scheme, Yee's 16th order (H.F.D.-16) and 22th order (H.F.D.-22) and S-MRTD and Wo-MRTD schemes with different stencils leads to interesting results. For comparison purposes, the values of $\Delta t = \Delta t_{max}/5$ and $\Delta t_{max} = 0.368112\Delta l/c$ have been used and all the dispersion curves are subtracted by the linear dispersion relation for 1D simulations. Fig.(20) shows that the S-MRTD scheme with stencil 10 has a comparable performance to the 16th order Yee's scheme. The enhancement of the wavelets for the same stencil improves significantly the dispersion characteristics of the MRTD scheme increasing the dynamic range of ω by approximately 90% and comparing favorable even to the 22th order Yee's scheme. This is expected due to the fact that the scaling+wavelet basis spans a larger ("more complete") subspace of \mathbb{R} than the scaling functions alone. Both S-MRTD and Wo-MRTD schemes have identical numerical phase errors up to the point that the S-MRTD scheme starts diverging (Fig.(21)). As the stencil size of the Wo-MRTD scheme is increasing from 6 to 12 (Fig.(22)-(23)), the oscillatory variation of the phase error is diminishing to a negligible level generating an almost flat algorithm similar to the higher order Yee's ones.

As a conclusion, due to the poor dispersion performance of the FDTD technique even for 10 $cells/\text{wavelength}$ a normal to coarse grid is always required to avoid significant pulse distortions especially for the higher-spatial-frequency components. MRTD offers low dispersion even for sparse grids very close to the Nyquist limit.

V Conclusion

The stability and the dispersion performance of the recently developed Battle-Lemarie MRTD schemes has been investigated for different stencil sizes and for 0-resolution wavelets. Analytical expressions for the maximum

stable time-step have been derived. Larger stencils decrease the numerical phase error making it significantly lower than FDTD for low and medium discretizations. Stencil sizes greater than 10 offer a smaller phase error than FDTD even for discretizations close to 50 cells/wavelength. The enhancement of wavelets further improves the dispersion performance for discretizations close to the Nyquist limit (2-3 cells/wavelength) making it comparable to that of much denser grids, though it decreases the value of the maximum time-step guaranteeing the stability of the scheme.

VI Acknowledgments

This work has been made possible by the U.S. Army Research Office.

References

- [1] A.Taflove, "Computational Electrodynamics", Artech House, 1995.
- [2] M.Krumpholz, L.P.B.Katehi, "MRTD: New Time Domain Schemes Based on Multiresolution Analysis", IEEE Trans. Microwave Theory and Techniques, vol. 44, no. 4, pp. 555-561, April 1996.
- [3] K.S.Yee, "Numerical solution of initial boundary value problems involving Maxwell's equations in isotropic media", IEEE Trans. Antennas Propagation, pp.302-307, May 1966.
- [4] K.L.Shlager and J.B.Schneider, "Analysis of the Dispersion Properties of the Multiresolution Time-Domain Method", IEEE AP-S 1997 Proceedings, vol. 4, pp. 2144-2147, 1997.
- [5] W.Y.Tam, "Comments on "New Prospects for Time Domain Analysis"", IEEE Microwave and Guided Wave Letters, vol. 6, pp. 422-423, 1996.

LIST OF FIGURE CAPTIONS

- Figure 1: Stability Parameters for MRTD.
- Figure 2: Dispersion Characteristics of S-MRTD for $n_a=8$.
- Figure 3: Dispersion Characteristics of S-MRTD for $n_a=10$.
- Figure 4: Dispersion Characteristics of S-MRTD for $n_a=12$.
- Figure 5: Dispersion Characteristics of S-MRTD for $n_a=14$.
- Figure 6: Stencil Effect on the Dispersion Characteristics of S-MRTD. (Sparse Grid).
- Figure 7: Stencil Effect on the Dispersion Characteristics of S-MRTD. (Dense Grid).
- Figure 8: Wavelets Effect on the Dispersion Characteristics of MRTD for $n_a=8$ (Coarse Grid).
- Figure 9: Wavelets Effect on the Dispersion Characteristics of MRTD for $n_a=8$ (Denser Grid).
- Figure 10: Wavelets Effect on the Dispersion Characteristics of MRTD for $n_a=10$ (Coarse Grid).
- Figure 11: Wavelets Effect on the Dispersion Characteristics of MRTD for $n_a=10$ (Denser Grid).
- Figure 12: Wavelets Effect on the Dispersion Characteristics of MRTD for $n_a=12$ (Coarse Grid).
- Figure 13: Wavelets Effect on the Dispersion Characteristics of MRTD for $n_a=12$ (Denser Grid).
- Figure 14: Effect of the Courant Number on the Dispersion Characteristics of $W_0 - MRTD$ for $n_a = n_b = n_c =$
- Figure 15: Effect of the Courant Number on the Dispersion Characteristics of $W_0 - MRTD$ for $n_a = n_b = n_c =$
- Figure 16: Effect of the Courant Number on the Dispersion Characteristics of $W_0 - MRTD$ for $n_a = n_b = n_c =$
- Figure 17: Effect of the Courant Number on the Dispersion Characteristics of $W_0 - MRTD$ for $n_a = n_b = n_c =$
- Figure 18: Effect of the Courant Number on the Dispersion Characteristics of FDTD (Coarse Grid).
- Figure 19: Effect of the Courant Number on the Dispersion Characteristics of FDTD (Denser Grid).
- Figure 20: Comparison of the Dispersion Performance of S-MRTD and W_0 -MRTD with Different Higher Order
- Figure 21: Details of Fig.(20).
- Figure 22: Comparison of the Oscillations of W_0 -MRTD Scheme for Different Stencil Size.
- Figure 23: Details of Fig.(22).

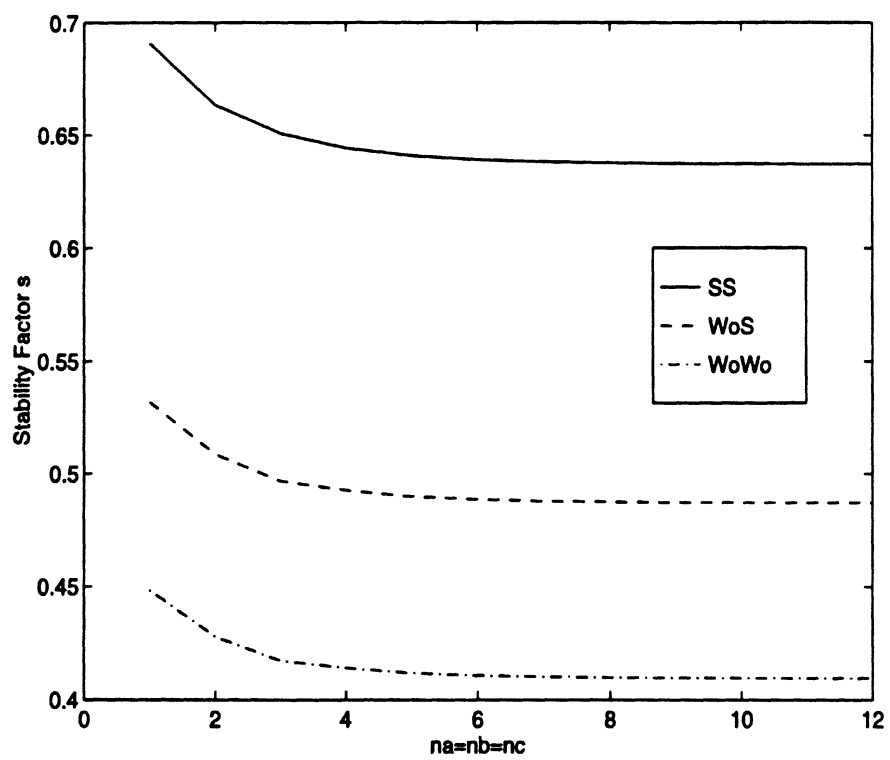


Figure 1: Stability Parameter s for MRTD.

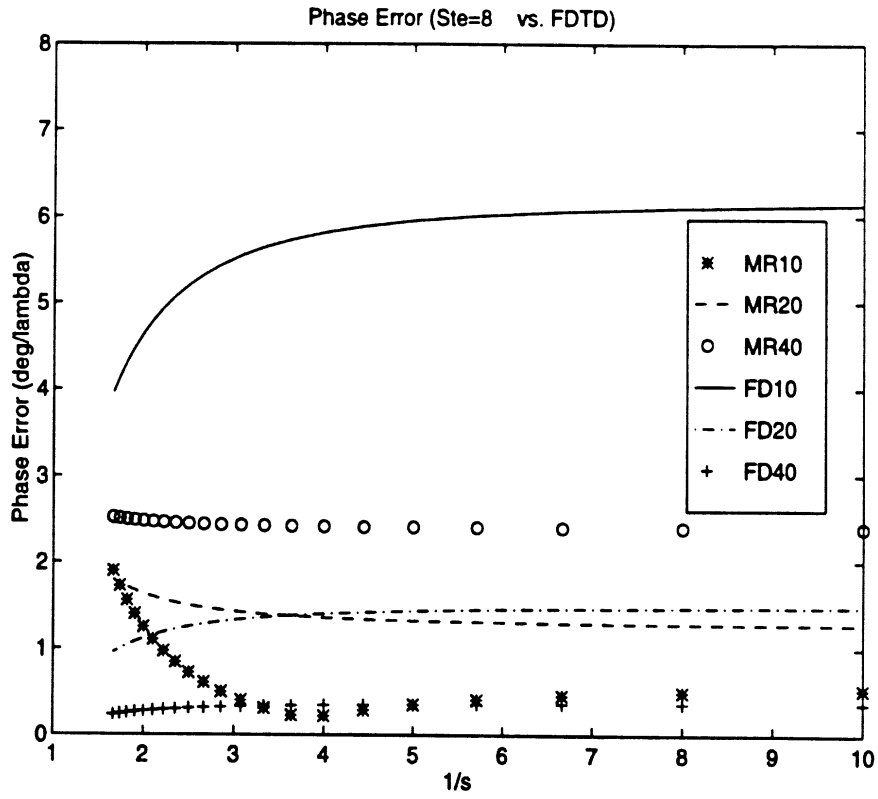


Figure 2: Dispersion Characteristics of S-MRTD for $n_a=8$.

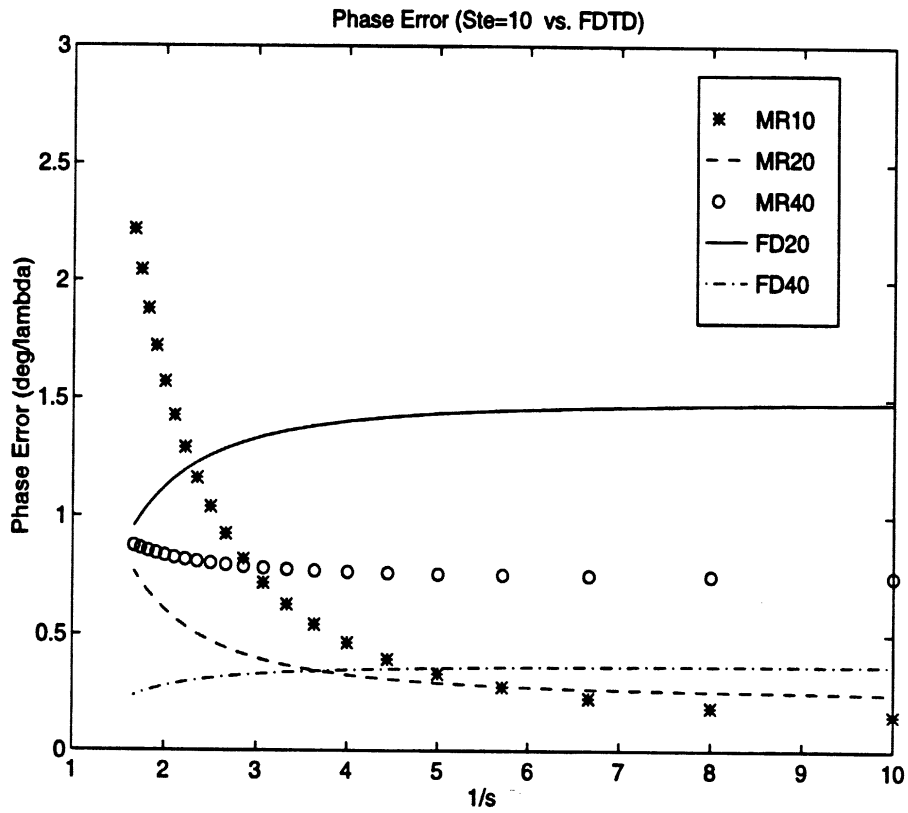


Figure 3: Dispersion Characteristics of S-MRTD for $n_a=10$.

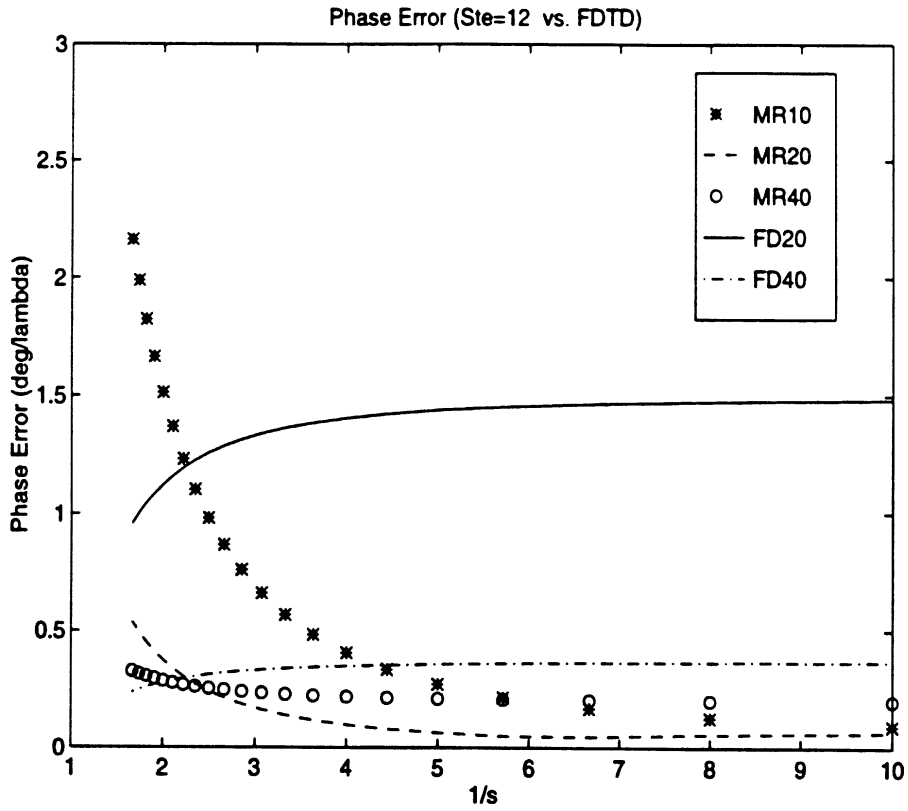


Figure 4: Dispersion Characteristics of S-MRTD for $n_a=12$.

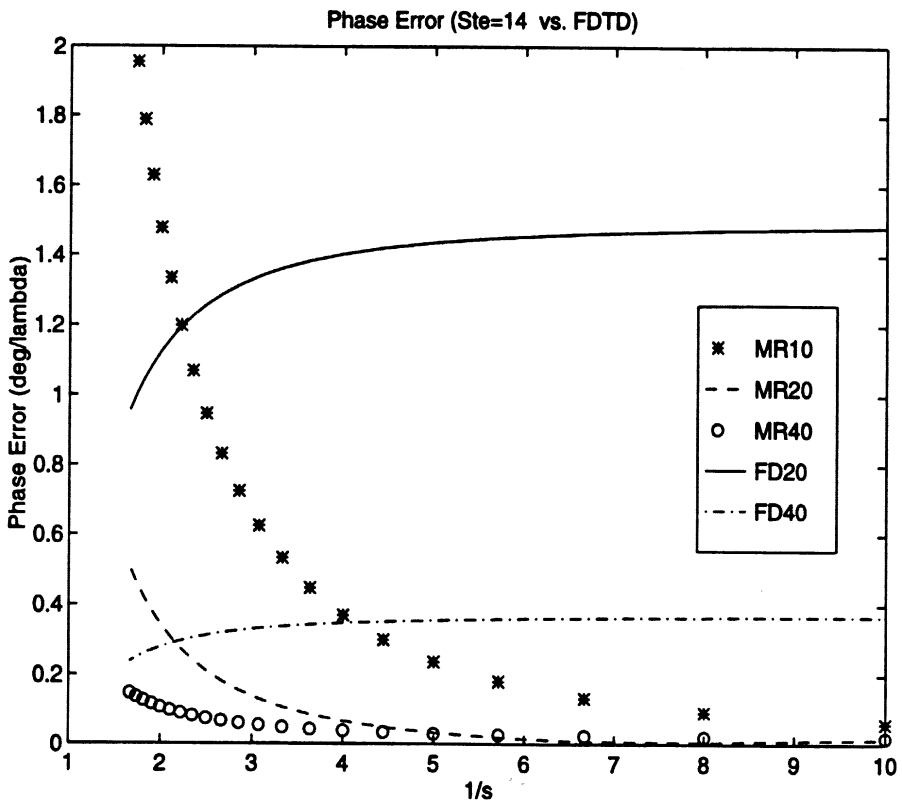


Figure 5: Dispersion Characteristics of S-MRTD for $n_a=14$.

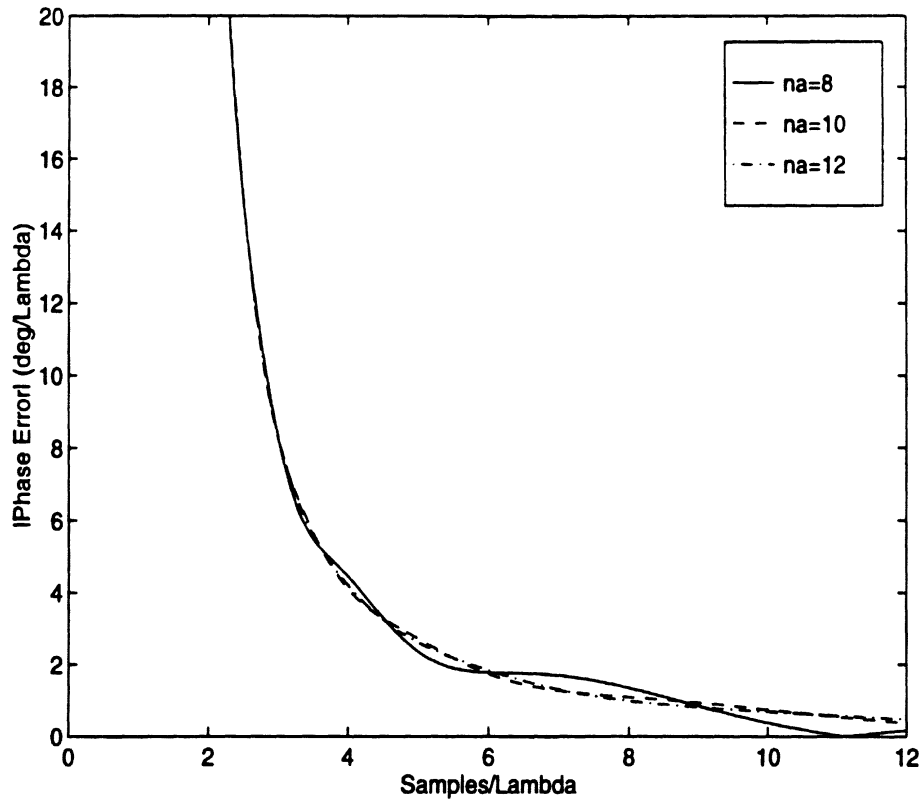


Figure 6: Stencil Effect on the Dispersion Characteristics of S-MRTD (Sparse Grid).

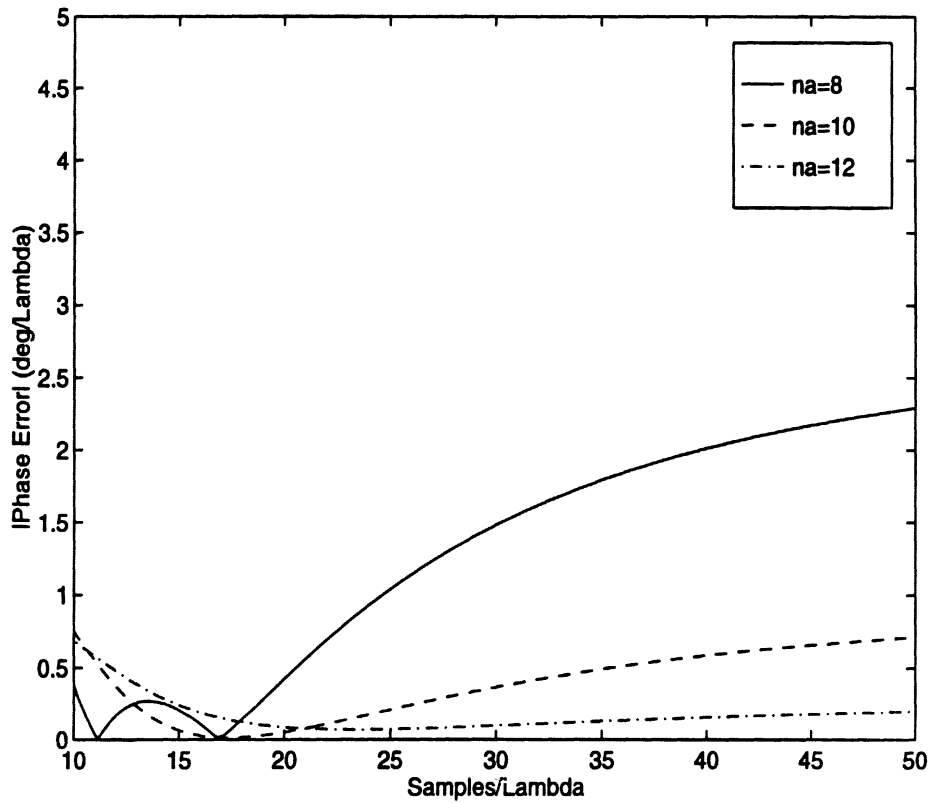


Figure 7: Stencil Effect on the Dispersion Characteristics of S-MRTD (Dense Grid).

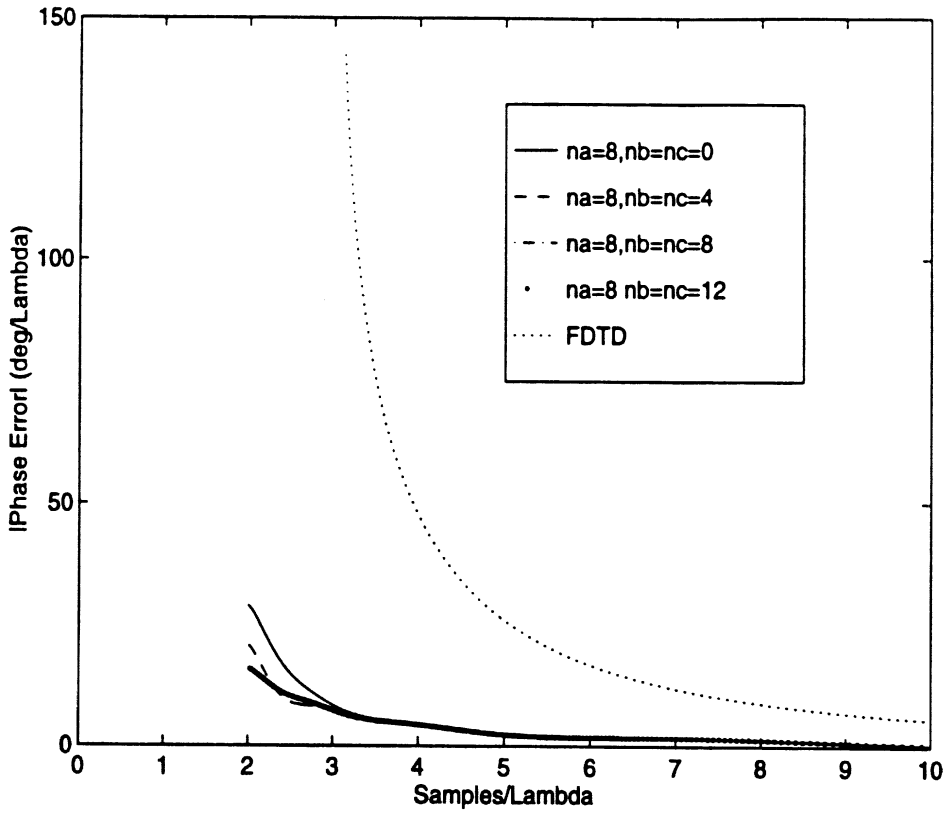


Figure 8: Wavelets Effect on the Dispersion Characteristics of MRTD for $n_a=8$ (Coarse Grid).

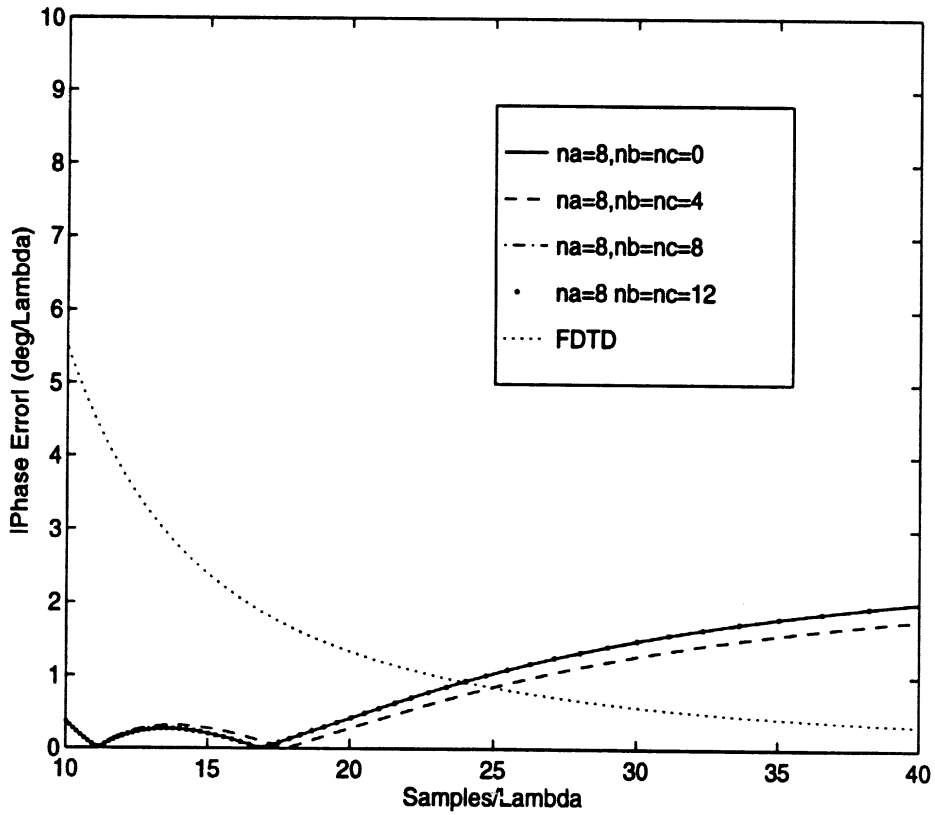


Figure 9: Wavelets Effect on the Dispersion Characteristics of MRTD for $n_a=8$ (Denser Grid).

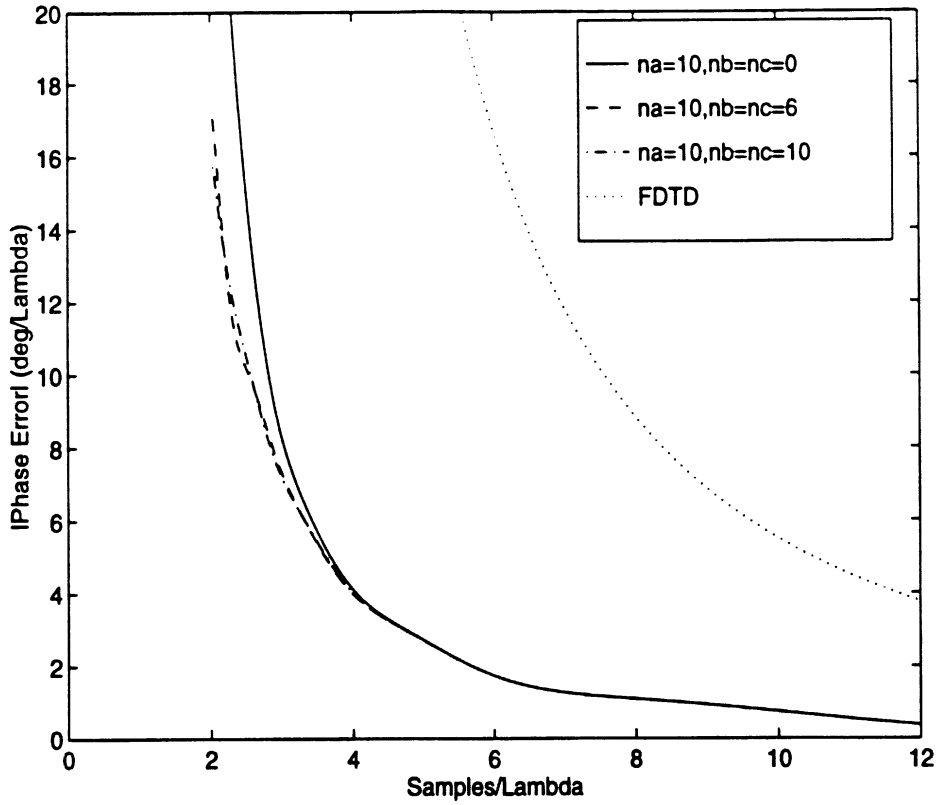


Figure 10: Wavelets Effect on the Dispersion Characteristics of MRTD for $n_a=10$ (Coarse Grid).

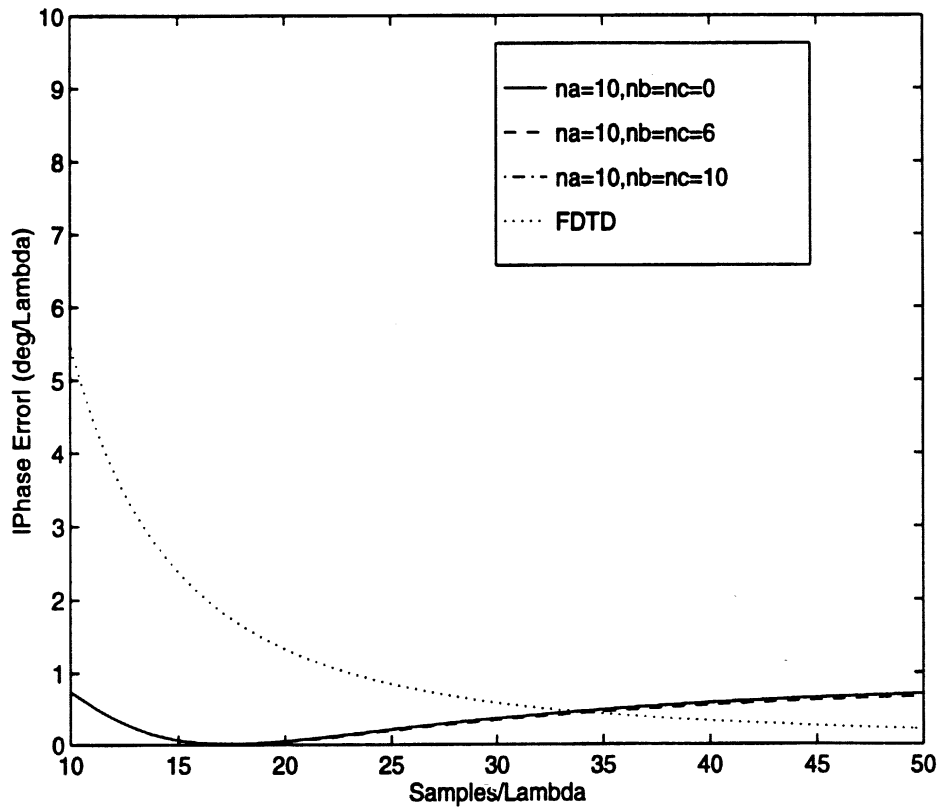


Figure 11: Wavelets Effect on the Dispersion Characteristics of MRTD for $n_a=10$ (Denser Grid).

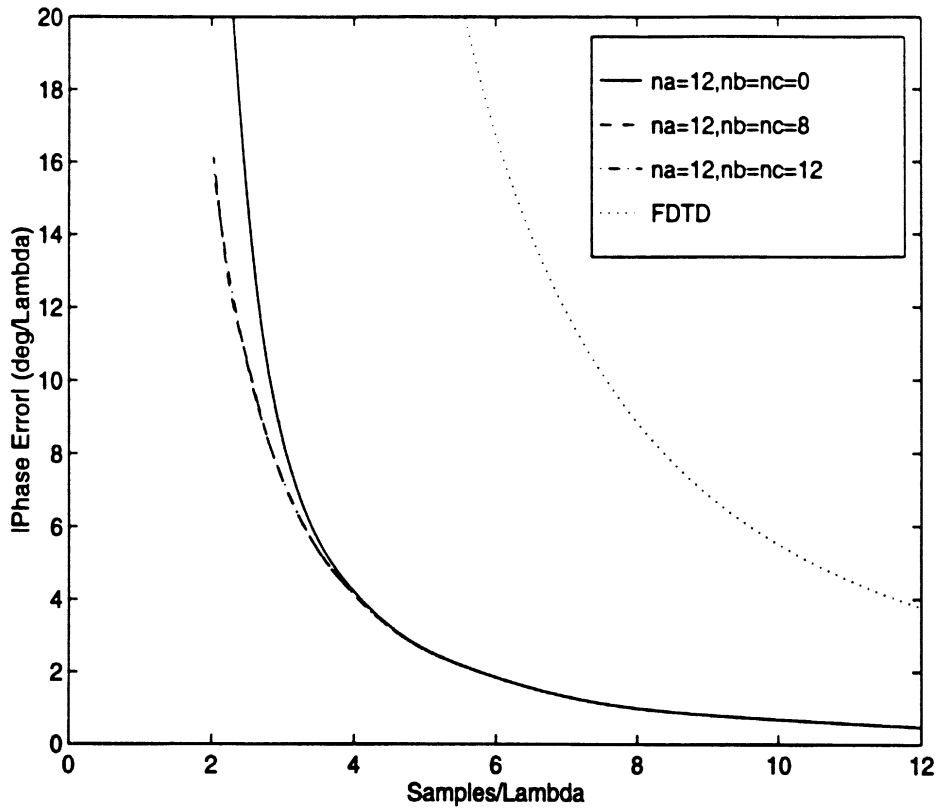


Figure 12: Wavelets Effect on the Dispersion Characteristics of MRTD for $n_a=12$ (Coarse Grid).

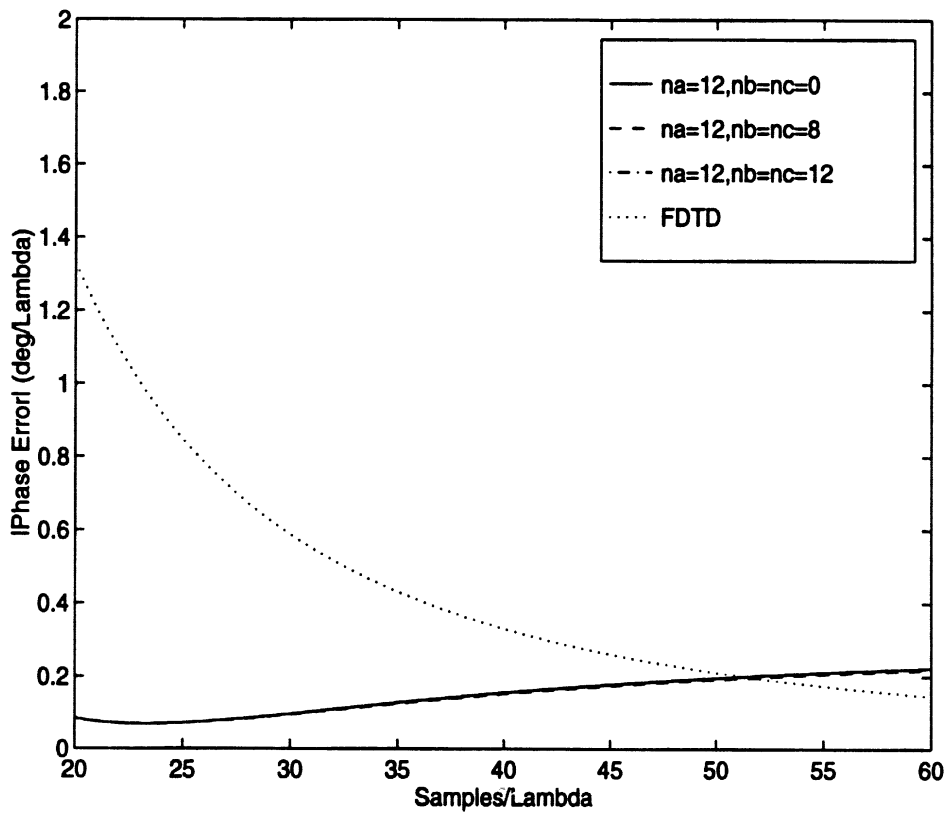


Figure 13: Wavelets Effect on the Dispersion Characteristics of MRTD for $n_a=12$ (Denser Grid).

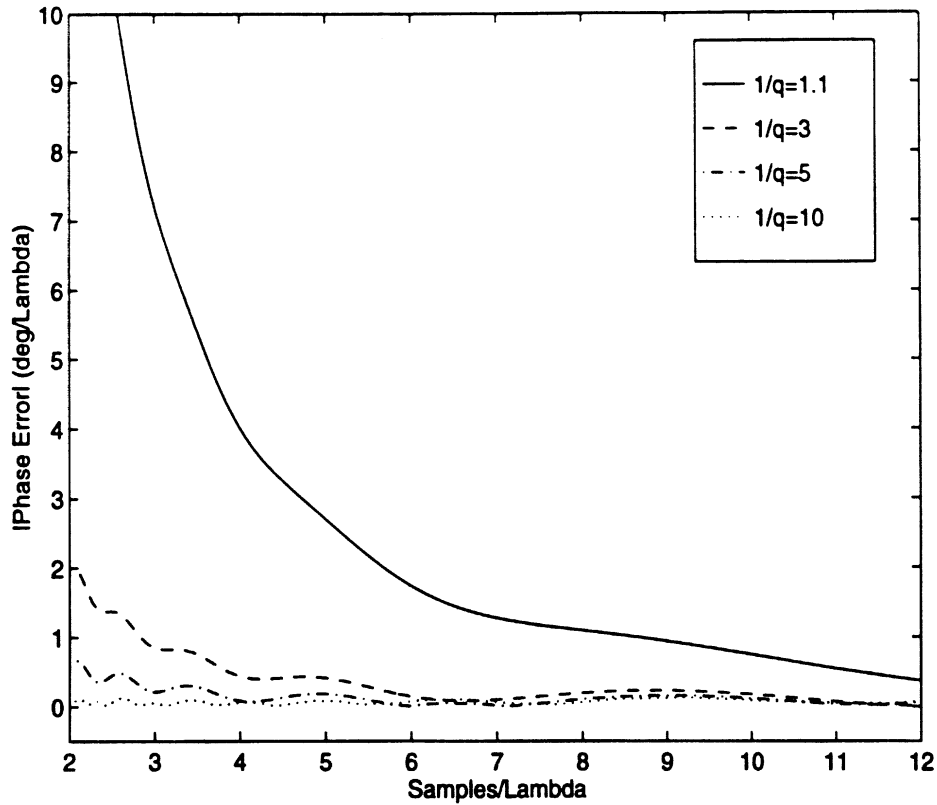


Figure 14: Effect of the Courant Number on the Dispersion Characteristics of $W_0 - MRTD$ for $n_a = n_b = n_c = 10$ (Coarse Grid).

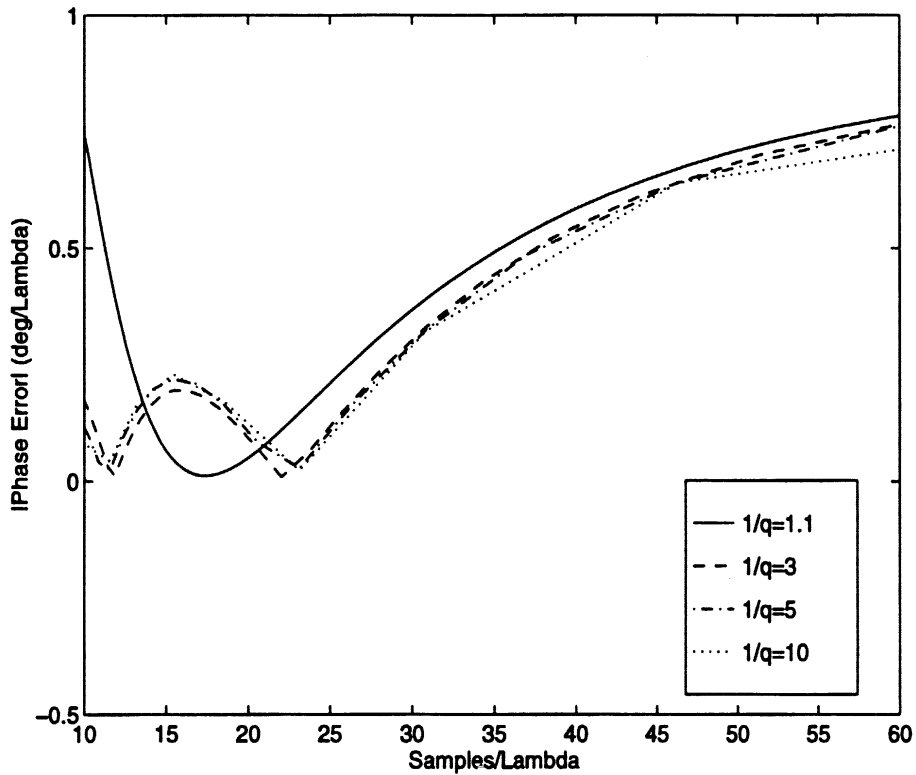


Figure 15: Effect of the Courant Number on the Dispersion Characteristics of $W_0 - MRTD$ for $n_a = n_b = n_c = 10$ (Denser Grid).

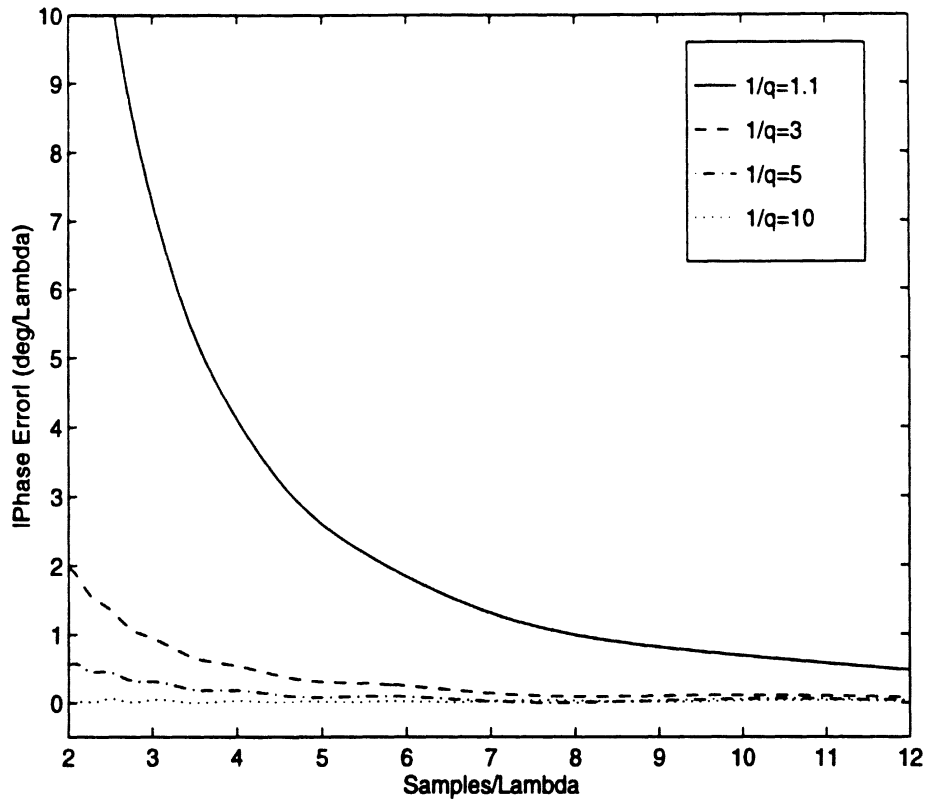


Figure 16: Effect of the Courant Number on the Dispersion Characteristics of $W_0 - MRTD$ for $n_a = n_b = n_c = 12$ (Coarse Grid).

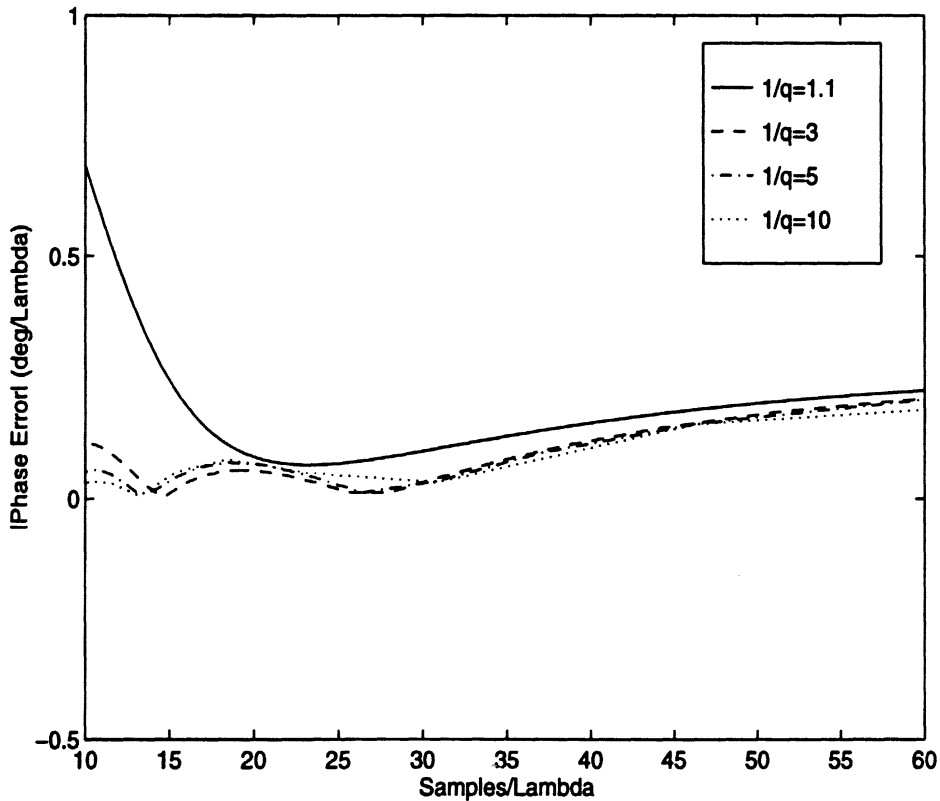


Figure 17: Effect of the Courant Number on the Dispersion Characteristics of $W_0 - MRTD$ for $n_a = n_b = n_c = 12$ (Denser Grid).

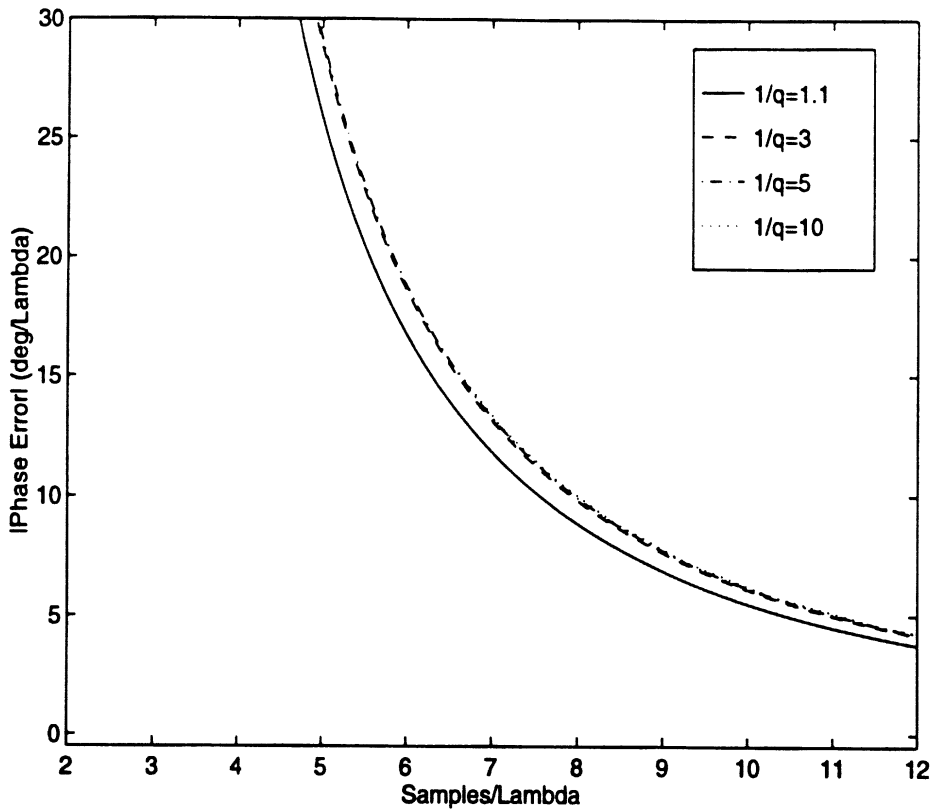


Figure 18: Effect of the Courant Number on the Dispersion Characteristics of FDTD (Coarse Grid).

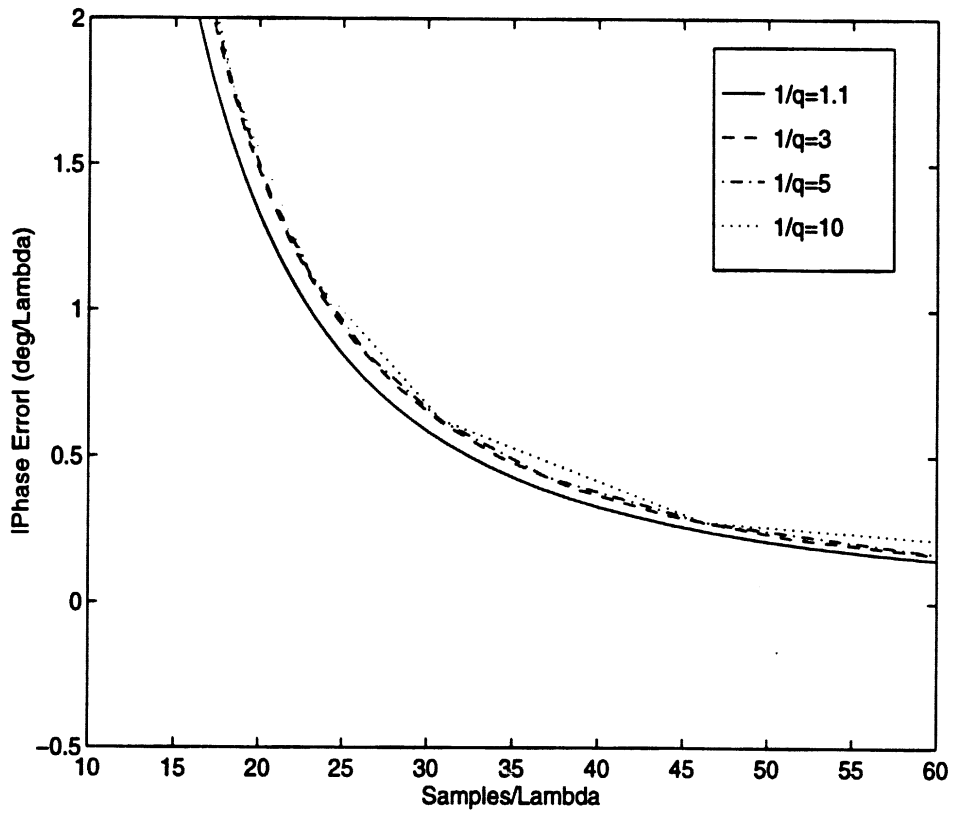


Figure 19: Effect of the Courant Number on the Dispersion Characteristics of FDTD (Denser Grid).

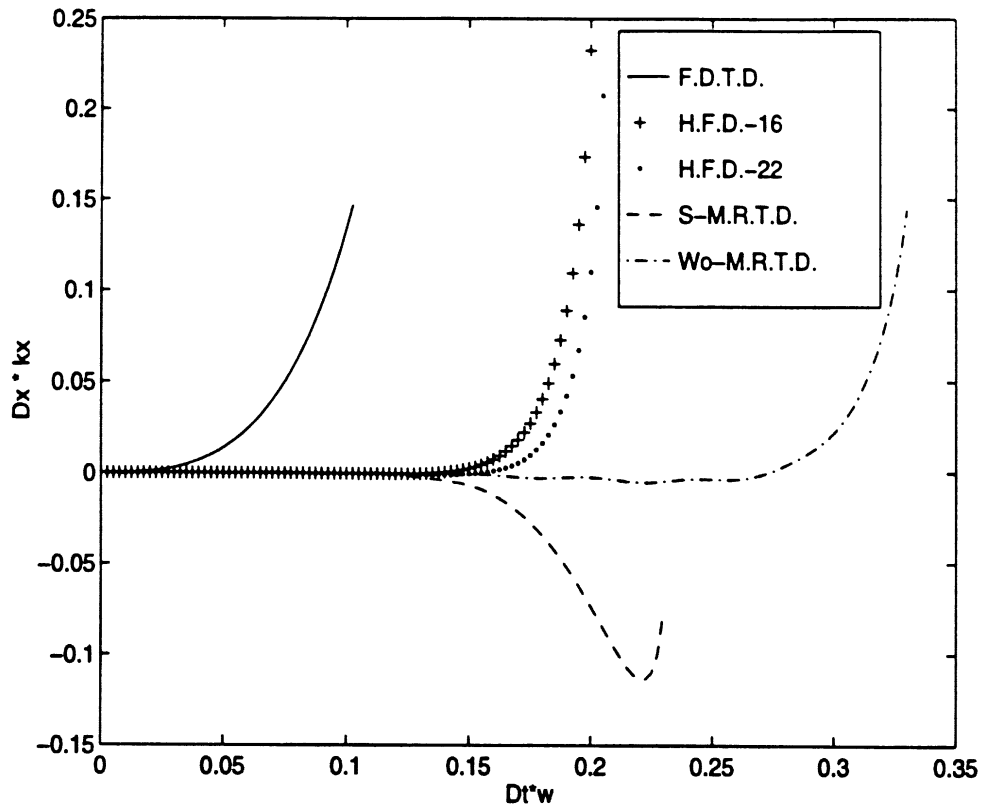


Figure 20: Comparison of the Dispersion Performance of S-MRTD and Wo-MRTD with Different Higher Order Yee's Schemes.

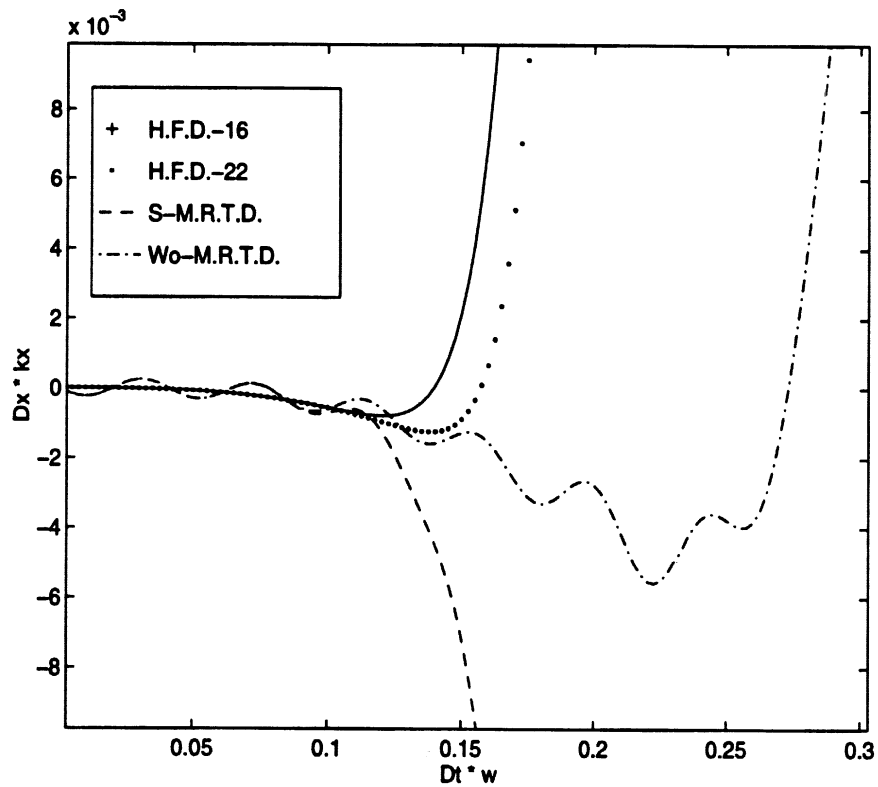


Figure 21: Details of Fig.(20).

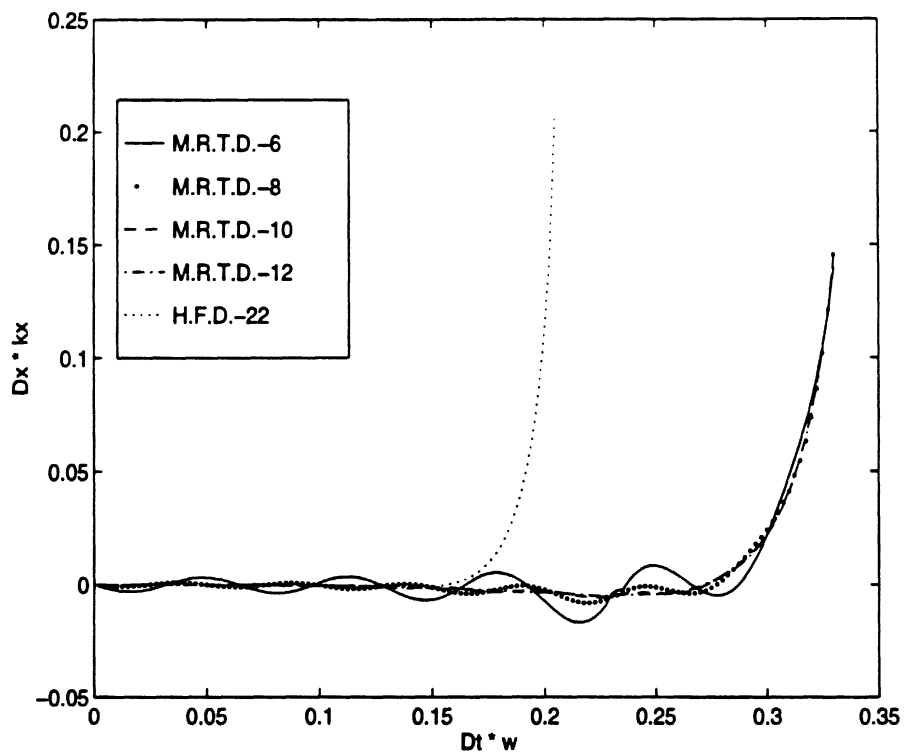


Figure 22: Comparison of the Oscillations of Wo-MRTD Scheme for Different Stencil Size.

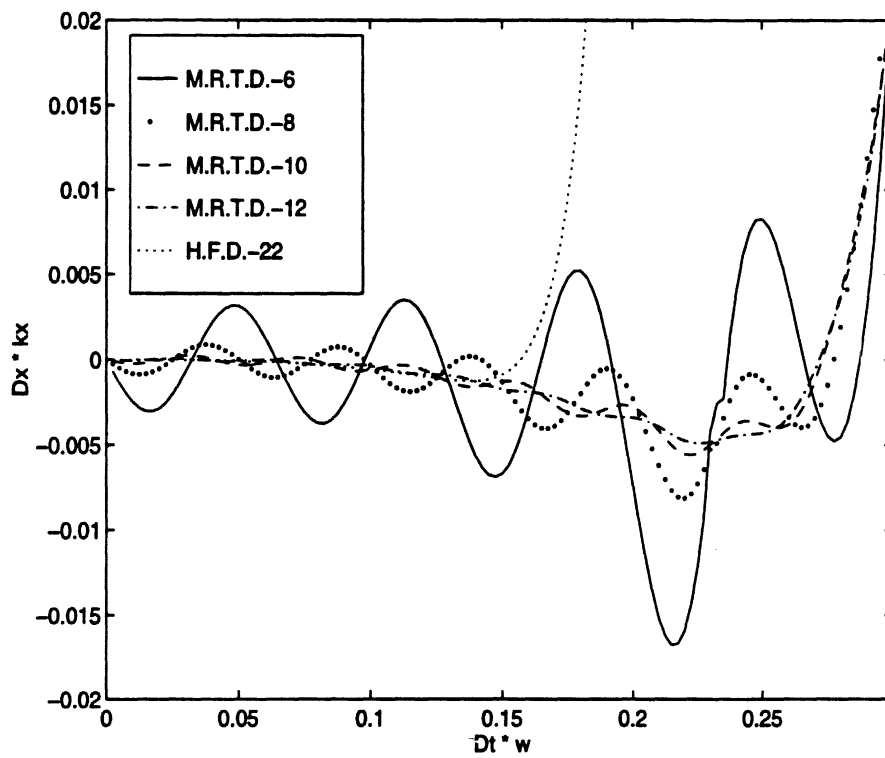


Figure 23: Details of Fig.(22).

TIME ADAPTIVE TIME-DOMAIN TECHNIQUES FOR THE DESIGN OF MICROWAVE CIRCUITS

Emmanouil M. Tentzeris¹, James Harvey², Linda P.B. Katehi¹

¹ Radiation Laboratory, Department of Electrical Engineering and Computer Science
University of Michigan, Ann Arbor, MI 48109-2122

² Army Research Office, NC

Abstract

A novel Time Adaptive Time-Domain Technique based on the Haar expansion basis is proposed and applied to various circuit problems. This scheme offers improved time resolution in comparison to conventional Time-Domain schemes (F.D.T.D.) while maintaining a similar accuracy with commercial circuit simulators.

I Discussion on the Expansion Basis Choice for MRTD

It is well known that the method of moments provides a mathematically correct approach for the discretization of integral and partial differential equations. Since it allows for the use of any complete and orthonormal set, the choice of an appropriate expansion set may lead to different time domain schemes. For example, the expansion of the unknown fields using pulse functions leads to Yee's FDTD scheme. In a MRTD scheme [?, ?] the fields are represented by a two-fold expansion in scaling and wavelet functions with respect to time/space. Scaling functions guarantee a correct modelling of smoothly-varying fields. In regions characterized by strong field variations or field singularities, higher resolution is enhanced by incorporating wavelets in the field expansions. The major advantage of the use of Multiresolution analysis to time domain is the capability to develop time and space adaptive grids. This is due to the property of the wavelet expansion functions to interact weakly and allow for a spatial sparsity that may vary with time through a thresholding process.

MRTD schemes based on cubic spline Battle-Lemarie scaling and wavelet functions have been successfully applied to the simulation of 2D and 3D open and shielded problems [?, ?, ?, ?]. The functions of this family do not have compact support, thus the MRTD schemes have to be truncated with respect to space. Localized boundary conditions (PECs, PMC's etc.) and material properties are modelled by use of the image principle and of matrix equations respectively. However, this disadvantage is offset by the low-pass (scaling) and band-pass (wavelets) characteristics in spectral domain, allowing for an a priori estimate of the number of resolution levels necessary for a correct field modelling. In addition, the evaluation of the moment method integrals during the discretization of Maxwell's PDEs is simplified due to the existence of closed form expressions in spectral domain and simple representations in space domain. Dispersion analysis of this MRTD scheme shows the capability of excellent accuracy with up to 2 points/wavelength (Nyquist Limit). However, specific circuit problems may require the use of functions with compact support. Especially in the approximation of time derivatives, the use of entire domain expansion basis would require very high memory resources for the storage of the field values everywhere on the grid for the whole or a large fraction of the simulation time. This problem does not exist in the approximation of the spatial derivatives since the field values on the neighboring spatial grid points have to be calculated and stored no matter what expansion basis are used. For that reason, Haar basis functions have been utilized and have led to [?]. As an extension to this approach, intervalic wavelets (Fig.1) may be incorporated into the solution of SPICE-type circuits. Results from that new technique will be presented in this Chapter .

II Applications in SPICE problems

For simplicity, the 1D MRTD scheme will be derived. It can be extended to 2D and 3D in a straightforward way. In addition, only the 0-resolution of wavelets is enhanced. The Voltage and the Current are displaced by half step in both time- and space-domains (Yee cell formulation) and are expanded in a summation of scaling functions in space and scaling (ϕ) and wavelet (ψ_0) components in time

$$\begin{aligned} V(z, t) &= \sum_{m=-\infty}^{\infty} \sum_{i=-\infty}^{\infty} ({}_i V_m^\phi \phi_i(t) + {}_i V_m^{\psi_0} \psi_{0,i}(t)) \phi_m(z) \\ I(z, t) &= \sum_{m=-\infty}^{\infty} \sum_{i=-\infty}^{\infty} ({}_{i-0.5} I_{m-0.5}^\phi \phi_{i-0.5}(t) + {}_{i-0.5} I_{m-0.5}^{\psi_0} \psi_{0,i-0.5}(t)) \phi_{m-0.5}(z) \quad , \end{aligned} \quad (1)$$

where $\phi_i(t) = \phi(t/\Delta t - i)$ and $\psi_{0,i}(t) = \psi_0(t/\Delta t - i)$ represent the 0-order intervalic scaling and 0-resolution wavelet functions. The conventional notation ${}_k V_m$ is used for the voltage component at time $t = k\Delta t$ and $z = m\Delta z$, where Δt and Δz are the time-step and the spatial cell size respectively. The notation for the current I is similar.

Due to the finite-domain nature of the expansion basis, the Hard Boundary conditions (Open/Short Circuit) can be easily modeled. If a Short Circuit exists at the $z = m\Delta z$, then both scaling and wavelet voltage coefficients for the m - cell must be set to zero for each time-step k .

$${}_k V_m^\phi = {}_k V_m^{\psi_0} = 0, \quad k = 0, 1, 2, \dots \quad (2)$$

Similarly, an Open Circuit at $z = (m - 0.5)\Delta z$ can be modeled by applying the conditions

$${}_{k-0.5} I_{m-0.5}^\phi = {}_{k-0.5} I_{m-0.5}^{\psi_0} = 0, \quad k = 0, 1, 2, \dots \quad (3)$$

The alternating nature of the 0-resolution wavelet function guarantees the double time-domain resolution of the MRTD scheme. Assuming that the voltage scaling and wavelet coefficients at $m = \Delta z$ for a specific time-step k , two values can be defined for the time span $[(k - 0.5)\Delta t, (k + 0.5)\Delta t]$ of this time-step

$${}_k V_m^{total,1} = {}_k V_m^\phi + {}_k V_m^{\psi_0}, \quad t \in [(k - 0.5)\Delta t, k\Delta t] \quad (4)$$

$${}_k V_m^{total,2} = {}_k V_m^\phi - {}_k V_m^{\psi_0}, \quad t \in [k\Delta t, (k + 0.5)\Delta t] \quad (5)$$

II.1 Distributed Elements

II.1.1 Lossless Line

The ideal transmission line (Fig.2) equations are given by

$$\begin{aligned} \frac{dV}{dz} &= -L_{dis} \frac{dI}{dt} \\ \frac{dI}{dz} &= -C_{dis} \frac{dV}{dt} \quad , \end{aligned} \quad (6)$$

where L_{dis}, C_{dis} are the distributed inductance and capacitance of the line. Inserting the expansions of Eq.(1) and applying the Method of Moments, the following MRTD equations are derived

$$\frac{C_{dis}}{\Delta t} ({}_{k+1} V_m^\phi - {}_k V_m^\phi) = -\frac{1}{\Delta z} ({}_{k+0.5} I_{m+0.5}^\phi - {}_{k+0.5} I_{m-0.5}^\phi) \quad (7)$$

$$\frac{C_{dis}}{\Delta t} ({}_{k+1}V_m^{\psi_0} - {}_kV_m^{\psi_0}) = -\frac{1}{\Delta z} ({}_{k+0.5}I_{m+0.5}^{\psi_0} - {}_{k-0.5}I_{m-0.5}^{\psi_0}) \quad (8)$$

$$\frac{L_{dis}}{\Delta t} ({}_{k+0.5}I_{m-0.5}^{\phi} - {}_{k-0.5}I_{m-0.5}^{\phi}) = -\frac{1}{\Delta z} ({}_kV_m^{\phi} - {}_kV_{m-1}^{\phi}) \quad (9)$$

$$\frac{L_{dis}}{\Delta t} ({}_{k+0.5}I_{m-0.5}^{\psi_0} - {}_{k-0.5}I_{m-0.5}^{\psi_0}) = -\frac{1}{\Delta z} ({}_kV_m^{\psi_0} - {}_kV_{m-1}^{\psi_0}) \quad (10)$$

It can be observed that Eqs.(7) and (9) updating the scaling coefficients only are independent of the Eqs.(8) and (10) updating the wavelet coefficients. To create an efficient time adaptive algorithm, all four equations must be coupled. An efficient way is to apply the excitation in a physically correct manner. If the excitation has the time-dependence $g(t)$ at the location $z = m_e \Delta z$, then the scaling and wavelet coefficients for this cell have to take the values

$$\begin{aligned} {}_kV_{m_e}^{\phi} &= \int_{(k-0.5)\Delta t}^{(k+0.5)\Delta t} g(t) \phi_k(t) dt \\ {}_kV_{m_e}^{\psi_0} &= \int_{(k-0.5)\Delta t}^{(k+0.5)\Delta t} g(t) \psi_{0,k}(t) dt \end{aligned} \quad (11)$$

To validate this approach, the MRTD algorithm was applied to the simulation of a lossless transmission line with $(L_{dis}, C_{dis}) = (20nH/m, 3nF/m)$ for a Gabor excitation and time-step $dt = dt_{max}/1.01$. Fig.(3) which displays the Voltage Scaling and Wavelet Coefficients evolution at $z = 200\Delta z$ for the first 800 time-steps of the simulation, shows that the wavelet coefficients have the correct shape (significant values only at areas with significant scaling function values) and are close to the 12% of the respective scaling functions. Fig.(4) which compares the total voltage value at $z = 200\Delta z$ calculated by FDTD (Sc.ONLY) and MRTD (Sc.+Wav.) for the time-steps 357–362 demonstrates the ability of this MRTD scheme to double the conventional FDTD resolution in the time-domain by providing two values for each time-step. The fact that the wavelet coefficients take significant values only for a small number of time-steps allows for their thresholding by comparing them to a combination of relative to the respective value of the scaling coefficient ($5.e-4$) and absolute ($1.e-6$) thresholds. Fig.(5) proves that up to 60% of the maximum number of wavelet coefficients are necessary for an accurate simulation, offering an extra economy in memory by a factor of 20%.

II.1.2 Lossy Line

The lossy transmission line (Fig.6) equations are derived by the ideal transmission line equations (Eq.(6)) adding the Conductor Loss R_{dis} and the Dielectric Loss G_{dis}

$$\begin{aligned} \frac{dV}{dz} &= -R_{dis}I - L_{dis} \frac{dI}{dt} \\ \frac{dI}{dz} &= -G_{dis}V - C_{dis} \frac{dV}{dt} \end{aligned} \quad (12)$$

Following a procedure similar to the previous section, the following MRTD equations are derived

$$\begin{aligned} {}_{k+1}V_m^{\phi} &= -\frac{(C_1 - C_2)}{C_1^2} \Delta t ({}_{k+0.5}I_{m+0.5}^{\phi} - {}_{k-0.5}I_{m-0.5}^{\phi}) + \frac{C_2}{C_1^2} \Delta t ({}_{k+0.5}I_{m+0.5}^{\psi_0} - {}_{k-0.5}I_{m-0.5}^{\psi_0}) \\ &+ \frac{(C_1 - C_2)^2 + C_2^2}{C_1^2} {}_kV_m^{\phi} - 2 \frac{C_2^2}{C_1^2} {}_kV_m^{\psi_0} \end{aligned} \quad (13)$$

$$\begin{aligned} {}_{k+1}V_m^{\psi_0} &= -\frac{C_2}{C_1^2} \Delta t ({}_{k+0.5}I_{m+0.5}^{\phi} - {}_{k-0.5}I_{m-0.5}^{\phi}) - \frac{(C_1 + C_2)}{C_1^2} \Delta t ({}_{k+0.5}I_{m+0.5}^{\psi_0} - {}_{k-0.5}I_{m-0.5}^{\psi_0}) \\ &- 2 \frac{C_2^2}{C_1^2} {}_kV_m^{\phi} + \frac{(C_1 - C_2)^2 + C_2^2}{C_1^2} {}_kV_m^{\psi_0} \end{aligned} \quad (14)$$

$$\begin{aligned}
{}^{k+0.5}I_{m-0.5}^\phi &= - \frac{(C_3 - C_4)}{C_3^2} \Delta t ({}^kV_m^\phi - {}^kV_{m-1}^\phi) + \frac{C_4}{C_3^2} \Delta t ({}^kV_m^{\psi_0} - {}^kV_{m-1}^{\psi_0}) \\
&+ \frac{(C_3 - C_4)^2 + C_4^2}{C_3^2} {}^{k-0.5}I_{m-0.5}^\phi - 2 \frac{C_4^2}{C_3^2} {}^{k-0.5}I_{m-0.5}^{\psi_0}
\end{aligned} \tag{15}$$

$$\begin{aligned}
{}^{k+0.5}I_{m-0.5}^{\psi_0} &= - \frac{C_4}{C_3^2} \Delta t ({}^kV_m^\phi - {}^kV_{m-1}^\phi) - \frac{(C_3 + C_4)}{C_3^2} \Delta t ({}^kV_m^{\psi_0} - {}^kV_{m-1}^{\psi_0}) \\
&- 2 \frac{C_4^2}{C_3^2} {}^{k-0.5}I_{m-0.5}^\phi + \frac{(C_3 - C_4)^2 + C_4^2}{C_3^2} {}^{k-0.5}I_{m-0.5}^{\psi_0} \quad ,
\end{aligned} \tag{16}$$

with

$$\begin{aligned}
C_1 &= C_{dis} \Delta z \quad , \quad C_2 = 0.5 G_{dis} \Delta z \Delta t, \\
C_3 &= L_{dis} \Delta z \quad , \quad C_4 = 0.5 R_{dis} \Delta z \Delta t, \quad .
\end{aligned}$$

For this type of transmission line, the equations giving the scaling and wavelet coefficients for voltage and current are coupled. Nevertheless, the condition (11) has to be applied in order to satisfy the physical boundary condition at the excitation cell(s). It has to be noted, that Eqs.(13)–(16) can be used only for lossy lines with low to medium Loss Coefficients. The threshold $C_2 \leq 4C_1$ for G_{dis} ($C_4 \leq 4C_3$ for R_{dis}) gave satisfactory results for all simulations. For higher loss coefficients, the Loss can be modeled in an exponential way similar to [?]. For example, for large values of R_{dis} ($C_4 > C_3$), Eqs.(15)–(16) have to be replaced by the following uncoupled expressions

$${}^{k+0.5}I_{m-0.5}^\phi = e^{\frac{-R_{dis} \Delta t}{L_{dis}}} {}^{k-0.5}I_{m-0.5}^\phi - e^{\frac{-0.5R_{dis} \Delta t}{L_{dis}}} \frac{\Delta t}{C_3} ({}^kV_m^\phi - {}^kV_{m-1}^\phi) \tag{17}$$

$${}^{k+0.5}I_{m-0.5}^{\psi_0} = e^{\frac{-R_{dis} \Delta t}{L_{dis}}} {}^{k-0.5}I_{m-0.5}^{\psi_0} - e^{\frac{-0.5R_{dis} \Delta t}{L_{dis}}} \frac{\Delta t}{C_3} ({}^kV_m^{\psi_0} - {}^kV_{m-1}^{\psi_0}) \tag{18}$$

Using this procedure, a termination layer similar to the FDTD widely used PML layer can be easily modeled. The R_{dis}, G_{dis} should have a spatial parabolic distribution with very high maximum value and they should satisfy the condition $G_{dis} = R_{dis} L_{dis} / C_{dis}$ for each cell of the layer. In this way, one matched transmission line can be simulated by choosing the appropriate R_{dis}, G_{dis} that satisfy the specified numerical reflection coefficient (usually smaller than -80dB).

For validation purposes, the propagation of a Gabor pulse along a lossy line with $R_{dis} = 5\Omega/m$ has been simulated and the scaling and wavelet voltage coefficients have been probed at the positions $z = 140\Delta z$ and $z = 160\Delta z$. Data for the first 200 time-steps ($\Delta t = 2\Delta t/3$) have been plotted in Fig.(7). The maximum value of the wavelet coefficients (approximately 7% of the respective scaling coefficient) is smaller than that of the lossless line. By applying a thresholding procedure using an absolute threshold of 10^{-6} and a relative threshold of $5e - 4$, an extra economy of 29% is achieved, since only 60% of the voltage and 25% of the current wavelet coefficients take values above the thresholds throughout the simulation time (Fig.(8)).

II.2 Lumped Elements

II.2.1 Passive Elements

Lumped Passive Elements such as Capacitors, Inductors and Resistors can be modeled in a similar way with the Distributed ones by numerically distributing them along one cell. For example, if one lumped Capacitor C_{lum} is located at $z = m\Delta z$ along a lossy line with $(R_{dis}, G_{dis}, L_{dis}, C_{dis})$, the voltage coefficients ${}^{k+1}V_m^\phi, {}^{k+1}V_m^{\psi_0}$ will

still be given by Eqs.(13)–(14). The only difference is that the constant C_1 will have the new value $C_1 = C_{tot} \Delta z$ with

$$C_{tot} = C_{dis} + \frac{C_{lum}}{\Delta z} \quad . \quad (19)$$

II.2.2 PN-Diode

To model lumped active elements such as a PN-diode, their nonlinear equation has to be discretized after inserting the voltage and current expansions. The MRTD equations are not linear and require the use of numerical solvers for nonlinear systems. The combined Newton-Raphson/Bisection solver has provided stable solutions for PN-diode simulations with $I_0 \leq 1.e - 10A$, though sometimes diverges for larger values. The voltage scaling and wavelet coefficients for the diode cell are updated by inserting the voltage and current expansion in the equation

$$I_{DIODE}(V) = I_0 (e^{qV/kT} - 1) \quad (20)$$

adding the diode capacitance C_j to the C_{dis} and applying the moments method, thus giving the nonlinear system for a diode positioned in parallel

$$\begin{aligned} (C_5 + C_{dis}) {}_k V_m^\phi + C_5 {}_k V_m^{\psi_0} + (C_5 - C_{dis}) {}_{k-1} V_m^\phi - C_5 {}_{k-1} V_m^{\psi_0} + \frac{\Delta t}{\Delta z} ({}_{k-0.5} I_{m+0.5}^\phi - {}_{k-0.5} I_{m-0.5}^\phi) \\ + 0.5 \Delta t C_j (e^{kT/q} I_0 ({}_{k-1} V_m^\phi - {}_{k-1} V_m^{\psi_0}) + e^{kT/q} I_0 ({}_k V_m^\phi + {}_k V_m^{\psi_0})) = 0 \end{aligned} \quad (21)$$

$$\begin{aligned} -C_5 {}_k V_m^\phi - (C_5 - C_{dis}) {}_k V_m^{\psi_0} + C_5 {}_{k-1} V_m^\phi - (C_5 + C_{lum}) {}_{k-1} V_m^{\psi_0} + \frac{\Delta t}{\Delta z} ({}_{k-0.5} I_{m+0.5}^{\psi_0} - {}_{k-0.5} I_{m-0.5}^{\psi_0}) \\ + 0.5 \Delta t C_j (e^{kT/q} I_0 ({}_{k-1} V_m^\phi - {}_{k-1} V_m^{\psi_0}) - e^{kT/q} I_0 ({}_k V_m^\phi + {}_k V_m^{\psi_0})) = 0 \end{aligned} \quad (22)$$

with

$$C_5 = 0.5 \Delta t G_{lum} \quad . \quad (23)$$

To validate the algorithm, the rectifier topology of Fig.(9) is analyzed using FDTD (Scaling Only) with $\Delta t = \Delta t_{max}/4.4$ and MRTD (Scaling+wavelets) with double time-step $\Delta t = \Delta t_{max}/2.2$. A lossless line with $(L_{dis}, C_{dis}) = (20nH/m, 3nF/m)$ and a PN-Diode with $I_0 = 3pA$ are used in the simulation. The probed total voltage is plotted in Fig.(10) and the agreement is very good. The use of an absolute threshold of 10^{-6} and a relative threshold of $5e - 4$ offers an extra economy of 35% for the MRTD algorithm.

III Conclusion

A Time Adaptive Time-Domain Technique based on intervalic wavelets has been proposed and applied to various types of circuits problems with active and passive lumped and distributed elements. This scheme exhibits significant savings in execution time and memory requirements while maintaining a similar accuracy with conventional circuit simulators.

References

- [1] M.Krumpholz, L.P.B.Katehi, "MRTD: New Time Domain Schemes Based on Multiresolution Analysis", IEEE Trans. Microwave Theory and Techniques, vol. 44, no. 4, pp. 555-561, April 1996.
- [2] E.Tentzeris, M.Krumpholz and L.P.B. Katehi, "Application of MRTD to Printed Transmission Lines", Proc. MTT-S 1996, pp. 573-576.
- [3] R. Robertson, E. Tentzeris, M. Krumpholz, L.P.B. Katehi, "Application of MRTD Analysis to Dielectric Cavity Structures", Proc. MTT-S 1996, pp. 1861-1864.
- [4] E.Tentzeris, R.Robertson, M.Krumpholz and L.P.B. Katehi, "Application of the PML Absorber to the MRTD Technique", Proc. AP-S 1996, pp. 634-637.

- [5] K.Goverdhanam, E.Tentzeris, M.Krumpholz and L.P.B. Katehi, "An FDTD Multigrid based on Multiresolution Analysis", Proc. AP-S 1996, pp. 352-355.
- [6] E.Tentzeris, R.Robertson, A.Cangellaris and L.P.B. Katehi, "Space- and Time- Adaptive Gridding Using MRTD", Proc. MTT-S 1997, pp. 337-340.

LIST OF FIGURE CAPTIONS

- Figure 1: 0-Order Intervalic Function Basis.
- Figure 2: Ideal (Lossless) Transmission Line.
- Figure 3: Voltage Coefficients.
- Figure 4: Comparison MRTD-FDTD.
- Figure 5: Fraction of Wavelets above Threshold.
- Figure 6: Lossy Transmission Line.
- Figure 7: Voltage Coefficients.
- Figure 8: Fraction of Wavelets above Threshold.
- Figure 9: Rectifier Geometry.
- Figure 10: Comparison MRTD-FDTD.

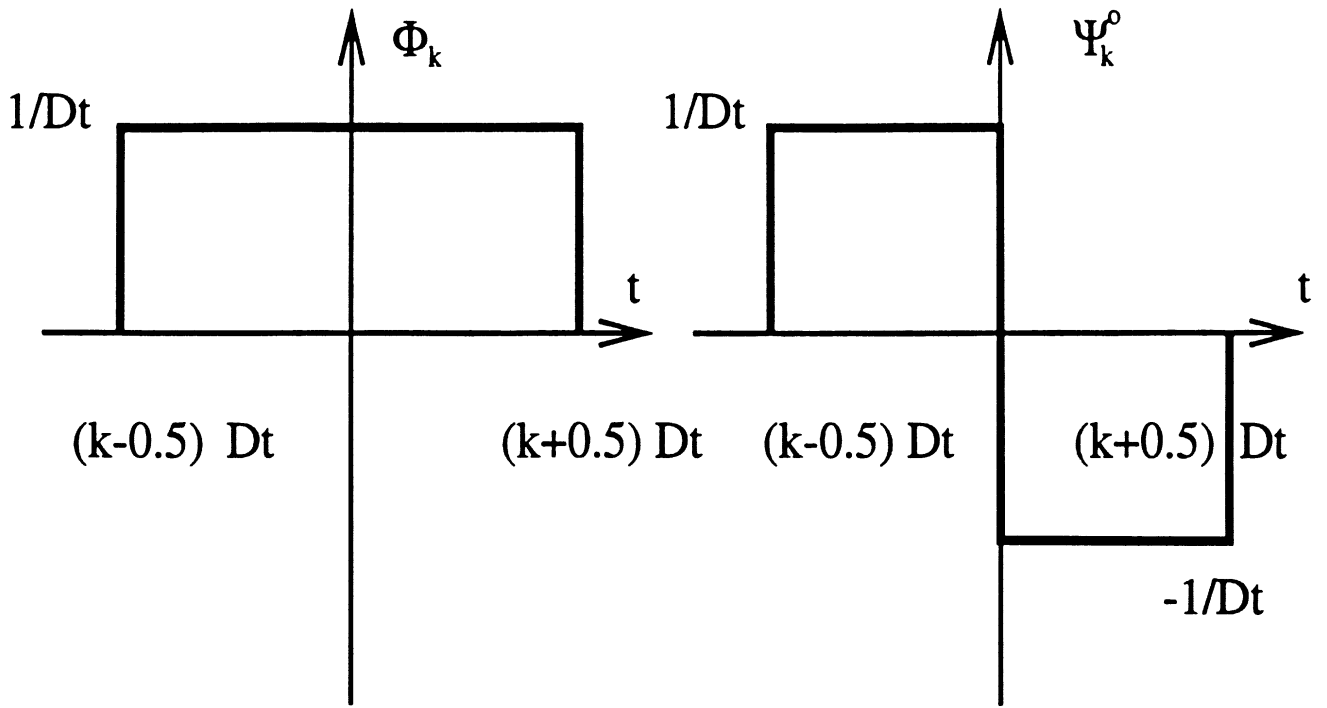


Figure 1: 0-Order Intervalic Function Basis.

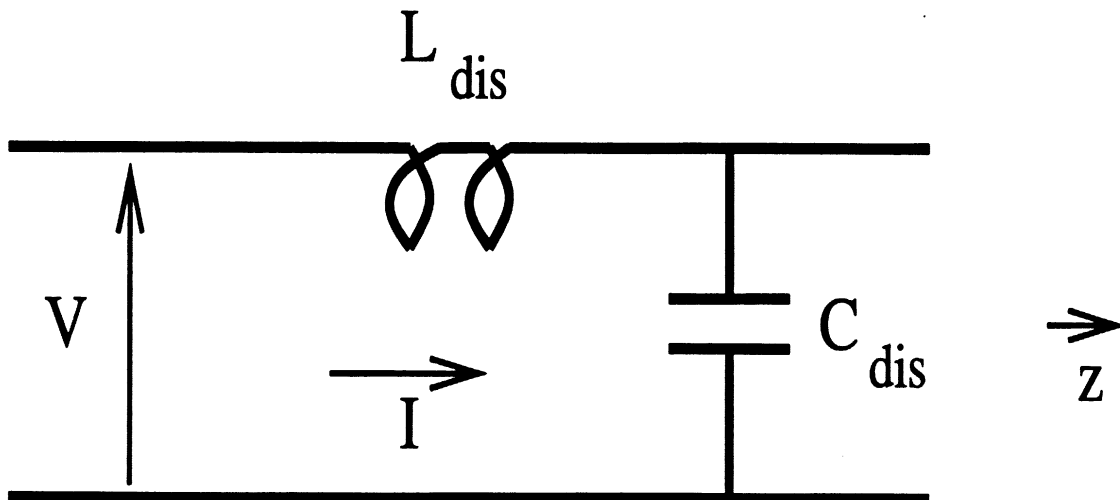


Figure 2: Ideal (Lossless) Transmission Line.

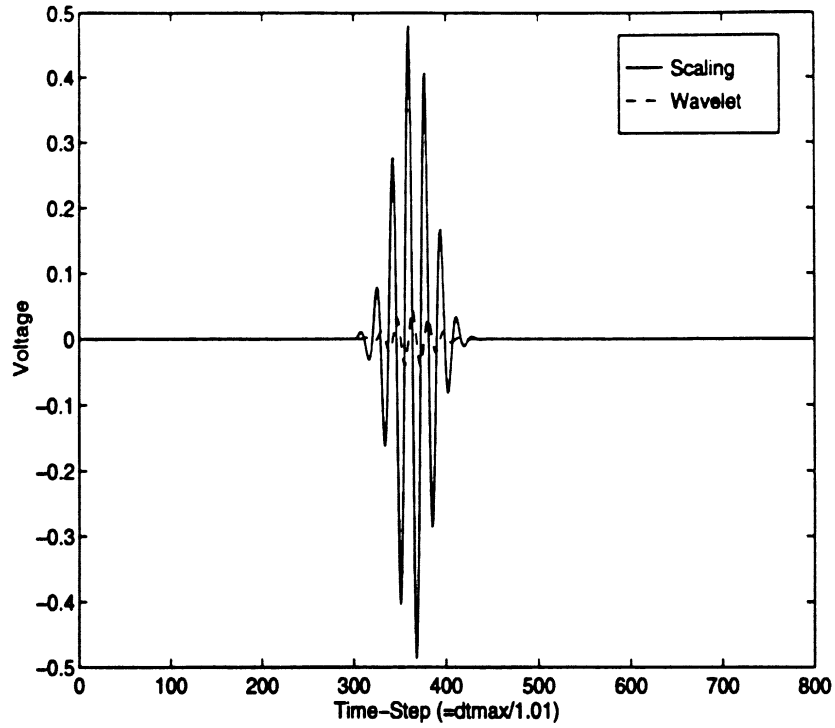


Figure 3: Voltage Coefficients.

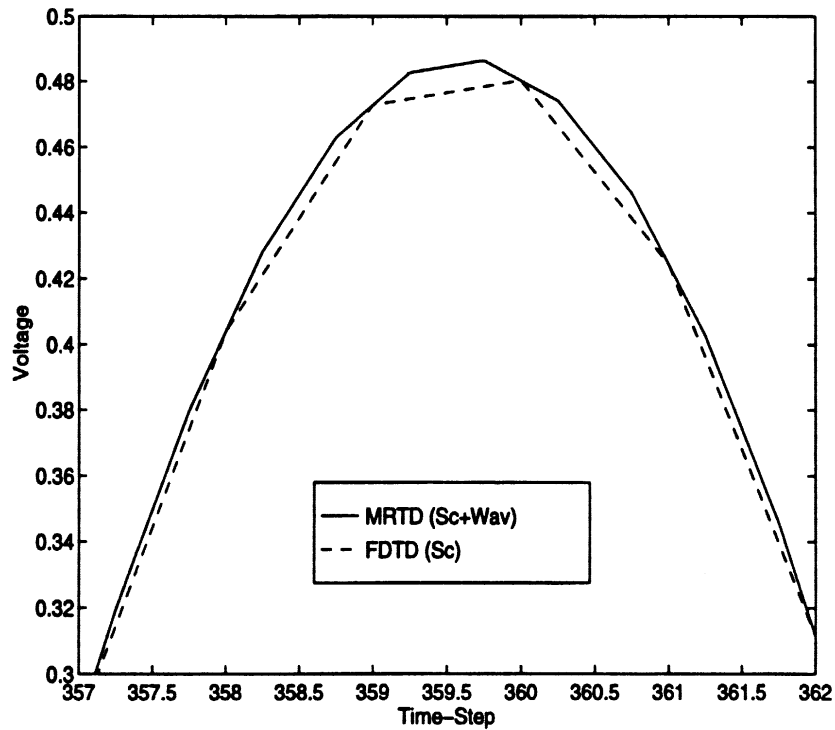


Figure 4: Comparison MRTD-FDTD.

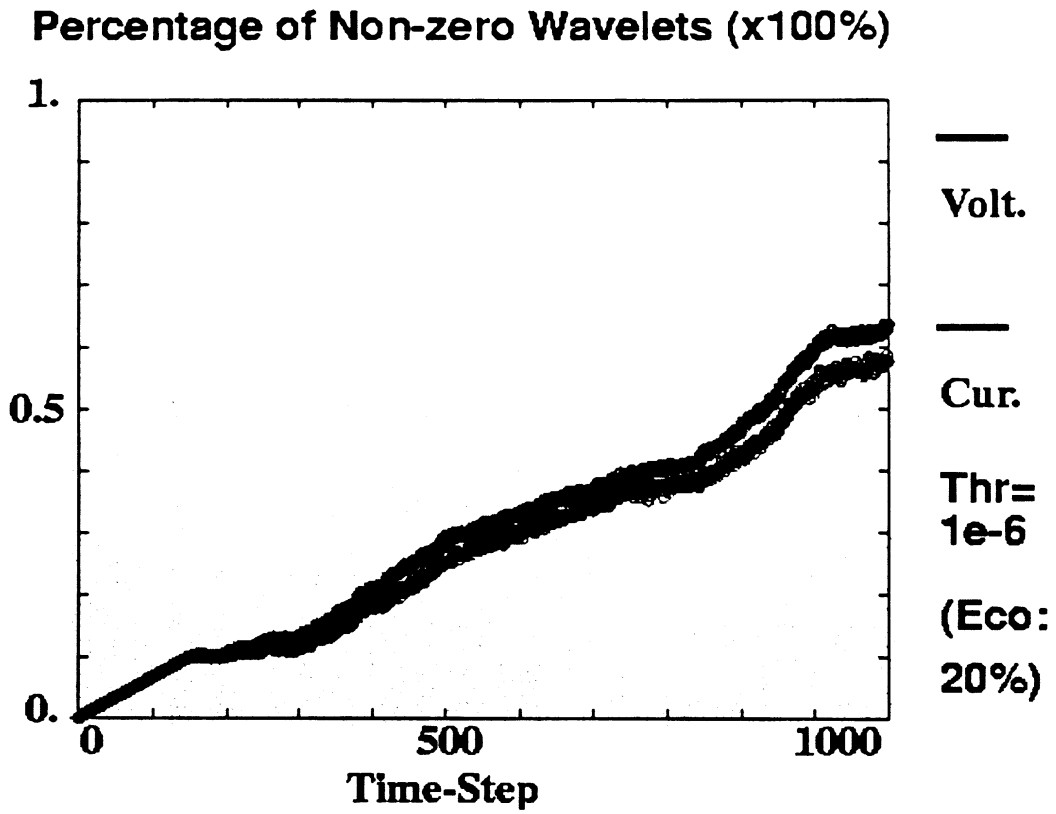


Figure 5: Fraction of Wavelets above Threshold.

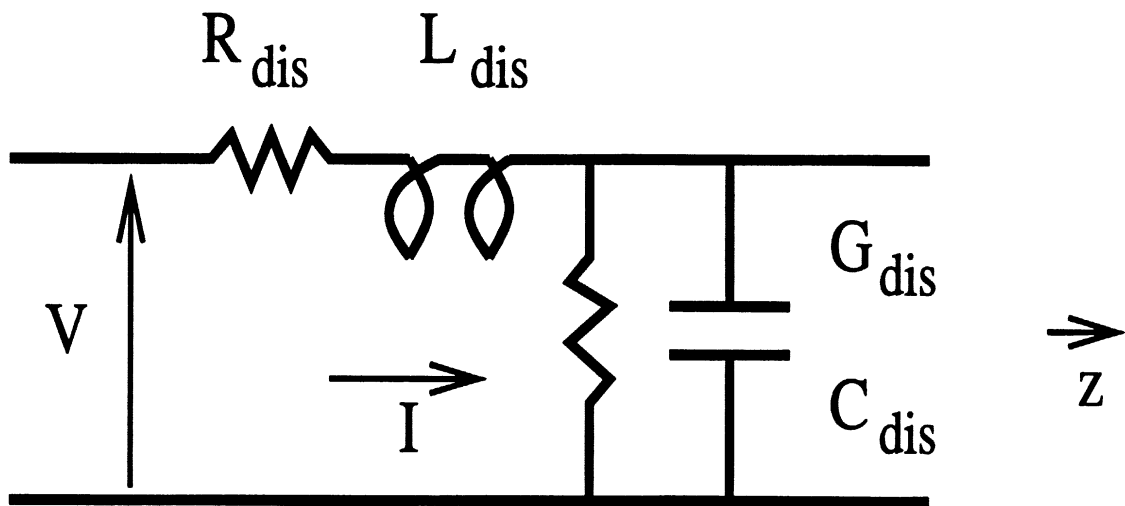


Figure 6: Lossy Transmission Line.

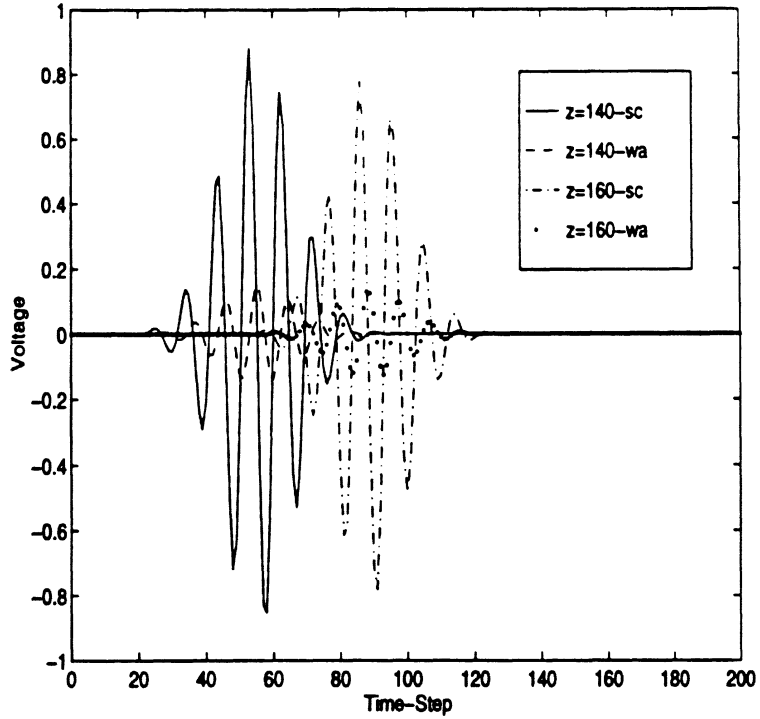


Figure 7: Voltage Coefficients.

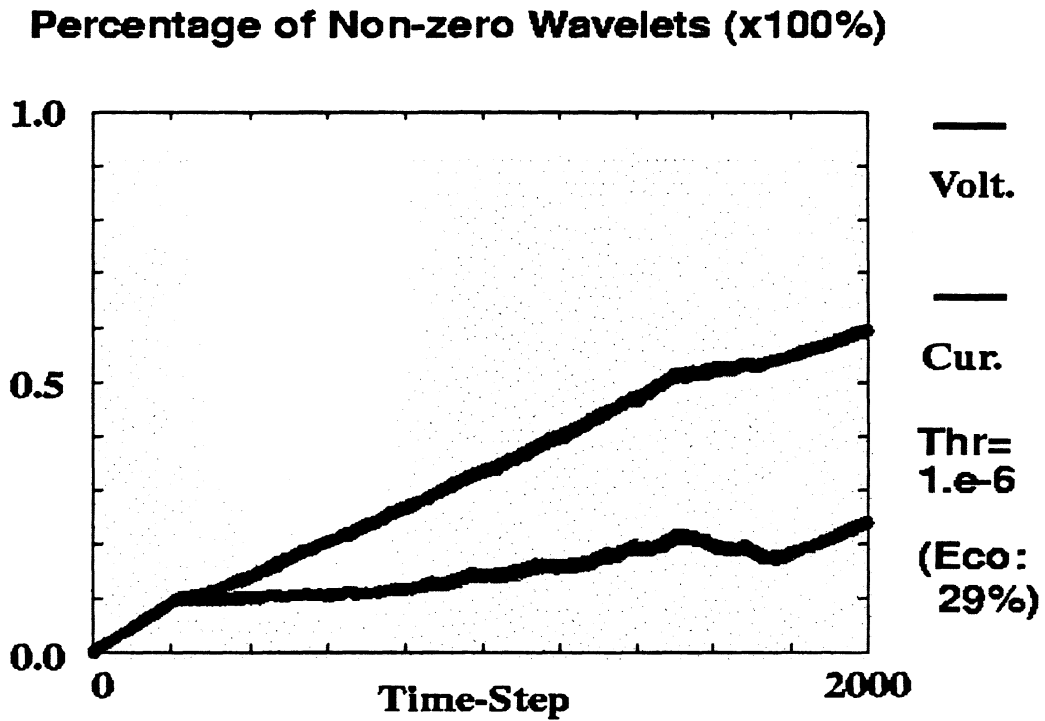


Figure 8: Fraction of Wavelets above Threshold.

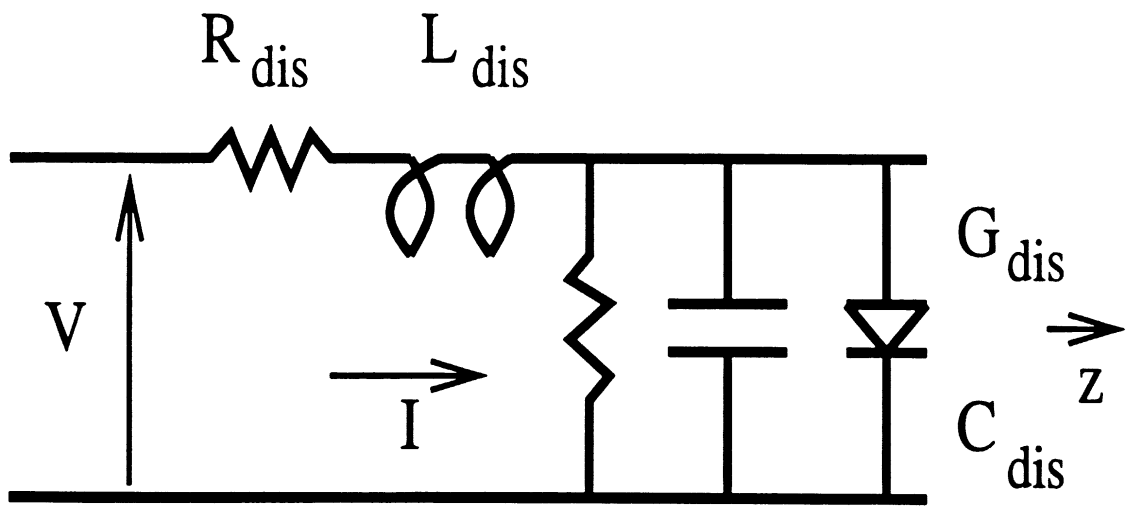


Figure 9: Rectifier Geometry.

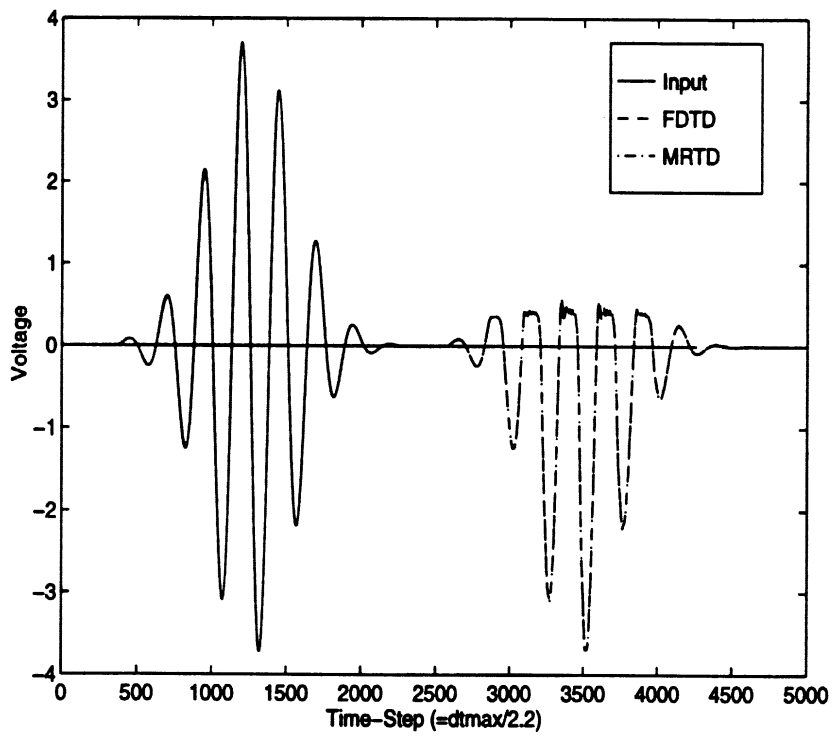


Figure 10: Comparison MRTD-FDTD.

Presented to the 1997 ACES Conference

Space/Time Adaptive Meshing and Multiresolution Time Domain Method (MRTD)

Emmanouil Tentzeris¹, Andreas Cangellaris², Linda P.B. Katehi¹

¹Radiation Laboratory, EECS Department, University of Michigan,
Ann Arbor, MI 48109-2122, USA

²University of Arizona, Tucson, AZ, USA

I Introduction

Recently the principles of the Multiresolution Analysis have been successfully applied [1, 2] to the time-domain numerical techniques used for the analysis of a variety of microwave problems. New techniques have been derived by the use of scaling and wavelet functions for the discretization of the time-domain Maxwell's equations. The multiresolution time domain technique (MRTD) based on Battle Lemarie functions has been used for the simulations of planar circuits and resonating structures. The conventional FDTD absorbers (e.g. PML) have been generalized in order to analyze open planar structures. MRTD has demonstrated unparalleled savings in execution time and memory requirements (2 orders of magnitude for 3D problems). In addition to time and memory, MRTD technique can provide space- and time- adaptive meshing without the problems that the conventional FDTD variable grids are encountering (e.g. reflections between dense-coarse regions). This unique feature stems from the use of two separate sets of basis functions, the scaling and wavelets. Due to the excellent conditioning of the formulated mathematical problem, MRTD offers the capability to threshold the wavelet field coefficients. This advantage of the MRTD Technique is demonstrated herein by performing a space-/time-adaptive meshing.

In this paper, a space-/time- adaptive meshing algorithm based on the MRTD scheme is proposed and validated for a specific waveguide problem. Wavelets up to the second resolution are placed only at locations where the EM fields have significant values. These locations are changing with the time as the pulse is propagating inside the waveguide and with the space as the pulse is approaching regions of discontinuities. The proposed algorithm offers the opportunity of a space-/time- adaptive mesh with variable resolution of the field representation. In this way, significant memory and execution time savings can be achieved in comparison to the conventional variable-mesh FDTD algorithms.

II MRTD Formulation

Without loss of generality, the 2D-MRTD scheme for the TM_z modes will be described herein. To derive the scheme equations, the field components are represented by a series of cubic spline Battle-Lemarie scaling and 1-order wavelet functions along the z-direction, while pulses are used for the time representation. Wavelets of higher-order can be included in a similar way. After inserting these series expansions in Maxwell's equations and sampling them with pulse functions in time and scaling/wavelet functions in space domain, we derive the following equations for the electric field:

$$\begin{aligned} \frac{1}{\Delta t}({}_{k+1}D_{l+1/2,m}^{\phi x} - {}_kD_{l+1/2,m}^{\phi x}) &= -\frac{1}{\Delta z} \left(\sum_{i=m-m_2}^{m+m_1} a(i)_{k+1/2} H_{l+1/2,i+1/2}^{\phi y} + \sum_{i=m-m_4}^{m+m_3} b(i)_{k+1/2} H_{l+1/2,i+1/2}^{\psi y} \right) , \\ \frac{1}{\Delta t}({}_{k+1}D_{l+1/2,m}^{\psi x} - {}_kD_{l+1/2,m}^{\psi x}) &= -\frac{1}{\Delta z} \left(\sum_{i=m-m_4}^{m+m_3} b(i)_{k+1/2} H_{l+1/2,i+1/2}^{\phi y} + \sum_{i=m-m_6}^{m+m_5} c(i)_{k+1/2} H_{l+1/2,i+1/2}^{\psi y} \right) , \\ \frac{1}{\Delta t}({}_{k+1}D_{l,m+1/2}^{\phi z} - {}_kD_{l,m+1/2}^{\phi z}) &= \frac{1}{\Delta x} \left(\sum_{i=l-l_2}^{l+l_1} a(i)_{k+1/2} H_{i+1/2,m+1/2}^{\phi y} \right) , \\ \frac{1}{\Delta t}({}_{k+1}D_{l,m+1/2}^{\psi z} - {}_kD_{l,m+1/2}^{\psi z}) &= \frac{1}{\Delta x} \left(\sum_{i=l-l_4}^{l+l_3} c(i)_{k+1/2} H_{i+1/2,l+1/2}^{\psi y} \right) , \end{aligned}$$

where ${}_kD_{l,m}^{\xi x}$, ${}_kE_{l,m}^{\xi x}$ and ${}_kH_{l,m}^{\xi y}$ with $\xi=\phi$ (scaling), ψ (wavelets) are the coefficients for the electric flux, electric and magnetic field expansions. The indices l , m and k are the discrete space and time indices, which are related to the space and time coordinates via $x = l\Delta x$, $z = m\Delta z$ and $t = k\Delta t$, where $\Delta x, \Delta z$ are the space discretization intervals in x- and z-direction and Δt is the time discretization interval. The coefficients $a(i)$, $b(i)$, $c(i)$ are derived and given in [1]. For an accuracy of 0.1% the values $m_1 = m_5 = 8$, $m_2 = m_3 = m_4 = m_6 = 9$ have been used. The indices l_i have to take similar values to achieve the same accuracy in the summations.

The use of non-localized basis functions in the 2D-MRTD scheme causes significant effects. Localized boundary conditions are impossible to be implemented, so the perfect electric boundary conditions are modelled by use of the image principle in a generic way. The implementation of the image theory is performed automatically for any number of PEC, PMC boundaries. The material discontinuities are represented in terms of scaling and wavelet functions resulting into a linear matrix equation as explained in [1, 3] where this technique was used in the modeling of anisotropic dielectric media. In addition, the total value of a field component at a specific point of the mesh is a summation of the contributions from the neighboring non-localized scaling and wavelet functions. The field values at the neighboring cells can be combined appropriately by adjusting the scaling and wavelet function values and by applying the image principle.

The demand for the simulation of open structures led to the generalization of the perfectly matched layer (PML) technique [4], so as it can be used in the MRTD simulations. The conductivity is expanded in terms of scaling functions instead of pulse functions with respect to

space. The amplitudes of the expansion scaling functions follow the PML spatial conductivity distribution. In our simulations, the parabolic distribution was used, though the realization of other distributions (linear, cubic, ...) is straightforward. For example, if we assume that the PML absorbing material (ϵ, μ, σ^E) extends to the z-direction, substituting

$$D^{(i)x,z}(x, z, t) = \tilde{D}^{(i)x,z}(x, z, t)e^{-\sigma_{(z)}^E t/\epsilon} \quad (1)$$

and

$$H^{(i)y}(x, z, t) = \tilde{H}^{(i)y}(x, z, t)e^{-\sigma_{(z)}^H t/\mu} \quad (2)$$

for $i=\phi, \psi$, leads to the following equation:

$$\frac{\partial \tilde{D}^x}{\partial t} = -\frac{\partial \tilde{H}^y}{\partial y} \quad (3)$$

Following a procedure similar to the one used for the derivation of the non-PML region equations, we get for D_x components

$$\begin{aligned} {}_{k+1}D_{l+1/2,m}^{\phi x} &= e^{-\sigma_{(m\Delta z)}^E \Delta t/\epsilon} {}_k D_{l+1/2,m}^{\phi x} \\ &- \frac{\Delta t}{\Delta z} e^{-\sigma_{(m\Delta z)}^E 0.5\Delta t/\epsilon} \left(\sum_{i=m-m_2}^{m+m_1} a(i)_{k+1/2} H_{l+1/2,i+1/2}^{\phi y} + \sum_{i=m-m_4}^{m+m_3} b(i)_{k+1/2} H_{l+1/2,i+1/2}^{\psi y} \right) \end{aligned} \quad ,$$

$$\begin{aligned} {}_{k+1}D_{l+1/2,m}^{\psi x} &= e^{-\sigma_{(m\Delta z)}^E \Delta t/\epsilon} {}_k D_{l+1/2,m}^{\psi x} \\ &- \frac{\Delta t}{\Delta z} e^{-\sigma_{(m\Delta z)}^E 0.5\Delta t/\epsilon} \left(\sum_{i=m-m_4}^{m+m_3} b(i)_{k+1/2} H_{l+1/2,i+1/2}^{\phi y} + \sum_{i=m-m_6}^{m+m_5} c(i)_{k+1/2} H_{l+1/2,i+1/2}^{\psi y} \right) \end{aligned} \quad ,$$

The finite-difference equations for $D^{(\phi,\psi)z}$ and $H^{(\phi,\psi)y}$ are similar. For all simulations, a parabolic distribution of the conductivity σ is used in the PML region (N cells):

$$\sigma_{(m\Delta z)}^{E,H} = \sigma_{max}^{E,H} \left(\frac{m}{N}\right)^2 \quad \text{for } m=0,1,\dots,N, \quad (4)$$

with $\sigma_{max}^{E,H}$ the maximum conductivity at the end of the absorbing layer. As in [5], the "magnetic" conductivity σ^H is given by:

$$\frac{\sigma_{(m\Delta z)}^E}{\epsilon} = \frac{\sigma_{(m\Delta z)}^H}{\mu} \quad \text{for } m=0,1,\dots,N, \quad (5)$$

and the MRTD mesh is terminated by a perfect electric conductor (PEC) at the end of the PML region. This PEC is modelled by applying the image theory.

III Space/Time Adaptive Meshing

The wavelet components' amplitudes have negligible values away from the discontinuities or at regions where the excitation pulse has not propagated yet. There are numerous ways of taking advantage of the above feature. The simplest one is to threshold the wavelet components to a fraction (usually $\leq 0.1\%$) of the scaling component at the same cell (space adaptivity) for each time-step. All components below this threshold are eliminated from the subsequent calculations for the same time-step (time adaptivity). This procedure offers only a moderate economy in memory (factor close to 2). Also, this algorithm allows for the dynamic memory allocation in its programming implementation, while maintaining a low complexity.

The above space-/time- adaptive meshing scheme is applied to the analysis of the partially-loaded parallel-plate waveguide of (Fig.1) for the frequency range 0-22.5GHz. The waveguide is half-filled with air and half-filled with dielectric with $\epsilon_r = 2.56$. An FDTD 16×640 (10240 cells) mesh and an MRTD 2×80 (160 cells) mesh (160 grid points with $dx = 0.18\lambda_o$, $dz = 0.3\lambda_o$ - close to the Nyquist Limit for $f = 22.5GHz$) are used for the Time-Domain simulations (3,000 time-steps). The 160 grid points of the MRTD mesh express the number of the used scaling functions. The number of the wavelets is varying with time and depends on the predefined threshold. For consistency, the time step for both schemes is chosen to be equal to the 1/8 of the FDTD maximum Δt .

The waveguide is excited with a Gabor function 0-22.5GHz along a vertical line for the FDTD simulation and for a rectangular region of 12 cells to the longitudinal direction (due to the non-localized character of the Battle-Lemarie scaling and wavelet functions) for the MRTD simulations. Other excitations (e.g.Gaussian) can be applied in a straightforward way. For both cases, a PML region of 16 cells and $\sigma_{max}^E = 0.4S/m$ absorbs the waves in the front and back open planes. The capability of the MRTD technique to provide space- and time- adaptive gridding is verified by thresholding the wavelet components to the 0.1% of the value of the scaling function at the same cell for each time-step. The accuracy achieved by using only the wavelets with values above the threshold is equal to what would be if wavelets were used everywhere. Though this number is varying in time, its maximum value is 36 out of a total of 160 to the z-direction (economy in memory by a factor of 52 instead of 32). In addition, execution time is reduced by a factor 4-5. For larger thresholds, the ringing effect due to the elimination of the wavelets deteriorates the performance of the algorithm. For example, using a threshold of 1% (13 out of a 160 wavelets to the z-direction) increases the error by a factor of 2.1.

The results for the Reflection Coefficient for 10 GHz are validated by comparison to the theoretical value $|R| = 0.231$ ($= (\sqrt{2.56}-1.0)/(\sqrt{2.56}+1.0)$). MRTD gives the value 0.2296 and FDTD gives 0.2304 (similar accuracy). The normal electric field is probed at a distance 10 cells away from the source and is plotted in (Fig.2) in time-domain. Similar accuracy can be observed for

the FDTD and the MRTD meshes.

Fig.3 demonstrates the space- and time-adaptive character of the meshing algorithm. It is clearly shown that the wavelets follow the propagating excitation pulse before and after the incidence to the dielectric interface and can be omitted elsewhere. The location and the number of the wavelet coefficients with values above the threshold ("effective wavelets") are different for each time-step, something that creates a mesh with high resolution ("dense") in regions of strong field variations, while maintaining a much lower resolution ("coarse") for the rest cells.

IV Conclusion

A simple space- and time- adaptive meshing algorithm based on an MRTD scheme has been proposed and has been validated for a parallel-plate waveguide problem. The electric field value and the reflection coefficient have been calculated and verified by comparison to reference data. The proposed scheme exhibits memory savings by a factor of 52 in 2D, as well as execution time savings by a factor of 4-5, while maintaining a similar accuracy with Yee's conventional FDTD scheme. In addition, this algorithm doesn't increase the programming complexity and can be effectively extended to 3D problems.

V Acknowledgments

This work has been partially funded by ARO and by NSF.

References

- [1] M.Krumpholz, L.P.B.Katehi, "MRTD: New Time Domain Schemes Based on Multiresolution Analysis", IEEE Trans. Microwave Theory and Techniques, vol. 44, no. 4, pp. 555-561, April 1996.
- [2] E.Tentzeris, M.Krumpholz and L.P.B. Katehi, "Application of MRTD to Printed Transmission Lines", Proc. MTT-S 1996, pp. 573-576.
- [3] R. Robertson, E. Tentzeris, M. Krumpholz, L.P.B. Katehi, "Application of MRTD Analysis to Dielectric Cavity Structures", Proc. MTT-S 1996, pp. .
- [4] E.Tentzeris, R.Robertson, M.Krumpholz and L.P.B. Katehi, "Application of the PML Absorber to the MRTD Technique", Proc. AP-S 1996, pp. 634-637.
- [5] J.-P. Berenger, "A Perfectly Matched Layer for the Absorption of Electromagnetic Waves", J. Computational Physics, vol. 114, pp. 185-200, 1994.

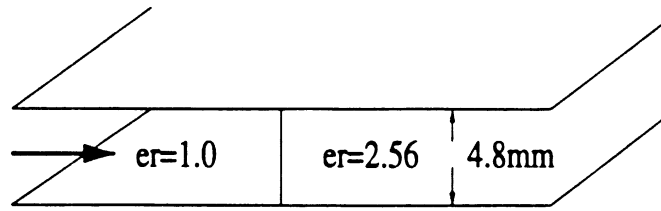


Figure 1: Dielectric-loaded Waveguide.

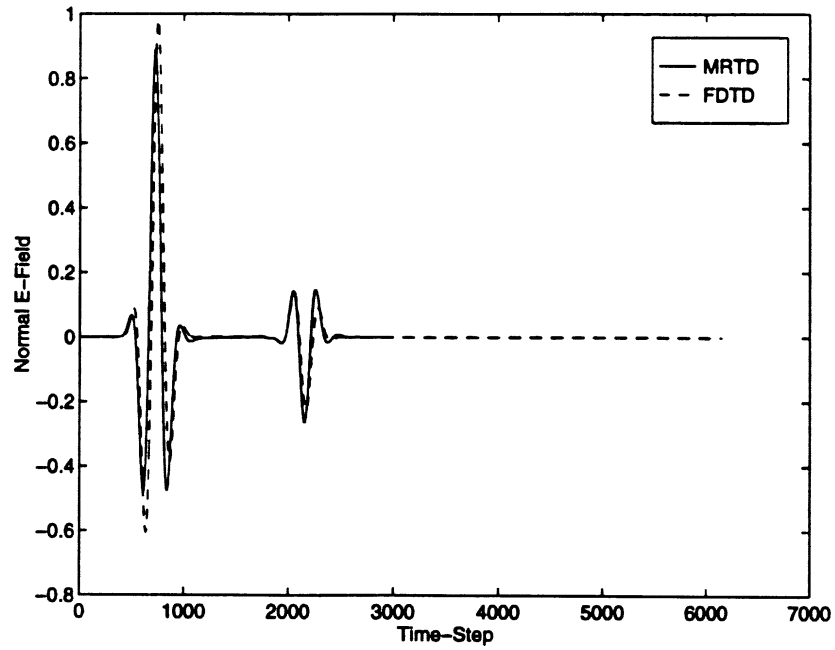


Figure 2: Normal E-field Time Evolution.

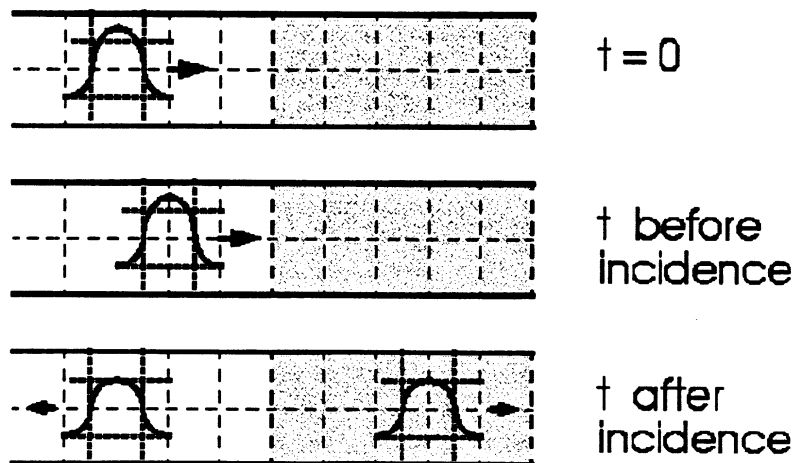


Figure 3: Space-/Time- Adaptive Meshing Demonstration.

SPACE- AND TIME- ADAPTIVE GRIDDING USING MRTD TECHNIQUE

Emmanouil M. Tentzeris, Robert L. Robertson, Linda P.B. Katehi
Radiation Laboratory, Department of Electrical Engineering and Computer Science
University of Michigan, Ann Arbor, MI 48109-2122

Andreas Cangellaris
Department of Electrical and Computer Engineering
University of Arizona, Tucson, AZ

Abstract- The MRTD scheme is applied to the analysis of waveguide problems. Specifically, the field pattern and the S-parameters of a dielectric-loaded parallel-plate waveguide are calculated. The use of wavelets enables the implementation of a space- and time-adaptive gridding technique. The results are compared to those obtained by use of the conventional FDTD scheme to indicate considerable savings in memory and computational time.

I Introduction

Recently a new technique has been successfully applied [1-4] to a variety of microwave problems and has demonstrated unparalleled properties. This technique is derived by the use of multiresolution analysis for the discretization of the time-domain Maxwell's equations. The multiresolution time domain technique (MRTD) based on Battle-Lemarie functions has been applied to linear as well as nonlinear propagation problems. The PML absorbing boundary condition has been generalized in order to analyze open planar structures. MRTD has demonstrated savings in time and memory of two orders of magnitude. In addition, the most important advantage of this new technique is its capability to provide space and time adaptive gridding without the problems that the conventional FDTD is encountering. This is due to the use of two separate sets of basis functions, the scal-

ing and wavelets and the capability to threshold the field coefficients due to the excellent conditioning of the formulated mathematical problem.

In this paper, a space/time adaptive gridding algorithm based on the MRTD scheme is proposed and applied to the waveguide problems. As an example, the propagation of a Gabor pulse in a partially-filled parallel-plate waveguide is simulated and the S-parameters are evaluated. Wavelets are placed only at locations where the EM fields have significant values, creating a space- and time- adaptive dense mesh in regions of strong field variations, while maintaining a much coarser mesh elsewhere.

II The 2D-MRTD scheme

For simplicity the 2D-MRTD scheme for the TM_z modes will be used herein. To derive the 2D-MRTD scheme, the field components are represented by a series of cubic spline Battle-Lemarie [5] scaling and wavelet functions to the longitudinal direction in space and pulse functions in time. After inserting the field expansions in Maxwell's equations, we sample them using pulse functions in time and scaling/wavelet functions in space domain.

As an example, sampling $\partial D_x/\partial t = -\partial H_y/\partial z$ in space and time, the following difference equation is obtained

$$\begin{aligned}
& \frac{1}{\Delta t} ({}_{k+1}D_{l+1/2,m}^{\phi z} - {}_kD_{l+1/2,m}^{\phi z}) = \\
& -\frac{1}{\Delta y} \left(\sum_{i=m-m_2}^{m+m_1} a(i) {}_{k+1/2}H_{l+1/2,i+1/2}^{\phi y} \right. \\
& + \sum_{i=m-m_4}^{m+m_3} b(i) {}_{k+1/2}H_{l+1/2,i+1/2}^{\psi y} \left. \right) , \quad (1) \\
& \frac{1}{\Delta t} ({}_{k+1}D_{l+1/2,m}^{\psi z} - {}_kD_{l+1/2,m}^{\psi z}) = \\
& -\frac{1}{\Delta y} \left(\sum_{i=m-m_4}^{m+m_3} b(i) {}_{k+1/2}H_{l+1/2,i+1/2}^{\phi y} \right. \\
& + \sum_{i=m-m_6}^{m+m_5} c(i) {}_{k+1/2}H_{l+1/2,i+1/2}^{\psi y} \left. \right) , \quad (2)
\end{aligned}$$

where ${}_kD_{l,m}^{\xi x}$ and ${}_kH_{l,m}^{\xi y}$ with $\xi=\phi$ (scaling), ψ (wavelets) are the coefficients for the electric and magnetic field expansions. The indices l, m and k are the discrete space and time indices, which are related to the space and time coordinates via $x = l\Delta x, z = m\Delta z$ and $t = k\Delta t$, where $\Delta x, \Delta z$ are the space discretization intervals in x- and z-direction and Δt is the time discretization interval. The coefficients $a(i), b(i), c(i)$ are derived and given in [2]. For an accuracy of 0.1% the values $m_1 = m_5 = 8, m_2 = m_3 = m_4 = m_6 = 9$ have been used.

For open structures, the perfectly matched layer (PML) technique can be applied by assuming that the conductivity is given in terms of scaling and wavelet functions instead of pulse functions with respect to space [4]. The spatial distribution of the conductivity for the absorbing layers is modelled by assuming that the amplitudes of the scaling functions have a parabolic distribution. The MRTD mesh is terminated by a perfect electric conductor (PEC) at the end of the PML region. Usually, 8-16 cells of PML medium with $\sigma_{max}^E = 0.4S/m$ provide reflection coefficients smaller than -90 dB.

In order to use a pulse excitation at $z = m\Delta z$ with respect to space and to obtain an excitation identical to an FDTD excitation, we decompose the pulse in terms of scaling and wavelet functions

$${}_kE_m^{exc} \approx E_F(0, k\Delta t) \left(\sum_{i=-4}^{+4} c_\phi(i) \phi_{m+i} + \sum_{i=-4}^{+4} c_\psi(i) \psi_{m+i} \right) \quad (3)$$

where the coefficients $c_\phi(i), c_\psi(i)$ are given in Table 1 for $i \geq 0$. For $i < 0$ it is $c_\phi(-i) = c_\phi(i)$ and

$c_\psi(i) = c_\psi(1-i)$. $E_F(0, k\Delta t)$ is the time dependence of the excitation. For $|i| \leq 4$, the above excitation components are superimposed to the field values obtained by the MRTD algorithm. For example, the total $E_{k,m+i}^\phi$ will be given by

$$E_{k,m+i}^\phi \Big|_{total} = E_F(0, k\Delta t) c_\phi(i) + E_{k,m+i}^\phi$$

Due to the nature of the Battle-Lemarie expansion functions, the total field is a summation of the contributions from the non-localized scaling and wavelet functions. For example, the total electric field $E_x(x_o, z_o, t_o)$ with $(k-1/2)\Delta t < t_o < (k+1/2)\Delta t$ is calculated in the same way with [2, 3] by

$$\begin{aligned}
E_x(x_o, z_o, t_o) = & \sum_{l', m'=-l_1}^{l_1} {}_kE_{l'+1/2, m'}^{\phi z} \phi_{l'+1/2}(x_o) \phi_{m'}(z_o) \\
& + \sum_i \sum_{l', m'=-l_{2,i}}^{l_{2,i}} {}_kE_{l'+1/2, m'}^{\psi i z} \phi_{l'+1/2}(x_o) \psi_{i, m'}(z_o)
\end{aligned}$$

where $\phi_m(x) = \phi(\frac{x}{\Delta x} - m)$ and $\psi_{i, m}(x) = \psi_i(\frac{x}{\Delta x} - m)$ represent the Battle-Lemarie scaling and i-resolution wavelet function respectively. For an accuracy of 0.1% the values $l_1 = l_{2,i} = 4$ have been used.

There are many different ways to take advantage of the capability of the MRTD technique to provide space and time adaptive gridding. In DSP, thresholding of the wavelet coefficients over a specific time- and space- window (5-10 points) contribute significant memory economy, but increase the implementation complexity and the execution time. The simplest way is to threshold the wavelet components to a fraction (usually $\leq 0.1\%$) of the scaling function at the same cell for each time-step. All components below this threshold are eliminated from the subsequent calculations. This is the simplest thresholding algorithm. It doesn't add any significant overhead in execution time, but it offers only a moderate (pessimistic) economy in memory (factor close to 2). Also, this algorithm allows for the dynamic memory allocation in its programming implementation.

III Applications of 2D-MRTD

The 2D-MRTD scheme is applied to the analysis of the partially-loaded parallel-plate waveguide of (Fig.1) for the frequency range 0-30GHz. For the

analysis based on Yee's FDTD scheme, a 16×800 mesh is used resulting in a total number of 14400 grid points. When the structure is analyzed with the 2D-MRTD scheme, a mesh 2×100 (200 grid points) is chosen ($dx = 0.24\lambda_0$, $dz = 0.4\lambda_0$ for $f = 30GHz$). This size is based on the number of the scaling functions, since the wavelets are used only when and where necessary. The time discretization interval is selected to be identical for both schemes and equal to the 1/10 of the 2D-MRTD maximum Δt . For the analysis we use 8,000 time-steps. The waveguide is excited with a Gabor function 0-30GHz along a vertical line for the FDTD simulation and for a rectangular region for the MRTD simulations. In all cases, the front and back open planes are terminated with a PML region of 16 cells and $\sigma_{max}^E = 0.4S/m$. The longitudinal distance between the excitation and the dielectric interface is chosen such that no reflections would appear before the Gabor function is complete.

The capability of the MRTD technique to provide space and time adaptive gridding is verified by thresholding the wavelet components to the 0.1% of the value of the scaling function at the same cell for each time-step. It has been observed that the accuracy by using only a small number of wavelets is equal to what would be achieved if wavelets were used everywhere. Though this number is varying in time, its maximum value is 22 out of a total of 100 to the z-direction (economy in memory by a factor of 28-30). In addition, execution time is reduced by a factor 4-5. For larger thresholds, the ringing effect due to the elimination of the wavelets deteriorates the performance of the algorithm. For example, using a threshold of 1% (6 out of a 100 wavelets to the z-direction) increases the error by a factor of 2.5.

The normal electric field is probed at a distance 10 cells away from the source and is plotted in (Fig.2) in time-domain. Comparable accuracy can be observed for the FDTD and the MRTD meshes. In addition, the reflection coefficient S_{11} is calculated by separating the incident and the reflected part of the probed field and taking the Fourier transform of their ratio (Fig.3). The results for 5 GHz (TEM propagation) are validated by comparison to the theoretic

cal value obtained applying ideal transmission line theory [6] and are plotted at Table 2. The time- and space-adaptive character of the gridding is exploited in (Figs.4,5) which show that the wavelets follow the propagating pulses before and after the incidence to the dielectric interfaces and have negligible values elsewhere. The location and the number of the wavelet coefficients with significant values are different for each time-step, something that creates a dense mesh in regions of strong field variations, while maintaining a much coarser mesh for the other cells.

IV Conclusion

A space- and time- adaptive gridding algorithm based on a multiresolution time-domain scheme in two dimensions has been proposed and has been applied to the numerical analysis of a waveguide problem. The field pattern and the reflection coefficient have been calculated and verified by comparison to reference data. In comparison to Yee's conventional FDTD scheme, the proposed scheme offers memory savings by a factor of 5-6 per dimension maintaining a similar accuracy. The above algorithm can be effectively extended to three-dimension problems.

V Acknowledgments

This work has been funded by NSF and ARO.

References

- [1] M.Krumpholz, L.P.B.Katehi, "New Prospects for Time Domain Analysis", IEEE Microwave and Guided Wave Letters, pp. 382-384, November 1995.
- [2] M.Krumpholz, L.P.B.Katehi, "MRTD: New Time Domain Schemes Based on Multiresolution Analysis", IEEE Transactions on Microwave Theory and Techniques, pp. 555-572, April 1996.
- [3] E.Tentzeris, M.Krumpholz and L.P.B. Katehi, "Application of MRTD to Printed Transmission Lines", Proc. MTT-S 1996, pp. 573-576.
- [4] E.Tentzeris, R.Robertson, M.Krumpholz and L.P.B. Katehi, "Application of the PML Absorber to the MRTD Technique", Proc. AP-S 1996, pp. 634-637.
- [5] I.Daubechies, "Ten Lectures on Wavelets", Philadelphia, PA: Society for Ind. and App. Math., 1992.
- [6] D.M.Pozar, "Microwave Engineering", pp. 94-96, Addison-Wesley, 1990.

Table 1: Excitation Decomposition Coeffs

i	0	1	2	3	4
$c_{\phi}(i)$	0.915	0.038	0.010	-0.009	0.005
$c_{\psi}(i)$	-0.103	-0.103	0.121	-0.030	0.015

Table 2: S_{11} calculated by 2D-MRTD

	S_{11} (Ω)	Relative error
Analyt. Value [6]	0.4298	0.0%
16x800 FDTD	0.4283	-0.3%
2x100 MRTD	0.4360	+1.4%

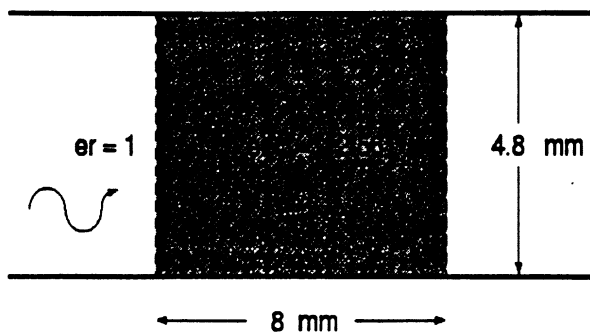


Figure 1: Dielectric-loaded Waveguide.

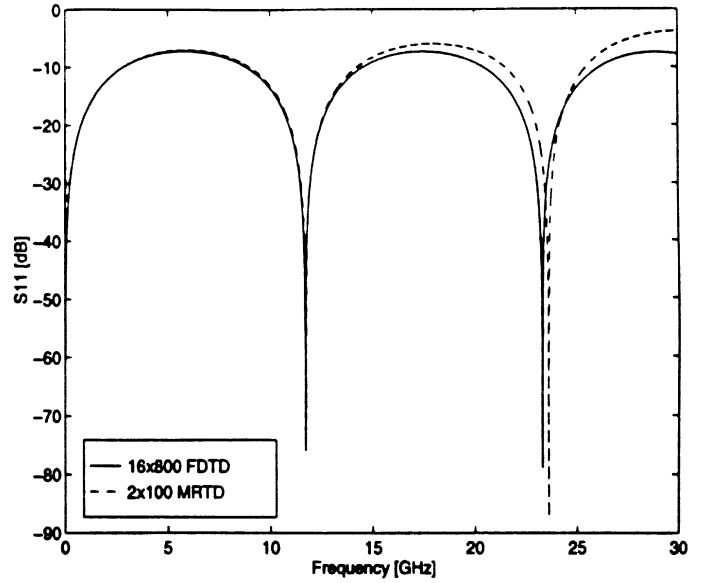


Figure 3: S_{11} values (Frequency-Domain).

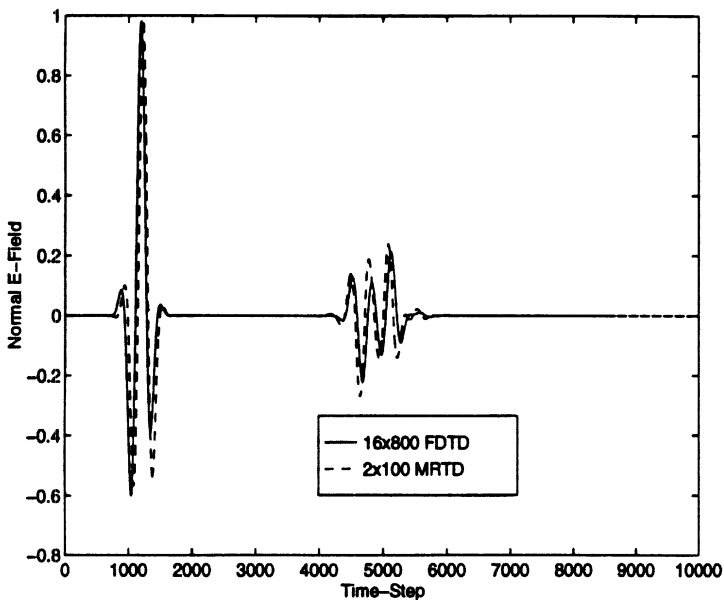


Figure 2: Normal E-field (Time-Domain).

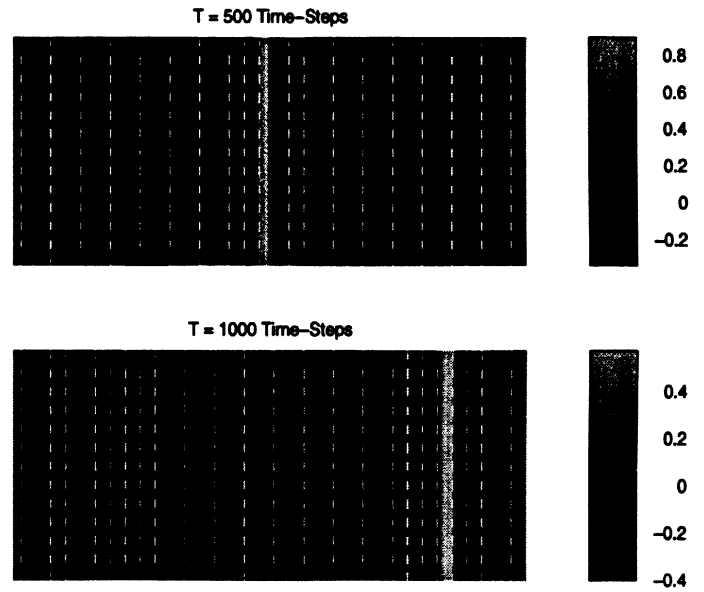


Figure 4: Adaptive Grid Demonstration.

Time Adaptive Time-Domain Techniques for the Design of Microwave Circuits

Emmanouil Tentzeris¹, James Harvey², Linda P.B. Katehi¹

¹Radiation Laboratory, EECS Department, University of Michigan

²Army Research Office

Abstract

The recently developed MRTD schemes are used for the development of a time adaptive time-domain technique for circuit design. The new technique exhibits considerable savings in memory and computational times in comparison to the conventional FDTD scheme.

I Introduction

Significant attention is being devoted now-a-days to the analysis and design of various types of microwave circuits. The finite-difference-time-domain (FDTD) scheme is one of the most powerful numerical techniques used for numerical simulations. However, despite its simplicity and modeling versatility, the FDTD scheme suffers from serious limitations due to the substantial computer resources required to model electromagnetic problems with medium or large computational volumes. In addition, the FDTD scheme cannot provide the accuracy required for computer simulations of time-dependent electromagnetic interactions in electrically long regions or in regions which contain non-linear materials. Such simulations are very important for integrated device modelling, especially in relation to the design of non-linear photonic devices. To alleviate these problems hybrid combinations of FDTD with other numerical techniques and higher order FDTD schemes based on Yee's grid have been proposed. MRTD (MultiResolution Time Domain Method) [1, 2] has shown unparalleled properties in comparison to Yee's FDTD. MRTD is not a new methodology. It is a correct and accurate generalization of the conventional discretization approaches. It provides the correct mathematical frame for solving problems in time domain and allows for the development of time/space adaptive grids.

II Introduction to MRTD

It is well known that the method of moments provides a mathematically correct approach for the discretization of integral and partial differential equations. Since it allows for the use of any complete and orthonormal set, the choice of an appropriate expansion set may lead to different time domain schemes. For example, the expansion of the unknown fields using pulse

functions leads to Yee's FDTD scheme. In a MRTD scheme the fields are represented by a two-fold expansion in scaling and wavelet functions with respect to time/space. Scaling functions guarantee a correct modelling of smoothly-varying fields. In regions characterized by strong field variations or field singularities, higher resolution is enhanced by incorporating wavelets in the field expansions. Wavelets are introduced only at specific locations, allowing for a time/space adaptive grid capability.

MRTD schemes based on cubic spline Battle-Lemarie scaling and wavelet functions (Fig.1) have been successfully applied to the simulation of 2D and 3D open and shielded problems [1, 2, 3, 4]. The functions of this family do not have compact support, thus the MRTD schemes have to be truncated with respect to space. Localized boundary conditions (PECs, PMCs etc.) and material properties are modelled by use of the image principle and of matrix equations respectively. However, this disadvantage is offset by the low-pass (scaling) and band-pass (wavelets) characteristics in spectral domain, allowing for an a priori estimate of the number of resolution levels necessary for a correct field modelling. In addition, the evaluation of the moment method integrals during the discretization of Maxwell's PDEs is simplified due to the existence of closed form expressions in spectral domain and simple representations in space domain. Dispersion analysis of this MRTD scheme shows the capability of excellent accuracy with up to 2 points/wavelength (Nyquist Limit). However, specific circuit problems may require the use of functions with compact support. For that reason, Haar basis functions have been utilized and have led to [5]. As an extension to this approach, intervalic wavelets of higher order may be incorporated into the solution of SPICE-type circuits. Results from that new technique will be shown at the Conference.

III Time Adaptive MRTD Scheme

The major advantage of the use of Multiresolution analysis to time domain is the capability to develop time and space adaptive schemes. This is due to the property of the wavelet expansion functions to interact weakly and allow for a spatial sparsity that may vary with time through a thresholding process. The adaptive character of this technique is extremely important for the accurate modelling of sharp field variations of the type encountered in beam focusing in nonlinear optics, etc. The use of the principles of the multiresolution analysis for adaptive grid computations for PDEs has been suggested by Perrier and Basdevant [6]. To understand the fundamental steps of such an adaptive scheme for Maxwell's hyperbolic system, let's consider Maxwell's equations in 2D (1 for space and 1 for time):

$$\frac{\partial \hat{u}}{\partial t} = A\hat{u} = \begin{bmatrix} 0 & -\epsilon(z)^{-1} \frac{\partial}{\partial z} \\ -\mu(z)^{-1} \frac{\partial}{\partial z} & 0 \end{bmatrix} \hat{u}, \quad \hat{u} = (E(z, t), H(z, t))^T, \quad (1)$$

After manipulation, the above equation can be written as

$$\mathbf{M}\hat{u} = \begin{bmatrix} \epsilon T_h^\dagger D_t & T_h^\dagger D_z \\ Z_h^\dagger D_z & \mu Z_h^\dagger D_t \end{bmatrix} \hat{u} = 0 \quad (2)$$

where Z_h, T_h are half shift operators for space and time coordinates z, t and Z_h^\dagger, T_h^\dagger are their Hermitian conjugates. D_t, D_z are difference operators given by:

$$D_t = \frac{1}{\Delta t} \left(\sum_{i=-9}^8 a_{\phi t}(i) T^{-i} + \sum_{i=-9}^9 a_{\psi t}(i) T^{-i} \right), \quad D_z = \frac{1}{\Delta z} \left(\sum_{i=-9}^8 a_{\phi z}(i) Z^{-i} + \sum_{i=-9}^9 a_{\psi z}(i) Z^{-i} \right) \quad , \quad (3)$$

where a_ϕ, a_ψ are the coefficients associated with the scalar and the wavelet functions respectively. At each time step we keep both the wavelet field values that are larger than a given threshold as well as the adjacent values. An adjacent wavelet field value is defined on the basis of the wavelet resolution level(s) incorporated in the solution. Recently, an efficient space/time adaptive meshing procedure was proposed [7] for Battle-Lemarie expansion functions. In this paper, intervalic wavelets are used for the expansion of the fields (Fig.2). The adaptive mesh will be applied to a variety of circuit problems and results will be discussed during the presentation.

IV Conclusion

A Time Adaptive Time-Domain Technique based on intervalic wavelets has been proposed and applied to various types of circuits problems with lumped and distributed elements. This scheme exhibits significant savings in execution time and memory requirements while maintaining a similar accuracy with conventional circuit simulators.

V Acknowledgments

This work has been partially funded by NSF.

References

- [1] M.Krumpholz, L.P.B.Katehi, "MRTD: New Time Domain Schemes Based on Multiresolution Analysis", IEEE Trans. Microwave Theory and Techniques, vol. 44, no. 4, pp. 555-561, April 1996.
- [2] E.Tentzeris, M.Krumpholz and L.P.B. Katehi, "Application of MRTD to Printed Transmission Lines", Proc. MTT-S 1996, pp. 573-576.
- [3] R. Robertson, E. Tentzeris, M. Krumpholz, L.P.B. Katehi, "Application of MRTD Analysis to Dielectric Cavity Structures", Proc. MTT-S 1996, pp. .
- [4] E.Tentzeris, R.Robertson, M.Krumpholz and L.P.B. Katehi, "Application of the PML Absorber to the MRTD Technique", Proc. AP-S 1996, pp. 634-637.
- [5] K.Goverdhanam, E.Tentzeris, M.Krumpholz and L.P.B. Katehi, "An FDTD Multigrid based on Multiresolution Analysis", Proc. AP-S 1996, pp..
- [6] V.Perrier and C.Basdevant, "La decomposition en ondelettes periodiques: un outil pour l'analyse des champs inhomogenes. Theorie et algorithmes", La Recherche Aerospaciale, no.3, pp.53-67, 1989.
- [7] E.Tentzeris, R.Robertson, A.Cangellaris and L.P.B. Katehi, "Space- and Time- Adaptive Gridding Using MRTD", to be presented in the 1997 IEEE MTT-S, Denver, CO.

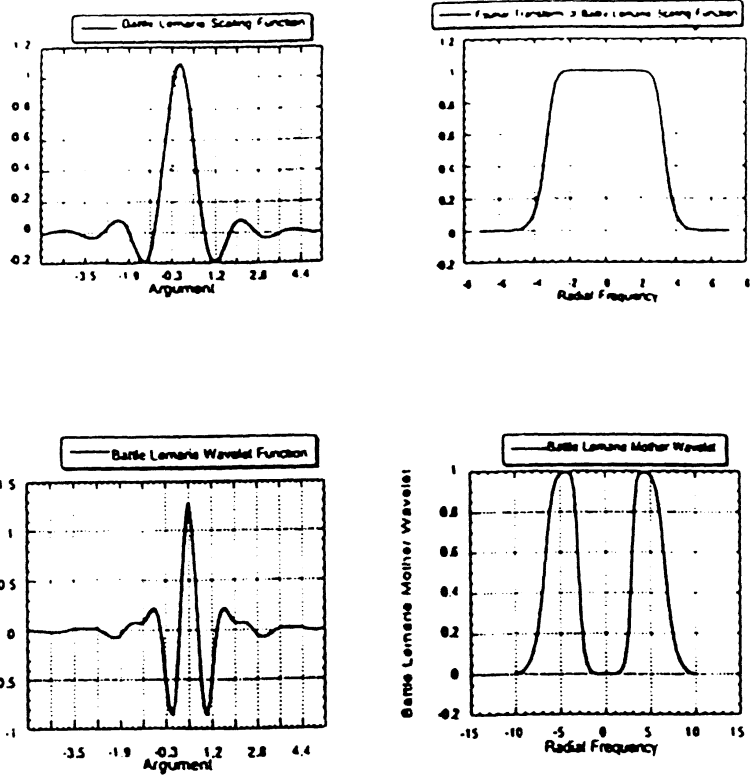


Figure 1: Battle-Lemarie Scaling and Wavelet Functions.

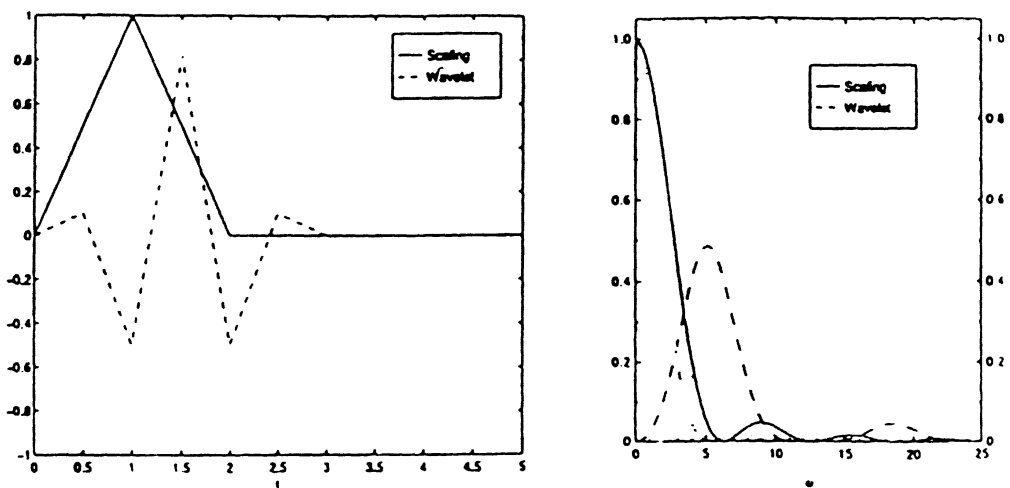


Figure 2: Intervalic Wavelets (Linear - Order 1).

Accepted for Presentation to the ACES Conference 1998

PML Implementation for the Battle-Lemarie Multiresolution Time-Domain Schemes

Emmanouil Tentzeris, Rob Robertson, Linda P.B. Katehi
Radiation Laboratory, EECS Department, University of Michigan,
Ann Arbor, MI 48109-2122, USA

I Introduction

The Multiresolution Time Domain (MRTD) Technique based on cubic-spline Battle Lemarie scaling and wavelet functions has shown successful application to a variety of microwave problems and has demonstrated unparalleled properties in terms of memory and execution time by one and two orders of magnitude respectively. This technique is used to model open and shielded propagation problems [1, 3] and non-linear optical applications [2]. In addition to time and memory, the most important advantage of this new technique is its capability to provide space and time adaptive meshing without the problems encountered by the conventional Finite Difference Time Domain (FDTD) [4] method. In this paper, an efficient non-split formulation of the PML absorber [5] for the Battle-Lemarie based MRTD scheme is presented. This formulation is validated and applied in the analysis of a two-dimensional parallel-plate waveguide geometry offering a numerical coefficient of reflection below -90dB. Additionally, examples for a three-dimensional patch antenna geometry are given.

II Derivation of the MRTD equations for the PML layer

Without loss of generality, the PML Absorber equations will be presented for a homogeneous medium for TM propagation in 2D. The Absorber formulation for TE propagation is straightforward. Assuming that the PML area is characterized by (ϵ_o, μ_o) and electric and magnetic conductivities (σ_E, σ_H) , the TM equations can be written

$$\epsilon_o \frac{\partial E_x}{\partial t} + \sigma_E E_x = - \frac{\partial H_y}{\partial z} \quad (1)$$

$$\epsilon_o \frac{\partial E_z}{\partial t} + \sigma_E E_z = \frac{\partial H_y}{\partial x} \quad (2)$$

$$\mu_o \frac{\partial H_y}{\partial t} + \sigma_H H_y = \frac{\partial E_z}{\partial x} - \frac{\partial E_x}{\partial z} \quad (3)$$

PML cells only to the z-direction are considered. Equations for PML cells in the x- and y-directions can be derived in a similar way. For each point z of the PML area, the magnetic conductivity σ^H needs to be chosen as [5]:

$$\frac{\sigma_E(z)}{\epsilon_o} = \frac{\sigma_H(z)}{\mu_o} \quad (4)$$

for a perfect absorption of the outgoing waves. A parabolic spatial distribution of $\sigma_{E,H}$,

$$\sigma_{E,H}(z) = \sigma_{E,H}^{max} \left(1 - \frac{z}{\delta}\right)^p, \quad \text{with } p=2 \quad \text{for } 0 \leq z \leq \delta = \text{PML thickness} \quad (5)$$

is used in the simulations, though higher order distributions (e.g. Cubic $p=3$) can give similar results. The PML area is terminated with a PEC and usually has a thickness varying between 4-16 cells. The maximum value σ_E^{max} is determined by the designated reflection coefficient R at normal incidence, which is given by the relationship

$$R = e^{-\frac{2}{\epsilon_o c} \int_0^\delta \sigma_E(z) dz} = e^{-\frac{2\sigma_E^{max} \delta}{\epsilon_o c(p+1)}} \quad (6)$$

The electric and magnetic field components incorporated in these equations are expanded in a series of Battle-Lemarie scaling and wavelet functions in both x- and z-directions. For example, E_x can be represented as:

$$\begin{aligned} E_x(x, z, t) = & \sum_{k,l,m=-\infty}^{+\infty} k E_{l+1/2,m}^{x,\phi\phi} h_k(t) \phi_{l+1/2}(x) \phi_m(z) \\ & + \sum_i \sum_{k,l,m=-\infty}^{+\infty} k E_{l+1/2,m}^{x,\phi\psi_i} h_k(t) \phi_{l+1/2}(x) \psi_{i,m}(z) \\ & + \sum_i \sum_{k,l,m=-\infty}^{+\infty} k E_{l+1/2,m}^{x,\psi_i\phi} h_k(t) \psi_{i,l+1/2}(x) \phi_m(z) \\ & + \sum_{i,j} \sum_{k,l,m=-\infty}^{+\infty} k E_{l+1/2,m}^{x,\psi_i\psi_j} h_k(t) \psi_{i,l+1/2}(x) \psi_{j,m}(z) \end{aligned} \quad (7)$$

where $\phi_m(x) = \phi\left(\frac{x}{\Delta x} - m\right)$ and $\psi_{i,m}(x) = \psi_i\left(\frac{x}{\Delta x} - m\right)$ represent the Battle-Lemarie scaling and i-th order resolution wavelet function respectively in space and $h_k(t)$ represent rectangular pulses in time. $k E_{l,m}^{\kappa,\mu\nu}$ and $k_{l+1/2} H_{l,m}^{\kappa,\mu\nu}$ with $\kappa = x, y, z$ and $\mu, \nu = \phi, \psi$ are the coefficients for the field expansions in terms of scaling and wavelet functions. The indices l, m and k are the discrete space and time indices related to the space and time coordinates via $x = l\Delta x, z = m\Delta z$ and $t = k\Delta t$, where $\Delta x, \Delta z$ are the space discretization intervals in x- and z-direction and Δt is the time discretization interval. For an accuracy of 0.1% the above summations are truncated to 16-24 terms. For simplicity, expansion only in scaling functions will be considered. Wavelets are implemented in a similar way. Upon inserting the field expansions, Maxwell's equations

are sampled [3] using pulse functions as time-domain test functions and scaling functions as space-domain test-functions and the following non-split formulation of the fields for the PML region is derived:

$$\begin{aligned}
{}_{k+1}E_{l+1/2,m}^{x,\phi\phi} &= e^{-\sigma_E^m \Delta t / \epsilon_0} {}_k E_{l+1/2,m}^{x,\phi\phi} \\
&\quad - e^{-0.5\sigma_E^m \Delta t / \epsilon_0} \left(\frac{1}{\Delta z} \sum_{i'=m-9}^{m+8} a(i')_{k+1/2} H_{l+1/2,i'+1/2}^{y,\phi\phi} \right) \\
{}_{k+1}E_{l,m+1/2}^{z,\phi\phi} &= e^{-\sigma_E^{m+1/2} \Delta t / \epsilon_0} {}_k E_{l,m+1/2}^{z,\phi\phi} \\
&\quad + e^{-0.5\sigma_E^{m+1/2} \Delta t / \epsilon_0} \left(\frac{1}{\Delta x} \sum_{i'=l-9}^{l+8} a(i')_{k+1/2} H_{i'+1/2,m+1/2}^{y,\phi\phi} \right) \\
{}_{k+1/2}H_{l+1/2,m+1/2}^{y,\phi\phi} &= e^{-\sigma_H^m \Delta t / \mu_0} {}_{k-1/2} H_{l+1/2,m+1/2}^{y,\phi\phi} \\
&\quad + e^{-0.5\sigma_H^m \Delta t / \mu_0} \left(\frac{1}{\Delta x} \sum_{i'=l-9}^{l+8} a(i')_k E_{i',m+1/2}^{z,\phi\phi} - \frac{1}{\Delta z} \sum_{i'=m-9}^{m+8} a(i')_k E_{l,i'}^{x,\phi\phi} \right) \quad (8)
\end{aligned}$$

where the terms $\sigma_{E,H}^m$ are given by Eq.(12).

A parallel-plate waveguide of width $d=48$ mm, terminated at both ends by PML, is used to validate the proposed algorithm. A TM source with a Gabor time variation is excited close to one side of the waveguide. The benchmark MRTD solution with no reflections is obtained by simulating the case of a much longer parallel-plate waveguide of the same width to provide a reflection-free observation area for the time interval of interest. A quadratic variation in PML conductivity is assumed for all cases, with maximum theoretical reflection coefficient of 10^{-5} at normal incidence. Numerical reflection is observed for the frequency range $[0, 0.9f_c^{TM_1}]$ (TEM propagation) where $f_c^{TM_1} = \frac{c}{2d} = 3.125$ (GHz) is the cutoff frequency of the TM_1 mode. It can be seen from Figs.(1)–(2) that for 8 PML cells and $\sigma_E^{max}=0.4$ S/m it is $S_{11} \leq -65$ dB and for 16 PML cells and $\sigma_E^{max}=0.2$ S/m the reflection is smaller than -91 dB. Thus, the non-split PML absorber can be used effectively in the simulation of antennas and active elements using MRTD.

III Application of PML to the Analysis of Antenna Geometries

MRTD can successfully model both planar circuits [6] and resonating structures [7]. Recently the techniques developed for the simulation of both structures are combined to model a three-dimensional patch antenna geometry [8]. Full three-dimensional MRTD analysis is used, with PML expanded through three coordinate directions. The procedure to derive an equation for the

	Δt	PML cells along z	σ_{max}^{Ex}	σ_{max}^{Ey}	σ_{max}^{Ez}
FDTD ($60 \times 100 \times 16$)	$1.3297 \cdot 10^{-13}s$	6	3.0	3.0	3.0
MRTD($30 \times 50 \times 9$)	$1.6008 \cdot 10^{-13}s$	2-6	3.0	3.0	11.53
MRTD ($20 \times 20 \times 9$)	$1.3297 \cdot 10^{-13}s$	6-10	3.0	3.0	11.53

Table 1: Computational Parameters.

three-dimensional MRTD scheme, with PML along all three coordinate directions is presented in [8].

The patch antenna used in our simulations has the dimensions $12.45mm \times 16mm$, with a microstrip line 20 mm long used as a feed. A Gaussian pulse 4 mm from the PML layer is used to excite the microstrip. The substrate has a thickness of 0.794 mm and a relative dielectric constant equal to 1. An FDTD mesh of $60 \times 100 \times 16$ is compared to MRTD grids of $30 \times 50 \times 9$ and $20 \times 20 \times 9$, which exhibit savings of memory over FDTD on the order of 7.22 and 33 respectively. Note that these values do not include the PML layers. Figure 3 shows a comparison plot of calculated S_{11} data for the three cases listed above. Six cells of PML are added along the $\pm x$, $\pm y$ and $+z$ directions with $\sigma_{max}^{Ex} = \sigma_{max}^{Ey} = 3.0$ and $\sigma_{max}^{Ez} = 11.53$ for all cases. The time discretization interval used for the MRTD $30 \times 50 \times 9$ scheme is $\Delta t = 1.6008 \cdot 10^{-13}s$ while the MRTD $20 \times 20 \times 9$ scheme uses a time discretization interval of $\Delta t = 1.42384 \cdot 10^{-13}s$. FDTD uses a time discretization interval of $\Delta t = 1.3297 \cdot 10^{-13}s$. In all three cases the simulation is performed for 10000 time steps. This information is summarized in Table 1.

Figure 4 shows a comparison of S_{11} data for different numbers of z -directed PML layers for an MRTD discretization of $30 \times 50 \times 9$. Note that the S_{11} values correlate very well even for only 2 PML layers in the z -direction. Figure 4 shows a comparison of S_{11} data for different numbers of z -directed PML layers for an MRTD discretization of $20 \times 20 \times 9$. Once again the values of S_{11} show good correlation.

IV Conclusion

An efficient PML absorber in non-split formulation is presented for the MRTD Scheme based on cubic spline Battle-Lemarie scaling functions. This absorber is used effectively to model an antenna geometry providing extremely small numerical reflections. In comparison to Yee's conventional FDTD scheme, the proposed MRTD scheme coupled with the PML absorber offer memory savings by a factor of 12-30 and execution time savings by a factor of about 3-5 maintaining a better accuracy for S-parameter calculations. For structures where the edge effect is prominent, additional wavelets can be used to improve the accuracy when using a

coarse MRTD mesh.

V Acknowledgements

This work was made possible by ONR contract N00014-95-1-1299 and ARO contract DAAH04-95-1-0321.

References

- [1] M.Krumpholz, L.P.B.Katehi, "MRTD: New Time Domain Schemes Based on Multiresolution Analysis", *IEEE Trans. Microwave Theory and Techniques*, vol. 44, no. 4, pp. 555-561, April 1996.
- [2] M.Krumpholz, L.P.B.Katehi, "MRTD Modeling of Nonlinear Pulse Propagation", to be published at the *IEEE Trans. Microwave Theory and Techniques*.
- [3] E.M.Tentzeris, R.Robertson, M.Krumpholz, L.P.B.Katehi, "Application of the PML Absorber to the MRTD Technique", *Proc. AP-S 1996*, pp. 634-637.
- [4] K.S.Yee, "Numerical solution of initial boundary value problems involving Maxwell's equations in isotropic media", *IEEE Trans. Antennas Propagation*, pp.302-307, May 1966.
- [5] J.-P. Berenger, "A Perfectly Matched Layer for the Absorption of Electromagnetic Waves", *J.Comput. Physics*, vol. 114, pp. 185-200, 1994.
- [6] E. Tentzeris, M. Krumpholz and L.P.B. Katehi, "Application of MRTD to Printed Transmission Lines", *Proc. MTT-S 1996*, pp. 573-576.
- [7] R. Robertson, E. Tentzeris, M. Krumpholz and L.P.B. Katehi, "Application of MRTD Analysis to Dielectric Cavity Structures", *Proc. MTT-S 1996*, pp. 1840-1843.
- [8] R. Robertson, E. Tentzeris, and L.P.B. Katehi, "Modelling of Membrane Patch Antennas using MRTD Analysis", *Proc. AP-S 1997*, pp. 126-129.

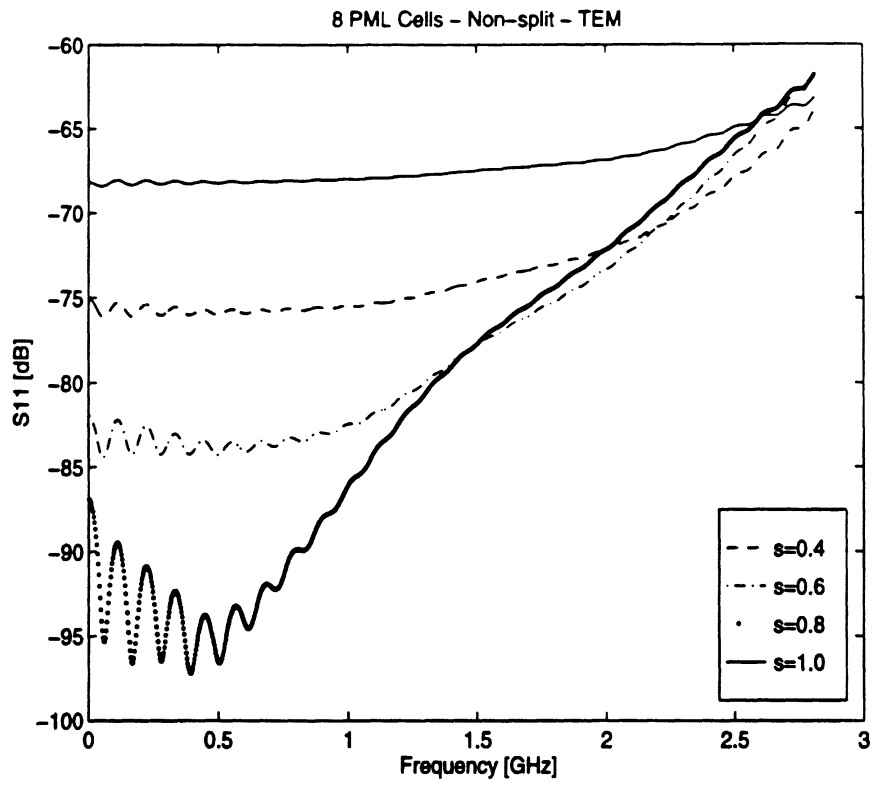


Figure 1: 8 PML cells.

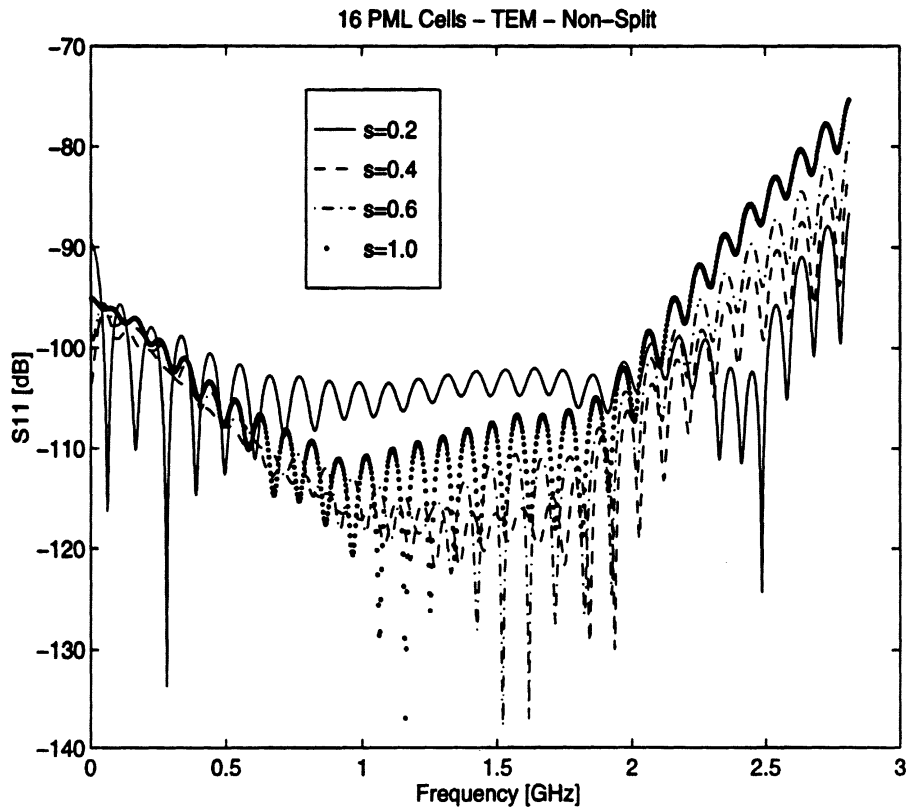


Figure 2: 16 PML cells.

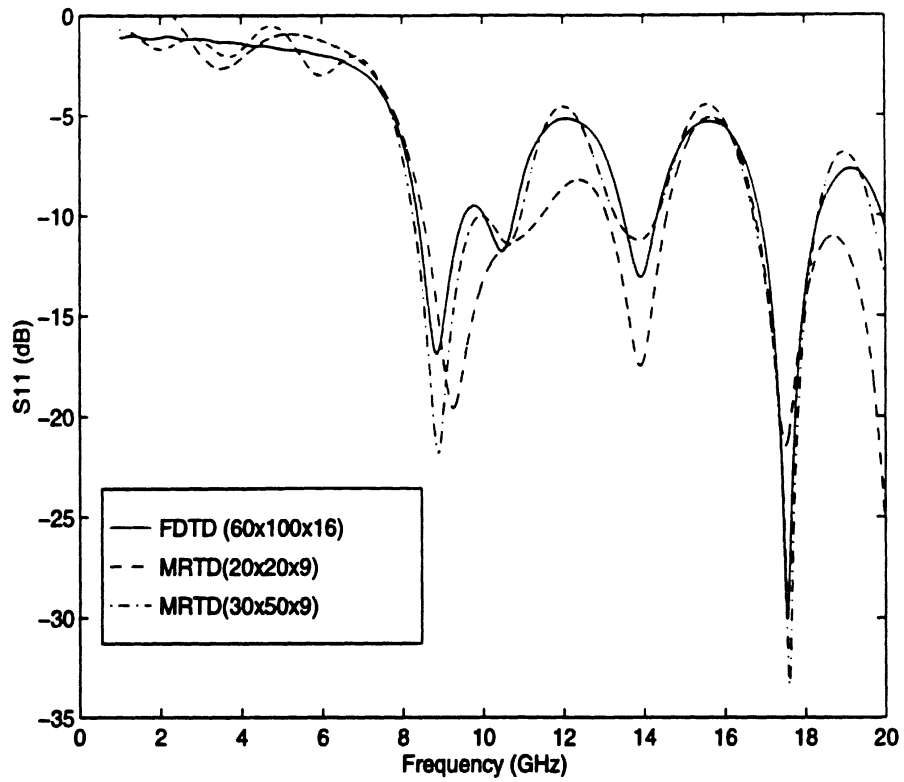


Figure 3: S_{11} comparison plots for a patch antenna

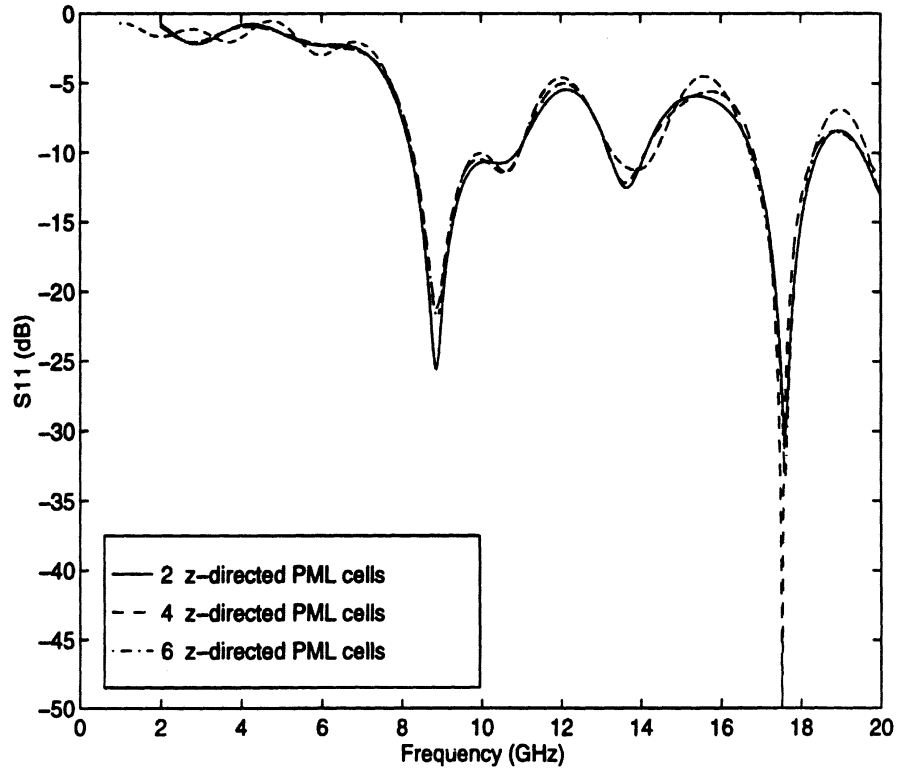


Figure 4: MRTD($30 \times 50 \times 9$) S_{11} plot for varying PML layers in the z -direction

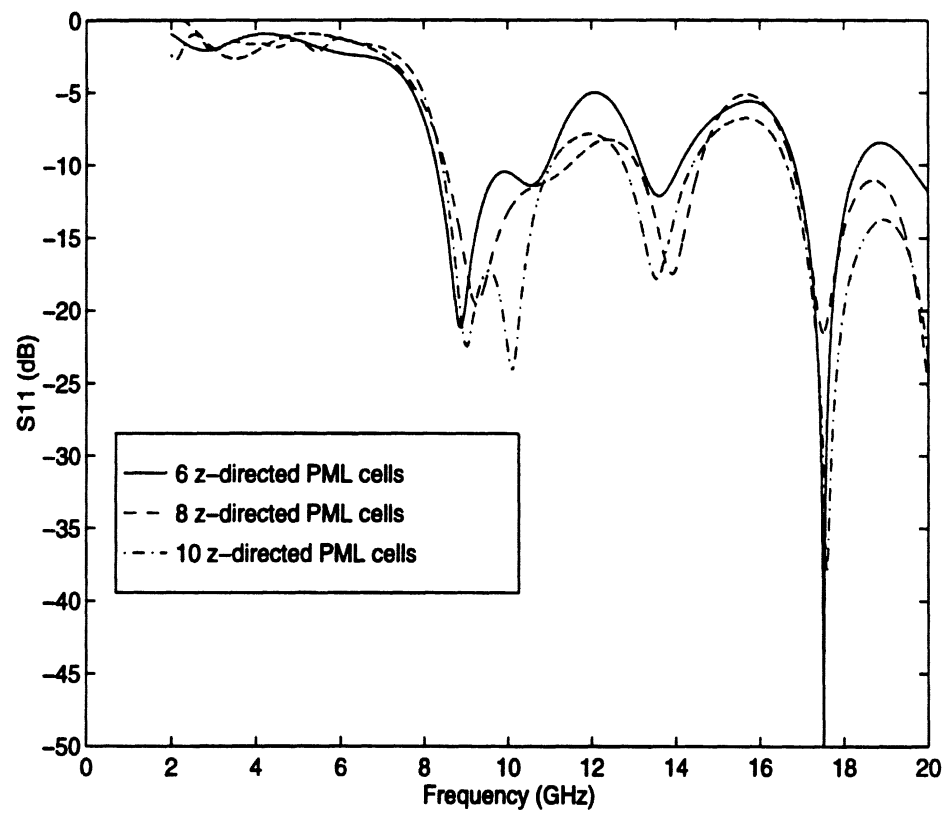


Figure 5: MRTD($20 \times 20 \times 9$) S_{11} plot for varying PML layers in the z-direction

NONLINEAR CIRCUIT CHARACTERIZATION USING A MULTIREOLUTION TIME DOMAIN TECHNIQUE (MRTD)

Luca Roselli¹, Emmanouil M. Tentzeris², Linda P.B. Katehi²

¹ University of Perugia, Perugia, ITALY

² Radiation Laboratory, Department of Electrical Engineering and Computer Science
University of Michigan, Ann Arbor, MI 48109-2122, U.S.A.

Abstract- The MRTD scheme is applied to the modeling of nonlinear circuits. Specifically, the implementation of passive and active elements is discussed. The results are compared to those obtained by use of the commercial CADs to indicate considerable savings in memory and computational time.

I Introduction

Recently, the use of multiresolution analysis for the discretization of the time-domain Maxwell's equations has led to the development of the Multiresolution Time Domain Technique (MRTD). This technique has been applied to linear as well as nonlinear propagation problems and has demonstrated savings in time and memory of two orders of magnitude. In addition, the most important advantage of this new technique is its capability to provide a very effective way for space and time adaptive gridding without encountering the problems that the conventional FDTD has to resolve.

In this paper, an algorithm to model nonlinear circuits using the MRTD scheme is proposed and applied to diode problems. As an example, the harmonic analysis of a diode enclosed in a metallic shield and terminated with lumped resistors is performed and a simple stripline mixer circuit using the same diode is analyzed.

II The MRTD scheme

To derive the MRTD scheme, the field components are expanded in a series of cubic spline Battle-Lemarie [1, 2] scaling and wavelet functions in space

and pulse functions in time. The MRTD equations are derived by applying the Method of Moments to the Maxwell's equations after inserting the field expansions.

For open structures, the perfectly matched layer (PML) technique can be applied by assuming that the conductivity is given in terms of scaling and wavelet functions instead of pulse functions with respect to space [3]. The MRTD mesh is terminated by a perfect electric conductor (PEC) at the end of the PML region. Unlike the FDTD, where the consistency with the image theory is implicit in the application of the boundary conditions, the entire-domain nature of the wavelet and scaling functions requires an explicit use of the boundary conditions. In particular, image theory has to be applied for the evaluation of the field component coefficients in the vicinity of Perfect Electric and Magnetic Walls. Due to the nature of the Battle-Lemarie expansion functions, the total field is a summation of the contributions from the non-localized scaling and wavelet functions.

III Lumped Elements

Similarly to LE-FDTD technique [4], the basis of the algorithm is given by a particular interpretation of the current density term contained in the $Curl(H)$ Maxwell's equation. Let's assume for the rest of the discussion that all the lumped elements are z-oriented.

$$\epsilon \frac{\partial E_z}{\partial t} = \hat{z} \cdot (\bar{\nabla} \times \bar{H}) + J_c^z \quad (1)$$

The current term can be considered as the superposition of two separate terms, one coming from the finite conductivity of the medium J_u^z and the other coming from the presence of a lumped element J_{lu}^z . Eq.(1) leads to the following general updating expression for the E-field S-MRTD (Scaling-functions-based) coefficients:

$$\epsilon \frac{{}^{k+1}E_{l,m,n+\frac{1}{2}}^{\phi z} - {}^k E_{l,m,n+\frac{1}{2}}^{\phi z}}{\Delta t} = \hat{z} \cdot (\bar{\nabla} \times \bar{H}) + {}^{k+\frac{1}{2}}J_{l,m,n+\frac{1}{2}}^{\phi z}$$

where an ideal dielectric medium with $\sigma = 0$ has been assumed. The discretization of the last term can be obtained by expressing the constitutive relationship of the related device in terms of electric field and current density (instead of V-I relation as usual).

Since the field components are expanded in pulses in the time-domain, the time discretization of the J-E relation of the lumped devices is straightforward and similar to FDTD.

III.1 Resistor

Assuming that the resistor is z-oriented and a positive voltage (with respect to the z-axis) is applied, we have:

$$V_z = -\Delta z E_z, \quad I_z = J_{lu}^z \Delta x \Delta y$$

Since the current flow due to a positive voltage is negative with respect to the z-axis, Ohm's Law can be written in the following form:

$$J_{lu}^z = \frac{\Delta z E_z}{R \Delta x \Delta y} \quad (2)$$

By discretizing equations 1 and 2 accordingly to the S-MRTD scheme and assuming that no current density is supported by the medium we obtain:

$$\begin{aligned} {}^{k+1}E_{l,m,n+\frac{1}{2}}^{\phi z} &= \frac{B}{C} {}^k E_{l,m,n+\frac{1}{2}}^{\phi z} + \\ &+ \frac{1}{C \Delta x} \sum_{i=l-9}^{l+8} a(i)_{k+\frac{1}{2}} H_{i+\frac{1}{2},m,n+\frac{1}{2}}^{\phi y} - \\ &- \frac{1}{C \Delta y} \sum_{j=m-9}^{m+8} a(j)_{k+\frac{1}{2}} H_{l,j+\frac{1}{2},n+\frac{1}{2}}^{\phi x} \end{aligned}$$

where

$$B = \frac{\epsilon}{\Delta t} - \frac{\Delta z}{2R \Delta x \Delta y}, \quad C = \frac{\epsilon}{\Delta t} + \frac{\Delta z}{2R \Delta x \Delta y}$$

III.2 Capacitor

The I-V Law of the capacitor is:

$$I(t) = C \frac{dV(t)}{dt}$$

Expanding the E- and H- components in scaling functions in space and pulses in time and applying the Moments Method, the capacitor can be described by

$$\begin{aligned} {}^{k+1}E_{l,m,n+\frac{1}{2}}^{\phi z} &= {}^k E_{l,m,n+\frac{1}{2}}^{\phi z} + \\ &+ \frac{1}{B \Delta x} \sum_{i=l-9}^{l+8} a(i)_{k+\frac{1}{2}} H_{i+\frac{1}{2},m,n+\frac{1}{2}}^{\phi y} - \\ &- \frac{1}{B \Delta y} \sum_{j=m-9}^{m+8} a(j)_{k+\frac{1}{2}} H_{l,j+\frac{1}{2},n+\frac{1}{2}}^{\phi x} \end{aligned}$$

where the coefficient B is given by:

$$B = \frac{\epsilon + C \frac{\Delta z}{\Delta x \Delta y}}{\Delta t}$$

III.3 Inductor

The constitutive relation of the inductor is:

$$I(t) = L \int V(t) dt$$

Following the same procedure described for the resistor and the capacitor we obtain:

$$\begin{aligned} {}^{k+1}E_{l,m,n+\frac{1}{2}}^{\phi z} &= \frac{C}{A} {}^k E_{l,m,n+\frac{1}{2}}^{\phi z} - \frac{B}{A} \sum_{i=1}^k i E_{l,m,n+\frac{1}{2}}^{\phi z} + \\ &+ \frac{1}{A \Delta x} \sum_{i=l-9}^{l+8} a(i)_{k+\frac{1}{2}} H_{i+\frac{1}{2},m,n+\frac{1}{2}}^{\phi y} - \\ &- \frac{1}{A \Delta y} \sum_{j=m-9}^{m+8} a(j)_{k+\frac{1}{2}} H_{l,j+\frac{1}{2},n+\frac{1}{2}}^{\phi x} \end{aligned}$$

where the coefficients A, B, C are given by:

$$A = \frac{\epsilon}{\Delta t} + \frac{\Delta z \Delta t}{2L \Delta x \Delta y}, \quad B = \frac{\Delta z \Delta t}{2L \Delta x \Delta y}, \quad C = \frac{\epsilon}{\Delta t}$$

III.4 Diode with Junction and Diffusion Capacitances

According to the model adopted in [5], the equivalent circuit of the diode includes both the non linear junction and diffusion capacitances ($C_{di}(V_d)$ and $C_j(V_d)$) and the total current can be expressed as:

$$I_d = I_j + I_{C_{di}} + I_{C_j}$$

with

$$I_j = I_0 \left(e^{\frac{q}{\eta k T} V_d} - 1 \right),$$

$$I_{C_{di}} = C_{di}(V_d) \frac{dV_d}{dt}, \quad I_{C_j} = C_j(V_d) \frac{dV_d}{dt}.$$

In the above equations K is the Boltzmann constant, T is the absolute temperature, I_0 is the inverse saturation current of the diode and η is the ideality factor that will be omitted in the rest of the discussion. The two non linear capacitances, in turn, are modeled by the following equations:

$$C_{di}(V_d) = \tau_d I_0 \frac{q}{KT} \left(e^{\frac{q}{\eta k T} V_d} - 1 \right)$$

$$C_j(V_d) = C_j(0) \left(1 - \frac{V_d}{\phi_0} \right)^{-m} \quad \text{if } V_d > F_c \phi_0$$

$$C_j(V_d) = \frac{C_j(0)}{F_2} \left(F_3 + \frac{m V_d}{\phi_0} \right)^{-m} \quad \text{if } V_d \leq F_c \phi_0$$

where F_c , F_2 , F_3 are suitable coefficients, m is the doping profile coefficient (usually 0.5 for abrupt junction), ϕ_0 is the built-in voltage and $C_j(0)$ is the static capacitance at $V_d = 0$.

The current equations are discretized in a similar way with the other lumped elements and two E-field transcendental equations are derived for $V_d < F_c \phi_0$ and $V_d \geq F_c \phi_0$. These equations can be solved in an iterative procedure (e.g. Newton-Raphson algorithm).

IV Applications of Nonlinear MRTD

The modeled Schottky GaAs diode has the following parameter values: $I_0 = 5.e - 11$ A, $\eta = 1.25$, $R_s = 13 \Omega$, $C_j(0) = .29pF$, $\tau_d = 0$, $m = 0.5$, $F_c = .5$. For the analysis of the testing structure of Fig.(1), we have set up a mesh of $8 \times 30 \times 6$ cells with a cell size equal to $30 \times 60 \times 30 \mu m$ ($60 \mu m$ is $\lambda/10$ at about $135 GHz$). The same structure has been also analyzed, for comparison, with FDTD method. This analysis has been performed by adopting two different meshes: the same mesh described before and a doubled mesh with the dimension: $16 \times 60 \times 12$ and $\lambda/10$ at about $270 GHz$. The structure has been excited at the center with an impressed current source window. A sine-wave with a frequency of $45 GHz$ has been used, while a probe at the center of the

structure has been considered. Figures (2),(3) and (4) show the results obtained with the coarse FDTD, the finer FDTD, and the MRTD respectively. The MRTD simulation has adopted the same mesh used in the coarsest FDTD analysis. The good agreement between the FDTD simulation with the fine mesh and the MRTD one, together with the fairly different results obtained with the coarse mesh FDTD analysis, put at the evidence the capability of the MRTD to better predict the frequency behavior of this non linear circuit. In particular, it is evident that with a coarse mesh, MRTD, in contrast to FDTD, can detect the harmonic null due to the location of the probe in the middle of the structure (in this position, in theory, no even harmonic mode should be detected).

Figure (5) shows the geometry of a stripline single-ended mixer, which is analyzed by use of MRTD. The used Schottky diode has the characteristics described above and is zero biased for simplicity. The LO and RF excitation signals have frequencies $43 GHz$ and $45 GHz$ and powers $20 dBm$ and $-20 dBm$ respectively. The left (short-circuited) stub with length $900 \mu m$ is used as an IF signal block and the right (open-circuited) stub with length $1640 \mu m$ blocks the LO/RF signals at the output section. For this configuration, MRTD gives a conversion loss of $-8.1 dB$. LIBRA, a commercial EM simulator, calculates the conversion loss at $-8.8 dB$. In addition, (Table 1) shows that the relative output power of the harmonics gets similar values for MRTD and LIBRA simulations. These results emphasize the inherent capability of MRTD to describe efficiently the nonlinear elements, which create a discrete but infinite spectrum. Moreover, the MRTD allows for a time adaptive scheme which offers significant computational profit due to the iterative algorithm for the solution of the nonlinear equations. It has to be pointed out that LIBRA can give reliable results only for quasi-static geometries such as Figure (5). On the contrary, MRTD can simulate efficiently structures with multimodal propagation without the huge memory requirements of the conventional FDTD schemes.

Table 1: Harmonics Power Distribution [dBm]

Freq [GHz]	2	41	43	45	88
LIBRA	-28.8	-56.1	-33.2	-40.1	-36.3
MRTD	-28.1	-54.7	-31.4	-38.2	-34.7

V Conclusion

An algorithm for the modeling of lumped elements with the MRTD scheme based on the Battle-Lemarie basis has been proposed and has been applied to the numerical analysis of a diode problem. The frequency spectrum has been calculated and verified by comparison to reference data. In comparison to Yee's conventional FDTD scheme, the proposed scheme offers memory savings by a factor of 2-6 per dimension maintaining a similar accuracy.

VI Acknowledgments

This work has been funded by NSF and ARO. The authors would like to thank Dr. F. Alimenti for the interesting and useful discussion about theoretical aspects concerning the multiresolution techniques and Prof. R. Sorrentino for the continuous support he gave to this work.

References

- [1] M.Krumpholz, L.P.B.Katehi, "MRTD: New Time Domain Schemes Based on Multiresolution Analysis", IEEE Trans. Microwave Theory Tech., pp. 555-572, 1996.
- [2] E.Tentzeris, M.Krumpholz and L.P.B. Katehi, "Application of MRTD to Printed Transmission Lines", Proc. MTT-S 1996, pp. 573-576.
- [3] E.Tentzeris, R.Robertson, M.Krumpholz and L.P.B. Katehi, "Application of the PML Absorber to the MRTD Technique", Proc. AP-S 1996, pp. 634-637.
- [4] W.Sui, D.Christensen and C.Durney, "Extending the two-dimensional FDTD Method to Hybrid Electromagnetic Systems with Active and Passive Lumped Elements", IEEE Trans. Microwave Theory Tech., pp. 724-730, 1992.
- [5] G.Massobrio and P.Antognetti, "Semiconductor Device Modeling with Spice 2/E", McGraw-Hill.

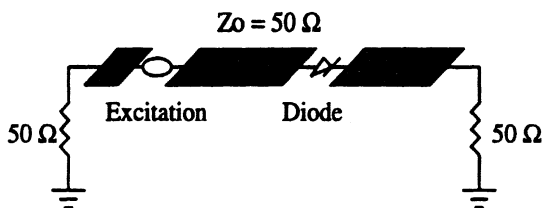


Figure 1: Diode Test Structure.

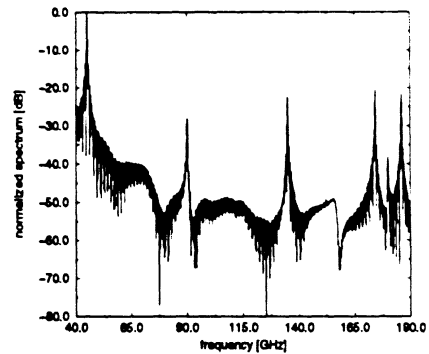


Figure 2: FDTD coarse mesh.

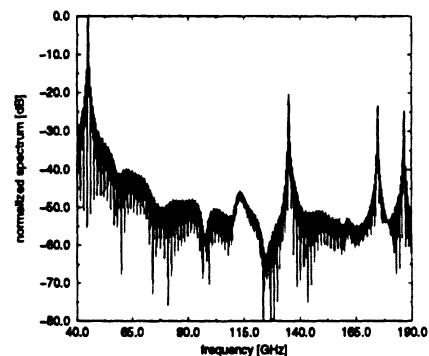


Figure 3: FDTD fine mesh.

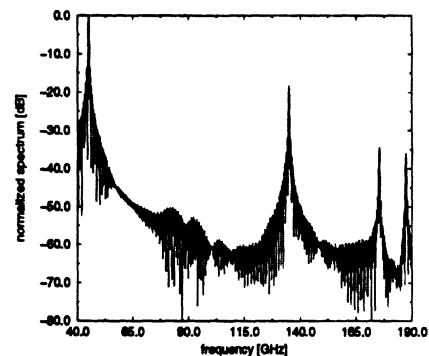


Figure 4: MRTD coarse mesh.

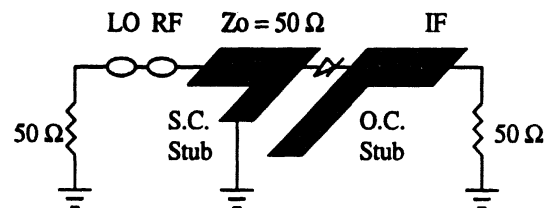


Figure 5: Mixer Geometry.

SPACE ADAPTIVE ANALYSIS OF EVANESCENT WAVEGUIDE FILTERS

Emmanouil M. Tentzeris, Linda P.B. Katehi

Radiation Laboratory, Department of Electrical Engineering and Computer Science
University of Michigan, Ann Arbor, MI 48109-2122, U.S.A.

Abstract- The MRTD scheme is applied to the analysis of evanescent waveguide filters. Specifically, a space adaptive algorithm in 3 dimensions is implemented by thresholding the wavelet values. The results are compared to those obtained by use of the conventional FDTD to indicate considerable savings in memory and computational time.

I Introduction

The Space Adaptive Gridding [1], based on the application of the Multiresolution Analysis principles to the discretization of the time-domain Maxwell's equations [2, 3], has been employed in the analysis of linear and nonlinear structures. It has offered significant savings in memory and execution time requirements. The application of the wavelets improve the conditioning of the simulating algorithm and allow for a space adaptive grid by thresholding the wavelet coefficients. This adaptivity is useful especially in evanescent mode structures that require time-domain simulations for a large time span in order to take into consideration the slow wave propagation.

In this paper, a space adaptive grid is applied for the analysis of evanescent-mode waveguide bandpass filters [4, 5, 6]. These structures have found many applications in satellite communication systems, as preselectors or in multiplexers, due to several advantages over the conventional coupled resonator filters, such as compactness and wide stopbands. The S-parameters of one specific geometry are calculated and compared to results obtained by the conventional FDTD.

II The MRTD scheme

The 3D-MRTD scheme can be derived by representing the field components as a series of cubic spline Battle-Lemarie scaling and wavelet functions in space-domain and pulse function in time. Applying the Method of Moments to the Maxwell's equations results in the MRTD equations. Generally, the features of the 3D-MRTD algorithm are similar to those of the 2D-MRTD algorithm. Nevertheless, there are some differences as far as it concerns the implementation of the excitation and of the PML absorber.

In order to use a pulse excitation with respect to space at a specific grid point for a 2D geometry and to obtain an excitation identical to that used by FDTD, the pulse is decomposed in terms of scaling and wavelet functions on a square surface around the excitation point. For the 3D-MRTD algorithm, this decomposition takes place in a cubic volume around this point, since the excitation affects the amplitudes of the scaling and the wavelet function in all 3 directions. It has been observed that 4 cells along each direction around the excitation point provide an accurate representation of the source for most cases.

The maximum allowable time step required for the stability of 3D-MRTD algorithms has to contain the effect of all three space discretizations. For a summation stencil of 9 terms per direction and for 0-resolution wavelet expansion it takes the value

$$\Delta t_{max} = \frac{0.37 c}{\sqrt{1/(\Delta x)^2 + 1/(\Delta y)^2 + 1/(\Delta z)^2}}$$

where c is the velocity of light. For larger stencils, the maximum value of the time step takes lower values.

The size of the stencil affects significantly the dispersion characteristics of the used algorithm. Larger stencil for the summations including scaling functions coefficients improves the phase error performance for medium and high sampling rates (discretization size $\leq \lambda/10$). Increasing the stencil size in summations of wavelet functions coefficients offers a better dispersion performance for lower sampling rates (between $\lambda/2.2$ and $\lambda/5$). In our simulations, the used stencil size has had the value of 9 for a phase error smaller than 1° for most discretizations.

The use of the non-localized Battle-Lemarie basis functions causes significant effects. Localized boundary conditions are impossible to be directly implemented, so perfect electric and magnetic boundary conditions are modelled by use of the image principle in a generic way. The implementation of image theory in 3 dimensions is performed automatically for any number of PEC, PMC boundaries.

Due to the nature of the Battle-Lemarie expansion functions, the total field is a summation of the contributions from the non-localized scaling and wavelet functions in 3 directions. For example, the total electric field $E_x(x_o, y_o, z_o, t_o)$ with $(k - 1/2) \Delta t < t_o < (k + 1/2) \Delta t$ is calculated

$$E_x(x_o, y_o, z_o, t_o) = \sum_{l_1}^{l_1} \sum_{l', m', n' = -l_1}^{l_1} k E_{l'+1/2, m', n'}^{\phi x} \phi_{l'+1/2}(x_o) \phi_{m'}(y_o) \phi_{n'}(z_o) + \sum_i \sum_{l', m', n' = -l_{2,i}}^{l_{2,i}} k E_{l'+1/2, m', n'}^{\psi_i x} \phi_{l'+1/2}(x_o) \phi_{m'}(y_o) \psi_{i, m'}(z_o)$$

where $\phi_m(x) = \phi(\frac{x}{\Delta x} - m)$ and $\psi_{i, m}(x) = \psi_i(\frac{x}{\Delta x} - m)$ represent the Battle-Lemarie scaling and i -resolution wavelet functions respectively. Only wavelets to z -direction have been included for simplicity. For an accuracy of 0.1% the values $l_1 = l_{2,i} = 6$ have been used.

The purpose of a space adaptive grid is to use a coarse mesh and implement a local magnification by the selective use of wavelets. Wavelets are placed only at locations where the EM fields have significant values, creating a space- and time- adaptive dense mesh in regions of strong field variations without adding a significant computational overhead. There are many

different ways to take advantage of the capability of the MRTD technique to provide space and time adaptive gridding. All of them rely on the fact that the wavelet values can be thresholded without affecting the accuracy of the algorithm. The simplest way is to threshold the wavelet components to a fraction (usually $\leq 0.5\%$) of the scaling function coefficient at the same cell for each time-step. All components below this threshold are eliminated from the subsequent calculations. This procedure doesn't add any significant overhead in execution time (usually $\leq 12\%$), but it offers only a moderate economy in memory requirements (round 28 – 35%). Comparison of the wavelet values over a specific space window of scaling neighbors (often equal to the stencil size) would offer a more significant economy in memory, but would demand more execution time. Another way of creating a space adaptive grid is to use an absolute threshold. This requires the knowledge of the spatial field distribution in advance, something that makes it inappropriate for simulations of complicated structures. Generally, in 3D cases where both memory and execution requirements are high, the first thresholding algorithm offers an optimized performance.

III Applications of Nonlinear MRTD

Without loss of generality, the space adaptive algorithm used in all simulations presented herein includes one resolution of wavelets only to the z - (longitudinal) direction. For validation purposes, this scheme has been used for the analysis of the testing structure of Figure (1). This filter geometry contains four bilateral E-plane fins in a single WR62 waveguide housing (15.799 mm \times 7.899 mm). The thickness of the fins is $t=0.9$ mm and the gap width is $w=3.1$ mm. The agreement of data obtained from the space adaptive grid for a relative threshold of 0.5% and those obtained by use of mode matching [4] is very good (Figure(2)).

Another evanescent-mode E-plane finned waveguide bandpass filter geometry is shown in Figure(3). A WR90 waveguide (22.86 mm \times 10.16 mm) is used at the input and output stages and a rectangular

waveguide with a cross-section of $7.06 \text{ mm} \times 6.98 \text{ mm}$ is used as the housing of the filter. Geometrical parameters of the filter take the values $l_1 = l_2 = 0.5 \text{ mm}$, $l_3 = 7.75 \text{ mm}$ and $l_4 = 0.94 \text{ mm}$. The width of the fins is chosen to be equal to the waveguide side length $a = w = 7.06 \text{ mm}$. The MRTD space adaptive grid is used to optimize the geometry. An $20 \times 20 \times 389$ grid is used for the simulations and 85,000 time steps are considered. A Gabor pulse from 10-18 GHz is used as the excitation along a plane at $z = 44$. Front and back waveguides are terminated with 8 PML layers with $R = 10^{-5}$. A relative threshold of 0.5% is employed and offers economy in memory at least by 32%.

In the geometry under study, we have different electrical paths between the input and output ports; one (the main path) is constructed with the coupled $TE_{10} - TE_{10} - TE_{10}$ modes, and the others (the subsidiary paths) are constructed with the coupled $TE_{10} - TE_{m0} - TE_{10}$ modes, where TE_{m0} for $m \geq 1$ express the higher order evanescent modes. These modes play primarily an important role to produce a desired off-passband performance, but it also affects significantly the passband behavior. Therefore, we can not use the conventional synthesis method. The slow velocity of the evanescent waves, require the use of very dense grids of the conventional FDTD algorithm for a large number of time-steps (close to 150,000). For example, a grid of $90 \times 20 \times 778$ has been used for 135,000 steps to provide comparable results. On the contrary, space adaptive MRTD algorithms can use coarse grids everywhere except from the areas that the evanescent modes have significant values. Localized use of wavelets in these regions offer the necessary grid magnification. This effect can be observed in Figure(4) that shows the wavelet coefficients amplitude for an arbitrary time step after the pulse has propagated along the whole structure. The results from the optimization (Figures (5)-(7)) show that as the used fins get wider and come closer, the S_{21} gets higher values without affecting the significantly the bandwidth of the filter.

IV Conclusion

A space adaptive 3D algorithm based on Battle-Lemarie scaling and wavelet functions has been applied in the numerical modeling of evanescent-mode waveguide bandpass filters. The S-parameters of one specific geometry are calculated and offer memory savings by a factor of 3-6 per dimension and execution time savings by a factor of 2.5 compared to results obtained by the conventional FDTD.

V Acknowledgments

This work has been funded by ARO.

References

- [1] E.Tentzeris, R.Robertson, A.Cangellaris and L.P.B.Katehi, "Space- and Time- Adaptive Gridding Using MRTD", Proc. MTT-S 1997, pp.337-340.
- [2] M.Krumpholz, L.P.B.Katehi, "MRTD: New Time Domain Schemes Based on Multiresolution Analysis", IEEE Trans. Microwave Theory Tech., pp. 555-572, 1996.
- [3] E.Tentzeris, R.Robertson, M.Krumpholz and L.P.B.Katehi, "Application of the PML Absorber to the MRTD Technique", Proc. AP-S 1996, pp. 634-637.
- [4] J.Bornemann and F.Arndt, "Rigorous Design of Evanescent-Mode E-Plane Finned Waveguide Bandpass Filters", Proc. MTT-S 1989, pp. 603-606.
- [5] V.Labay and J.Bornemann, "A New Evanescent-Mode Filter for Densely Packaged Waveguide Applications", Proc. MTT-S 1992, pp.901-904.
- [6] K.Iguchi, M.Tsuji and H.Shigesawa, "Negative Coupling between TE_{10} and TE_{20} Modes for Use in Evanescent-Mode Bandpass Filters and their Field-Theoretic CAD", Proc. MTT-S 1994, pp. 727-730.

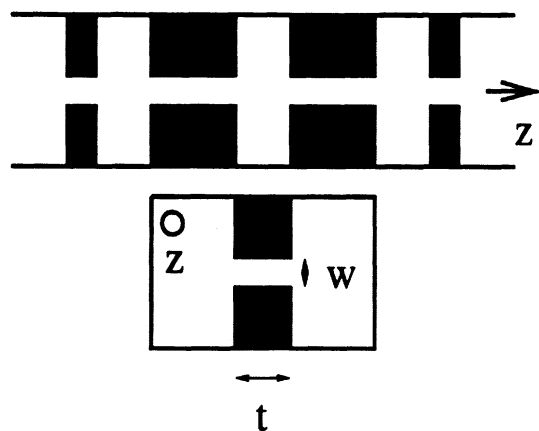


Figure 1: Validation Structure.

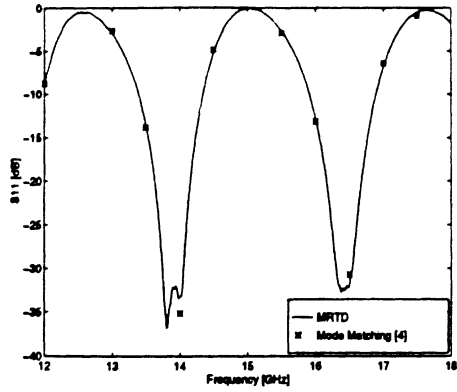


Figure 2: Validation Data.

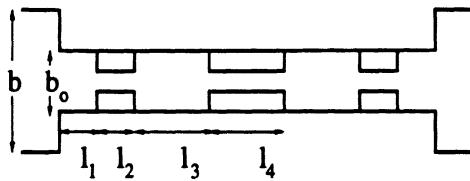


Figure 3: Optimized Filter Geometry.

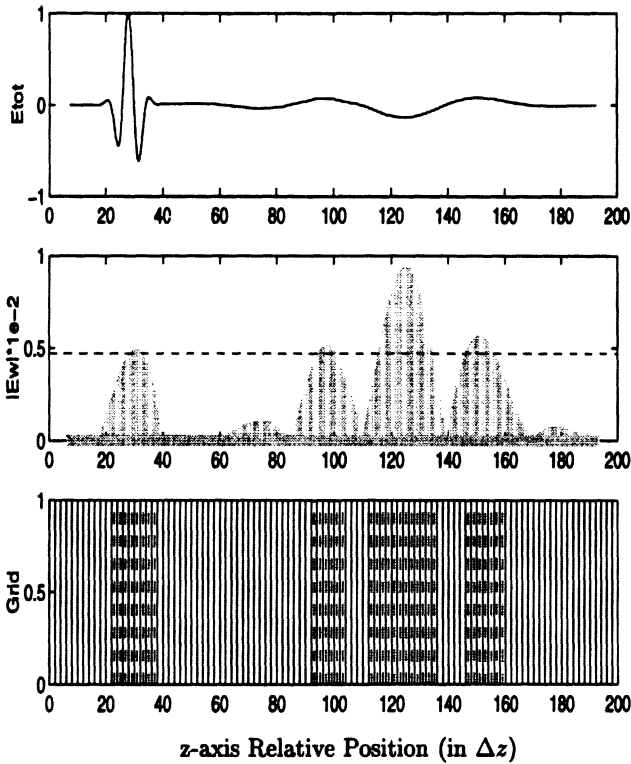


Figure 4: Wavelet Coefficients Spatial Distribution (Δz : cell size to the z-direction).

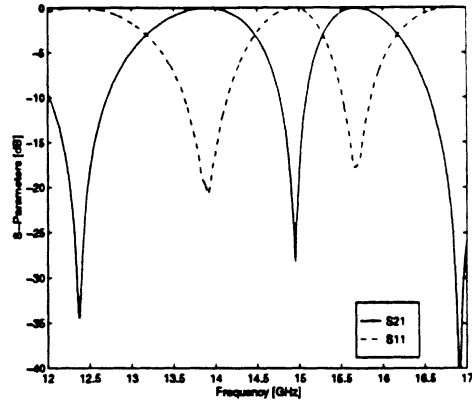


Figure 5: S-Parameters for $l_1 = l_4 = 1.0\text{mm}$, $l_2 = 0.5\text{mm}$, $l_3 = 6.75\text{mm}$.

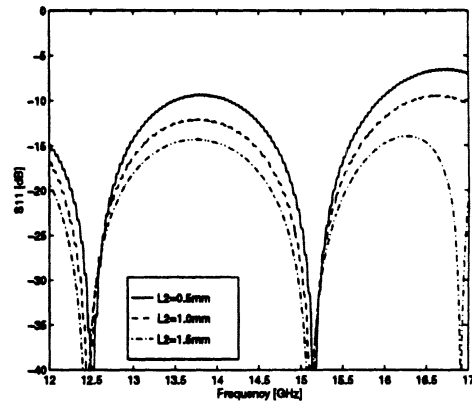


Figure 6: Parametric Variation of l_2 .

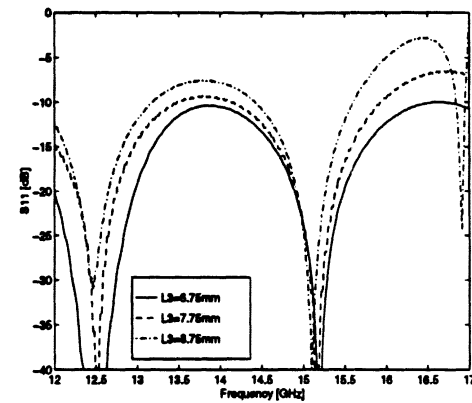


Figure 7: Parametric Variation of l_3 .

**TIME-DOMAIN NUMERICAL TECHNIQUES FOR THE
ANALYSIS AND DESIGN OF MICROWAVE CIRCUITS**

by

Emmanouil M. Tentzeris

A dissertation submitted in partial fulfillment
of the requirements for the degree of
Doctor of Philosophy
(Electrical Engineering)
in The University of Michigan
1998

Doctoral Committee:

Professor Linda P.B.Katehi, Chair
Professor John Volakis
Professor Andrew Yagle
Assoc. Professor Kamal Sarabandi
Dr. James Harvey

ABSTRACT

TIME-DOMAIN NUMERICAL TECHNIQUES FOR THE ANALYSIS AND DESIGN OF MICROWAVE CIRCUITS

by

Emmanouil M. Tentzeris

Chair: Linda P.B.Katehi

This dissertation investigates the effects of the application of the principles of Multiresolution Analysis (MRA) to time-domain numerical techniques used for the analysis and design of microwave circuits. The improvement in the efficiency in terms of memory and execution time requirements is quantified and the inherent capability of MRA to create a mathematically consistent time/space adaptive gridding is exploited.

Initially, various aspects concerning the popular finite-difference time-domain technique (F.D.T.D.) are investigated and a memory-efficient waveguide absorber based on analytical Green's functions is developed and applied to the optimization of a specific waveguide probe geometry.

After reviewing the general principles of Multiresolution Analysis, novel time-domain schemes based on space-domain expansions in scaling and wavelet functions are derived. FDTD implementation schemes (excitation, hard/open boundary and dielectric interfaces) are extended to Multiresolution schemes based on entire-domain expansion basis, while

maintaining similar performance characteristics. These schemes offer the unique opportunity of a multi-point field representation per cell. Battle-Lemarie functions are used throughout the dissertation due to their special qualities.

These Multiresolution Time-Domain Schemes in 2D are applied to the numerical analysis of shielded and open striplines and microstrips. The field patterns and the characteristic impedance are calculated and verified by comparison to reference data. In comparison to Yee's conventional FDTD scheme, the proposed 2.5D-MRTD scheme offer memory savings by a factor of 25 and execution time savings by a factor of about 4-5 maintaining a better accuracy for characteristic impedance calculations.

The stability and the dispersion performance of the Battle-Lemarie MRTD schemes is investigated for different stencil sizes and for 0-resolution wavelets. Analytical expressions for the maximum stable time-step are derived in a way similar to the "magic step" of the FDTD algorithm.

A dynamically changing space- and time- adaptive meshing algorithm based on a multiresolution time-domain scheme in two dimensions and on absolute and relative thresholding of the wavelet values is proposed and applied to the numerical analysis of various nonhomogeneous waveguide geometries offering additional memory economy.

In the last Chapter, intervalic wavelets are added in the time-domain. This Time-Adaptive Time-Domain Technique is used for the analysis of various types of circuits problems with active and passive lumped and distributed elements. This scheme exhibits significant savings in execution time and memory requirements while maintaining a similar accuracy with the FDTD technique.

© Emmanouil M. Tentzeris 1998
All Rights Reserved

“As you set out for Ithaka hope your road is a long one, full of adventure, full of discovery. Laistrygonians, Cyclops, angry Poseidon - don't be afraid of them: you'll never find things like that one on your way as long as you keep your thoughts raised high, as long as a rare sensation touches your spirit and your body.

Keep Ithaka always in your mind. Arriving there is what you're destined for. But don't hurry the journey at all. Better if it lasts for years, so you're old by the time you reach the island, wealthy with all you've gained on the way, not expecting Ithaka to make you rich. Ithaka gave you the marvellous journey. Without her you wouldn't have set out. She has nothing left to give you now. And if you find her poor, Ithaka won't have fooled you. Wise as you have become, so full of experience, you'll have understood by then what these Ithakas mean. ”

K.Kavafis, “Ithaka” (1911)

To my parents; To my brother, John.

ACKNOWLEDGEMENTS

The completion of this dissertation and my entire doctoral study at the University of Michigan would not have been possible without the support of many people. I would like to take this opportunity to express my sincere gratitude to all those who helped me in one way or another during these prolific and memorable years.

My first sincere gratitude and deepest appreciation goes to my advisor, Professor Linda Katehi, since without her insight, expertise, encouragement and understanding, this research would have been a much more difficult and painful journey. Her enthusiasm and boundless energy for research and teaching is very infectious. I am also grateful for her continuous financial support and for providing me with the opportunity to attend numerous conferences to present my research. I would also like to thank my committee members for their time and consideration.

Many friends and colleagues at the Radiation Laboratory have contributed to this work through discussions. Special thanks go to Dr. Michael Krumpholz, from whom I have constantly benefited through a great deal of fruitful conversations. Also, I would like to mention Mr. Robert Robertson. My close work with him and the understanding that we have between us made our research better and our friendship stronger. Dr. Nihad Dib and Ms. Kavita Goverdhanam are deeply appreciated for their useful suggestions. In summary, all Rad Lab friends, too many to mention by name, created a very enjoyable environment

for work and study.

I should mention that the theoretical work on the FG-CPW has been done in cooperation with Dr. George Ponchak from the NASA Lewis Research Center. I thank him for his time and for supplying us with the results which validated the developed theoretical analysis. I specially thank Professor Andreas Cangellaris at the University of Illinois at Urbana-Champaign for his comments on the development of an efficient Time and Space Adaptive Gridding Algorithm.

The major party of my study and research at the University of Michigan was sponsored by the Army Research Office. The continuous enthusiasm of this office, and especially of Dr. Harvey, in my research work is cordially appreciated.

Dr. George Eleftheriades, Messrs. John Papapolymerou, Hristos Anastasiou, Hristos Patonis, Loucas Louca, Nikos Zacharopoulos and Kostas Sarris with their dear friendship made difficult moments easier. In addition, my numerous friends from the Hellenic Students Association of the University of Michigan gave a nice flavor and broadened my outlook on life.

I also express my deepest gratitude to my parents Markos and Irene Tentzeris, who sowed in me from the early years the seeds of aspiration to ascend to the highest levels in every aspect of life, especially in education and knowledge. Finally, I wish to thank my younger brother John, who has always believed in me throughout my entire education.

TABLE OF CONTENTS

DEDICATION	ii
DEDICATION	ii
ACKNOWLEDGEMENTS	iii
LIST OF TABLES	viii
LIST OF FIGURES	ix
CHAPTERS	
1 Introduction	1
1.1 Time-Domain Techniques	1
1.2 Wavelets-Multiresolution Analysis	3
1.3 Overview of the Dissertation	5
2 The Finite Difference Time Domain Technique (F.D.T.D.) and its Applications in the Analysis and Design of Microwave Circuits and Waveguide Probes	8
2.1 Foundations of the Finite Diference Time Domain (F.D.T.D.) Technique	8
2.1.1 Overview of Numerical Absorbing Boundary Conditions	14
2.1.2 Excitation Topics	15
2.1.3 Linear Predictors	17
2.2 Applications of F.D.T.D. to Planar Circuits	20
2.2.1 Open Circuit Design	20
2.2.2 Viahole Analysis	21
2.2.3 Filter Design	22
2.2.4 Finite-Ground CPW Line Analysis	23
2.3 Application of FDTD to Waveguide Structures	24
2.3.1 FDTD and Waveguide Probe Structures	24
2.3.2 Novel Absorber Description	26
2.4 Conclusion	36
3 Development of New Time-Domain Schemes with Higher Order Basis Functions	54

3.1	Introduction	54
3.2	Fundamentals on Multiresolution Analysis	55
3.3	How to construct a Wavelet Function	57
3.4	The 2D MRTD scheme	63
3.4.1	Modeling of Hard Boundaries	71
3.4.2	Modeling of Excitation	72
3.4.3	Treatment of Open Boundaries - PML Absorber	75
3.4.4	Total Field Calculation	79
3.5	Conclusions	81
4	Characterization of Microwave Circuit Components Using the Multiresolution Time Domain Method (MRTD)	86
4.1	Introduction	86
4.2	The 2.5D-MRTD scheme	87
4.3	Applications of the 2.5D-MRTD scheme to Shielded Transmission Lines	89
4.4	Validation of the MRTD-PML Split and Non-split Algorithms . . .	94
4.5	Application of PML to the Analysis of Open Stripline Geometries .	95
4.6	Conclusion	98
5	Stability and Dispersion Analysis of Multiresolution Time-Domain Schemes	109
5.1	Introduction	109
5.2	Stability Analysis	110
5.3	Dispersion Analysis	113
5.4	Conclusion	118
6	Development of a Space- and Time-Adaptive MRTD Gridding Algorithm for the Analysis of 2D Microwave Dielectric Geometries	131
6.1	Introduction	131
6.2	The 2D-MRTD Nonhomogeneous scheme	132
6.2.1	The 2D-MRTD scaling and wavelets scheme	132
6.2.2	The PML numerical absorber	133
6.2.3	The Excitation Implementation	134
6.2.4	The Modelling of Dielectrics	135
6.2.5	Total Field Calculation	136
6.2.6	Time-Adaptive Gridding	137
6.3	Applications of 2D-MRTD	138
6.3.1	Air-Filled Parallel Plate Waveguide	138
6.3.2	Parallel-Plate Partially Filled Waveguide	139
6.3.3	Parallel-Plate Five-Stage Filter	140
6.4	Conclusion	141
7	Time Adaptive Time-Domain Techniques for the Design of Microwave Cir- cuits	149
7.1	Introduction	149
7.2	Time Adaptive MRTD Scheme	150
7.3	Applications in SPICE problems	151
7.3.1	Distributed Elements	152

7.3.2 Lumped Elements	156
7.4 Conclusion	158
8 Summary of Achievements-Future Work	164
BIBLIOGRAPHY	166

LIST OF TABLES

Table		
3.1	Coefficients $a(i), b_0(i), c_0(i)$	69
3.2	Excitation Scaling Decomposition Coefficients	74
3.3	Excitation Wavelet Decomposition Coefficients	74
4.1	Mode frequencies for $\beta = 30$	90
4.2	Z_o for different number of subpoints/cell (8x4 Grid).	92
4.3	Z_o for different mesh sizes (11 subpoints/cell).	93
4.4	Dominant mode frequency for $\beta = 30$	97
4.5	Z_o for different mesh sizes.	98
5.1	Coefficients C_i for Different MRTD Schemes	115
6.1	S_{11} calculated by 2D-MRTD	142

LIST OF FIGURES

Figure	
2.1 Yee's FDTD cell.	37
2.2 Patch Geometry to be used as Open.	38
2.3 Reflection Coefficient of the Open.	38
2.4 Viahole Structure.	39
2.5 S-Parameters of the Viahole.	39
2.6 E-Distribution across Top Viahole (Top), Middle Ground Plane (Bottom). .	40
2.7 E-Distribution across Bottom Viahole.	41
2.8 Coupled Line Filter Geometry.	42
2.9 Coupled Line Filter S_{21}	42
2.10 Coplanar waveguide with finite width ground planes (F.G.C.).	43
2.11 Normal H-Distribution (Log) for $B=25 \mu\text{m}$ (up), $100 \mu\text{m}$ (bottom).	44
2.12 Waveguide probe structure.	45
2.13 Waveguide Test Structure.	46
2.14 Reflection coefficient for the $TE_{1,0}^z$ mode.	47
2.15 Comparison of Green's Function ABC and PML.	47
2.16 Validation Data for the Reflection Coefficient.	48
2.17 Reflection Coefficient for different Dielectric Thicknesses.	49
2.18 E- and H-field Distributions across the Probe Structure Symmetry Plane. .	50
2.19 E- and H-field Distributions across the Coplanar Feedline Plane.	51
2.20 Reflection Coefficient for different Patch Widths.	52
2.21 Reflection Coefficient for different Distances from the Top Surface Short- Circuit.	52
2.22 Experimental Validation for S_{11}	53
2.23 Experimental Validation for S_{21}	53
3.1 BL Cubic Spline Scaling - Spatial Domain.	82
3.2 BL Cubic Spline Wavelet - Spatial Domain.	82
3.3 BL Cubic Spline Scaling - Spectral Domain.	83
3.4 BL Cubic Spline Wavelet - Spectral Domain.	83
3.5 Image Theory Application for tangential-to-PEC E-field.	84
3.6 Treatment of Wavelet Components of normal-to-PEC E-field.	85
4.1 Printed Lines Geometries.	100

4.2	Shield TE_{10} E_y pattern.	101
4.3	TEM E_y Pattern Components (8x8 Grid).	101
4.4	TEM E_y Pattern Comparison (8x8 Grid).	102
4.5	Tangential E-field Distribution (Shielded - Even Mode).	102
4.6	4 PML cells - Non-split formulation - Dense Grid.	103
4.7	8 PML cells - Non-split formulation - Dense Grid.	103
4.8	16 PML cells - Non-split formulation - Dense Grid.	104
4.9	Multimodal Propagation - Dense Grid.	104
4.10	TEM Propagation - Coarse Grid.	105
4.11	Multimodal Propagation - Coarse Grid.	105
4.12	Comparison of Sampled vs. Non-sampled PML.	106
4.13	Comparison of the Split and Non-split Formulations.	106
4.14	Open Single Stripline - E_y TEM Distribution.	107
4.15	Open Coupled Stripline Geometry.	107
4.16	Tangential E-field Distribution (Open - Even Mode).	108
4.17	Tangential E-field Distribution (Open - Odd Mode).	108
5.1	Stability Parameter s for MRTD.	119
5.2	Dispersion Characteristics of S-MRTD for $n_a=8$	119
5.3	Dispersion Characteristics of S-MRTD for $n_a=10$	120
5.4	Dispersion Characteristics of S-MRTD for $n_a=12$	120
5.5	Dispersion Characteristics of S-MRTD for $n_a=14$	121
5.6	Stencil Effect on the Dispersion Characteristics of S-MRTD (Sparse Grid).	122
5.7	Stencil Effect on the Dispersion Characteristics of S-MRTD (Dense Grid).	122
5.8	Wavelets Effect on the Dispersion Characteristics of MRTD for $n_a=8$ (Coarse Grid).	123
5.9	Wavelets Effect on the Dispersion Characteristics of MRTD for $n_a=8$ (Denser Grid).	123
5.10	Wavelets Effect on the Dispersion Characteristics of MRTD for $n_a=10$ (Coarse Grid).	124
5.11	Wavelets Effect on the Dispersion Characteristics of MRTD for $n_a=10$ (Denser Grid).	124
5.12	Wavelets Effect on the Dispersion Characteristics of MRTD for $n_a=12$ (Coarse Grid).	125
5.13	Wavelets Effect on the Dispersion Characteristics of MRTD for $n_a=12$ (Denser Grid).	125
5.14	Effect of the Courant Number on the Dispersion Characteristics of $W_0 - MRTD$ for $n_a = n_b = n_c=10$ (Coarse Grid).	126
5.15	Effect of the Courant Number on the Dispersion Characteristics of $W_0 - MRTD$ for $n_a = n_b = n_c=10$ (Denser Grid).	126
5.16	Effect of the Courant Number on the Dispersion Characteristics of $W_0 - MRTD$ for $n_a = n_b = n_c=12$ (Coarse Grid).	127
5.17	Effect of the Courant Number on the Dispersion Characteristics of $W_0 - MRTD$ for $n_a = n_b = n_c=12$ (Denser Grid).	127
5.18	Effect of the Courant Number on the Dispersion Characteristics of FDTD (Coarse Grid).	128

5.19	Effect of the Courant Number on the Dispersion Characteristics of FDTD (Denser Grid).	128
5.20	Comparison of the Dispersion Performance of S-MRTD and Wo-MRTD with Different Higher Order Yee's Schemes.	129
5.21	Details of Fig.(5.20).	129
5.22	Comparison of the Oscillations of Wo-MRTD Scheme for Different Stencil Size.	130
5.23	Details of Fig.(5.22).	130
6.1	Time- and Space- adaptive grid.	142
6.2	Normal E-field (Time-Domain).	143
6.3	Non-zero Wavelets' Number	143
6.4	Adaptive Grid Demonstration (t=1000 steps).	144
6.5	Parallel-Plate Partially Filled Waveguide.	144
6.6	S-Parameters of the Waveguide.	145
6.7	Non-zero Wavelets' Number.	145
6.8	Adaptive Grid Demonstration (t=1000 steps).	146
6.9	Parallel-Plate Five-Stage Filter.	146
6.10	S-Parameters of the Filter.	147
6.11	Non-zero Wavelets' Number.	147
6.12	Adaptive Grid Demonstration (t=1000 steps).	148
7.1	0-Order Intervalic Function Basis.	159
7.2	Ideal (Lossless) Transmission Line.	159
7.3	Voltage Coefficients.	160
7.4	Comparison MRTD-FDTD.	160
7.5	Fraction of Wavelets above Threshold.	161
7.6	Lossy Transmission Line.	161
7.7	Voltage Coefficients.	162
7.8	Fraction of Wavelets above Threshold.	162
7.9	Rectifier Geometry.	163
7.10	Comparison MRTD-FDTD.	163

CHAPTER 1

Introduction

1.1 Time-Domain Techniques

With the advent of microwave circuits used in high-frequency communications, there is a compelling need to develop efficient and reliable full wave simulation techniques for the modeling process. Until 1990, the modeling of electromagnetic wave interactions was dominated by frequency-domain techniques. Apart from high-frequency asymptotic methods [1, 2], electromagnetic simulations involved setting up and solving frequency-domain integral equations [3, 4] for the phasor electric and magnetic currents induced on the surfaces of the geometries of interest. This Method of Moments (MoM) involves setting up and solving dense, full, complex-valued systems of tens of thousands of linear equations using direct or iterative techniques. Though MoM has been proven to be a very robust technique, it is plagued by significant computational burdens, when it is used at very large geometries. In addition, modeling of a new structure requires the reformulation of the integral equation, a task that may require the very difficult derivation of a geometry-specific Green's function.

On the contrary, techniques based on the partial differential equation (PDE) solutions of the Maxwell's equations yield either sparse matrices (frequency-domain finite-element

methods) or no matrices at all (time-domain finite-difference or finite-volume methods). In addition, specifying a new geometry is reduced to a problem of mesh generation only. Thus, time-domain PDE solvers could provide a framework for a space/time microscope permitting the EM designer to visualize with submicron/subpicosecond resolution the dynamics of electromagnetic wave phenomena propagating at light speed within proposed geometries. Finite-Difference Time-Domain (FDTD) is a direct solution method for Maxwell's time dependent curl equations. It is based upon volumetric sampling of the unknown near-field distribution within and around the structure of interest over a period of time. No potentials are employed. The sampling is set below the Nyquist limit and typically more than 10 samples per wavelength are required. The time-step has to satisfy the stability condition. For simulations of open geometries, absorbing boundary conditions (ABC) are employed at the outer grid truncation planes in order to reduce spurious numerical reflection from the grid termination.

In 1966, Yee [5] introduced the first finite-difference time-domain technique (FDTD) for the solution of Maxwell's curl equations. Interleaved positioning of the electric and magnetic field components provided a second-order accuracy of the algorithm. Taflove and Boldwin [6] presented the numerical stability criterion for Yee's algorithm and Mur [7] published the first numerically stable second-order accurate absorbing boundary condition (ABC) for the Yee's mesh. The perfectly Matched Layer (PML) ABC, introduced in 2D by Berenger in 1994 [8] and extended to 3D by Katz et al. [9], provides numerical reflection comparable to the reflection of anechoic chambers with values -40dB lower than the Mur ABC. The FDTD technique has been applied to various High-Frequency simulations with remarkable success. Taflove [10] and Umashankar [11] used FDTD to model scattering and compute near/far fields and RCS for 2D and 3D structures. Waveguide - Cavity struc-

tures and microstrips were analyzed with FDTD by Choi [12] and Zhang [13] respectively. Maloney [14] introduced the FDTD modeling of antennas and El-Ghazaly [15] applied this technique to picosecond optoelectronic switches. Toland et al. [16] published the first FDTD models of nonlinear devices (tunnel diodes and Gunn diodes) exciting cavities and antennas and Sui et al. [17] modeled lumped electronic circuit elements in 2D.

Despite the numerous applications of FDTD, many practical geometries, especially in microwave and millimeter-wave integrated circuits (MMIC), packaging, interconnects, sub-nanosecond digital electronic circuits (such as multichip modules (MCM)) and antennas used in wireless and microwave communication systems, have been left untreated due to their complexity and the inability of the existing techniques to deal with requirements for large size and high resolution. Multiresolution analysis based on the expansion in scaling and wavelet functions has demonstrated a capability to provide space and time adaptive gridding without the problems encountered by the conventional Finite Difference Time-Domain schemes. As a result, it could be used as a powerful foundation for the development of very efficient electromagnetic simulation techniques.

1.2 Wavelets-Multiresolution Analysis

The term "wavelets" has a very broad meaning, ranging from singular integral operators in harmonic analysis to subband coding algorithms in signal processing, from coherent states in quantum analysis to spline analysis in approximation theory, from multiresolution transform in computer vision to a multilevel approach in the numerical solution of partial differential equations, and so on. Considering the characteristics of time-domain numerical techniques for the solution of Maxwells' equations, wavelets could be considered to be mathematical tools for waveform representations and segmentations, time-frequency anal-

ysis and fast and efficient algorithms for easy implementation in both time and frequency domains.

One of the most important characteristics of expansion to scaling and wavelet functions is the time-frequency localization. The standard approach in ideal lowpass ("scaling") and bandpass ("wavelet") filtering for separating an analog signal into different frequency bands emphasizes the importance of time localization. The Multiresolution Analysis (MRA), introduced by Mallat and Meyer [18, 19], provides a very powerful tool for the construction of wavelets and implementation of the wavelet decomposition/reconstruction algorithms. The sampling theorem can be used to formulate analog signal representations in terms of superpositions of certain uniform shifts of a single function called a scaling function. Stability of this signal representation is achieved by imposing the Riesz condition on the scaling function. Another important condition of an MRA is the nested sequence of subspaces as a result of using scales by integer powers of 2.

In the case of cardinal B-splines [20], an orthonormalization process is used to produce an orthonormal scaling function and, hence, its corresponding orthonormal wavelet by a suitable modification of the two-scale sequence. The orthonormalization process was introduced by Schweinler and Wigner [21] and the resulting wavelets are the Battle-Lemarie wavelets, obtained independently by Battle [22] and Lemarie [23] using different methods. The only orthonormal wavelet that is symmetric or antisymmetric and has compact support (to give finite decomposition and reconstruction series) is the Haar [24] wavelet [25]. Nevertheless, these wavelets exhibit poor time-frequency localization. Throughout this Thesis, Battle-Lemarie and Haar scaling and wavelet functions will be used as an expansion basis for the E- and H- field components in space and time domain respectively, in order to derive an efficient and fast Multiresolution Time-Domain Scheme for the numerical approximation

of Maxwell's equations in a way similar to [26].

1.3 Overview of the Dissertation

Chapter 2 gives a general overview of the FDTD Technique. Excitation topics and ways of improving the algorithm performance are discussed separately. Next, FDTD is used in the analysis of various planar circuits and waveguide probe structures. A new waveguide absorber based on analytic modal green's functions is developed; it is characterized by a better performance in memory requirements than the PML absorber, while maintaining similar accuracy. The scattering parameters of the probe structures are calculated and verified by comparison with FEM and experimental data. The effect of critical geometrical parameters on the probe performance are investigated and the probe behavior is optimized.

Chapter 3 starts with a discussion on the need of development of novel time-domain schemes which would alleviate the serious memory and execution time limitations of the existing techniques. The basic principles of the Multiresolution Analysis as well as the technique of the construction of wavelet functions are presented. Analytical spectral expressions for the linear and cubic cardinal splines are derived as an example. The 2D MRTD algorithm based on Battle-Lemarie expansion basis is developed for a grid similar to that of the FDTD. Hard Boundaries, such as Perfect Electric Conductors, and arbitrary excitations are implemented in an automatic way. The principles of the PML absorber are extended in split and nonsplit formulations providing a very efficient absorber. Notes on the total field value calculation at every spatial point conclude this Chapter.

In Chapter 4, the MRTD scheme is applied to the numerical analysis of 2.5D shielded and open striplines and microstrips. The field patterns and the characteristic impedance are calculated and verified by comparison to reference data. Simulations display memory

savings by a factor of 25 and execution time savings by a factor of 4-5. For structures where the edge effect is prominent, additional wavelet resolutions have to be introduced to maintain a satisfactory performance while using a coarse MRTD grid. The non-split PML algorithm is evaluated for different cells sizes and its performance is comparable to that of the conventional FDTD PML absorber.

Chapter 5 investigates the stability and the dispersion performance of MRTD for different stencil (number of summation terms) sizes and for 0-resolution of wavelets. Analytical expressions for the maximum stable time-step are derived for schemes containing only scaling functions or combination of scaling and wavelet functions. It is proved that larger stencils decrease the numerical phase error making it significantly lower than FDTD for low and medium discretizations. The addition of wavelets further improves the dispersion characteristics for discretizations close to the Nyquist limit, though it decreases the value of the maximum stable time-step.

A mathematically correct way of dielectric modeling is presented and evaluated in the first part of Chapter 6. A dynamically changing space- and time- adaptive meshing MRTD algorithm based on a combination of absolute and relative thresholding of the wavelet values is proposed. Different thresholding implementations are evaluated by the application of the dynamically changing grid to the numerical analysis of various nonhomogeneous 2D waveguide structures. This scheme offers memory savings by a factor of 5-6 per dimension in comparison to FDTD.

The direct application of the principles of the Multiresolution Analysis to the time domain is presented in Chapter 7. A Time Adaptive Time-Domain Technique based on Haar basis is proposed and applied to various types of circuits problems with active and passive lumped and distributed elements. The addition of the wavelets increases the resolution in

time, something that is very important especially in circuits with nonlinear devices such as diodes and transistors. This scheme exhibits significant savings in execution time and memory requirements while maintaining a similar accuracy with conventional circuit simulators. The Thesis closes with ideas for future work described in Chapter 8.

CHAPTER 2

The Finite Difference Time Domain Technique (F.D.T.D.) and its Applications in the Analysis and Design of Microwave Circuits and Waveguide Probes

2.1 Foundations of the Finite Diference Time Domain (F.D.T.D.) Technique

Considering an area with no electric or magnetic current sources, the time-depen dent Maxwell's equations are given in differential form by

Faraday's Law:

$$\frac{\partial B}{\partial t} = \nabla \times E - J_m$$

Ampere's Law:

$$\frac{\partial D}{\partial t} = \nabla \times H - J_e$$

Gauss's Law for the electric field:

$$\nabla \cdot D = 0$$

Gauss's Law for the magnetic field:

$$\nabla \cdot B = 0$$

Here, E is the electric field vector, D is the electric flux density vector, H is the magnetic field vector, B is the magnetic flux density vector, J_e is the electric conduction current density, J_m is the equivalent magnetic conduction current density. In linear, isotropic nondispersive materials, B and D can be related to H and E , respectively, using the constitutive equations:

$$\begin{aligned} B &= \mu H \\ D &= \epsilon E \end{aligned} \tag{2.1}$$

where μ is the magnetic permeability and ϵ is the electric permittivity. To account for the electric and magnetic loss mechanisms, an equivalent electric and magnetic current can be introduced

$$\begin{aligned} J_e &= \sigma E \\ J_m &= \rho' H \end{aligned} \tag{2.2}$$

with σ the electric conductivity and ρ' the equivalent magnetic resistivity. Combining Eqs.(2.1)–(2.2) with Maxwell's equations, we obtain

$$\frac{\partial H}{\partial t} = -\frac{1}{\mu} \nabla \times E - \frac{\rho'}{\mu} H \tag{2.3}$$

$$\frac{\partial E}{\partial t} = \frac{1}{\epsilon} \nabla \times H - \frac{\sigma}{\epsilon} E \tag{2.4}$$

The curl equations (2.3)–(2.4) yield the following system of six coupled scalar equations in the 3-D rectangular coordinate system (x, y, z) :

$$\frac{\partial H_x}{\partial t} = \frac{1}{\mu} \left(\frac{\partial E_y}{\partial z} - \frac{\partial E_z}{\partial y} - \rho' H_x \right)$$

$$\begin{aligned}
\frac{\partial H_y}{\partial t} &= \frac{1}{\mu} \left(\frac{\partial E_z}{\partial x} - \frac{\partial E_x}{\partial z} - \rho' H_y \right) \\
\frac{\partial H_z}{\partial t} &= \frac{1}{\mu} \left(\frac{\partial E_x}{\partial y} - \frac{\partial E_y}{\partial x} - \rho' H_z \right) \\
\frac{\partial E_x}{\partial t} &= \frac{1}{\epsilon} \left(\frac{\partial H_z}{\partial y} - \frac{\partial H_y}{\partial z} - \sigma E_x \right) \\
\frac{\partial E_y}{\partial t} &= \frac{1}{\epsilon} \left(\frac{\partial H_x}{\partial z} - \frac{\partial H_z}{\partial x} - \sigma E_y \right) \\
\frac{\partial E_z}{\partial t} &= \frac{1}{\epsilon} \left(\frac{\partial H_y}{\partial x} - \frac{\partial H_x}{\partial y} - \sigma E_z \right)
\end{aligned} \tag{2.5}$$

Eq.(2.5) forms the basis of the FDTD numerical algorithm for general 3-D objects. The FDTD algorithm need not explicitly enforce the Gauss's Law relations. This occurs because they are theoretically a direct consequence of the curl equations. However, the FDTD space grid must be structured so that the Gauss's Law relations are implicit in the positions of the electric and magnetic field vector components in the grid and the numerical space derivative operations upon these vector components that model the action of the curl operator.

The above system of equations can be reduced to 2-D assuming no variation in the z -direction. That means that all partial derivatives with respect to z equal zero and that the analyzed structure extends to infinity in the z -direction with no change in the shape or position of its transverse cross section. Eq.(2.5) will give in rectangular coordinates:

$$\frac{\partial H_x}{\partial t} = \frac{1}{\mu} \left(-\frac{\partial E_z}{\partial y} - \rho' H_x \right) \tag{2.6}$$

$$\frac{\partial H_y}{\partial t} = \frac{1}{\mu} \left(\frac{\partial E_z}{\partial x} - \rho' H_y \right) \tag{2.7}$$

$$\frac{\partial H_z}{\partial t} = \frac{1}{\mu} \left(\frac{\partial E_x}{\partial y} - \frac{\partial E_y}{\partial x} - \rho' H_z \right) \tag{2.8}$$

$$\frac{\partial E_x}{\partial t} = \frac{1}{\epsilon} \left(\frac{\partial H_z}{\partial y} - \sigma E_x \right) \tag{2.9}$$

$$\frac{\partial E_y}{\partial t} = \frac{1}{\epsilon} \left(-\frac{\partial H_z}{\partial x} - \sigma E_y \right) \tag{2.10}$$

$$\frac{\partial E_z}{\partial t} = \frac{1}{\epsilon} \left(\frac{\partial H_y}{\partial x} - \frac{\partial H_x}{\partial y} - \sigma E_z \right) \tag{2.11}$$

Eqs.(2.6),(2.7),(2.11) constitute the transverse magnetic (TM^z) mode; the rest the trans-

verse electric (TE^z) mode 2-D equations. The TE^z and TM^z modes are decoupled since they contain no common field vector components. These modes are completely independent for structures composed of isotropic materials or anisotropic materials having no off-diagonal components in the constitutive tensors. That means that they can exist simultaneously with no mutual interactions.

Equations for 1-D cases can be derived in a similar way assuming no variation in the x- or y-direction in excess to no variation in the z-direction.

Yee [5] proposed a set of finite-difference equations for the time-dependent Maxwell's curl equations, solving for both electric and magnetic fields in time and space instead of solving for the electric field alone (or the magnetic field alone) with a wave equation. In this way, the solution is more robust and more accurate for a wider class of structures. In addition, both electric and magnetic material properties can be modeled in a straightforward manner. In Yee's discretization cell (Fig.2.1), E- and H- fields are interlaced by half space and time gridding steps. The spatial displacement is very useful in specifying field boundary conditions and singularities and creates finite-difference expressions for the space derivatives which are central in nature and second-order accurate. It has been proven that the Yee mesh is divergence-free with respect to its electric and magnetic fields, and thereby properly enforces the absence of free electric and magnetic charge in the source-free space being modeled. The time displacement (leapfrog) is fully explicit, completely avoiding the problems involved with simultaneous equations and matrix inversion. The resulting time-stepping algorithm is non-dissipative; numerical wave modes propagating in the mesh do not spuriously decay due to a nonphysical artifact of the time-stepping algorithm.

Denoting any function u of space and time evaluated at a discrete point in the grid and

at a discrete point in time as

$$u(i\Delta x, j\Delta y, k\Delta z, l\Delta t) = {}_l u_{i,j,k}$$

where Δt is the time step and $\Delta x, \Delta y, \Delta z$ the cell size to the x-, y- and z-direction, the first partial space derivative of u in the x-direction and the first time derivative of u are approximated with the following central differences respectively

$$\begin{aligned} \frac{\partial u}{\partial x}(i\Delta x, j\Delta y, k\Delta z, l\Delta t) &= \frac{{}_l u_{i+1/2,j,k} - {}_l u_{i-1/2,j,k}}{\Delta x} + O[(\Delta x)^2] \\ \frac{\partial u}{\partial t}(i\Delta x, j\Delta y, k\Delta z, l\Delta t) &= \frac{{}_{l+1/2} u_{i,j,k} - {}_{l-1/2} u_{i,j,k}}{\Delta t} + O[(\Delta t)^2] \end{aligned} \quad (2.12)$$

Applying the above notation, the following FDTD equations are derived for 3-D geometries

$$\begin{aligned} {}_{l_{0.5}} H_{i,j-0.5,k-0.5}^x &= \left(\frac{1 - \frac{\rho'_{i,j,k} \Delta t}{2\mu_{i,j,k}}}{1 + \frac{\rho'_{i,j,k} \Delta t}{2\mu_{i,j,k}}} \right) {}_{l_{-0.5}} H_{i,j-0.5,k-0.5}^x \\ &+ \left(\frac{\frac{\Delta t}{\mu_{i,j,k}}}{1 + \frac{\rho'_{i,j,k} \Delta t}{2\mu_{i,j,k}}} \right) \left(\frac{{}_l E_{i,j-0.5,k}^y - {}_l E_{i,j-0.5,k-1}^y}{\Delta z} - \frac{{}_l E_{i,j,k-0.5}^z - {}_l E_{i,j-1,k-0.5}^z}{\Delta y} \right) \end{aligned} \quad (2.13)$$

$$\begin{aligned} {}_{l_{0.5}} H_{i-0.5,j,k-0.5}^y &= \left(\frac{1 - \frac{\rho'_{i,j,k} \Delta t}{2\mu_{i,j,k}}}{1 + \frac{\rho'_{i,j,k} \Delta t}{2\mu_{i,j,k}}} \right) {}_{l_{-0.5}} H_{i-0.5,j,k-0.5}^y \\ &+ \left(\frac{\frac{\Delta t}{\mu_{i,j,k}}}{1 + \frac{\rho'_{i,j,k} \Delta t}{2\mu_{i,j,k}}} \right) \left(\frac{{}_l E_{i,j,k-0.5}^z - {}_l E_{i-1,j,k-0.5}^z}{\Delta x} - \frac{{}_l E_{i-0.5,j,k}^x - {}_l E_{i-0.5,j,k-1}^x}{\Delta z} \right) \end{aligned} \quad (2.14)$$

$$\begin{aligned} {}_{l_{0.5}} H_{i-0.5,j-0.5,k}^z &= \left(\frac{1 - \frac{\rho'_{i,j,k} \Delta t}{2\mu_{i,j,k}}}{1 + \frac{\rho'_{i,j,k} \Delta t}{2\mu_{i,j,k}}} \right) {}_{l_{-0.5}} H_{i-0.5,j-0.5,k}^z \\ &+ \left(\frac{\frac{\Delta t}{\mu_{i,j,k}}}{1 + \frac{\rho'_{i,j,k} \Delta t}{2\mu_{i,j,k}}} \right) \left(\frac{{}_l E_{i-0.5,j,k}^x - {}_l E_{i-0.5,j-1,k}^x}{\Delta y} - \frac{{}_l E_{i,j-0.5,k}^y - {}_l E_{i-1,j-0.5,k}^y}{\Delta x} \right) \end{aligned} \quad (2.15)$$

$$\begin{aligned} {}_{l_1} E_{i-0.5,j,k}^x &= \left(\frac{1 - \frac{\sigma_{i,j,k} \Delta t}{2\epsilon_{i,j,k}}}{1 + \frac{\sigma_{i,j,k} \Delta t}{2\epsilon_{i,j,k}}} \right) {}_l E_{i-0.5,j,k}^x + \left(\frac{\frac{\Delta t}{\epsilon_{i,j,k}}}{1 + \frac{\sigma_{i,j,k} \Delta t}{2\epsilon_{i,j,k}}} \right) \\ &\cdot \left(\frac{{}_{l_{0.5}} H_{i-0.5,j_{0.5},k}^z - {}_{l_{0.5}} H_{i-0.5,j-0.5,k}^z}{\Delta y} - \frac{{}_l H_{i-0.5,j,k_{0.5}}^y - {}_l H_{i-0.5,j,k-0.5}^y}{\Delta z} \right) \end{aligned}$$

(2.16)

$$\begin{aligned}
l_1 E_{i,j-0.5,k}^y &= \left(\frac{1 - \frac{\sigma_{i,j,k} \Delta t}{2\epsilon_{i,j,k}}}{1 + \frac{\sigma_{i,j,k} \Delta t}{2\epsilon_{i,j,k}}} \right) l E_{i,j-0.5,k}^y + \left(\frac{\frac{\Delta t}{\epsilon_{i,j,k}}}{1 + \frac{\sigma_{i,j,k} \Delta t}{2\epsilon_{i,j,k}}} \right) \\
&\cdot \left(\frac{l_{0.5} H_{i,j_{0.5},k_{0.5}}^x - l_{0.5} H_{i,j_{0.5},k-0.5}^x}{\Delta z} - \frac{l_{0.5} H_{i_{0.5},j_{0.5},k}^z - l_{0.5} H_{i-0.5,j_{0.5},k}^z}{\Delta x} \right)
\end{aligned} \tag{2.17}$$

$$\begin{aligned}
l_1 E_{i,j,k-0.5}^z &= \left(\frac{1 - \frac{\sigma_{i,j,k} \Delta t}{2\epsilon_{i,j,k}}}{1 + \frac{\sigma_{i,j,k} \Delta t}{2\epsilon_{i,j,k}}} \right) l E_{i,j,k-0.5}^z + \left(\frac{\frac{\Delta t}{\epsilon_{i,j,k}}}{1 + \frac{\sigma_{i,j,k} \Delta t}{2\epsilon_{i,j,k}}} \right) \\
&\cdot \left(\frac{l_{0.5} H_{i_{0.5},j,k-0.5}^y - l_{0.5} H_{i-0.5,j,k-0.5}^y}{\Delta x} - \frac{l_{0.5} H_{i,j_{0.5},k-0.5}^x - l_{0.5} H_{i,j-0.5,k-0.5}^x}{\Delta y} \right)
\end{aligned} \tag{2.18}$$

where $\sigma_{i,j,k}$ and $\rho'_{i,j,k}$ are the electric and magnetic loss coefficients for the (i, j, k) -cell. The notation

$$l_a u_{i,b,j,c,k_d} = l_{-a} u_{i-b,j-c,k-d}$$

is used for compactness. It can be observed that a new value of a field vector component at any space lattice point depends only on its previous value and the previous values of the components of the other field vectors at adjacent points. Therefore, at any given time step, the value of a field vector component at p different lattice points can be calculated simultaneously if p parallel processors are employed, something that demonstrates the fact that the FDTD algorithm is highly parallelizable.

The exponential decay of propagating waves in certain highly lossy media is so rapid that the standard Yee time-stepping algorithm fails to describe. Holland [27] has proposed an exponential time-stepping. For example, for large values of σ , the field component E_x is given by

$$\begin{aligned}
l_1 E_{i-0.5,j,k}^x &= e^{-\sigma_{i,j,k} \Delta t / \epsilon_{i,j,k}} l E_{i-0.5,j,k}^x - \frac{1}{\sigma_{i,j,k}} (e^{-\sigma_{i,j,k} \Delta t / \epsilon_{i,j,k}} - 1) \\
&\cdot \left(\frac{l_{0.5} H_{i-0.5,j_{0.5},k}^z - l_{0.5} H_{i-0.5,j-0.5,k}^z}{\Delta y} - \frac{l_{0.5} H_{i-0.5,j,k_{0.5}}^y - l_{0.5} H_{i-0.5,j,k-0.5}^y}{\Delta z} \right)
\end{aligned} \tag{2.19}$$

instead of Eq.(2.16).

Stability analysis [57] has shown that the upper bound for the FDTD time step for a homogeneous region of space (ϵ_r, μ_r) is given by

$$\Delta t \leq \frac{\sqrt{\epsilon_r \mu_r}}{c \sqrt{\frac{1}{(\Delta x)^2} + \frac{1}{(\Delta y)^2} + \frac{1}{(\Delta z)^2}}}$$

for 3-D simulations and

$$\Delta t \leq \frac{\sqrt{\epsilon_r \mu_r}}{c \sqrt{\frac{1}{(\Delta x)^2} + \frac{1}{(\Delta y)^2}}}$$

for 2-D simulations. Lower values of upper bounds are used in case a highly lossy material or a variable grid is employed. Discretization with at least 10-20 cells/wavelength almost guarantee that the FDTD algorithm will have satisfactory dispersion characteristics (phase error smaller than $5^\circ/\lambda$ for time step close to the upper bound value).

2.1.1 Overview of Numerical Absorbing Boundary Conditions

It is very common for the geometries of interest to be defined in "open" regions where the spatial domain of the computed EM fields is unbounded in one or more coordinate directions. Since no computer can store an unlimited amount of data, the field computation domain must be limited in size. The computation domain must be large enough to enclose the structure of interest, and a suitable absorbing boundary condition (ABC) on the outer perimeter of the domain must be used to simulate its extension to infinity. ABC's cannot be directly obtained from the numerical algorithms for Maxwells' curl equations defined by the Yee's finite-difference systems. This is due to the fact that these systems employ a central spatial difference scheme that requires knowledge of the field one-half cell to each side of an observation point. Central differences cannot be implemented at the outermost lattice planes, since by definition there exists no information concerning the fields at points one-half space cell outside of these planes. Backward finite differences are generally of lower accuracy

for a given space discretization, so they cannot be used as a reliable solution. Several approximate ABC's have been proposed [28, 29, 30, 31]. In our FDTD simulations, 1st and 2nd order Mur ABC [7], coupled with Mei-Fang Superabsorption [32] for complicated structures, have been used to terminate open domains due to their simplicity and versatility. Reflection coefficients close to $-60dB$ have been achieved for a wide range of incidence angles and frequencies. For waveguide structures a new ABC based on Green's functions has been developed. Reflection coefficients obtained by the recently developed PML [8] have been used as a reference for the validation of the novel ABC.

2.1.2 Excitation Topics

The first source to be modeled in FDTD was a plane wave incoming from infinity [5]. The plane wave source is very useful in modeling radar scattering problems, since in most cases of this type the target of interest is in the near field of the radiating antenna, and the incident illumination can be considered to be a plane wave.

The hard source [33] is another common FDTD source implementation. It is set up simply by assigning a desired time function to specific electric or magnetic field components in the FDTD space lattice. In this way, it radiates a numerical wave having a time waveform corresponding to the source function. This numerical wave propagates symmetrically in both directions from the source point. However, this way of excitation has some drawbacks. As time-stepping is continued to obtain either the sinusoidal steady state or the late-time impulse response, the reflected - from the discontinuities - numerical wave eventually returns to the source grid location. Since the total electric field is specified at the excitation point without regard to any possible reflected waves, the hard source causes a spurious, nonphysical retroreflection of these waves toward the structure of interest, failing

to simulate the propagation of the reflected wave energy. A simple way to avoid this problem is to remove the source from the algorithm after the pulse has decayed essentially to zero and apply instead the regular Yee update. However, this approach cannot be used for continuous source waveforms where the source remains active even after reflections propagate back to it. It has been observed that much less error occurs for hard sources in 2-D and 3-D than in 1-D because the hard sources in 2-D and 3-D intercept and retroreflect much smaller fractions of the total energy in the FDTD grid. Collinear arrays of hard-source field vector components in 3D can be useful for exciting waveguides and strip lines.

The total field excitation eliminates the retroreflection problems of the hard source. A proper field component is simply added to the field values given by the regular FDTD equations. Let's consider for example Eq.(2.16) for $\sigma_{i,j,k} = 0$ and no field variation to the z-direction

$${}_{l_1}E_{i-0.5,j,k}^x = {}_lE_{i-0.5,j,k}^x + \frac{\Delta t}{\epsilon_{i,j,k}} \left(\frac{{}_{l_{0.5}}H_{i-0.5,j_{0.5},k}^z - {}_{l_{0.5}}H_{i-0.5,j-0.5,k}^z}{\Delta y} \right)$$

In the total field implementation of the source, one time dependent term is added to the field component of interest. Calling for simplicity this term Δs , E_x component at the excitation cell is updated by

$${}_{l_1}E_{i-0.5,j,k}^x = {}_lE_{i-0.5,j,k}^x + \frac{\Delta t}{\epsilon_{i,j,k}} \left(\frac{{}_{l_{0.5}}H_{i-0.5,j_{0.5},k}^z - {}_{l_{0.5}}H_{i-0.5,j-0.5,k}^z}{\Delta y} \right) + \Delta s$$

If the circuit and the position where the source is applied allow a conductance current to flow, this term actually can be seen as an impressed conductance current density given by

$$\Delta s = \frac{\Delta t}{\epsilon} J_{cz}^{n+1/2}$$

On the other side, if a conductance current cannot flow, and thus only a displacement current can exist (e.g. the excitation of an empty cavity by applying a point source in

the middle), it actually works as if an additional term added to the E_x component. The modified discretized Maxwell equation can be written as:

$${}_{l_1}E_{i-0.5,j,k}^x - {}_lE_{i-0.5,j,k}^x - \Delta s = \frac{\Delta t}{\epsilon_{i,j,k}} \left(\frac{{}_{l_{0.5}}H_{i-0.5,j_{0.5},k}^z - {}_{l_{0.5}}H_{i-0.5,j-0.5,k}^z}{\Delta y} \right)$$

That corresponds to the following analytical expression

$$\epsilon \frac{\partial E_x}{\partial t} - \frac{ds(t)}{dt} = \frac{\partial H_z}{\partial y}$$

Thus, the term added to the field component is the derivative of the waveform we want to obtain. As a conclusion, if the circuit allows a conductive current density to be supported, the desired waveform must be simply added to the field component at the location of the source; if only a displacement current can be supported by the structure, the derivative of the desired waveform must be added instead. In the FDTD simulations reported in this Chapter, a gaussian pulse (nonzero DC content) was used as the excitation of the microstrip and stripline structures. The Gabor function

$$s(t) = e^{-((t-t_o)/(pw))^2} \sin(wt) \quad (2.20)$$

where $pw = 2 \cdot \frac{\sqrt{6}}{\pi(f_{max} - f_{min})}$, $t_o = 2pw$, $w = \pi(f_{min} + f_{max})$, was used as the excitation of the waveguide structures, since it has zero DC content. By modifying the parameters pw and w , the frequency spectrum of the Gabor function can be practically restricted to the interval $[f_{min}, f_{max}]$. As a result, the envelope of the Gabor function represents a gaussian function in both time and frequency domain.

2.1.3 Linear Predictors

It is very common, especially for high-speed circuit structures, to use a cell size Δ that is dictated by the very fine dimensions of the circuit and is almost always much finer than

needed to resolve the smallest spectral wavelength propagating in the circuit. As a result, with the time step Δt bound to Δ by numerical stability considerations, FDTD simulations have to run for tens of thousands of time steps in order to fully evolve the impulse responses needed for calculating impedances, S-parameters or resonant frequencies. One popular way to avoid virtually prohibitive execution time has been to apply contemporary analysis techniques from the discipline of digital signal processing and spectrum estimation. The strategy is to extrapolate the electromagnetic field time waveform by 10:1 or more beyond the actual FDTD time window, allowing a very good estimate of the complete system response with 90% or greater reduction in computation time.

The class of linear predictors or autoregressive models (AR) is the most popular time series modeling approach due to the fact that an accurate estimate of the AR parameters can be derived by solving a set of linear equations. Though Prony's method [34] uses a sum of deterministic exponential functions to fit the data, the AR approach constructs a random model to fit a statistical data base to the second-order. Let's consider the FDTD impulse response $p + 1$ equally spaced time samples after at time-step n

$$f|_{i,j,k}^n, f|_{i,j,k}^{n+1}, \dots, f|_{i,j,k}^{n+p}$$

This time series is said to represent the realization of an AR process of order p if it satisfies the following relationship

$$f|_{i,j,k}^n = -a_1 f|_{i,j,k}^{n+1} - \dots - a_p f|_{i,j,k}^{n+p} + q(n)$$

where the constants a_1, \dots, a_p are the AR parameters to be determined from the previous values of f and $q(n)$ is a white noise process whose variance has to be calculated before carrying out the extrapolation of f . Once the AR coefficients have been determined, the above equation permits the prediction of a new value of the time series from p known

previous values. Numerous different approaches for the evaluation of a_i have been proposed. Three of them of the most widely used: the covariance method, the forward-backward method and the nonlinear predictor. The covariance method involves setting up and solving a $p \times p$ linear system of equations

$$\begin{pmatrix} c_{ff}(1,1) & c_{ff}(1,2) & \dots & c_{ff}(1,p) \\ c_{ff}(2,1) & c_{ff}(2,2) & \dots & c_{ff}(2,p) \\ \vdots & \vdots & \ddots & \vdots \\ c_{ff}(p,1) & c_{ff}(p,2) & \dots & c_{ff}(p,p) \end{pmatrix} \begin{pmatrix} a_1 \\ a_2 \\ \vdots \\ a_p \end{pmatrix} = - \begin{pmatrix} c_{ff}(1,0) \\ c_{ff}(2,0) \\ \vdots \\ c_{ff}(p,0) \end{pmatrix}$$

where c_{ff} are the covariances defined by

$$c_{ff}(a,b) = \frac{1}{N-p} \sum_{n=p}^{N-1} (f_{i,j,k}^{M+n-a} + f_{i,j,k}^{M+n-b})$$

The above matrix can be solved with Cholesky decomposition. The order p of the model is very critical. The use of low order AR model causes the extrapolated waveform to attenuate quickly in a nonphysical manner. However, a high-order model can cause divergence problems in some cases because of statistical instabilities introduced by the large order. A common way to estimate p is the use of the Akaike Information criterion [34].

Forward and backward prediction methods avoid these problems by working directly with the time-domain data, rather than calculating the covariance functions of the data. It solves the following $(p+1) \times (p+1)$ linear system

$$\begin{pmatrix} r(0,0) & \dots & r(0,p) \\ r(1,0) & \dots & r(1,p) \\ \vdots & \ddots & \vdots \\ r(p,0) & \dots & r(p,p) \end{pmatrix} \begin{pmatrix} 1 \\ a_1 \\ \vdots \\ a_p \end{pmatrix} = - \begin{pmatrix} e_p \\ 0 \\ \vdots \\ 0 \end{pmatrix}$$

where for $0 \leq a, b \leq p$,

$$r(a,b) = \sum_{l=1}^{N-p} (f_{i,j,k}^{M+p+l-b} f_{i,j,k}^{M+p+l-a} + f_{i,j,k}^{M+l+b} f_{i,j,k}^{M+l+a})$$

$$e_p = \sum_{l=0}^p a_l r(0, l)$$

Marple [35] reported favorable results for the forward-backward method versus existing popular AR approaches such as the Burg and the Yule-Walker algorithms. It provided more accurate spectra and its order was much lower (close to 10% – 15% of the order of the other approaches). In addition, the forward-backward method is sufficiently robust and fast, though it's slightly less stable than the covariance methods.

2.2 Applications of F.D.T.D. to Planar Circuits

2.2.1 Open Circuit Design

The F.D.T.D. is initially applied in the design of a patch to be used as an open for the frequency range from 0-6 GHz (Fig.2.2). The dielectric constant of the substrate is $\epsilon_r = 5.46$ and the dielectric thickness is 0.5 mm. The feeding microstrip line (104.86875 mm) is excited by applying horizontally the Gaussian pulse $e^{-\left(\frac{t\Delta t - t_0}{pw}\right)^2}$ with $pw = 8.333 \cdot 10^{-11}$, $dt = 2.9 \cdot 10^{-13} \text{sec}$, $t_0 = 3pw$. The excitation is on for $t = 0, \dots, t_{ab}$ time-steps with $t_{ab} = 6pw/\Delta t$. During this period, a PEC (perfect electric conductor) is placed behind the source at the vertical to the propagation plane. After t becomes larger than t_{ab} , this PEC is replaced with a 1st order Mur's absorber and the results converge after 30,000 time steps. After numerical experimentation, it is observed that the smallest vertical distance the top-plane 1st order Mur absorber can work efficiently equals to 30 times the substrate thickness. The front and the side absorbers are placed at a distance 49.35 mm and 7.7425 mm away from the patch respectively. In addition, the resonant frequency of the patch antenna should be such that it would not cause any problems for the operating frequency range. As a result, the almost square shape of the patch is maintained, but the dimensions

have to be appropriately modified. After using a mesh with cell size $dx = 0.1mm$, $dy = 0.20375mm$, $dz = 1.23375mm$, the optimum performance patch dimensions are found to be: 7.4025 mm (length) x 7.335 mm (width). (Fig. 2.3) demonstrates that the performance of the open is almost perfect since the reflection coefficient is larger than 0.97 for the whole frequency range.

2.2.2 Viahole Analysis

The viahole transition between two bended microstrips (Fig.2.4) is another geometry analyzed with F.D.T.D. The two microstrip lines are sandwiched on a dielectric substrate with $\epsilon_r = 7$ and the ground plane is placed in the middle of their distance. The top stripline is excited by applying horizontally a Gaussian pulse 0-20GHz. The discretization cell has dimensions $10\mu m \times 50\mu m \times 50\mu m$ and the time step is 31ps. A forward-backward predictor based on the first 4,300 steps with order $p = 27$ is employed to shorten the computation time of the 18,000 steps. The S-parameters are calculated (Fig.2.5). (Fig.2.6-2.7) showing the total E-field distribution along the top and bottom microstrip planes as well as along the ground plane at frequency 10 GHz, demonstrate the capability of the F.D.T.D. technique for an accurate spatial mapping of EM energy. Knowledge of the electric field intensity over a microwave circuit is extremely useful in directly identifying microwave circuit problems such as the existence of substrate modes, circuit radiation, device to device coupling. With tighter control over line lengths and losses that may be derived from electric field intensity (and phase), it may be possible to reduce the number of iterations during the design of MMIC's. Also, with a map of the electric field intensity above the substrate it would be possible to define low electric field regions around a device that could be used for placement of more circuitry, thus saving valuable chip real-estate.

2.2.3 Filter Design

(Fig.2.8) displays the geometry of a three stage coupled line filter fabricated on Duroid ($\epsilon_r=10.8$, $h=635 \mu\text{m}$). All dimensions are in μm . The bandpass filter has a measured insertion loss of 2.0 dB in the passband from 8.0GHz to 10.5GHz and provides better than -25dB rejection at 12GHz. (Fig.2.9) shows that good agreement is achieved between measurements and FDTD calculations. The FDTD cell was chosen to be $52.9 \mu\text{m}$ for the vertical direction, $100 \mu\text{m}$ for the propagation direction and $25 \mu\text{m}$ for the direction normal to propagation. The time step is chosen to be 73 fsec to satisfy the stability criterion. These choices result in a grid with $140 \times 234 \times 448$ cells. The 1st-order Mur's ABC is applied to the boundaries of the computational domain and superabsorber is enhanced at the input and output planes.

For wideband S-parameter extraction, a Gaussian pulse of 100 psec is used as the vertical microstrip excitation. The source is applied 5 cells inside the feedline in the propagation direction. Two simulations of pulse propagation along the microstrip line are made: one simulation for the filter and one for a 50Ω microstrip through-line. The filter simulation gives the sum of the incident and the reflected waveforms and the through-line simulation gives only the incident waveform. By subtracting the incident from the total waveform, the reflected waveform at the input port is derived, which permits the calculation of the reflection coefficient S_{11} . The transmission coefficient S_{21} is given by the ratio of the Fourier transforms of the transmitted and the incident waveforms. The field probes are located at distances far enough from the filter discontinuities to eliminate evanescent waves.

2.2.4 Finite-Ground CPW Line Analysis

Coplanar waveguide with finite width ground planes (F.G.C.) (Fig.2.10) is characterized through measurements and F.D.T.D. to determine the optimum ground plane width. It is found that the characteristics (attenuation, effective permittivity) of the Finite Ground Coplanar Line are not dependent on the ground plane width if it is greater than twice the center conductor width, but less than $\lambda_d/8$ to keep the radiation losses and dispersion small. Also, the field distribution plots show that the power that propagates along the F.G.C. is concentrated on the surface of the substrate and the magnitude of this power is inversely dependent on the ground plane width. For small finite ground plane, there exists a significant amount of power on the surface of the substrate outside of the ground planes. This is demonstrated by the distribution of the normal-to-strip magnetic field H_y for lines with ground plane widths of $B=25$ and $B=100 \mu\text{m}$ (Fig.2.11) and $S = W = 25\mu\text{m}$ on Si wafers of $\epsilon_r=11.9$ and of thickness of $400 \mu\text{m}$. The field is approximately twice as strong for the narrower ground plane, and decays away from the outer edge of the ground plane. As a conclusion, coplanar waveguide with a finite ground plane width as small as twice the center strip width may be used without adversely affecting the attenuation and permittivity of the lines.

The 2.5-D FDTD algorithm is used in the simulations. The dimensions of the Yee's cell are chosen to be $2.5\mu\text{m}$ for the direction parallel to the coplanar line and $25\mu\text{m}$ for the normal direction. The time step is 7.45 ps and the 1st-order Mur's ABC is applied to the top, left and right boundaries of the computational domain. The top absorber is placed at a distance equal to 15 times the dielectric thickness and the side absorbers at a distance equal to 7 times the gap of the coplanar line. A delta function with even (odd) symmetry is used for the excitation of the horizontal electric field across the gaps. The propagation

constant used in the simulations has the value 100.

2.3 Application of FDTD to Waveguide Structures

2.3.1 FDTD and Waveguide Probe Structures

Significant attention is being devoted now-a-days to the analysis and design of waveguide-probes [36] – [53]. Many different configurations of waveguide probes are used either to sense the modal propagation inside the waveguides or to mount active elements inside cavities. The common design objective is to maximize the coupling between the probe and the waveguide over the widest possible frequency range. The characterization of waveguide-probes demands an accurate calculation of the scattering parameters over a wide band of frequencies. In this Section, FDTD is used in the RF characterization of diode mounting and waveguide probe structures. The waveguide probe geometry analyzed in this section is shown in (Fig.2.12). The probe is fed by a shielded coplanar line and has the shape of a patch. It is inserted into the waveguide through a slot and it is supported by a dielectric substrate which is not connected to any waveguide wall. The dimensions of the probe as well as the thickness and the dielectric constant of the substrate are of critical importance to achieve broadband coupling and low reflection loss.

Usually more than one mode are excited inside the rectangular waveguide, making the numerical simulation tedious when using the conventional absorbing boundary conditions (ABC's) [7], [32]. These ABC's specify the tangential electric field components at the boundary of the mesh in such a way that waves are not reflected. For TEM structures the waves will be normally incident to the boundaries of the mesh, thus requiring a simple approximate absorbing boundary condition, Mur's first order absorbing boundary condition

[7]. The assumption of normal incidence is not valid for the fringing fields propagating tangential to the walls. For this reason, for non-TEM structures the superabsorption boundary condition [32] is used in conjunction with Mur's absorber for better accuracy. This combination results in an improvement with respect to the reflection coefficient. However, despite the use of superabsorber, when the frequency range of interest becomes large, significant reflections occur, even if there is only one propagating mode. To overcome this difficulty, numerous approaches have been proposed. The technique of diakoptics [40], initially developed for TLM [41] and later for FDTD [42], used in conjunction with the modal Green's function has been successfully applied to TLM [43], [44], [45]. In the analogous FDTD approach [46], the fields are decomposed into incident and reflected wave amplitudes ("TLM" approach) and the characteristic impedance is used for the calculation of the reflected wave amplitudes. A similar absorber based on a circuit (voltage-current) approach has been proposed by F. Moglie et al. [47]. Due to the field decomposition, both of these approaches are characterized by higher memory and execution time requirements than the conventional FDTD absorbers.

In contrast to these approaches, the Diakoptics technique is derived directly from Maxwell's equations following an approach similar to [48] and only total field values are used. The absorber proposed is based on the analytic Green's functions of the waveguide modes. These Green's functions are used to calculate the tangential electric (for TE modes) and magnetic (for TM modes) field components located at the boundary of the mesh. The tangential fields one cell away from the boundary are decomposed into modes and for each mode the tangential field at the boundary is calculated by taking the convolution of the mode amplitude and the Green's function for this mode with respect to time. For simplicity, we consider only TE propagating modes, while the approach for the TM propagating modes

is dual and straightforward. A similar approach based on numerical Green's functions has been presented in [49]. This approach requires the numerical evaluation of each mode's Green's function that is obtained by running an FDTD simulation for each mode and/or the application of the FD^2 principles. On the contrary, the proposed absorber evaluates analytically the Green's functions by applying the Inverse Fourier transform to the well-known expressions in frequency domain. Thus, similar accuracy is obtained without a significant computational overhead.

2.3.2 Novel Absorber Description

For the sake of simplicity in the presentation, we consider only $TE_{m,n}^z$ modes, propagating in the z-direction, and assume that the waveguide cross-section is located on the xy-plane. For the tangential magnetic field adjacent to the boundary of the mesh at $k = n_z - 0.5$, eqs.(2.13),(2.14) for non-lossy material are simplified to

$${}^{l+1/2}H_{i,j+1/2,n_z-0.5}^x - {}^{l-1/2}H_{i,j+1/2,n_z-0.5}^x = \frac{\Delta t}{\mu_o} \left(\frac{{}^l E_{i,j+1/2,n_z}^y - {}^l E_{i,j+1/2,n_z-1}^y}{\Delta z} \right) \quad (2.21)$$

$${}^{l+1/2}H_{i+1/2,j,n_z-0.5}^y - {}^{l-1/2}H_{i+1/2,j,n_z-0.5}^y = \frac{\Delta t}{\mu_o} \left(\frac{{}^l E_{i+1/2,j,n_z-1}^x - {}^l E_{i+1/2,j,n_z}^x}{\Delta z} \right) \quad (2.22)$$

The absorber is used to calculate the tangential electric field components at the boundary of the mesh ($k = n_z$) from the tangential electric field components one cell away from the boundary plane ($k = n_z - 1$). The tangential magnetic field components $H_{i,j,n_z-0.5}^x$ and $H_{i,j,n_z-0.5}^y$ are updated using eqs.(2.21)–(2.22) and depend both on the values of the electric field components calculated by Yee's FDTD scheme and on the values of the electric field components calculated by the absorber. Using eq.(2.15), the normal magnetic field components at $k = n_z$, $H_{i+1/2,j+1/2,n_z}^z$, may be calculated from $E_{i+1/2,j,n_z}^x$ and $E_{i,j+1/2,n_z}^y$. Thus, for the $TE_{m,n}^z$ modes, the normal magnetic field components are also determined so

that the reflection from the boundary is minimized. A similar argument can be used for the position of the absorber for the $TM_{m,n}^z$ modes.

In order to derive the absorber based on the analytic Green's functions, we start with the wave equation in cartesian coordinates

$$\nabla^2 F - \frac{1}{c^2} \frac{\partial^2 F}{\partial t^2} = \left(\frac{\partial^2}{\partial x^2} + \frac{\partial^2}{\partial y^2} + \frac{\partial^2}{\partial z^2} - \frac{1}{c^2} \frac{\partial^2}{\partial t^2} \right) F = 0 \quad (2.23)$$

where F indicates the tangential electric field components $E^x(x, y, z, t)$, $E^y(x, y, z, t)$ and c represents the velocity of light. The tangential electric field components in the waveguide can be written as

$$E^x(x, y, z, t) = \sum_{m=0}^{\infty} \sum_{n=1}^{\infty} E_{m,n}^x(z, t) \cos(\beta_{x,m}x) \sin(\beta_{y,n}y) \quad (2.24)$$

$$E^y(x, y, z, t) = \sum_{m=1}^{\infty} \sum_{n=0}^{\infty} E_{m,n}^y(z, t) \sin(\beta_{x,m}x) \cos(\beta_{y,n}y) \quad (2.25)$$

where

$$\beta_{x,m} = \frac{m\pi}{a}, \quad \beta_{y,n} = \frac{n\pi}{b} \quad , \quad (2.26)$$

$m, n \in \mathbb{N}$, $a \times b$ are the waveguide cross section area and $E_{m,n}^x(z, t)$ and $E_{m,n}^y(z, t)$ are the modal coefficients given by

$$E_{m,n}^x(z, t) = \frac{2(2 - \delta_{m,0})}{ab} \int_0^a \int_0^b E^x(x, y, z, t) \cos\left(\frac{m\pi}{a}x\right) \sin\left(\frac{n\pi}{b}y\right) dx dy \quad (2.27)$$

$$E_{m,n}^y(z, t) = \frac{2(2 - \delta_{n,0})}{ab} \int_0^a \int_0^b E^y(x, y, z, t) \sin\left(\frac{m\pi}{a}x\right) \cos\left(\frac{n\pi}{b}y\right) dx dy \quad (2.28)$$

In eqs. (2.27) and (2.28), $\delta_{m,0}$ is the Kroenecker delta given by

$$\delta_{m,0} = \begin{cases} 1 & \text{for } m = 0 \\ 0 & \text{for } m \neq 0 \end{cases} .$$

In view of the above, eq.(2.23) yields

$$\frac{\partial^2 F_{m,n}(z,t)}{\partial z^2} - \left(\beta_{x,m}^2 + \beta_{y,n}^2 + \frac{1}{c^2} \frac{\partial^2}{\partial t^2} \right) F_{m,n}(z,t) = 0 \quad , \quad (2.29)$$

where $F_{m,n}(z,t) = E_{m,n}^{x,y}(z,t)$.

Applying the Fourier transformation ($\bar{F}_{m,n}(z,\omega) = \mathcal{F}\{F_{m,n}(z,t)\}$) with the angular frequency $\omega=2\pi f$, the wave equation is transformed into frequency domain, and eq.(2.29) yields

$$\frac{\partial^2 \bar{F}_{m,n}(z,\omega)}{\partial z^2} - \left(\beta_{x,m}^2 + \beta_{y,n}^2 - \frac{\omega^2}{c^2} \right) \bar{F}_{m,n}(z,\omega) = 0 \quad . \quad (2.30)$$

Following a procedure analogous to [48] and assuming a given amplitude $\bar{F}_{m,n}((n_z-1)\Delta z, \omega)$ of the $TE_{m,n}^z$ mode at $k = n_z - 1$, we obtain

$$\begin{aligned} \bar{F}_{m,n}(z,\omega) = & \frac{e^{j\beta_{z,mn}(z-(n_z-1)\Delta z)}}{2} \left(\bar{F}_{m,n}((n_z-1)\Delta z, \omega) - \frac{j}{\beta_{z,mn}} \frac{\partial \bar{F}_{m,n}(z,\omega)}{\partial z} \Big|_{z=(n_z-1)\Delta z} \right) \\ & + \frac{e^{-j\beta_{z,mn}(z-(n_z-1)\Delta z)}}{2} \left(\bar{F}_{m,n}((n_z-1)\Delta z, \omega) + \frac{j}{\beta_{z,mn}} \frac{\partial \bar{F}_{m,n}(z,\omega)}{\partial z} \Big|_{z=(n_z-1)\Delta z} \right) \end{aligned} \quad (2.31)$$

with

$$\beta_{z,mn} = \begin{cases} \frac{1}{c} \sqrt{\omega^2 - \omega_{c,mn}^2} & \text{for } \omega \geq \omega_{c,mn} \\ -j \frac{1}{c} \sqrt{\omega_{c,mn}^2 - \omega^2} & \text{for } \omega \leq \omega_{c,mn} \end{cases} \quad , \quad (2.32)$$

where $\omega_{c,mn} = c\sqrt{(\beta_{x,m})^2 + (\beta_{y,n})^2}$ is the cutoff frequency of the $TE_{m,n}^z$ mode. The function $\bar{F}_{m,n}(z,\omega)$ has exponentially increasing and decreasing solutions with respect to z for $\omega \leq \omega_{c,mn}$. The exponentially increasing solutions have to vanish for $z \rightarrow \infty$ for $\omega \leq \omega_{c,mn}$, thus eq.(2.31) yields

$$\bar{F}_{m,n}((n_z-1)\Delta z, \omega) = \frac{j}{\beta_{z,mn}} \frac{\partial \bar{F}_{m,n}(z,\omega)}{\partial z} \Big|_{z=(n_z-1)\Delta z} \quad (2.33)$$

and

$$\bar{F}_{m,n}(z, \omega) = \bar{G}_{TE_{m,n}^z}(z - (n_z - 1)\Delta z, \omega) \bar{F}_{m,n}((n_z - 1)\Delta z, \omega) \quad , \quad (2.34)$$

where $\bar{G}_{TE_{m,n}^z}(z, \omega) = e^{-j\beta_{z,mn}z}$ is the Green's function for the $TE_{m,n}^z$ modes. By satisfying eq.(2.33), $\bar{F}_{m,n}((n_z - 1)\Delta z, \omega)$ results in an outward propagating solution with respect to z for $\omega \geq \omega_{c,mn}$ only. Thus, computation of $\bar{F}_{m,n}(z, \omega)$ according to eq.(2.34) requires no backward propagating solution.

Applying the convolution theorem [50], eq.(2.34) in time-domain reduces to

$$F_{m,n}(z, t) = \int_{-\infty}^{+\infty} G_{TE_{m,n}^z}(z - (n_z - 1)\Delta z, t - t') F_{m,n}((n_z - 1)\Delta z, t') dt' \quad (2.35)$$

where $G_{TE_{m,n}^z}(z, t) = \mathcal{F}^{-1}\{\bar{G}_{TE_{m,n}^z}(z, \omega)\}$. As a result, the tangential electric field components at the boundary of the mesh at $k=n_z$ are expressed in the form:

$$F_{m,n}(n_z\Delta z, t) = \int_{-\infty}^{+\infty} G_{TE_{m,n}^z}(\Delta z, t - t') F_{m,n}((n_z - 1)\Delta z, t') dt' \quad . \quad (2.36)$$

Following a procedure similar to [63], $F_{m,n}((n_z - 1)\Delta z, t')$ can be expanded in a series of triangle basis functions in time-domain. Inserting this expansion in eq.(2.36) and sampling $F_{m,n}(n_z\Delta z, t)$ using delta functions with respect to time, we obtain

$$F_{m,n}(n_z\Delta z, l\Delta t) = \sum_{l'=-\infty}^{\infty} {}_l l' G_{TE_{m,n}^z} F_{m,n}((n_z - 1)\Delta z, l'\Delta t) \quad , \quad (2.37)$$

where the discrete FDTD Green's function ${}_l l' G_{TE_{m,n}^z}$ may be calculated analytically by

$${}_l l' G_{TE_{m,n}^z} = \int_{-\infty}^{+\infty} G_{TE_{m,n}^z}(\Delta z, l\Delta t - x) g(x) dx = \frac{1}{2\pi} \int_{-\infty}^{+\infty} \bar{G}_{TE_{m,n}^z}(\Delta z, \omega) \bar{g}(\omega) e^{j\omega l\Delta t} d\omega \quad (2.38)$$

and $x = t' - l'\Delta t$. The triangle basis function is given by:

$$g(x) = \begin{cases} 1 - \left|\frac{x}{\Delta t}\right| & \text{for } |x| \leq \Delta t \\ 0 & \text{for } |x| \geq \Delta t \end{cases} \quad .$$

and its Fourier transform is:

$$\bar{g}(\omega) = \mathcal{F}\{g(t)\} = \Delta t \left[\frac{\sin(\frac{\omega\Delta t}{2})}{\frac{\omega\Delta t}{2}} \right]^2 \quad (2.39)$$

Due to causality, we have

$${}_l G_{TE_{m,n}^z} = 0 \quad \text{for } l < 0 \quad (2.40)$$

and as a result,

$$F_{m,n}(n_z \Delta z, l \Delta t) = \sum_{l'=-\infty}^l {}_{l-l'} G_{TE_{m,n}^z} F_{m,n}((n_z - 1) \Delta z, l' \Delta t) \quad , \quad (2.41)$$

which represents the mathematical formulation of the Diakoptics technique.

As an example, let's consider the $TE_{1,0}^z$ mode. For the y-component ${}_l E_{i,j,n_z}^y$ of the tangential electric field at $k = n_z$, eqs.(2.25) and (2.41) yield

$${}_l E_{i,j,n_z}^y = \sum_{l'=-\infty}^l {}_{l-l'} G_{TE_{1,0}^z} E_{1,0}^y((n_z - 1) \Delta z, l' \Delta t) \sin(\pi i \Delta x / a) \quad , \quad (2.42)$$

where $E_{1,0}^y((n_z - 1) \Delta z, l' \Delta t)$ may be calculated from eq.(2.28). The discrete FDTD Green's function ${}_{l-l'} G_{TE_{1,0}^z}$ is given by

$${}_{l-l'} G_{TE_{1,0}^z} = \frac{1}{2\pi} \int_{-\infty}^{+\infty} \bar{G}_{TE_{1,0}^z}(\Delta z, \omega) g(\omega) e^{j\omega(l-l')\Delta t} d\omega \quad (2.43)$$

with $g(\omega)$ given by eq.(2.39) and

$$\bar{G}_{TE_{1,0}^z}(\Delta z, \omega) = e^{-j\beta_{z,10} \Delta z} \quad , \quad (2.44)$$

where $\beta_{z,10}$ is calculated by eq.(2.32) for $m = 1, n = 0$.

Absorber Evaluation

To validate the absorber presented herein, we calculate the magnitude of the reflection coefficient in frequency domain for the waveguide structure shown in (Fig.2.13). The xy-plane of the waveguide at $z = 0$ is short-circuited and the ABC is utilized to calculate the

electric field components in the xy-plane at $z = 2880\Delta z$. The waveguide cross-section is $47.6mm \times 22mm$ and the cell size is given by $\Delta x = 4.76mm$, $\Delta y = 1.1mm$ and $\Delta z = 0.4mm$. We use a mesh of the size $10 \times 20 \times 2880$ and run the simulation for 25000 time-steps. All conductors are assumed to be perfect electric conductors.

We simulate the wave propagation for frequencies between $3.1GHz$ and $7.4GHz$ so that three different modes are excited, $TE_{1,0}^z$, $TE_{2,0}^z$ and $TE_{0,1}^z$. To accommodate the presence of these three modes, we use a superposition of three Gaussian pulses multiplied with the corresponding mode patterns at $z = 2840\Delta z$ to provide the correct excitation. For the calculation of the reflection coefficient ρ , we use the formula

$$\rho = \frac{E_t - E_{ref}}{E_{ref}} \quad , \quad (2.45)$$

where E_t is the tangential electric field probed at $z = 2860\Delta z$ and E_{ref} is the tangential electric field probed at the same position of a semi-infinitely long waveguide (no effect from reflections from the ABC) with the same cross section. The semi-infinite length of the waveguide is approximated by $6700\Delta z$ and the tangential electric field is probed again at $z = 2860\Delta z$. The evaluated ABC is replaced by a PEC. The length of this reference waveguide is chosen such as no reflections from the PEC plane return to the probe position for the 25000 steps of simulation. The absorber based on the analytic Green's function is compared to the 1st-order Mur's ABC coupled with the superabsorption condition. The effective dielectric constant [32] for the superabsorber is chosen to 0.407.

For practical applications, the infinite summation in eq.(2.41) has to be approximated by a finite number of terms T . This approximation corresponds to a truncation of the discrete FDTD Green's function according to

$${}_l G_{TE_{m,n}^z} = 0 \quad \text{for } l > T \quad , \quad (2.46)$$

where T represents the length of the discrete FDTD Green's function with respect to time.

We obtain

$$F_{m,n}(n_z, t) = \sum_{l'=l-T}^l {}_{l-l'}G_{TE_{m,n}^z} F_{m,n}(n_z - 1, l') \quad . \quad (2.47)$$

and eq.(2.42) can be written as

$${}^l E_{i,j,n_z}^y = \sum_{l'=l-T}^l {}_{l-l'}G_{TE_{1,0}^z} E_{1,0}^y(n_z - 1, l') \sin(\pi i \Delta x/a) \quad . \quad (2.48)$$

The reflection coefficient is minimized if we truncate the discrete FDTD Green's function at its zeros. In (Fig.2.14), results for the reflection coefficient for the $TE_{1,0}^z$ mode are shown for three different values of T , 616, 1127 and 2646. The graph for the 1st-order Mur ABC with the Superabsorption condition is symbolized with (sup). The larger the length T of the discrete FDTD Green's function, the more effective the absorber becomes. For $T = 2646$, the amplitude of the reflection coefficient is less than -40dB for almost the whole frequency range. Thus, the ABC based on the analytic Green's function is effective in a much wider frequency range than the super-absorbing 1st-order Mur ABC. This is true even when we improve the performance of the superabsorbing 1st-order Mur ABC by applying it to each waveguide mode separately. Similar results were observed for the reflection coefficient for the $TE_{2,0}^z$ and $TE_{0,1}^z$ modes.

The PML absorber [8] achieves a comparable behavior for a wide frequency range. For example, the length $T = 2646$ of the discrete $TE_{1,0}^z$ Green's function offers a reflection coefficient very close to that of a PML layer of 4 cells with $R = 10^{-5}$ (Fig.2.15) and $T = 4161$ has similar performance with a PML layer of 8 cells with $R = 10^{-5}$. Generally, considering larger values of the length T is equivalent to increasing the number of the PML cells. Nevertheless, the memory requirements of the proposed absorber are much lower than the memory requirements for the PML absorber. For each mode, the convolution of eq.(2.42)

requires the storage of the T terms of the modal Green's function and of the T previous values of the mode amplitude at the $z = (n_z - 1)\Delta z$. Thus, the extra memory requirement of the Green's function absorber is $2 \times T$ real numbers per mode. A PML layer of N cells to the z -direction requires $M = 6 \times N \times n_x \times n_y$ new variables, where $n_x \times n_y$ is the grid size for the waveguide cross-section. Generally $M \gg 2 \times T$, especially for large grids. Due to the details of the waveguide probe structure analyzed in the next section, the waveguide cross-section grid has a size of 477×220 cells. That means that even a PML layer of 4 cells to the z -direction requires the storage of $M = 2,518,560$ new variables !! Using an absorber based on Green's functions with length $T = 2646$ for the $TE_{1,0}^z$, $T = 2238$ for the $TE_{2,0}^z$ and $T = 2412$ for the $TE_{0,1}^z$, only 14,592 new variables have to be stored (0.58% of the PML memory requirements). As a result, the Green's function-based ABC offers a significant economy in memory while maintaining similar accuracy with the PML absorber.

Waveguide Probe Structure Characterization

The FDTD technique coupled with the proposed waveguide absorber is used in the RF characterization of the waveguide probe geometry shown in (Fig.2.12). The probe in the shape of a rectangular patch is fed by a shielded 50Ω coplanar line and is inserted into the waveguide through a slot. The dielectric substrate carrying the probe is not connected to any waveguide wall. This type of probe can be used as a coupler to a rectangular waveguide or as a diode mounting structure. The dimensions of the probe as well as the substrate thickness and the dielectric constant of the substrate are of critical importance in optimizing coupling to the waveguide.

In our simulations, we try to optimize the thickness of the dielectric substrate carrying a probe which is 3.6mm wide. The dielectric constant of the substrate is assumed to be

$\epsilon_r=12$ (GaAs). The width of the dielectric substrate entering the waveguide is 5.8mm and its thickness is limited to less than 2mm. The probe is designed to feed a WR-187 rectangular waveguide and for this reason, excitation is provided on the coplanar feedline by a Gabor function which covers the frequency range of 3.1 GHz to 7.4 GHz. For the simulated frequency range, three different modes are excited inside the waveguide, $TE_{1,0}^z$, $TE_{2,0}^z$ and $TE_{0,1}^z$, with the cutoff frequencies 3.15 GHz, 6.30 GHz and 6.82 GHz respectively. The mesh used in the FDTD simulation consists of 480x477x52 cells with a time step of $\Delta t = 0.31425ps$. The simulation runs for 20,000 time steps to achieve converging results. The absorber discussed previously is used to absorb simultaneously all propagating modes of the waveguide for the simulated frequency range.

To characterize the probe performance for different dielectric thicknesses, the magnitude of the reflection coefficient $|S_{11}|$ for the dominant $TE_{1,0}^z$ mode is calculated. For validation purposes, the calculated results are compared to data derived by the FEM (Finite Element Method) assuming a probe width of 3.6mm and a dielectric thickness of 2.0 mm (See (Fig.2.16)). For the FDTD simulation, the waveguide absorber based on the Green's functions for the three propagating waveguide modes is used at the terminal plane. For the FEM simulation, an artificial absorber depending on frequency and angle of incidence is applied to terminate the waveguide. For the whole operating frequency range (3.1-7.5 GHz) the performance of both absorbers is comparable and the results show very good agreement.

The dimensions of the shield of the coplanar feedline are chosen to be 5.8mm x 3.8mm, such as only the CPW dominant mode can propagate and the field patterns are not disturbed by the side walls in the frequency range of the simulation. In this way, the superabsorption condition can be applied effectively at the input plane of the feedline.

The performance of the probe has been evaluated for three different dielectric thicknesses

2.0mm, 1.2mm and 0.0 mm, with the last value corresponding to a microwave probe printed on a dielectric membrane [52]. Results in terms of the reflection coefficient are shown in (Fig.2.17). As it can be observed from this figure, the value of the reflection coefficient reduces over a large frequency range and shows symmetrical behavior round the center design frequency as the dielectric thickness approaches zero. The electric field (E) and magnetic field (H) distributions for zero dielectric thickness are plotted for $t = 6,000$ time steps across the probe structure symmetry plane (Fig.2.18) and across the coplanar feedline plane (Fig.2.19) and represent the transmitted and the reflected energy respectively.

The reflection coefficient of the Si-membrane printed probe has been calculated for four different patch widths 3.6mm, 9.8mm, 11.4mm and 13.0mm and the results are shown in (Fig.2.20). From this figure, it can be concluded that the width of 9.8mm offers the most symmetrical behavior for the frequency of operation. The reflection coefficient for widths larger than 9.8mm is much smaller than that of 3.6mm for most of the simulated frequencies except a small region round 4.6 GHz. Nevertheless, the widths of 11.4mm and 13.0mm offer no significant improvement over the width of 9.8mm.

Another geometry parameter of the Si-membrane printed probe that has been investigated is the distance of the probe patch from the short circuit of the waveguide. Lengths of 8.8mm, 10.4mm, 12.0mm and 13.6mm have been used and the results are plotted in (Fig.2.21) it can be noticed that the value of 12.0mm offers the best performance in terms of the value and the bandwidth of the reflection coefficient.

The FDTD results derived by using the absorber presented in Section III.2 have been validated by comparing to experimental data. The probe has dimensions 13.2mm x 4.3mm on a dielectric substrate with thickness 2.1mm, width 28.7mm and $\epsilon_r=13$. The probe has been inserted in a WR229 waveguide and is located at a distance of 14.7mm from the top

surface short circuit. For the FDTD absorber there have been used $T=2871$ time steps. The performance of the probe has been evaluated for the frequency range of 3.3-4.6GHz and the results are shown in (Figs.2.22-2.23). The agreement between the FDTD and the experimental results is good especially in the frequency range of the optimum performance of the probe. The abrupt variation in S_{21} observed for the higher frequencies in the experiment is maybe due to calibration or other reasons related to the experimental setup.

2.4 Conclusion

The finite-difference time-domain method has been used to analyze planar circuits and waveguide probe structures. For the analysis, a waveguide absorber based on analytic Green's functions has been developed. This absorber is characterized by a better performance in accuracy and computational efficiency than the super-absorbing 1st-order Mur ABC and by a better performance in memory requirements than the PML absorber. The scattering parameters of the probe structures have been calculated and the results have been verified by comparison with FEM and experimental data. The influence of critical geometrical parameters on the probe performance has been investigated and optimized.

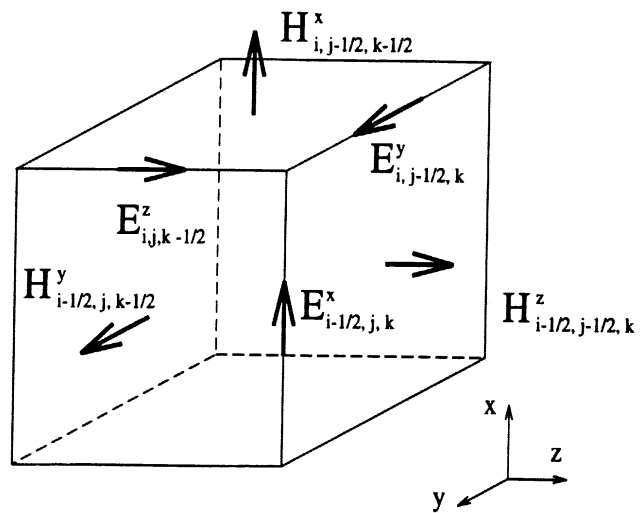


Figure 2.1: Yee's FDTD cell.

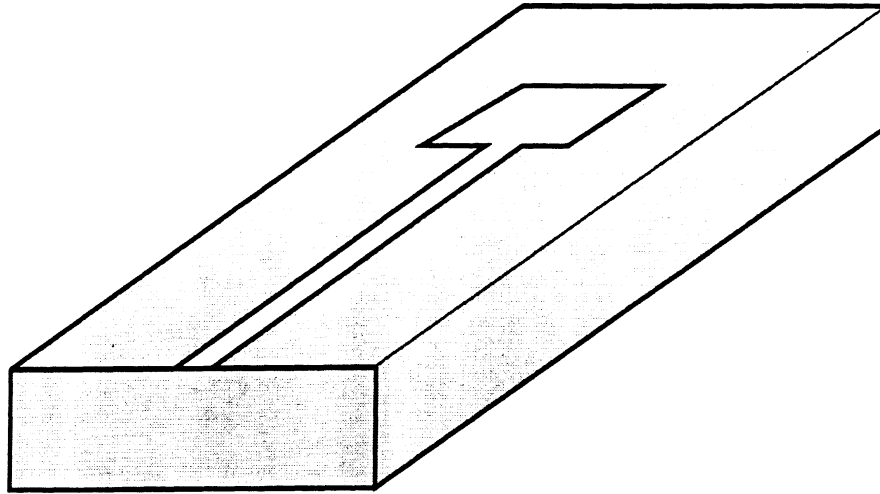


Figure 2.2: Patch Geometry to be used as Open.

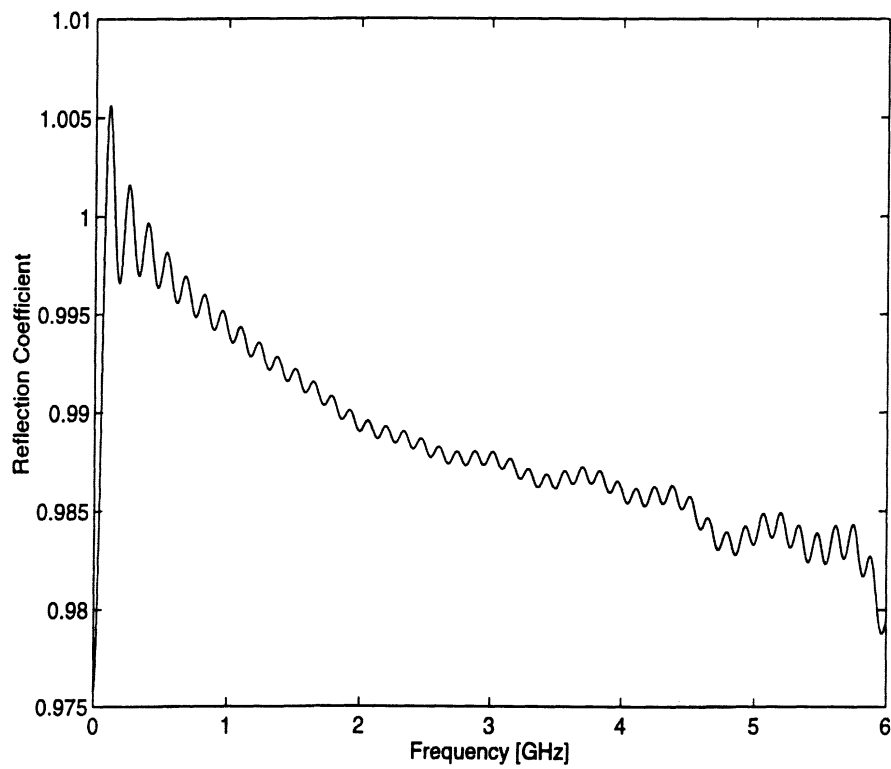


Figure 2.3: Reflection Coefficient of the Open.

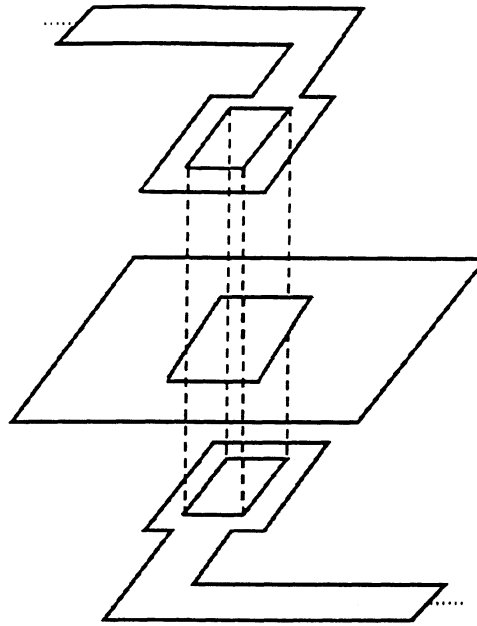


Figure 2.4: Viahole Structure.

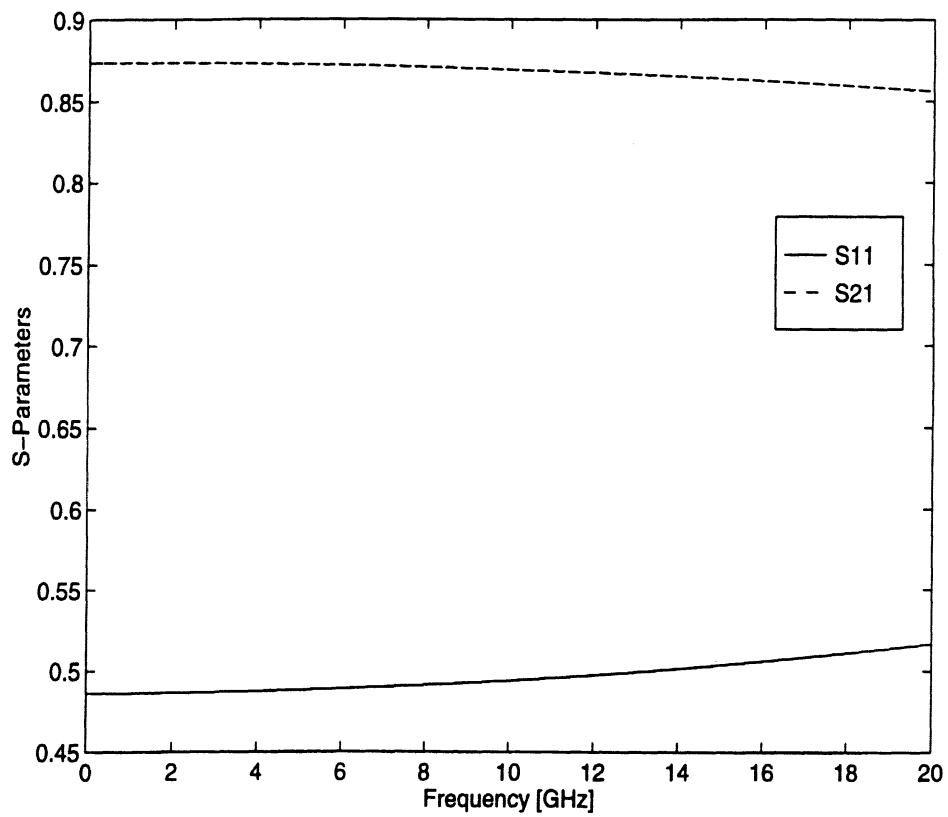


Figure 2.5: S-Parameters of the Viahole.

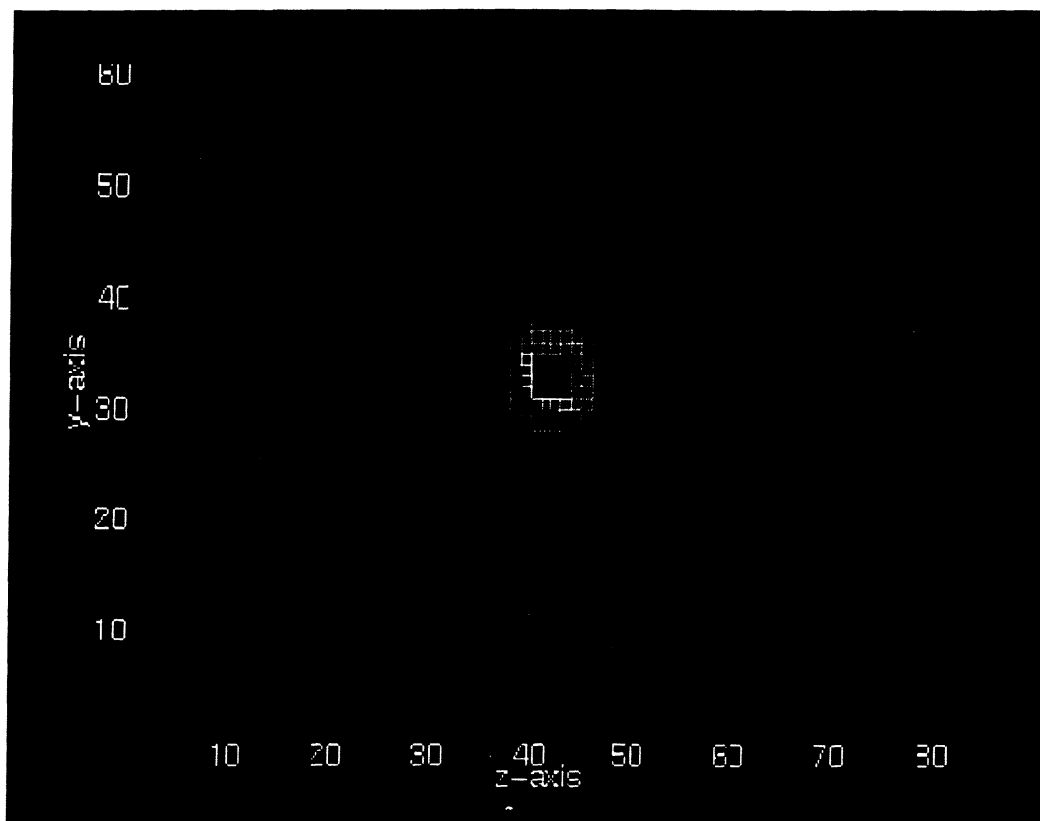
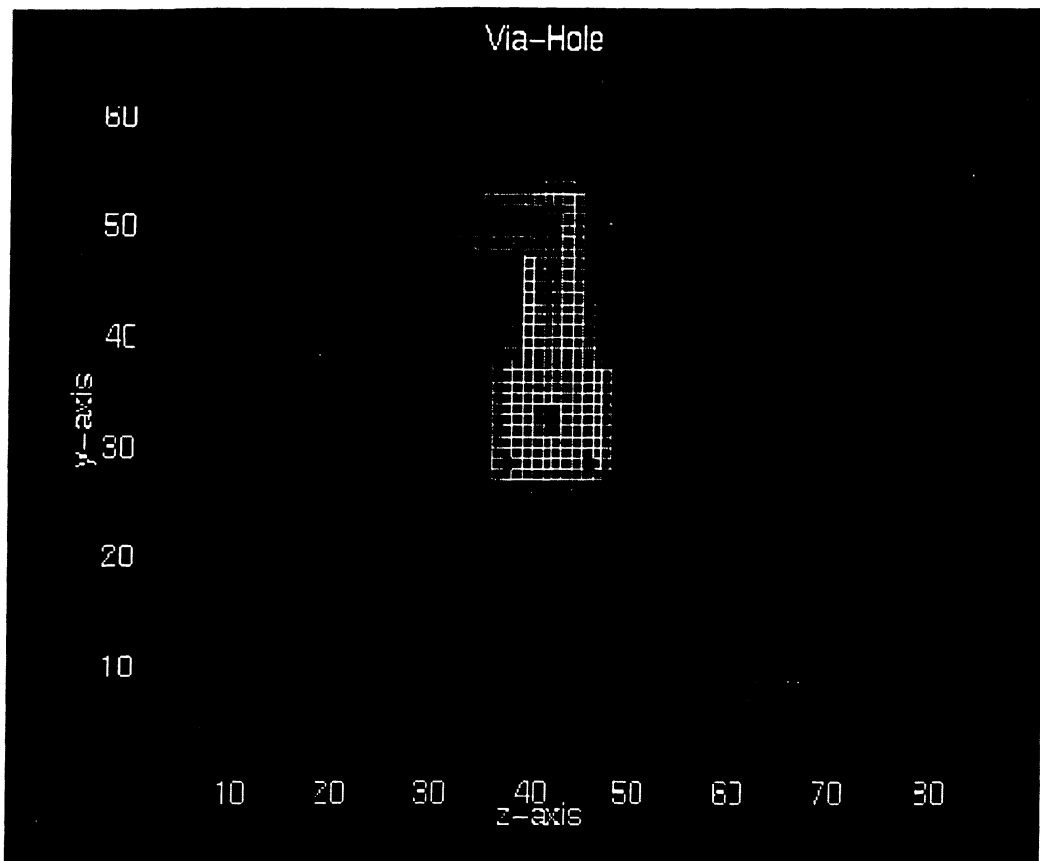


Figure 2.6: E-Distribution across Top Viahole (Top), Middle Ground Plane (Bottom).

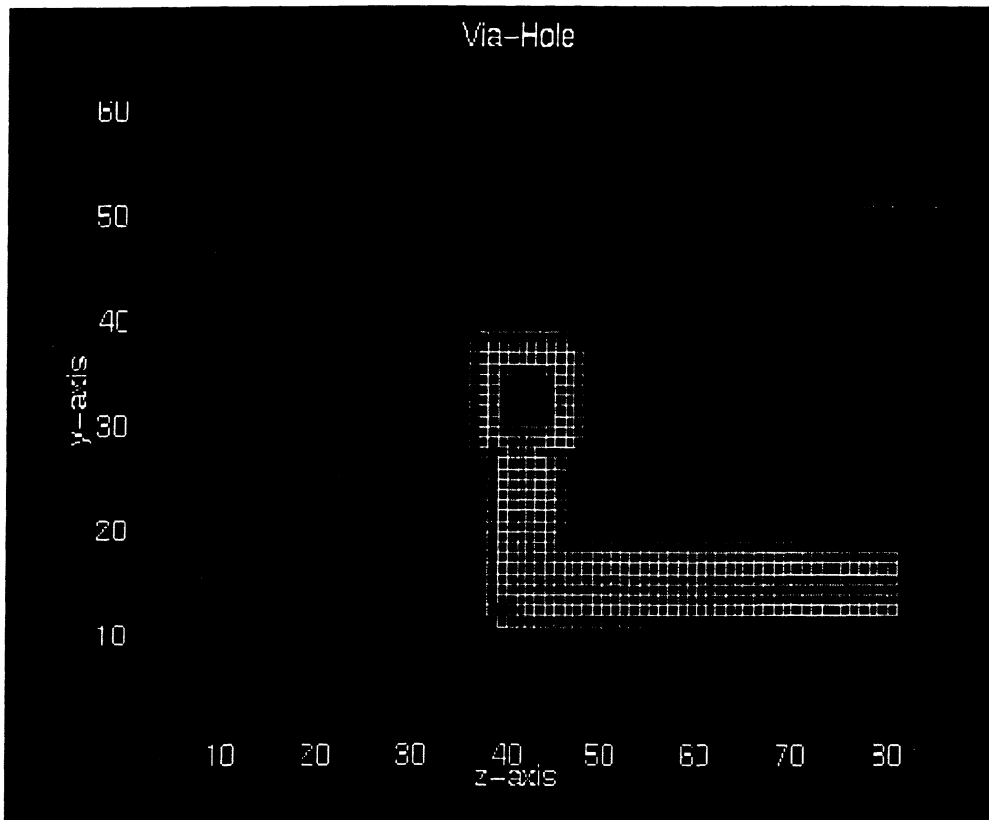


Figure 2.7: E-Distribution across Bottom Viahole.

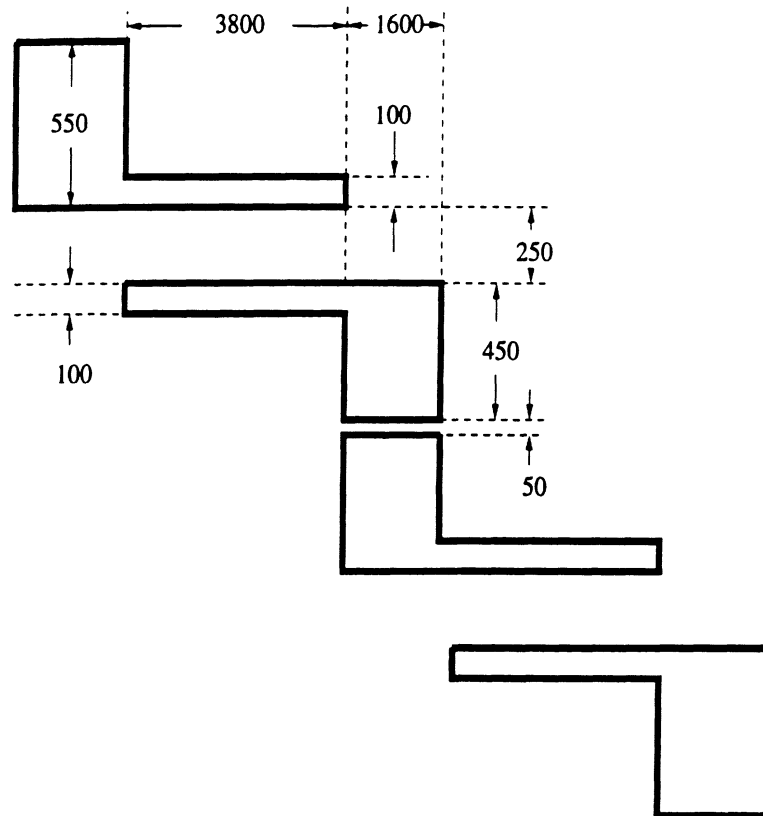


Figure 2.8: Coupled Line Filter Geometry.

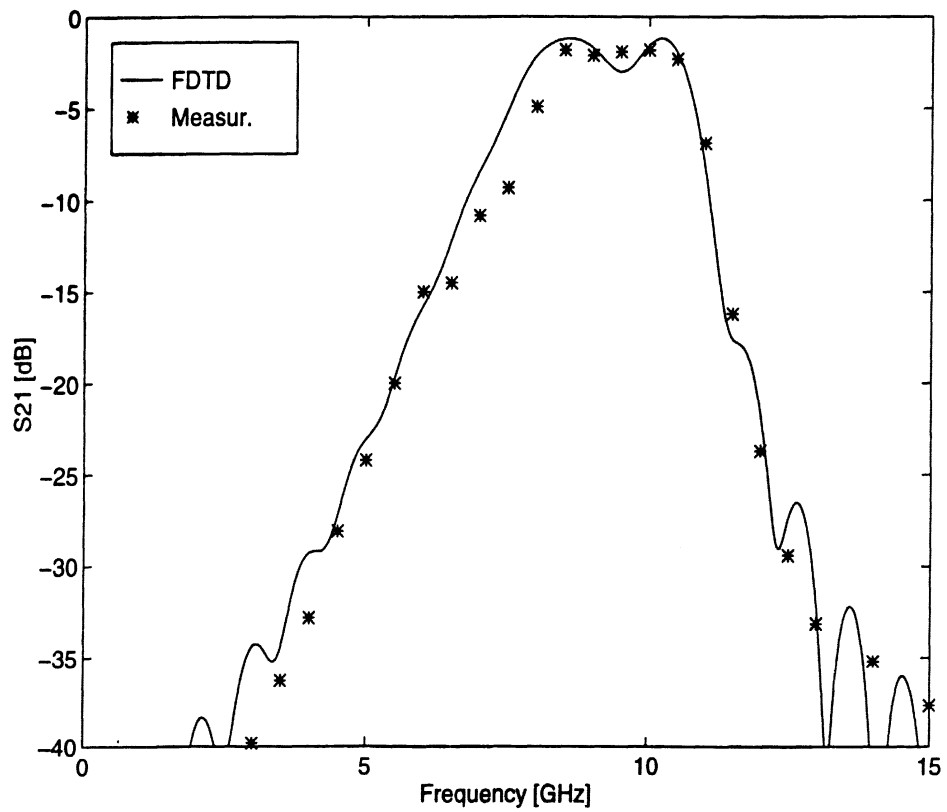


Figure 2.9: Coupled Line Filter S_{21} .

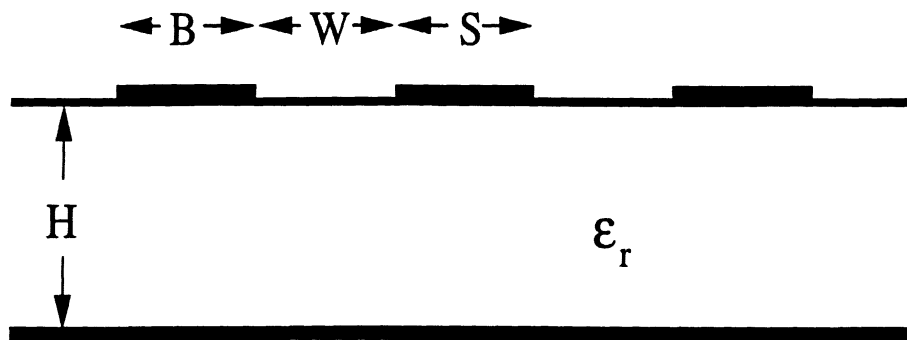


Figure 2.10: Coplanar waveguide with finite width ground planes (F.G.C.).

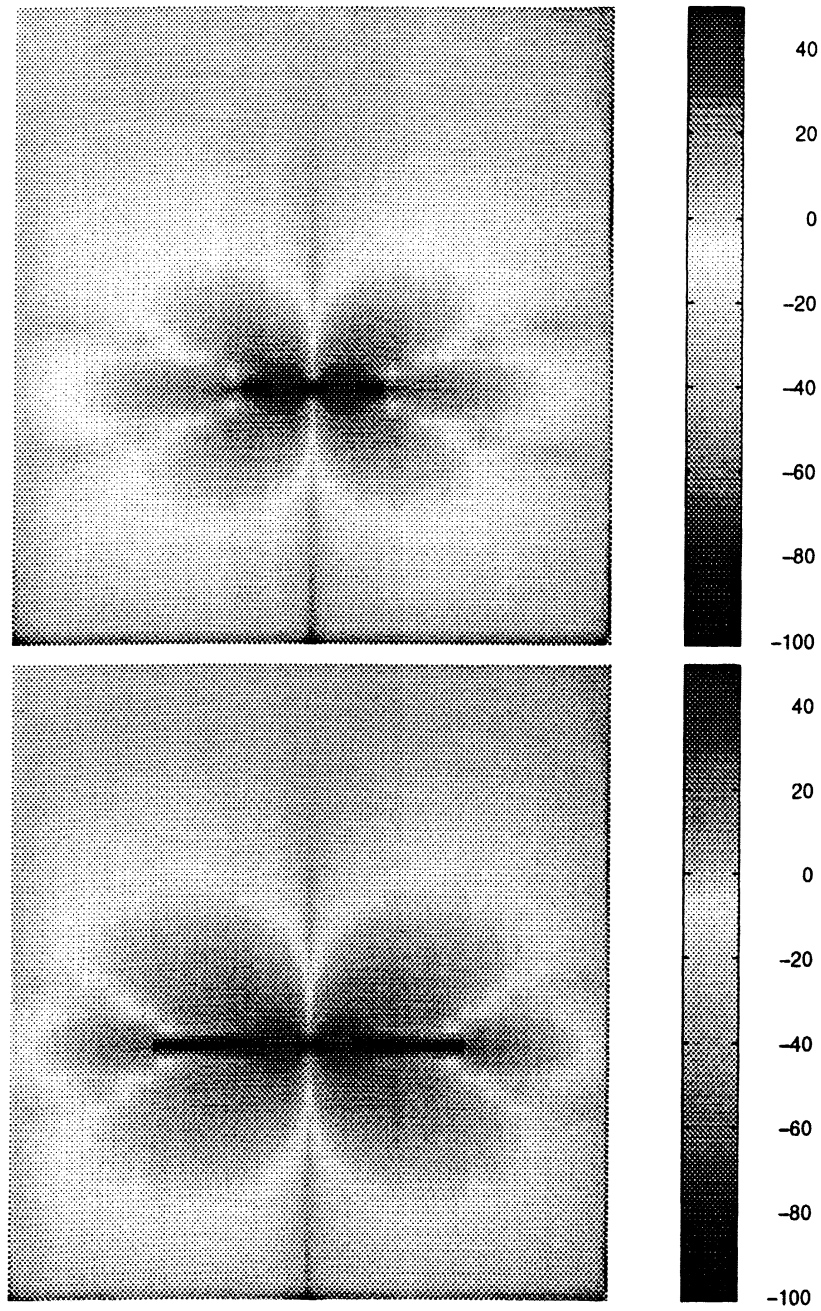


Figure 2.11: Normal H-Distribution (Log) for $B=25 \mu\text{m}$ (up), $100 \mu\text{m}$ (bottom).

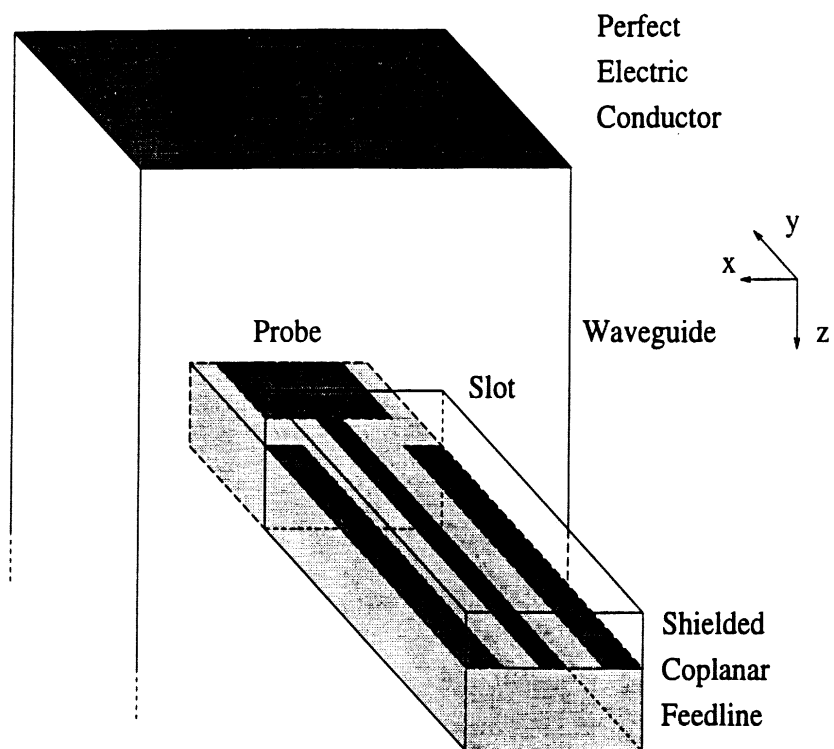


Figure 2.12: Waveguide probe structure.

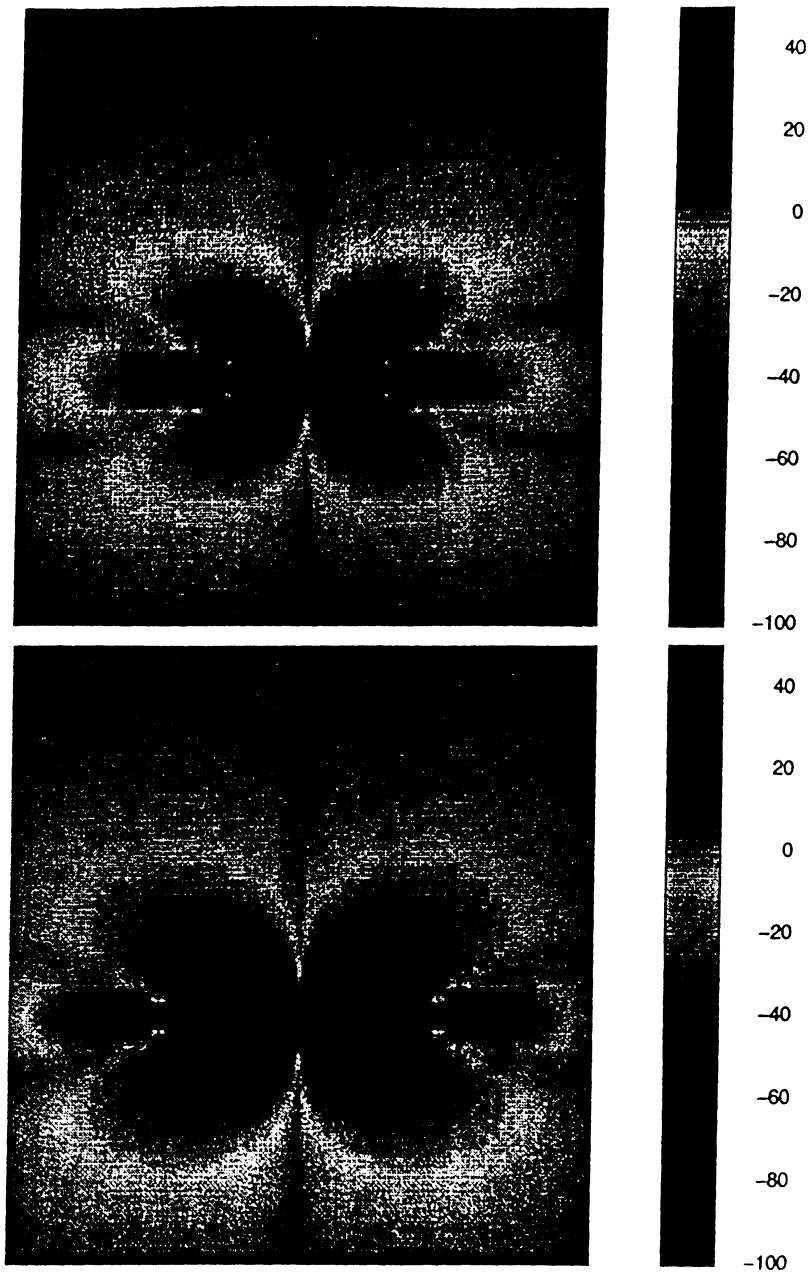


Figure 2.11: Normal H-Distribution (Log) for $B=25 \mu\text{m}$ (up), $100 \mu\text{m}$ (bottom).

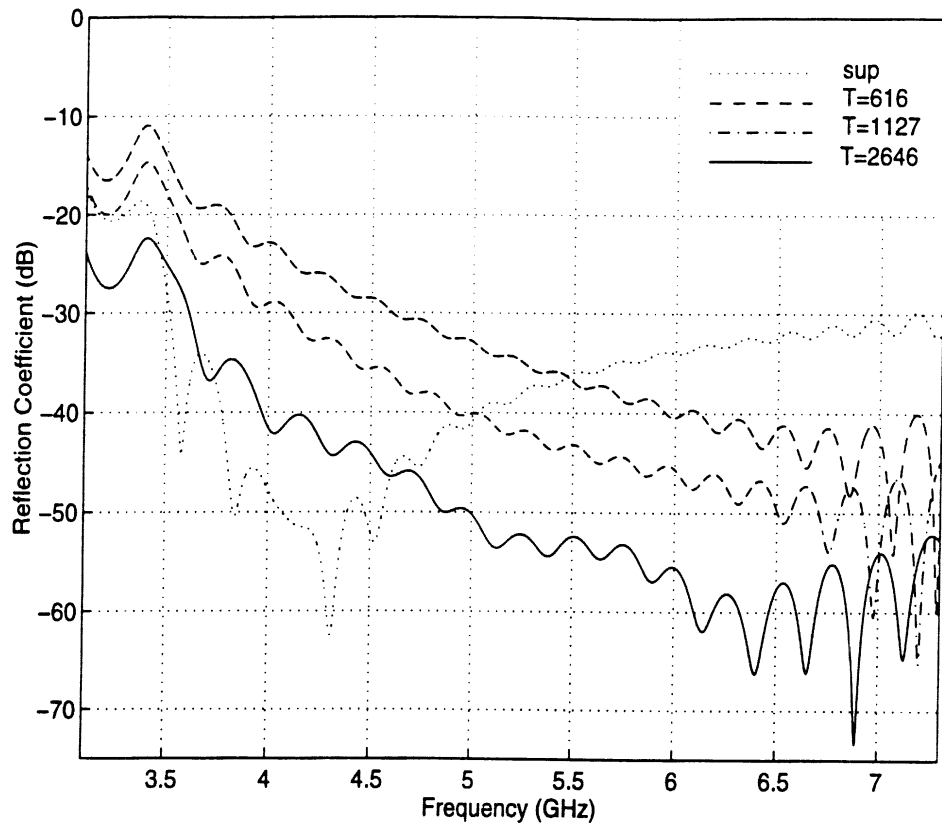


Figure 2.14: Reflection coefficient for the $TE_{1,0}^z$ mode.

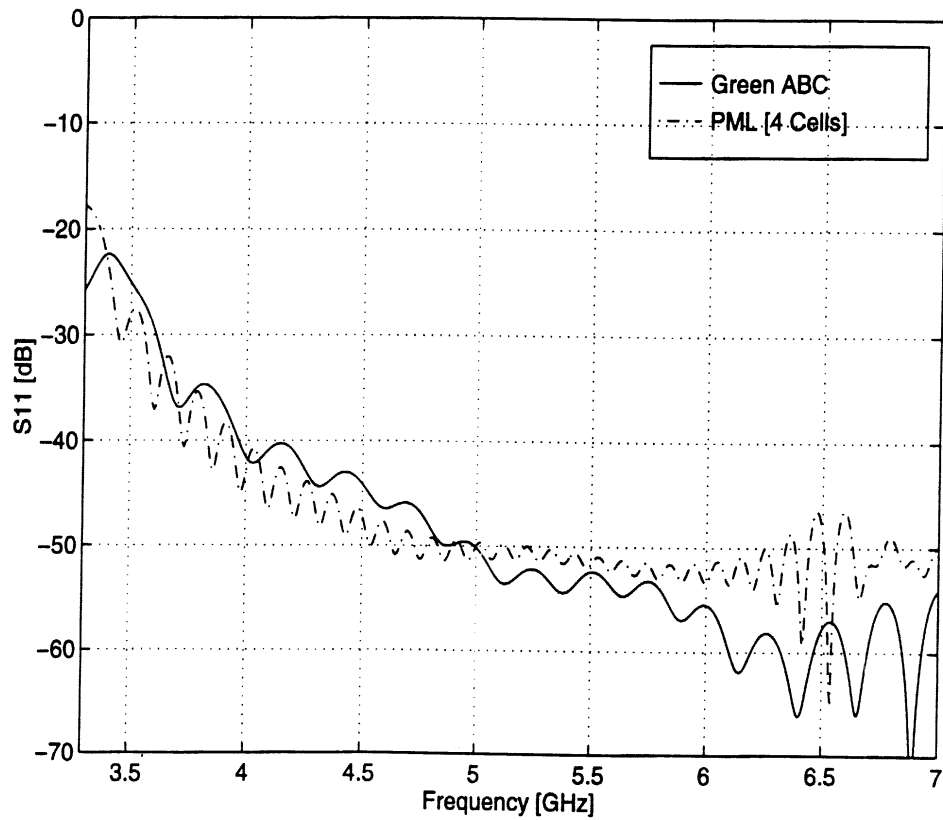


Figure 2.15: Comparison of Green's Function ABC and PML.

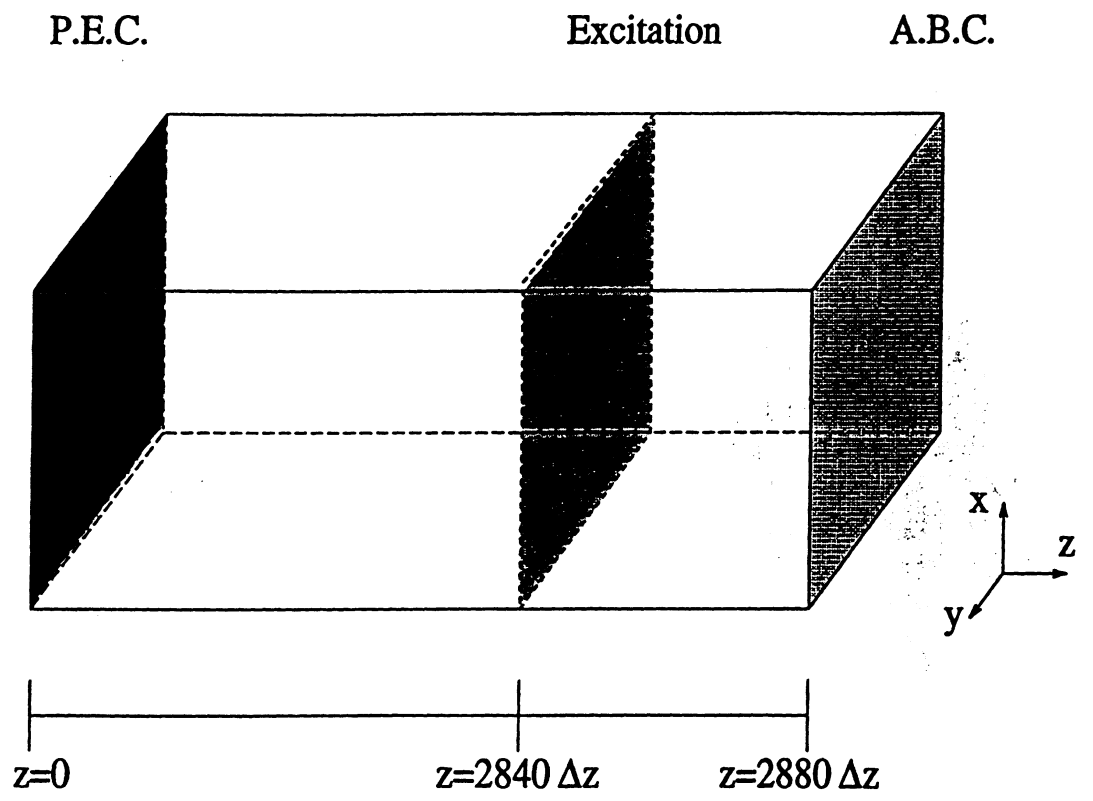


Figure 2.13: Waveguide Test Structure.

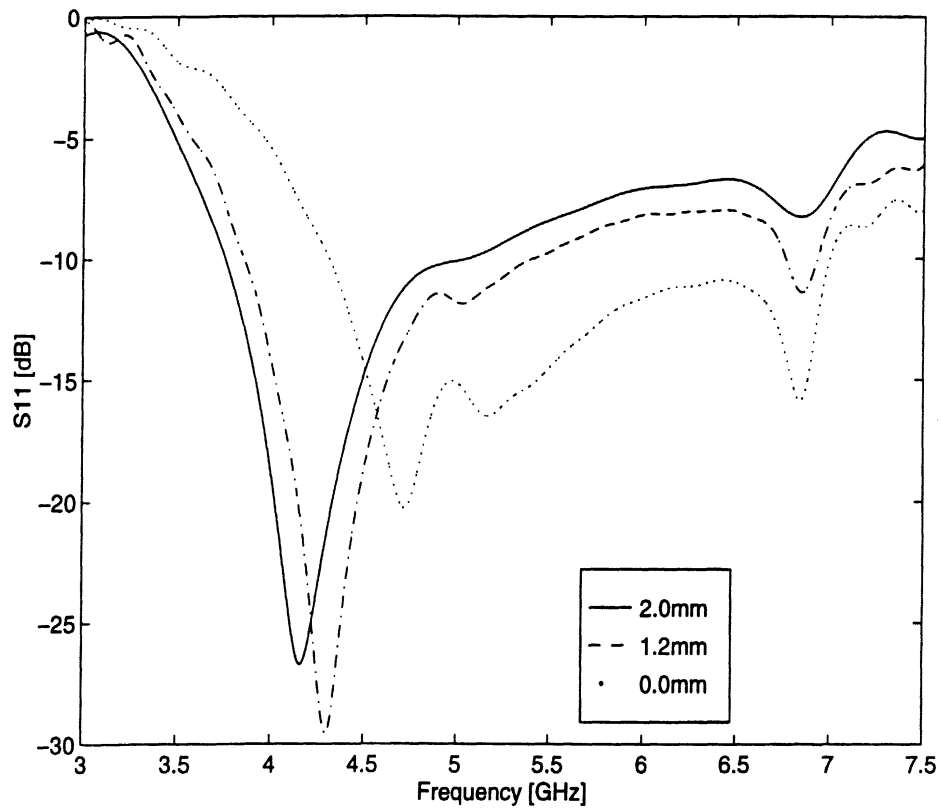


Figure 2.17: Reflection Coefficient for different Dielectric Thicknesses.

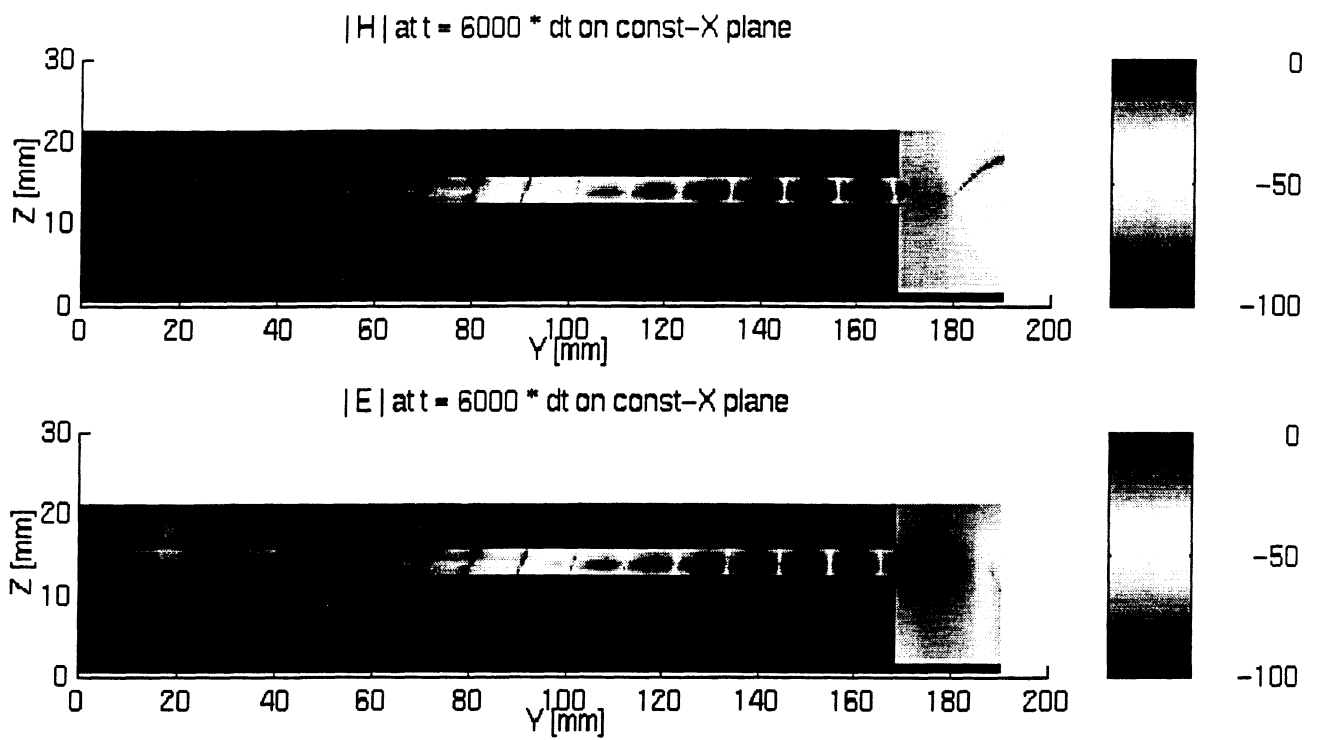


Figure 2.18: E- and H-field Distributions across the Probe Structure Symmetry Plane.

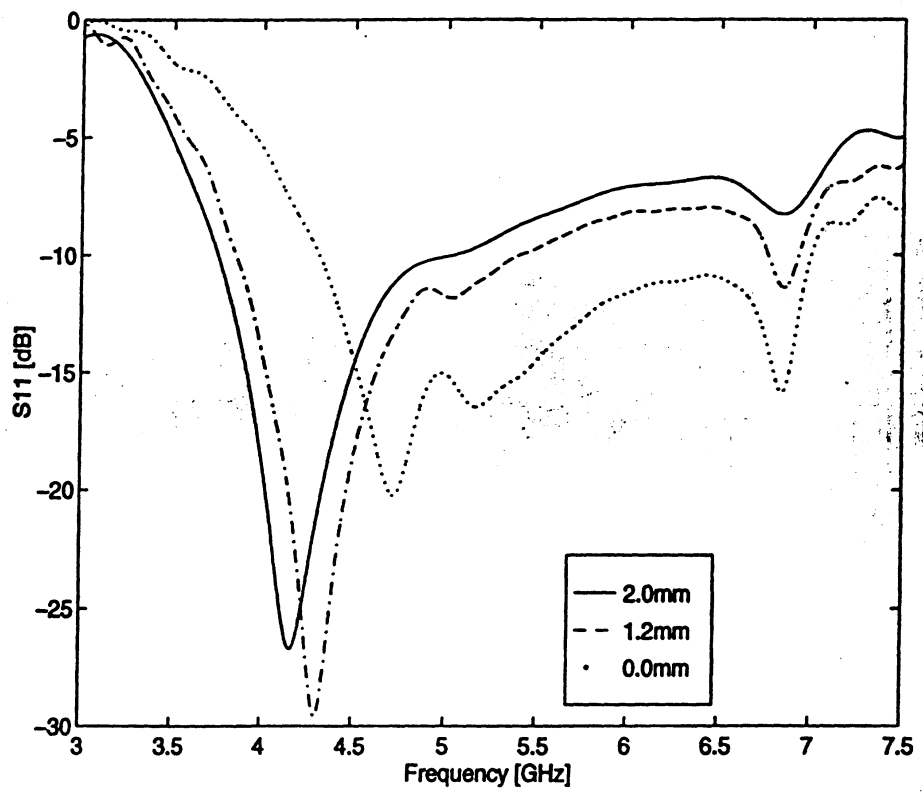


Figure 2.17: Reflection Coefficient for different Dielectric Thicknesses.

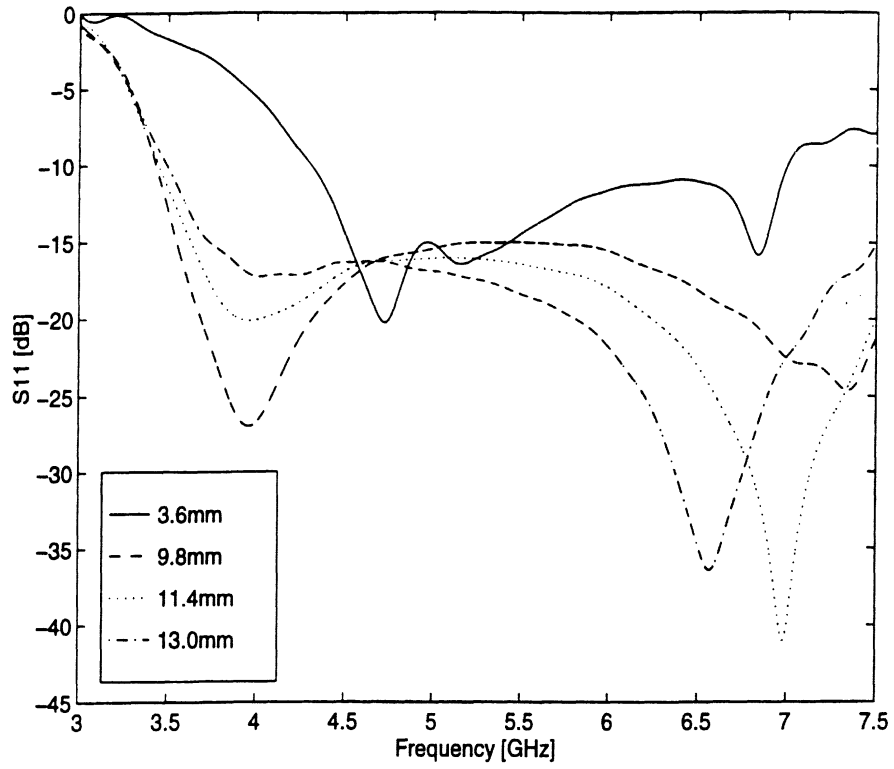


Figure 2.20: Reflection Coefficient for different Patch Widths.

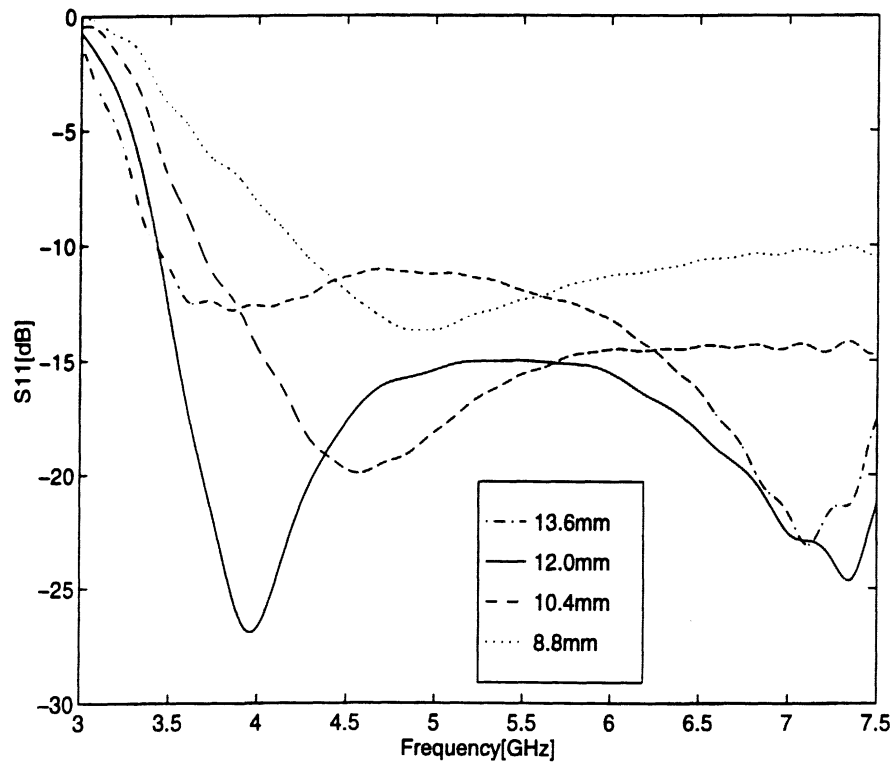


Figure 2.21: Reflection Coefficient for different Distances from the Top Surface Short-Circuit.

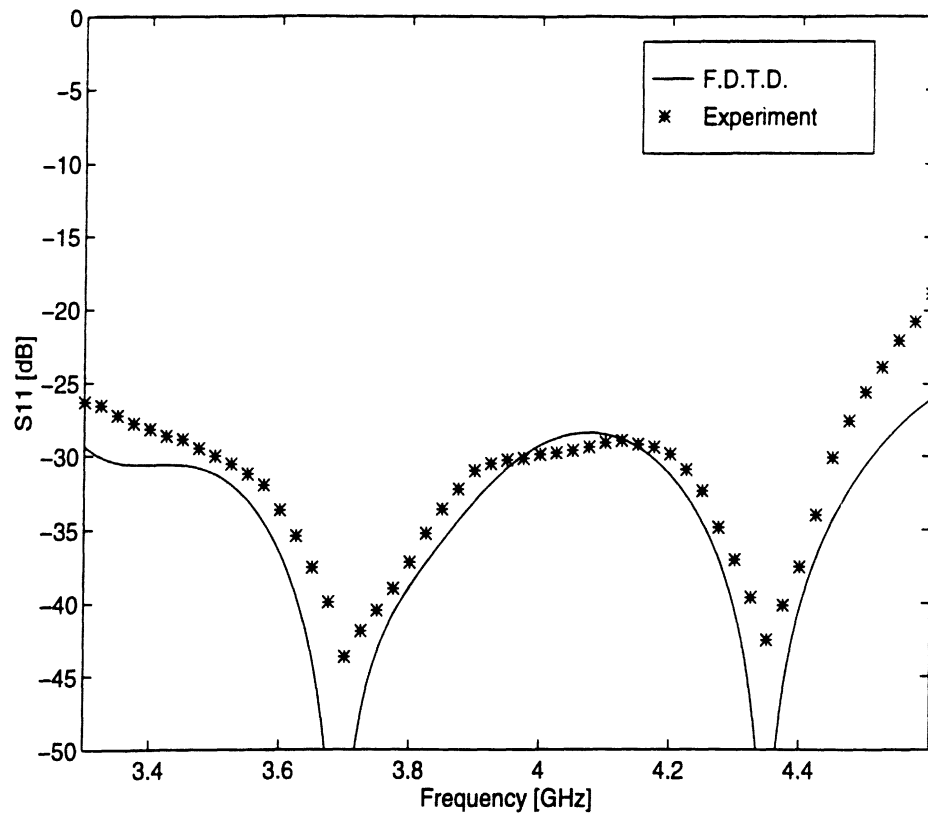


Figure 2.22: Experimental Validation for S_{11} .

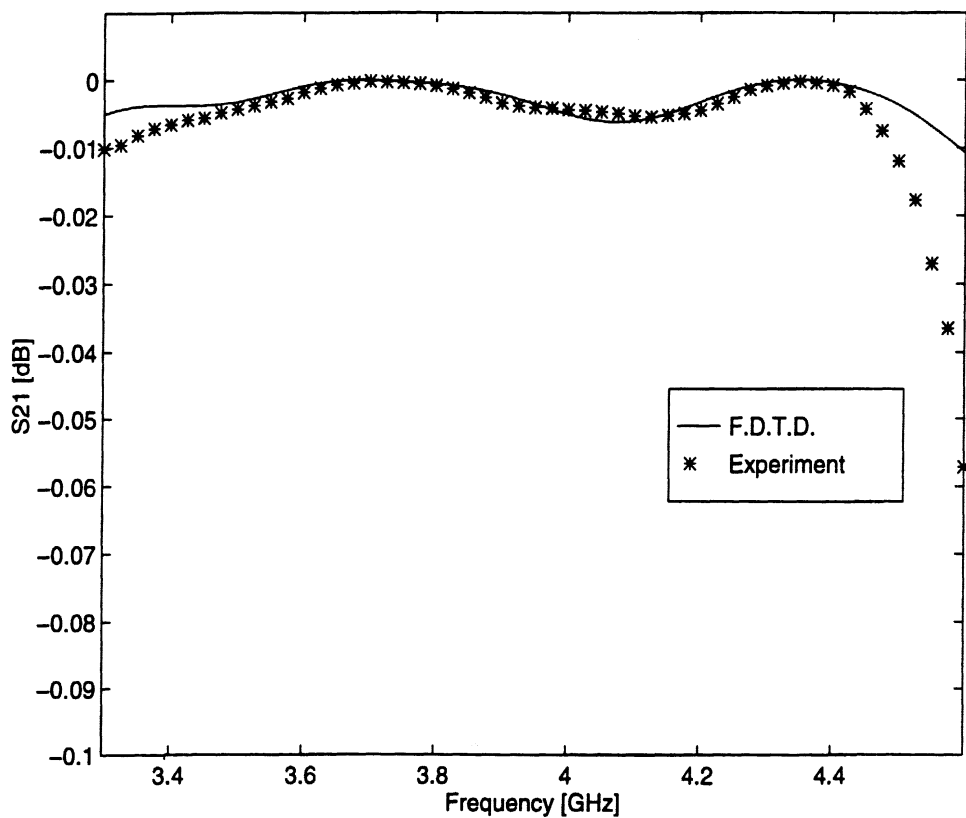


Figure 2.23: Experimental Validation for S_{21} .

CHAPTER 3

Development of New Time-Domain Schemes with Higher Order Basis Functions

3.1 Introduction

Significant attention is being devoted now-a-days to the analysis and design of various types of printed components for microwave applications. To understand high-frequency effects and incorporate them into the design process, there is a compelling need to implement full-wave solutions during the modeling process. There has been a variety of full wave techniques developed for this purpose, with many of them available commercially. Despite the wealth of available codes, many problems in electromagnetics and specifically in circuit and antenna problems have been left untreated due to the complexity of the geometries and the inability of the existing techniques to deal with the requirements for large size and high resolution due to the fine but electrically important geometrical details. The straightforward use of existing discretization methods suffers from serious limitations due to the required substantial computer resources and unrealistically long computation times. As a result, during the past thirty years the available techniques are almost incapable of dealing with the needs of technology leading into a quest for fundamentally different

modeling approaches.

The use of multiresolution analysis in time domain has shown that Yee's FDTD scheme can be derived by applying the method of moments for the discretization of Maxwell's equations [51] using pulse basis functions for the expansion of the unknown fields. The use of scaling and wavelet functions as a complete set of basis functions is called multiresolution analysis and demonstrates that Multiresolution Time-Domain (MRTD) schemes are generalizations to Yee's FDTD and can extend the capabilities of the conventional FDTD by improving computational efficiency and substantially reducing computer resources.

3.2 Fundamentals on Multiresolution Analysis

A multiresolution analysis consists of a sequence of successive approximation spaces V_j . More precisely, the closed subspaces V_j satisfy

$$\dots V_2 \subset V_1 \subset V_0 \subset V_{-1} \subset V_{-2} \subset \dots \quad (3.1)$$

with

$$\overline{\bigcup_{j \in \mathbb{Z}} V_j} = L^2(\mathbb{R}) \text{ (density)} \quad (3.2)$$

$$\bigcap_{j \in \mathbb{Z}} V_j = \{0\} \text{ (separation)} \quad (3.3)$$

There exist many ladders of spaces satisfying the above conditions that have nothing to do with "multiresolution"; the multiresolution aspect is a consequence of the additional requirement

$$f(x) \in V_j \leftrightarrow f(2^j x) \in V_0 \text{ (scaling)} \quad (3.4)$$

That is, all the spaces are scaled versions of the central space V_0 . Another feature that we

CHAPTER 3

Development of New Time-Domain Schemes with Higher Order Basis Functions

3.1 Introduction

Significant attention is being devoted now-a-days to the analysis and design of various types of printed components for microwave applications. To understand high-frequency effects and incorporate them into the design process, there is a compelling need to implement full-wave solutions during the modeling process. There has been a variety of full wave techniques developed for this purpose, with many of them available commercially. Despite the wealth of available codes, many problems in electromagnetics and specifically in circuit and antenna problems have been left untreated due to the complexity of the geometries and the inability of the existing techniques to deal with the requirements for large size and high resolution due to the fine but electrically important geometrical details. The straightforward use of existing discretization methods suffers from serious limitations due to the required substantial computer resources and unrealistically long computation times. As a result, during the past thirty years the available techniques are almost incapable of dealing with the needs of technology leading into a quest for fundamentally different

modeling approaches.

The use of multiresolution analysis in time domain has shown that Yee's FDTD scheme can be derived by applying the method of moments for the discretization of Maxwell's equations [56] using pulse basis functions for the expansion of the unknown fields. The use of scaling and wavelet functions as a complete set of basis functions is called multiresolution analysis and demonstrates that Multiresolution Time-Domain (MRTD) schemes are generalizations to Yee's FDTD and can extend the capabilities of the conventional FDTD by improving computational efficiency and substantially reducing computer resources.

3.2 Fundamentals on Multiresolution Analysis

A multiresolution analysis consists of a sequence of successive approximation spaces V_j .

More precisely, the closed subspaces V_j satisfy

$$\dots V_2 \subset V_1 \subset V_0 \subset V_{-1} \subset V_{-2} \subset \dots \quad (3.1)$$

with

$$\overline{\bigcup_{j \in \mathbb{Z}} V_j} = L^2(\mathbb{R}) \text{ (density)} \quad (3.2)$$

$$\bigcap_{j \in \mathbb{Z}} V_j = \{0\} \text{ (separation)} \quad (3.3)$$

There exist many ladders of spaces satisfying the above conditions that have nothing to do with "multiresolution"; the multiresolution aspect is a consequence of the additional requirement

$$f(x) \in V_j \leftrightarrow f(2^j x) \in V_0 \text{ (scaling)} \quad (3.4)$$

That is, all the spaces are scaled versions of the central space V_0 . Another feature that we

require from multiresolution analysis is the invariance of V_0 under integer translations

$$f(x) \in V_0 \leftrightarrow f(x - n) \in V_0, \forall n \in \mathbf{Z} \quad (3.5)$$

Because of Eq.(3.4), this implies that if $f(x) \in V_j$, then $f(x - 2^j n) \in V_j$ for all $n \in \mathbf{Z}$.

Finally, we require that there exists $\phi \in V_0$ such that $\{\phi_{0,n}, n \in \mathbf{Z}\}$ is an orthonormal basis in V_0 , where for all $j, n \in \mathbf{Z}$, $\phi_{j,n}(x) = 2^{-j/2} \phi(2^{-j}x - n)$. As a result, $\{\phi_{j,n}, n \in \mathbf{Z}\}$ is an orthonormal basis for V_j for all $j \in \mathbf{Z}$; that is,

$$\langle \phi_{j,m}, \phi_{j,n} \rangle = \delta_{m,n}, \quad m, n \in \mathbf{Z} \quad (3.6)$$

where δ notates the Kronecker symbol

$$\delta_{m,n} = \begin{cases} 1 & m = n \\ 0 & \text{elsewhere} \end{cases}$$

Throughout this Chapter, there will be used the following notations for the *inner product* and *norm* for the space $L^2(\mathbf{R})$:

$$\langle f, g \rangle = \int_{-\infty}^{\infty} f(x) \overline{g(x)} dx$$

$$\|f\| = \|f\|_2 = \langle f, f \rangle^{1/2}$$

The basic idea of the multiresolution analysis is that whenever a collection of closed subspaces satisfy Eqs.(3.1)–(3.5), then there exists an orthonormal wavelet basis $\{\psi_{j,n}, n \in \mathbf{Z}\}$ of $L^2(\mathbf{R})$, $\psi_{j,n}(x) = 2^{-j/2} \psi(2^{-j}x - n)$, such that for all f in $L^2(\mathbf{R})$,

$$P_{j-1}f = P_j f + \sum_{k \in \mathbf{Z}} \langle f, \psi_{j,k} \rangle \psi_{j,k} \quad , \quad (3.7)$$

where P_j is the orthogonal projection onto V_j . For every $j \in \mathbf{Z}$, define W_j to be the orthogonal complement of V_j in V_{j-1} . We have

$$V_{j-1} = V_j \oplus W_j \quad (3.8)$$

with ρ 2π -periodic and $|\rho(\xi)|=1$. In particular, we can choose $\rho(\xi) = \rho_0 e^{im\xi}$ with $m \in \mathbb{Z}$, $|\rho_0| = 1$, which corresponds to a phase change and a shift by m for ψ . We will use this freedom to define

$$\psi = \sum_n g_n \phi_{-1,n}, \quad g_n = (-1)^n h_{-n+1} \quad (3.23)$$

The orthonormality condition of Eq.(3.6) can be relaxed. It is sufficient to require that the $\phi(x - k)$ constitute a Riesz basis of V_0 ; that means that they span V_0 and for all $(c_k)_{k \in \mathbb{Z}} \in L^2(\mathbb{Z})$ with $\sum_k |c_k|^2 < \infty$ it holds

$$A \sum_k |c_k|^2 \leq \left\| \sum_k c_k \phi(x - k) \right\|^2 \leq B \sum_k |c_k|^2 \quad (3.24)$$

or equivalently

$$0 < (2\pi)^{-1} A \leq \sum_l |\hat{\phi}(\xi + 2\pi l)|^2 \leq (2\pi)^{-1} B < \infty \quad (3.25)$$

where $A > 0, B < \infty$ are independent of the c_n . Supposing that $\phi \in L^2(\mathbb{R})$ satisfies Eq.(3.25) and defining $V_j = \overline{\text{Span}\{\phi_{j,k}; k \in \mathbb{Z}\}}$, then $\bigcap_{j \in \mathbb{Z}} V_j = 0$. Also, if $\hat{\phi}(\xi)$ is bounded for all ξ and continuous near $\xi = 0$, with $\hat{\phi}(0) \neq 0$, then $\overline{\bigcup_{j \in \mathbb{Z}} V_j} = L^2(\mathbb{R})$. One Riesz basis which satisfies these criteria, satisfies the density and separation qualities of the multiresolution analysis.

Chui [?] has proven that $\{\phi(x - k) : k \in \mathbb{Z}\}$ is an orthonormal family if and only if $2\pi \sum_{k=-\infty}^{\infty} |\hat{\phi}(\xi + 2\pi k)|^2 = 1, \forall \xi \in \mathbb{R}$. This is a very useful criterion for the orthonormality of a specific scaling family.

We can therefore construct an orthonormal basis ϕ^\perp for V_0 by defining

$$\hat{\phi}^\perp = (2\pi)^{-1/2} \left[\sum_l |\hat{\phi}(\xi + 2\pi l)|^2 \right]^{-1/2} \hat{\phi}(\xi) \quad (3.26)$$

Clearly, $\sum_l |\hat{\phi}^\perp(\xi + 2\pi l)|^2 = (2\pi)^{-1}$, which means that the $\phi^\perp(x - k)$ are orthonormal.

Finally,

$$\hat{\psi}(\xi) = e^{i\xi/2} \overline{m_0^\perp(\xi/2 + \pi)} \hat{\phi}^\perp(\xi/2) \quad (3.27)$$

with

$$m_0^\perp(\xi) = m_0(\xi) \left[\sum_l |\hat{\phi}(\xi + 2\pi l)|^2 \right]^{1/2} \left[\sum_l |\hat{\phi}(2\xi + 2\pi l)|^2 \right]^{-1/2} \quad (3.28)$$

or equivalently

$$\psi(x) = \sum_n (-1)^n h_{-n+1}^\perp \phi^\perp(x - n) \quad (3.29)$$

with $m_0^\perp(\xi) = \frac{1}{\sqrt{2}} \sum_n h_n^\perp e^{-in\xi}$.

The Battle-Lemarié wavelets [22, 23] are associated with multiresolution analysis ladders consisting of spline function spaces. A B-spline with knots at the integers is considered the original scaling function. The zero order cardinal B-spline N_0 is the characteristic function of the unit interval $[0,1)$

$$N_0(x) = \begin{cases} 1 & 0 \leq x \leq 1 \\ 0 & \text{elsewhere} \end{cases}$$

For $m \geq 1$, the m -th order cardinal B-spline N_m is defined recursively by the following convolution:

$$\begin{aligned} N_m(x) &= \int_{-\infty}^{\infty} N_{m-1}(x-t) N_0(t) dt \\ &= \int_0^1 N_{m-1}(x-t) dt \end{aligned} \quad (3.30)$$

with the Fourier transform

$$\hat{N}_m(\omega) = (2\pi)^{-1/2} e^{-i\varrho\xi/2} \left(\frac{\sin(\xi/2)}{\xi/2} \right)^{m+1}$$

where $\varrho = 0$ if m is odd and $\varrho = 1$ if m is even. For even m , $\phi = N_m$ is symmetric around $x = 1/2$, for odd m , around $x = 0$. Except for $m = 0$ the scaling functions constitute a Riesz basis, but they are not orthonormal. To apply the orthonormalization of Eq.(3.26), Daubechies [25] has shown that

$$2\pi \sum_{k=-\infty}^{\infty} |\hat{N}_m(2x + 2\pi k)|^2 = -\frac{\sin^{2m+2}(x)}{(2m+1)!} \frac{d^{2m+1}}{dx^{2m+1}} \cot(x)$$

The result of the orthonormalization is that support of the $\phi^\perp = \mathbb{R} = \text{support of the } \psi$ for all the Battle-Lemarie wavelets. The "orthonormalized" ϕ^\perp has the same symmetry axis as ϕ . The symmetry axis of ψ always lies at $x = 1/2$. (For m even, ψ is antisymmetric around this axis, for m odd, ψ is symmetric). Even though the supports of ϕ^\perp and ψ equal the whole \mathbb{R} , ϕ^\perp and ψ still have very good (exponential) decay

$$|\phi^\perp, \psi(x)| \leq C e^{-\gamma|x|}, x \in \mathbb{R}$$

The Battle-Lemarie wavelets based on the m -th order cardinal B-splines belong to C^k with $k \leq m - 1$ and have m vanishing moments: $\int dx x^l \psi(x) = 0$ for $l=0,1,\dots,m$ for $\psi^{(l)}$ bounded for $l \leq m$. It is impossible for orthonormal ψ , to have exponential decay and to belong to C^∞ , with all derivatives bounded, unless $\psi \equiv 0$. As a result, to achieve fast (exponential) decay, only a finite number k of derivatives can be continuous. The decay rate decreases as k increases. On the contrary, the Meyer wavelet, which is C^∞ , decays faster than any inverse polynomial, but not exponentially fast.

In the general case, $\phi = N_m$, the ϕ satisfies $\int dx \phi(x) = 1$ and

$$\phi(x) = \begin{cases} 2^{-2n} \sum_{j=0}^{2n+1} \binom{2n+1}{j} \phi(2x - n - 1 + j), & m = 2n = \text{even} \\ 2^{-2n-1} \sum_{j=0}^{2n+2} \binom{2n+2}{j} \phi(2x - n - 1 + j), & m = 2n + 1 = \text{odd} \end{cases}$$

If we choose ϕ to be the 0-th order cardinal spline,

$$\phi(x) = \begin{cases} 1 & 0 \leq x \leq 1 \\ 0 & \text{elsewhere} \end{cases}$$

and we follow the previous steps, we end up with the Haar basis

$$\psi(x) = \begin{cases} 1 & 0 \leq x \leq 1/2 \\ -1 & -1/2 \leq x \leq 1/2 \\ 0 & \text{elsewhere} \end{cases}$$

No orthonormalization is needed since ϕ is orthogonal to its translations.

Choosing the piecewise linear spline ($m=1$) as the scaling function,

$$\phi(x) = \begin{cases} 1 - |x| & 0 \leq |x| \leq 1 \\ 0 & \text{elsewhere} \end{cases}$$

it satisfies

$$\phi(x) = 0.5\phi(2x + 1) + \phi(2x) + 0.5\phi(2x - 1) \quad (3.31)$$

and its Fourier transform is

$$\hat{\phi}(\xi) = (2\pi)^{-1/2} e^{-i\xi/2} \left(\frac{\sin \xi/2}{\xi/2} \right)^2$$

It can be observed that

$$2\pi \sum_{l \in \mathbb{Z}} |\hat{\phi}(\xi + 2\pi l)|^2 = \frac{2}{3} + \frac{1}{3} \cos \xi = \frac{1}{3} (1 + 2\cos^2(\xi/2))$$

Since ϕ is not orthogonal to its translates, it is needed to apply the orthogonalization trick described above. The orthonormalized scaling function is given by

$$\hat{\phi}^\perp(\xi) = \sqrt{3}(2\pi)^{-1/2} \frac{4\sin^2(\xi/2)}{\xi^2 [1 + 2\cos^2(\xi/2)]^{1/2}}$$

The ϕ^\perp is not compactly supported unlike ϕ itself. The corresponding m_0^\perp is

$$\hat{m}_0^\perp(\xi) = \cos^2(\xi/2) \left[\frac{1 + 2\cos^2(\xi/2)}{1 + 2\cos^2(\xi)} \right]^{1/2}$$

and the wavelet ψ is given by

$$\hat{\psi}(\xi) = e^{i\xi/2} \sin^2(\xi/4) \left[\frac{1 + 2\sin^2(\xi/4)}{1 + 2\cos^2(\xi/2)} \right]^{1/2} \hat{\phi}^\perp(\xi/2) \quad (3.32)$$

$$= \sqrt{3} e^{i\xi/2} \sin^2(\xi/4) \left[\frac{1 + 2\sin^2(\xi/4)}{(1 + 2\cos^2(\xi/2))(1 + 2\cos^2(\xi/4))} \right]^{1/2} \hat{\phi}(\xi/2) \quad (3.33)$$

The choice of the scaling function for the development of the new Time-Domain MRTD scheme is the cubic cardinal spline ($m = 3$). After orthonormalization, the spectral expressions of the scaling and the wavelet functions are

$$\hat{\phi}^\perp(\xi) = (2\pi)^{-1/2} \left(\frac{\sin(\frac{\xi}{2})}{\frac{\xi}{2}} \right)^4 \frac{1}{\sqrt{1 - \frac{4}{3}\sin^2(\frac{\xi}{2}) + \frac{2}{5}\sin^4(\frac{\xi}{2}) - \frac{4}{315}\sin^6(\frac{\xi}{2})}} \quad (3.34)$$

and

$$\hat{\psi}^\perp(\xi) = e^{i\xi/2} \frac{\hat{\phi}^\perp(\xi + 2\pi)}{\hat{\phi}^\perp(\xi/2 + \pi)} \hat{\phi}^\perp(\xi/2) = \hat{\psi}_0(\xi) \quad (3.35)$$

The Cubic Spline Battle-Lemarie Scaling and Wavelet functions are plotted in (Figs.3.1–3.2) in Spatial Domain and in (Figs.3.3–3.4) in Spectral Domain.

3.4 The 2D MRTD scheme

For simplicity, the 2D MRTD scheme is analyzed for a homogeneous lossless medium with the permittivity ϵ and the permeability μ . Assuming no variation along the y-direction, the Maxwell's equations for the two-dimensional TM^z mode [62] can be written as:

$$\frac{\partial E_x}{\partial t} = -\frac{1}{\epsilon} \frac{\partial H_y}{\partial z} \quad (3.36)$$

$$\frac{\partial H_y}{\partial t} = \frac{1}{\mu} \left(\frac{\partial E_z}{\partial x} - \frac{\partial E_x}{\partial z} \right) \quad (3.37)$$

$$\frac{\partial E_z}{\partial t} = \frac{1}{\epsilon} \frac{\partial H_y}{\partial x} \quad (3.38)$$

To derive the 2D MRTD Scheme, the electric and magnetic field components incorporated in these equations are expanded in a series of Battle-Lemarie scaling and wavelet functions in both x- and z-directions and in pulse functions in time.

$$E_x(x, z, t) = \sum_{k,l,m=-\infty}^{+\infty} {}_k E_{l-1/2,m}^{x,\phi\phi} h_k(t) \phi_{l-1/2}(x) \phi_m(z)$$

$$\begin{aligned}
& + \sum_{k,l,m=-\infty}^{+\infty} \sum_{r_z=0}^{+\infty} \sum_{p_z=0}^{2^{r_z}-1} k E_{l-1/2,m}^{x,\phi\psi_{r_z,p_z}} h_k(t) \phi_{l-1/2}(x) \psi_{m,p_z}^{r_z}(z) \\
& + \sum_{k,l,m=-\infty}^{+\infty} \sum_{r_x=0}^{+\infty} \sum_{p_x=0}^{2^{r_x}-1} k E_{l-1/2,m}^{x,\psi_{r_x,p_x}\phi} h_k(t) \psi_{l-1/2,p_x}^{r_x}(x) \phi_m(z) \\
& + \sum_{k,l,m=-\infty}^{+\infty} \sum_{r_x,r_z=0}^{+\infty} \sum_{p_x,p_z=0}^{2^{r_x,r_z}-1} k E_{l-1/2,m}^{x,\psi_{r_x,p_x}\psi_{r_z,p_z}} h_k(t) \psi_{l-1/2,p_x}^{r_x}(x) \psi_{m,p_z}^{r_z}(z) \\
E_z(x, z, t) = & \sum_{k,l,m=-\infty}^{+\infty} k E_{l,m-1/2}^{z,\phi\phi} h_k(t) \phi_l(x) \phi_{m-1/2}(z) \\
& + \sum_{k,l,m=-\infty}^{+\infty} \sum_{r_z=0}^{+\infty} \sum_{p_z=0}^{2^{r_z}-1} k E_{l,m-1/2}^{z,\phi\psi_{r_z,p_z}} h_k(t) \phi_l(x) \psi_{m-1/2,p_z}^{r_z}(z) \\
& + \sum_{k,l,m=-\infty}^{+\infty} \sum_{r_x=0}^{+\infty} \sum_{p_x=0}^{2^{r_x}-1} k E_{l,m-1/2}^{z,\psi_{r_x,p_x}\phi} h_k(t) \psi_{l,p_x}^{r_x}(x) \phi_{m-1/2}(z) \\
& + \sum_{k,l,m=-\infty}^{+\infty} \sum_{r_x,r_z=0}^{+\infty} \sum_{p_x,p_z=0}^{2^{r_x,r_z}-1} k E_{l,m-1/2}^{z,\psi_{r_x,p_x}\psi_{r_z,p_z}} h_k(t) \psi_{l,p_x}^{r_x}(x) \psi_{m-1/2,p_z}^{r_z}(z) \\
H_y(x, z, t) = & \sum_{k,l,m=-\infty}^{+\infty} k_{+1/2} H_{l-1/2,m-1/2}^{y,\phi\phi} h_{k+1/2}(t) \phi_{l-1/2}(x) \phi_{m-1/2}(z) \\
& + \sum_{k,l,m=-\infty}^{+\infty} \sum_{r_z=0}^{+\infty} \sum_{p_z=0}^{2^{r_z}-1} k_{+1/2} H_{l-1/2,m-1/2}^{y,\phi\psi_{r_z,p_z}} h_{k+1/2}(t) \phi_{l-1/2}(x) \psi_{m-1/2,p_z}^{r_z}(z) \\
& + \sum_{k,l,m=-\infty}^{+\infty} \sum_{r_x=0}^{+\infty} \sum_{p_x=0}^{2^{r_x}-1} k_{+1/2} H_{l-1/2,m-1/2}^{y,\psi_{r_x,p_x}\phi} h_{k+1/2}(t) \psi_{l-1/2,p_x}^{r_x}(x) \phi_{m-1/2}(z) \\
& + \sum_{k,l,m=-\infty}^{+\infty} \sum_{r_x,r_z=0}^{+\infty} \sum_{p_x,p_z=0}^{2^{r_x,r_z}-1} k_{+1/2} H_{l-1/2,m-1/2}^{y,\psi_{r_x,p_x}\psi_{r_z,p_z}} h_{k+1/2}(t) \psi_{l-1/2,p_x}^{r_x}(x) \psi_{m-1/2,p_z}^{r_z}(z) \quad , \\
\end{aligned} \tag{3.39}$$

where $\phi_n(x) = \phi(\frac{x}{\Delta x} - n)$ and $\psi_{n,p}^r(x) = 2^{r/2} \psi_0(2^r[\frac{x}{\Delta x} - n] - p)$ represent the Battle-Lemarie scaling and r-resolution wavelet function respectively. The expressions of the scaling and the 0-resolution wavelet in the spectral domain are given in Eqs.(3.34)–(3.35). Since higher resolutions of wavelets are shifted and dilated versions of the 0-resolution, their domain will be a fraction of that of the 0-resolution wavelet; thus there are going to be more than one higher resolution wavelet coefficients for each MRTD cell. Specifically, for the the arbitrary r-resolution and for the n-cell to the x-direction, there exist 2^r wavelet

coefficients located at $\frac{x}{\Delta x} = n + \frac{p}{2^{r+1}}$, $p = 0, \dots, 2^r - 1$. This is the reason for the summation of the p terms for each resolution r in the expansion of Eq.(39). ${}_k E_{l,m}^{\kappa,\mu\nu}$ and ${}_{k+1/2} H_{l,m}^{\kappa,\mu\nu}$ with $\kappa = x, y, z$ and $\mu, \nu = \phi, \psi$ are the coefficients for the field expansions in terms of scaling and wavelet functions. The indices l, m and k are the discrete space and time indices related to the space and time coordinates via $x = l\Delta x, z = m\Delta z$ and $t = k\Delta t$, where $\Delta x, \Delta z$ are the space discretization intervals in x - and z -direction and Δt is the time discretization interval. For an accuracy of 0.1% the above summations are truncated to a finite number of terms determined by the dispersion and stability requirements (typically between 22-26). The time-domain expansion function $h_k(t)$ is defined as

$$h_k(t) = h\left(\frac{t}{\Delta t} - k\right) \quad (3.40)$$

with the rectangular pulse function

$$h(t) = \begin{cases} 1 & \text{for } |x| < 1/2 \\ 1/2 & \text{for } |x| = 1/2 \\ 0 & \text{for } |x| > 1/2 \end{cases} .$$

The magnetic field components are shifted by half a discretization interval in space and time-domain with respect to the electric field components (leap-frog).

Upon inserting the field expansions, Maxwell's equations are sampled using pulse functions as time-domain test functions and scaling/wavelet functions as space-domain test-functions. For the sampling in time-domain, the following integrals are utilized

$$\int_{-\infty}^{+\infty} h_k(t) h_{k'}(t) dt = \delta_{k,k'} \Delta x \quad (3.41)$$

and

$$\int_{-\infty}^{+\infty} h_k(t) \frac{\partial h_{k'+1/2}(t)}{\partial t} dt = \delta_{k,k'} - \delta_{k,k'+1} \quad (3.42)$$

where $\delta_{k,k'}$ is the Kroenecker symbol,

$$\delta_{k,k'} = \begin{cases} 1 & \text{for } k = k' \\ 0 & \text{for } k \neq k' \end{cases} .$$

Sampling in space-domain is obtained by use of the orthogonality relationships for the scaling and for the wavelet functions [25]

$$\int_{-\infty}^{+\infty} \phi_m(x) \phi_{m'}(x) dx = \delta_{m,m'} \Delta x, \quad (3.43)$$

$$\int_{-\infty}^{+\infty} \phi_m(x) \psi_{m',p'}^r(x) dx = 0, \quad \forall r, p \quad (3.44)$$

and

$$\int_{-\infty}^{+\infty} \psi_{m,p}^r(x) \psi_{m',p'}^r(x) dx = \delta_{r,r'} \delta_{m,m'} \delta_{m,m'} \Delta x \quad (3.45)$$

The integrals containing derivatives can be approximated by the following expressions:

$$\int_{-\infty}^{+\infty} \phi_m(x) \frac{\partial \phi_{m'+1/2}(x)}{\partial x} dx \approx \sum_{i=-n_a}^{n_a-1} a(i) \delta_{m+i,m'} \quad (3.46)$$

with

$$a(i) = \frac{1}{\pi} \int_0^{\infty} |\hat{\phi}(\xi)|^2 \xi \sin[\xi(i+1/2)] d\xi, \quad (3.47)$$

$$\int_{-\infty}^{+\infty} \phi_m(x) \frac{\partial \psi_{m'+1/2,p}^r(x)}{\partial x} dx \approx \sum_{i=-n_{d,r,1}}^{n_{d,r,2}} d_r(i,p) \delta_{m+i,m'} \quad (3.48)$$

with

$$d_r(i, p) = \frac{1}{\pi} \int_0^\infty 2^{-r/2} \hat{\phi}_m(\xi) |\hat{\psi}_0(\xi/2^r)| \xi \sin[\xi (i + 0.5 + p/2^r + 1/2^{r+1})] d\xi \quad , \quad (3.49)$$

$$\int_{-\infty}^{+\infty} \psi_{m,p}^r(x) \frac{\partial \phi_{m'+1/2}(x)}{\partial x} dx \approx \sum_{i=-n_{c,r,1}}^{n_{c,r,2}} c_r(i, p) \delta_{m+i, m'} \quad (3.50)$$

with

$$c_r(i, p) = \frac{1}{\pi} \int_0^\infty 2^{-r/2} \hat{\phi}_m(\xi) |\hat{\psi}_0(\xi/2^r)| \xi \sin[\xi (i + 0.5 - p/2^r - 1/2^{r+1})] d\xi \quad , \quad (3.51)$$

$$\int_{-\infty}^{+\infty} \psi_{m,p_1}^{r_1}(x) \frac{\partial \psi_{m'+1/2, p_2}^{r_2}(x)}{\partial x} dx \approx \sum_{i=-n_{b,r_1,r_2,1}}^{n_{b,r_1,r_2,2}} b_{r_1,r_2}(i, p_1, p_2) \delta_{m+i, m'} \quad (3.52)$$

with

$$b_{r_1,r_2}(i, p_1, p_2) = \int_0^\infty |\hat{\psi}_0(\xi/2^{r_1})| |\hat{\psi}_0(\xi/2^{r_2})| \xi \sin[\xi (i + 1/2 + p_2/2^{r_2} - p_1/2^{r_1} + 1/2^{r_2+1} - 1/2^{r_1+1})] d\xi \quad (3.53)$$

For the rest of the MRTD Technique description, an expansion only in a series of scaling and 0-resolution wavelet functions will be considered. Hints for the enhancement of additional wavelet resolutions will be presented where needed. Since for the 0-resolution ($r = 0$) there is only one wavelet coefficient per cell ($p = 0$), the p symbols will be omitted from the definition of the b, c, d coefficients, which will be given by

$$\int_{-\infty}^{+\infty} \psi_m^0(x) \frac{\partial \phi_{m'+1/2}(x)}{\partial x} dx \approx \sum_{i=-n_{c,0,1}}^{n_{c,0,2}} c_0(i) \delta_{m+i, m'} \quad (3.54)$$

with

$$c_0(i) = \frac{1}{\pi} \int_0^\infty \hat{\phi}_m(\xi) |\hat{\psi}_0(\xi)| \xi \sin[\xi i] d\xi \quad , \quad (3.55)$$

$$\int_{-\infty}^{+\infty} \phi_m(x) \frac{\partial \psi_{m'+1/2}^0(x)}{\partial x} dx \approx \sum_{i=-n_{d,0,1}}^{n_{d,0,2}} d_0(i) \delta_{m+i, m'} \quad (3.56)$$

with

$$d_0(i) = \int_0^{\infty} \hat{\phi}_m(\xi) |\hat{\psi}_0(\xi)| \xi \sin(\xi i + 1) d\xi = c_0(i + 1) \quad (3.57)$$

Thus, eq.(3.56) can be written as

$$\int_{-\infty}^{+\infty} \phi_m(x) \frac{\partial \psi_{0,m'+1/2}(x)}{\partial x} dx \approx \sum_{i=-n_{c,0,1}-1}^{n_{c,0,2}-1} c_0(i + 1) \delta_{m+i,m'} \quad (3.58)$$

$$\int_{-\infty}^{+\infty} \psi_m^0(x) \frac{\partial \psi_{m'+1/2}^0(x)}{\partial x} dx \approx \sum_{i=-n_{b,0,0,1}}^{n_{b,0,0,2}} b_0(i) \delta_{m+i,m'} \quad (3.59)$$

with

$$b_0(i) = b_{0,0}(i) = \int_0^{\infty} |\hat{\psi}_0(\xi)|^2 \xi \sin[\xi(i + 1/2)] d\xi \quad (3.60)$$

with $a(i)$, $b_0(i)$, $c_0(i)$ given in Table (3.1) [26]. Due to symmetries in the integrals for the 0-resolution, the coefficients satisfy the conditions: $a(-1 - i) = -a(i)$, $b_0(-1 - i) = -b_0(i)$ and $c_0(-i) = -c_0(i)$ for $i < 0$. Hence, the stencil lengths have to be: $n_{b,0,0,1} = n_{b,0,0,2} - 1 = n_b$ and $n_{c,0,1} = n_{c,0,2} = n_c$. These conditions are not general and do not hold for any other arbitrary resolution. The stencil size is determined by the dispersion requirements. It has to be noted that the Battle-Lemarie scaling function has exponential decay; thus, the coefficients $a(i)$ for $i > 12$ are not zero, but their value is negligible ($\leq 10^{-4}$).

After applying the Galerkin technique to Eqs.(3.36)–(3.38), the following MRTD equations are derived:

$$\begin{aligned} \frac{{}^{k+1}E_{i-1/2,j}^{x,\phi\phi} - {}^kE_{i-1/2,j}^{x,\phi\phi}}{\Delta t} &= - \frac{1}{\epsilon \Delta z} \left(\sum_{j'=-n_a}^{n_a-1} a(j') {}^{k+1/2}H_{i-1/2,j+j'+1-1/2}^{y,\phi\phi} \right. \\ &\quad \left. + \sum_{j'=-n_c}^{n_c} c_0(j') {}^{k+1/2}H_{i-1/2,j+j'-1/2}^{y,\phi\psi_0} \right) \\ \frac{{}^{k+1}E_{i-1/2,j}^{x,\psi_0\phi} - {}^kE_{i-1/2,j}^{x,\psi_0\phi}}{\Delta t} &= - \frac{1}{\epsilon \Delta z} \left(\sum_{j'=-n_a}^{n_a-1} a(j') {}^{k+1/2}H_{i-1/2,j+j'+1-1/2}^{z,\psi_0\phi} \right) \end{aligned}$$

i	$a(i)$	$b_0(i)$	$c_0(i)$
0	1.29161604157839	2.47253977327429	0.
1	-0.155978843323672	0.9562282774123074	-4.659725793402785E-02
2	5.9606303324687290E-02	0.1660591600788887	5.453939813583327E-02
3	-2.929157759806890E-02	9.392437777679437E-02	-3.699957746974982E-02
4	1.5362399457426780E-02	3.141444475216036E-03	2.057449098775452E-02
5	-8.184462325283712E-03	1.349356908709108E-02	-1.115303180864957E-02
6	4.3757585552354830E-03	-2.858941810094752E-03	5.976877725279031E-03
7	-2.342365356649461E-03	2.778680514115529E-03	-3.202621363952005E-03
8	1.252877717042020E-03	-1.129446167303586E-03	1.714086849566890E-03
9	-6.716635068590737E-04	7.071507309377701E-04	-9.176508438494196E-04
10	3.583506907489797E-04	-3.491267305845643E-04	4.911754748072018E-04
11	-1.931321684715780E-04	1.952711419194906E-04	-2.629253013538502E-04
12	1.019327767057869E-04	-1.021304423384722E-04	1.407386855875626E-04
13	-5.613943183518454E-05	5.531259273864269E-05	-7.533840689573666E-05
14	2.834596805928539E-05	-2.947330468694831E-05	4.033146235099674E-05
15	-1.700348604873522E-05	1.572110653438641E-05	-2.159462850665844E-05

Table 3.1: Coefficients $a(i)$, $b_0(i)$, $c_0(i)$

$$\begin{aligned}
& + \sum_{j'=-n_c}^{n_c} c_0(j')_{k+1/2} H_{i-1/2, j+j'-1/2}^{y, \psi_0 \psi_0} \\
\frac{k+1 E_{i-1/2, j}^{x, \phi \psi_0} - k E_{i-1/2, j}^{x, \phi \psi_0}}{\Delta t} &= - \frac{1}{\epsilon \Delta z} \left(\sum_{j'=-n_c}^{n_c} c_0(j')_{k+1/2} H_{i-1/2, j+j'+1-1/2}^{y, \phi \phi} \right. \\
& + \sum_{j'=-n_b}^{n_b-1} b_0(j')_{k+1/2} H_{i-1/2, j+j'+1-1/2}^{y, \phi \psi_0} \left. \right) \\
\frac{k+1 E_{i-1/2, j}^{x, \psi_0 \psi_0} - k E_{i-1/2, j}^{x, \psi_0 \psi_0}}{\Delta t} &= - \frac{1}{\epsilon \Delta z} \left(\sum_{j'=-n_c}^{n_c} c_0(j')_{k+1/2} H_{i-1/2, j+j'+1-1/2}^{y, \psi_0 \phi} \right. \\
& + \sum_{j'=-n_b}^{n_b-1} b_0(j')_{k+1/2} H_{i-1/2, j+j'+1-1/2}^{y, \psi_0 \psi_0} \left. \right) \\
\frac{k+1 E_{i, j-1/2}^{z, \phi \phi} - k E_{i, j-1/2}^{z, \phi \phi}}{\Delta t} &= \frac{1}{\epsilon \Delta x} \left(\sum_{i'=-n_a}^{n_a-1} a(i')_{k+1/2} H_{i+i'+1-1/2, j-1/2}^{y, \phi \phi} \right. \\
& + \sum_{i'=-n_c}^{n_c} c_0(i')_{k+1/2} H_{i+i'-1/2, j-1/2}^{y, \psi_0 \phi} \left. \right) \\
\frac{k+1 E_{i, j-1/2}^{z, \phi \psi_0} - k E_{i, j-1/2}^{z, \phi \psi_0}}{\Delta t} &= \frac{1}{\epsilon \Delta x} \left(\sum_{i'=-n_a}^{n_a-1} a(i')_{k+1/2} H_{i+i'+1-1/2, j-1/2}^{y, \phi \psi_0} \right. \\
& + \sum_{i'=-n_c}^{n_c} c_0(i')_{k+1/2} H_{i+i'-1/2, j-1/2}^{y, \psi_0 \psi_0} \left. \right) \\
\frac{k+1 E_{i, j-1/2}^{z, \psi_0 \phi} - k E_{i, j-1/2}^{z, \psi_0 \phi}}{\Delta t} &= \frac{1}{\epsilon \Delta x} \left(\sum_{i'=-n_c}^{n_c} c_0(i')_{k+1/2} H_{i+i'+1-1/2, j-1/2}^{y, \phi \phi} \right. \\
& + \sum_{i'=-n_b}^{n_b-1} b_0(i')_{k+1/2} H_{i+i'+1-1/2, j-1/2}^{y, \psi_0 \phi} \left. \right) \\
\frac{k+1 E_{i, j-1/2}^{z, \psi_0 \psi_0} - k E_{i, j-1/2}^{z, \psi_0 \psi_0}}{\Delta t} &= \frac{1}{\epsilon \Delta x} \left(\sum_{i'=-n_c}^{n_c} c_0(i')_{k+1/2} H_{i+i'+1-1/2, j-1/2}^{y, \phi \psi_0} \right. \\
& + \sum_{i'=-n_b}^{n_b-1} b_0(i')_{k+1/2} H_{i+i'+1-1/2, j-1/2}^{y, \psi_0 \psi_0} \left. \right) \quad (3.61)
\end{aligned}$$

$$\begin{aligned}
\frac{k+1/2 H_{i-1/2, j-1/2}^{y, \phi \phi} - k-1/2 H_{i-1/2, j-1/2}^{y, \phi \phi}}{\Delta t} &= \frac{1}{\mu} \left[\frac{1}{\Delta x} \left(\sum_{i'=-n_a}^{n_a-1} a(i')_k E_{i+i', j-1/2}^{z, \phi \phi} \right. \right. \\
& + \sum_{i'=-n_c}^{n_c} c_0(i')_k E_{i+i'-1, j-1/2}^{z, \psi_0 \phi} \left. \right) - \frac{1}{\Delta z} \left(\sum_{j'=-n_a}^{n_a-1} a(j')_k E_{i-1/2, j+j'}^{x, \phi \phi} + \sum_{j'=-n_c}^{n_c} c_0(j')_k E_{i-1/2, j+j'-1}^{x, \phi \psi_0} \right) \left. \right] \\
\frac{k+1/2 H_{i-1/2, j-1/2}^{y, \psi_0 \phi} - k-1/2 H_{i-1/2, j-1/2}^{y, \psi_0 \phi}}{\Delta t} &= \frac{1}{\mu} \left[\frac{1}{\Delta x} \left(\sum_{i'=-n_c}^{n_c} c_0(i')_k E_{i+i', j-1/2}^{z, \phi \phi} \right. \right. \\
& + \sum_{i'=-n_b}^{n_b-1} b_0(i')_k E_{i+i', j-1/2}^{z, \psi_0 \phi} \left. \right) - \frac{1}{\Delta z} \left(\sum_{j'=-n_a}^{n_a-1} a(j')_k E_{i-1/2, j+j'}^{x, \psi_0 \phi} + \sum_{j'=-n_c}^{n_c} c_0(j')_k E_{i-1/2, j+j'-1}^{x, \psi_0 \psi_0} \right) \left. \right]
\end{aligned}$$

$$\begin{aligned}
\frac{k+1/2 H_{i-1/2,j-1/2}^{y,\phi\psi_0} - k-1/2 H_{i-1/2,j-1/2}^{y,\phi\psi_0}}{\Delta t} &= \frac{1}{\mu} \left[\frac{1}{\Delta x} \left(\sum_{i'=-n_a}^{n_a-1} a(i')_k E_{i+i',j-1/2}^{z,\phi\psi_0} \right. \right. \\
&\quad \left. \left. + \sum_{i'=-n_c}^{n_c} c_0(i')_k E_{i+i'-1,j-1/2}^{z,\psi_0\psi_0} \right) - \frac{1}{\Delta z} \left(\sum_{j'=-n_c}^{n_c} c_0(j')_k E_{i-1/2,j+j'}^{x,\phi\phi} + \sum_{j'=-n_b}^{n_b-1} b_0(j')_k E_{i-1/2,j+j'}^{x,\phi\psi_0} \right) \right] \\
\frac{k+1/2 H_{i-1/2,j-1/2}^{y,\psi_0\psi_0} - k-1/2 H_{i-1/2,j-1/2}^{y,\psi_0\psi_0}}{\Delta t} &= \frac{1}{\mu} \left[\frac{1}{\Delta x} \left(\sum_{i'=-n_c}^{n_c} c_0(i')_k E_{i+i',j-1/2}^{z,\phi\psi_0} \right. \right. \\
&\quad \left. \left. + \sum_{i'=-n_b}^{n_b-1} b_0(i')_k E_{i+i',j-1/2}^{z,\psi_0\psi_0} \right) - \frac{1}{\Delta z} \left(\sum_{j'=-n_c}^{n_c} c_0(j')_k E_{i-1/2,j+j'}^{x,\psi_0\phi} + \sum_{j'=-n_b}^{n_b-1} b_0(j')_k E_{i-1/2,j+j'}^{x,\psi_0\psi_0} \right) \right]
\end{aligned} \tag{3.62}$$

The indices i, j and k are the discrete space and time indices related to the space and time coordinates via $x = i\Delta x, z = j\Delta z$ and $t = k\Delta t$, where $\Delta x, \Delta z$ are the space discretization intervals in x- and z-direction and Δt is the time discretization interval. The values of the stencil lengths n_a, n_b, n_c depends on the accuracy and dispersion requirements.

3.4.1 Modeling of Hard Boundaries

Unlike the FDTD where the consistency with the image theory is implicit in the application of the boundary conditions, for MRTD schemes based on entire-domain functions this theory must be applied explicitly in the locations of Perfect Electric (PEC) or Magnetic Conductors (PMC). The total value of a field component at a specific cell is affected by a theoretically infinite - practically finite - number of neighboring cells due to the fact that the basis functions extend from $-\infty$ to ∞ . Some of these neighbors may be located on the other side of the conductor. This effect is taken into consideration by applying the image theory (Fig.3.5). In this way, the physical boundary condition of zeroing-out the E-field tangential to the PEC is automatically satisfied. For example, even symmetry is applied for the normal-to-PEC electric field components and odd symmetry for the parallel-to-PEC. Image Theory can be implemented automatically for an arbitrary number of hard boundaries.

The time-domain numerical techniques are modeling the real space by creating a discrete numerical grid. Sometimes, this mesh does not coincide with the electrical one and MRTD is one example. The enhancement of wavelets on MRTD requires a special treatment of the wavelet components of the normal-to-PEC electric field. Assuming a vertical PEC in (Fig.3.6), the electrical domains (I) and (II) are isolated from each other. That means that one wavelet component value of the normal electric field EXACTLY ON the PEC would create a non-physical electrical coupling. Thus, TWO wavelet components, one located infinitesimally left of the PEC and the other infinitesimally right of the PEC, have to be defined in order to satisfy the electrical isolation condition. The H-field component that is parallel to the PEC has to be treated in a similar way. The rest components of the E- and H-field have to be zeroed-out on both sides of the PEC, so one value is sufficient. In FDTD the interleaved positioning of the field components on the Yee's cell (which are the same with the scaling functions components on the MRTD's cell) requires that the normal-to-PEC E-field component is located half cell size away from the conductor. In this way, the definition of only one field component per cell is sufficient.

3.4.2 Modeling of Excitation

Without loss of generality, the modeling of the excitation for the 2D and 2.5D MRTD is presented. The 3D algorithm is a direct extension of the 2D. For simplicity, only 0-resolution wavelets are used.

In order to apply a point (pulse) excitation $P(x_o, z_o)$ for $x_o = m\Delta x, z_o = n\Delta z$, the pulse has to be decomposed in terms of scaling and wavelet functions

$$P(x_o, z_o) = \sum_{l_{x,\phi}=-\infty}^{\infty} \sum_{l_{z,\phi}=-\infty}^{\infty} c_{\phi\phi}(l_{x,\phi}, l_{z,\phi}) \phi(m + l_{x,\phi}) \phi(n + l_{z,\phi})$$

$$\begin{aligned}
& + \sum_{l_{x,\phi}=-\infty}^{\infty} \sum_{l_{z,\psi}=-\infty}^{\infty} c_{\phi\psi}(l_{x,\phi}, l_{z,\psi}) \phi(m + l_{x,\phi}) \psi(n + l_{z,\psi}) \\
& + \sum_{l_{x,\psi}=-\infty}^{\infty} \sum_{l_{z,\phi}=-\infty}^{\infty} c_{\psi\phi}(l_{x,\psi}, l_{z,\phi}) \psi(m + l_{x,\psi}) \phi(n + l_{z,\phi}) \\
& + \sum_{l_{x,\psi}=-\infty}^{\infty} \sum_{l_{z,\psi}=-\infty}^{\infty} c_{\psi\psi}(l_{x,\psi}, l_{z,\psi}) \psi(m + l_{x,\psi}) \psi(n + l_{z,\psi}) \quad . \quad (3.63)
\end{aligned}$$

with

$$\begin{aligned}
c_{\phi\phi}(l_{x,\phi}, l_{z,\phi}) & = \int_{m-0.5}^{m+0.5} \int_{n-0.5}^{n+0.5} \phi(m + l_{x,\phi}) \phi(n + l_{z,\phi}) dz dx \\
c_{\phi\psi}(l_{x,\phi}, l_{z,\psi}) & = \int_{m-0.5}^{m+0.5} \int_{n-0.5}^{n+0.5} \phi(m + l_{x,\phi}) \psi(n + l_{z,\psi}) dz dx \\
c_{\psi\phi}(l_{x,\psi}, l_{z,\phi}) & = \int_{m-0.5}^{m+0.5} \int_{n-0.5}^{n+0.5} \psi(m + l_{x,\psi}) \phi(n + l_{z,\phi}) dz dx \\
c_{\psi\psi}(l_{x,\psi}, l_{z,\psi}) & = \int_{m-0.5}^{m+0.5} \int_{n-0.5}^{n+0.5} \psi(m + l_{x,\psi}) \psi(n + l_{z,\psi}) dz dx \quad . \quad (3.64)
\end{aligned}$$

Practically, the summations of Eq.(3.63) can be truncated to a finite number of terms.

Usually 6-8 terms on each side of the excitation point per direction can offer an accuracy of representation close to 0.1%. In case the neighboring scaling or wavelet functions are located outside the computational domain (e.g. $m + l_{x,\phi} > n_x$ or $m + l_{x,\phi} < 0$ for a domain $[0, n_x]$ to the x-direction), image theory has to be applied for their translation inside the computational grid.

If there is no discontinuity (hard boundary or dielectric interface) in the summation interval of Eq.(3.63), the double integrals of Eq.(3.64) can be split in two single integrals

$$\begin{aligned}
c_{\phi\phi}(l_{x,\phi}, l_{z,\phi}) & = \int_{m-0.5}^{m+0.5} \phi(m + l_{x,\phi}) dx \int_{n-0.5}^{n+0.5} \phi(n + l_{z,\phi}) dz = c_{\phi}(l_{x,\phi}) c_{\phi}(l_{z,\phi}) \\
c_{\phi\psi}(l_{x,\phi}, l_{z,\psi}) & = \int_{m-0.5}^{m+0.5} \phi(m + l_{x,\phi}) dx \int_{n-0.5}^{n+0.5} \psi(n + l_{z,\psi}) dz = c_{\phi}(l_{x,\phi}) c_{\psi}(l_{z,\psi}) \\
c_{\psi\phi}(l_{x,\psi}, l_{z,\phi}) & = \int_{m-0.5}^{m+0.5} \psi(m + l_{x,\psi}) dx \int_{n-0.5}^{n+0.5} \phi(n + l_{z,\phi}) dz = c_{\psi}(l_{x,\psi}) c_{\phi}(l_{z,\phi}) \\
c_{\psi\psi}(l_{x,\psi}, l_{z,\psi}) & = \int_{m-0.5}^{m+0.5} \psi(m + l_{x,\psi}) dx \int_{n-0.5}^{n+0.5} \psi(n + l_{z,\psi}) dz = c_{\psi}(l_{x,\psi}) c_{\psi}(l_{z,\psi}) \quad ,
\end{aligned}$$

with c_{ϕ}, c_{ψ} given in Tables (3.2)–(3.3).

Due to the symmetries of the Battle-Lemarie scaling and wavelet functions, the decomposition coefficients have to satisfy the following conditions

$$c_\phi(l_\phi) = c_\phi(-l_\phi), \quad l_\phi = -1, -2, ..$$

$$c_\psi(l_\psi) = c_\psi(1 - l_\psi), \quad l_\psi = 0, -1, -2, ..$$

For each time-step, the excitation scaling and wavelet components have to be superimposed to the respective field values obtained by the MRTD algorithm in order to provide a transparent source similar to that described in Ch.2.

$${}^k E_{m+l_x, \phi, n+l_z, \phi}^{\phi\phi, total} = {}^k E_{m+l_x, \phi, n+l_z, \phi}^{\phi\phi} + c_{\phi\phi}(l_x, \phi, l_z, \phi)$$

$${}^k E_{m+l_x, \phi, n+l_z, \psi}^{\phi\psi, total} = {}^k E_{m+l_x, \phi, n+l_z, \psi}^{\phi\psi} + c_{\phi\psi}(l_x, \phi, l_z, \psi)$$

$${}^k E_{m+l_x, \psi, n+l_z, \phi}^{\psi\phi, total} = {}^k E_{m+l_x, \psi, n+l_z, \phi}^{\psi\phi} + c_{\psi\phi}(l_x, \psi, l_z, \phi)$$

$${}^k E_{m+l_x, \psi, n+l_z, \psi}^{\psi\psi, total} = {}^k E_{m+l_x, \psi, n+l_z, \psi}^{\psi\psi} + c_{\psi\psi}(l_x, \psi, l_z, \psi)$$

For the 2.5D-MRTD algorithm that requires impulse excitation in time-domain, the above superposition takes place only for the first time step ($t=0$). Nevertheless, for the 2D-MRTD it has to be repeated throughout the number of time-steps that the excitation is on. The

l_ϕ	0	1	2	3	4	5	6
$c_\phi(l_\phi)$	0.91507	0.03820	0.00963	-0.00863	0.00502	-0.00268	0.00141

Table 3.2: Excitation Scaling Decomposition Coefficients

l_ψ	1	2	3	4	5	6	7
$c_\psi(l_\psi)$	-0.10250	0.12115	-0.02975	0.01501	-0.00598	0.00298	-0.00139

Table 3.3: Excitation Wavelet Decomposition Coefficients

appropriate number of the time-steps will depend on the time dependence of the excitation (Gaussian, Gabor, ...).

Arbitrary excitation spatial distributions $f(x, z)$ for an area $[x_1 = m_1\Delta x, x_2 = m_2\Delta x] \times [z_1 = n_1\Delta z, z_2 = n_2\Delta z]$ can be modeled in a similar way. The spatial distribution has to be sampled with scaling and wavelet functions, giving the new decomposition coefficients

$$\begin{aligned}
c_{\phi\phi}(l_{x,\phi}, l_{z,\phi}) &= \int_{m_1-0.5}^{m_2+0.5} \int_{n_1-0.5}^{n_2+0.5} f(x, z) \phi(m_1 + l_{x,\phi}) \phi(n_1 + l_{z,\phi}) dz dx \\
c_{\phi\psi}(l_{x,\phi}, l_{z,\psi}) &= \int_{m_1-0.5}^{m_2+0.5} \int_{n_1-0.5}^{n_2+0.5} f(x, z) \phi(m_1 + l_{x,\phi}) \psi(n_1 + l_{z,\psi}) dz dx \\
c_{\psi\phi}(l_{x,\psi}, l_{z,\phi}) &= \int_{m_1-0.5}^{m_2+0.5} \int_{n_1-0.5}^{n_2+0.5} f(x, z) \psi(m_1 + l_{x,\psi}) \phi(n_1 + l_{z,\phi}) dz dx \\
c_{\psi\psi}(l_{x,\psi}, l_{z,\psi}) &= \int_{m_1-0.5}^{m_2+0.5} \int_{n_1-0.5}^{n_2+0.5} f(x, z) \psi(m_1 + l_{x,\psi}) \psi(n_1 + l_{z,\psi}) dz dx \quad .
\end{aligned}$$

For most simulations the choice of $-8 \leq l_{x,\phi}, l_{x,\psi} \leq (m_2 - m_1) + 8$ and $-8 \leq l_{z,\phi}, l_{z,\psi} \leq (n_2 - n_1) + 8$ offer an accuracy close to 0.1%.

3.4.3 Treatment of Open Boundaries - PML Absorber

As it was discussed in Ch.2, for all discrete-space full wave techniques a special treatment should be given to geometries of interest defined in "open" regions where the computational grid is unbounded in one or more directions. Since the computational domain is limited in space by storage limitations, an appropriate boundary condition should be implemented to effectively simulate open space and satisfy the radiation condition. Berenger [8] proposed the Perfect Matched Layer (PML) Absorber, which is based upon splitting the E- and H- field components in the ABC area and assigning artificial electric and magnetic loss coefficients. On the condition that these loss coefficients satisfy the PML relationship for each point of the absorber area, this nonphysical absorbing medium has a wave impedance less sensitive to the angle of incidence and frequency of outgoing waves than the preexisting

absorbers. In this Subsection, the non-split and split extensions of the PML absorber for the 2D- TM^z Battle-Lemarie MRTD are discussed. Their performance is going to be validated in Ch.4. Assuming that the PML area is characterized by (ϵ_o, μ_o) and electric and magnetic conductivities (σ_E, σ_H) , the TM^z equations can be written by adding an extra term to Eqs.(3.36)–(3.38)

$$\epsilon_o \frac{\partial E_x}{\partial t} + \sigma_E E_x = -\frac{\partial H_y}{\partial z} \quad (3.65)$$

$$\epsilon_o \frac{\partial E_z}{\partial t} + \sigma_E E_z = \frac{\partial H_y}{\partial x} \quad (3.66)$$

$$\mu_o \frac{\partial H_y}{\partial t} + \sigma_H H_y = \frac{\partial E_z}{\partial x} - \frac{\partial E_x}{\partial z} \quad (3.67)$$

Without loss of generality, PML cells only along the z -direction are considered. The extension to the x - and y - directions is straightforward. For each point z of the PML area, the magnetic conductivity σ_H needs to be chosen as [8]:

$$\frac{\sigma_E(z)}{\epsilon_o} = \frac{\sigma_H(z)}{\mu_o} \quad , \quad (3.68)$$

for a perfect absorption of the outgoing waves. A parabolic spatial distribution of $\sigma_{E,H}$,

$$\sigma_{E,H}(z) = \sigma_{E,H}^{max} \left(1 - \frac{z}{\delta}\right)^p \quad , \quad \text{with } p=2 \quad \text{for } 0 \leq z \leq \delta \quad (3.69)$$

is used in the simulations, though higher order distributions (e.g. Cubic $p=3$) can give similar results. The PML area is terminated with a PEC and usually has a thickness varying between 4-32 cells. The maximum value σ_E^{max} is determined by the designated reflection coefficient R at normal incidence, which is given by the relationship

$$R = e^{-\frac{2}{\epsilon_o c} \int_0^\delta \sigma_E(z) dz} = e^{-\frac{2\sigma_E^{max} \delta}{\epsilon_o c(p+1)}} \quad (3.70)$$

In MRTD, the PML area can be modeled by discretizing the above equations in a similar way to the non-conductive area described in the beginning of Section 3.4 and split and non-split formulations can be derived.

Similarly, the PML equations for the TE^z can be written as,

$$\mu_o \frac{\partial H_x}{\partial t} + \sigma_H H_x = \frac{\partial E_y}{\partial z} \quad (3.71)$$

$$\mu_o \frac{\partial H_z}{\partial t} + \sigma_H H_z = -\frac{\partial E_y}{\partial x} \quad (3.72)$$

$$\epsilon_o \frac{\partial E_y}{\partial t} + \sigma_E E_y = -\frac{\partial H_z}{\partial x} + \frac{\partial H_x}{\partial z} \quad (3.73)$$

Split Formulation

Following the approach of [8], H_y is split in two subcomponents, H_{yx} , H_{yz} and Eqs.(3.65)–(3.67) are written as,

$$\epsilon_o \frac{\partial E_x}{\partial t} + \sigma_E(z) E_x = -\frac{\partial H_{yx} + H_{yz}}{\partial z} \quad (3.74)$$

$$\epsilon_o \frac{\partial E_z}{\partial t} = \frac{\partial H_{yx} + H_{yz}}{\partial x} \quad (3.75)$$

$$\mu_o \frac{\partial H_{yx}}{\partial t} = \frac{\partial E_z}{\partial x} \quad (3.76)$$

$$\mu_o \frac{\partial H_{yz}}{\partial t} + \sigma_H(z) H_{yz} = -\frac{\partial E_x}{\partial z} \quad (3.77)$$

For the sake of simplicity in the presentation and without loss of generality, the fields E_x, E_z, H_{yx}, H_{yz} are expanded in terms of scaling functions only in space domain and pulse functions in time domain. By applying Galerkin's technique [26, 53], the following split PML equations are obtained

$$\begin{aligned} {}^{k+1}E_{i-1/2,j}^{x,\phi\phi} &= e^{-\sigma_E^j \Delta t / \epsilon_o} {}^k E_{i-1/2,j}^{x,\phi\phi} \\ &+ \frac{1}{\Delta z \sigma_E^j} (e^{-\sigma_E^j \Delta t / \epsilon_o} - 1) \\ &\quad \sum_{i'=-n_a}^{n_a-1} a(i') ({}^{k+1/2}H_{i-1/2,j+j'+1-1/2}^{yx,\phi\phi} + {}^{k+1/2}H_{i-1/2,j+j'+1-1/2}^{yz,\phi\phi}) \\ {}^{k+1}E_{i,j-1/2}^{z,\phi\phi} &= {}^k E_{i,j-1/2}^{z,\phi\phi} \\ &+ \frac{\Delta t}{\epsilon_o \Delta x} \sum_{i'=-n_a}^{n_a-1} a(i') ({}^{k+1/2}H_{i+i'+1-1/2,j-1/2}^{yx,\phi\phi} + {}^{k+1/2}H_{i+i'+1-1/2,j-1/2}^{yz,\phi\phi}) \\ {}^{k+1/2}H_{i-1/2,j-1/2}^{yx,\phi\phi} &= {}^{k-1/2}H_{i-1/2,j-1/2}^{yx,\phi\phi} \end{aligned}$$

$$\begin{aligned}
& + \frac{\Delta t}{\mu_o \Delta x} \left(\sum_{i'=-n_a}^{n_a-1} a(i')_k E_{i+i',j-1/2}^{z,\phi\phi} \right) \\
{}_{k+1/2} H_{i-1/2,j-1/2}^{yz,\phi\phi} & = e^{-\sigma_H^{j-1/2} \Delta t / \mu_o} {}_{k-1/2} H_{i-1/2,j-1/2}^{yz,\phi\phi} \\
& + \frac{1}{\Delta z \sigma_H^{j-1/2}} (e^{-\sigma_H^{j-1/2} \Delta t / \mu_o} - 1) \sum_{j'=-n_a}^{n_a-1} a(j')_k E_{i-1/2,j+j'}^{x,\phi\phi} \quad . \quad (3.78)
\end{aligned}$$

Exponential time-stepping is being used for the field components affected by the PML conductivities σ_E, σ_H . Due to the entire-domain nature of the Battle-Lemarie scaling functions, the PML conductivity must be sampled by them over at least 12 cells (6 cells per side),

$$\sigma_{E,H}^j = \int_{j-6}^{j+6} \sigma_{E,H}(z) \phi_j(z) dz \quad . \quad (3.79)$$

Image theory is applied to extend the conductivity layer outside the terminating PEC's. The presented formulation follows the idea introduced by Berenger for the FDTD. Nevertheless, an efficient non-split form of the PML equations does not demand extra memory for the storage of two H_y subcomponents per cell.

Non-split Formulation

Substituting in Eqs.(3.65)–(3.67) [54]:

$$E_i(x, z, t) = \tilde{E}_i(x, z, t) e^{-\sigma_E(z)t/\epsilon_o} \quad (3.80)$$

and

$$H_j(x, z, t) = \tilde{H}_j(x, z, t) e^{-\sigma_H(z)t/\mu_o} \quad (3.81)$$

for $i=x,z$ and $j=y$ leads to the following system of equations:

$$\epsilon_o \frac{\partial \tilde{E}_x}{\partial t} = -\frac{\partial \tilde{H}_y}{\partial z} \quad (3.82)$$

$$\epsilon_o \frac{\partial \tilde{E}_z}{\partial t} = \frac{\partial \tilde{H}_y}{\partial x} \quad (3.83)$$

$$\mu_o \frac{\partial \bar{H}_y}{\partial t} = \frac{\partial \bar{E}_z}{\partial x} - \frac{\partial \bar{E}_x}{\partial z} \quad (3.84)$$

Discretizing Eqs.(3.82)–(3.84) and inserting Eqs.(3.80)–(3.81) yields the unsplit formulation of the fields for the PML region:

$$\begin{aligned} {}^{k+1}E_{i-1/2,j}^{x,\phi\phi} &= e^{-\sigma_E^j \Delta t / \epsilon_o} {}^k E_{i-1/2,j}^{x,\phi\phi} \\ &- e^{-0.5\sigma_E^j \Delta t / \epsilon_o} \frac{\Delta t}{\epsilon_o} \left(\frac{1}{\Delta z} \sum_{j'=-n_a}^{n_a-1} a(i') {}^{k+1/2} H_{i-1/2,j+j'+1-1/2}^{y,\phi\phi} \right) \\ {}^{k+1}E_{i,j-1/2}^{z,\phi\phi} &= e^{-\sigma_E^{j-1/2} \Delta t / \epsilon_o} {}^k E_{i,j-1/2}^{z,\phi\phi} \\ &+ e^{-0.5\sigma_E^{j-1/2} \Delta t / \epsilon_o} \frac{\Delta t}{\epsilon_o} \left(\frac{1}{\Delta x} \sum_{i'=-n_a}^{n_a-1} a(i') {}^{k+1/2} H_{i+i'+1-1/2,j-1/2}^{y,\phi\phi} \right) \\ {}^{k+1/2}H_{i-1/2,j-1/2}^{y,\phi\phi} &= e^{-\sigma_H^{j-1/2} \Delta t / \mu_o} {}^{k-1/2} H_{i-1/2,j-1/2}^{y,\phi\phi} \\ &+ e^{-0.5\sigma_H^{j-1/2} \Delta t / \mu_o} \frac{\Delta t}{\mu_o} \\ &\left(\frac{1}{\Delta x} \sum_{i'=-n_a}^{n_a-1} a(i') {}^k E_{i+i',j-1/2}^{z,\phi\phi} - \frac{1}{\Delta z} \sum_{j'=-n_a}^{n_a-1} a(j') {}^k E_{i-1/2,j+j'}^{x,\phi\phi} \right) \quad , \end{aligned} \quad (3.85)$$

where the terms $\sigma_{E,H}^j$ are given by Eq.(3.79).

3.4.4 Total Field Calculation

Due to the nature of the Battle-Lemarie expansion functions, the total field is a summation of the contributions from the non-localized scaling and wavelet functions. For example, the total electric field $E_x(x_o, z_o, t_o)$ with $(k - 1/2) \Delta t < t_o < (k + 1/2) \Delta t$, $(i - 1) \Delta x < x_o < i \Delta x$ and $(j - 1/2) \Delta z < z_o < (j + 1/2) \Delta z$ is calculated in the same way with [26, 53] by

$$\begin{aligned} E_x(x_o, z_o, t_o) &= \sum_{i',j'=-l_1}^{l_1} {}^k E_{i+i'-1/2,j+j'}^{x,\phi\phi} \phi_{i+i'-1/2}(x_o) \phi_{j+j'}(z_o) \\ &+ \sum_{r_z=0}^{r_{max}} \sum_{i',j'=-l_{2,r}}^{l_{2,r}} \sum_{p_z=0}^{2^{r_z}-1} {}^k E_{i+i'-1/2,j+j'}^{x,\phi\psi_{r_z,p_z}} \phi_{i+i'-1/2}(x_o) \psi_{j+j',p_z}^{r_z}(z_o) \end{aligned}$$

$$\begin{aligned}
& + \sum_{r_x=0}^{r_{max}} \sum_{i',j'=-l_{3,r}}^{l_{3,r}} \sum_{p_x=0}^{2^{r_x}-1} k E_{i+i'-1/2,j+j'}^{x,\psi_{r_x,p_x}\phi} \psi_{i+i'-1/2,p_x}^{r_x}(x_o) \phi_{j+j'}(z_o) \\
& + \sum_{r_x,r_z=0}^{r_{max}} \sum_{i',j'=-l_{4,r}}^{l_{4,r}} \sum_{p_x,p_z=0}^{2^{r_x,r_z}-1} k E_{i+i'-1/2,j+j'}^{x,\psi_{r_x,p_x}\psi_{r_z,p_z}} \psi_{i+i'-1/2,p_x}^{r_x}(x_o) \psi_{j+j',p_z}^{r_z}(z_o)
\end{aligned} \tag{3.86}$$

where $\phi_n(x) = \phi(\frac{x}{\Delta x} - n)$ and $\psi_{n,p}^r(x) = 2^{r/2} \psi_0(2^r[\frac{x}{\Delta x} - n] - p)$ represent the Battle-Lemarie scaling and r-resolution wavelet function respectively and r_{max} is the maximum wavelet resolution used in this area of the computational domain. It has been observed that the values $l_1 = l_{2,0} = l_{3,0} = l_{4,0} = 10$ and $l_{2,1} = l_{3,1} = l_{4,1} = 6$ offer accuracy close to 0.5% for most simulations incorporating the first two wavelet resolutions. For the cases of narrow strips with very sharp field discontinuities, the summation limits must increase up to 15-20 terms per direction.

The fact that the MRTD is based on entire-domain basis functions with varying values along each cell offers the unique opportunity of a multi-point field representation per cell. The neighboring scaling and wavelet coefficients can be combined in an appropriate way to calculate the total field value for more than one interior cell points. In this way, MRTD creates a mesh with much larger density than that offered by the nominal number of the cells without increasing the memory requirements. This additional density is very useful in the calculation of the characteristic impedance of planar lines, where even a small field variation can cause a perturbation of the impedance value by $5 - 10\Omega$. On the contrary, FDTD is based on pulse basis functions that have a constant value for each cell, offering a single-point field representation.

3.5 Conclusions

After reviewing the general principles of Multiresolution Analysis, novel time-domain schemes based on expansions in scaling and wavelet functions (MRTD) have been derived. FDTD implementation schemes (excitation, hard/open boundary and dielectric interfaces) have been extended to Multiresolution schemes based on entire-domain expansion basis, while maintaining similar performance characteristics. These schemes offer the unique opportunity of a multi-point field representation per cell. Battle-Lemarie functions are used throughout the dissertation due to their special qualities.

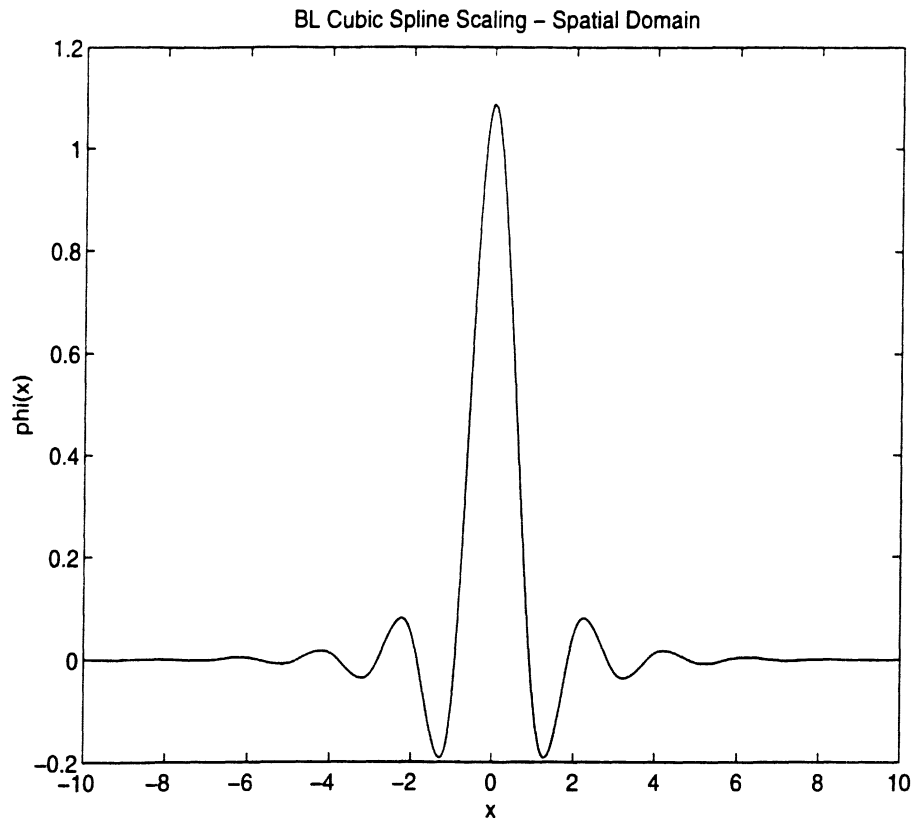


Figure 3.1: BL Cubic Spline Scaling - Spatial Domain.

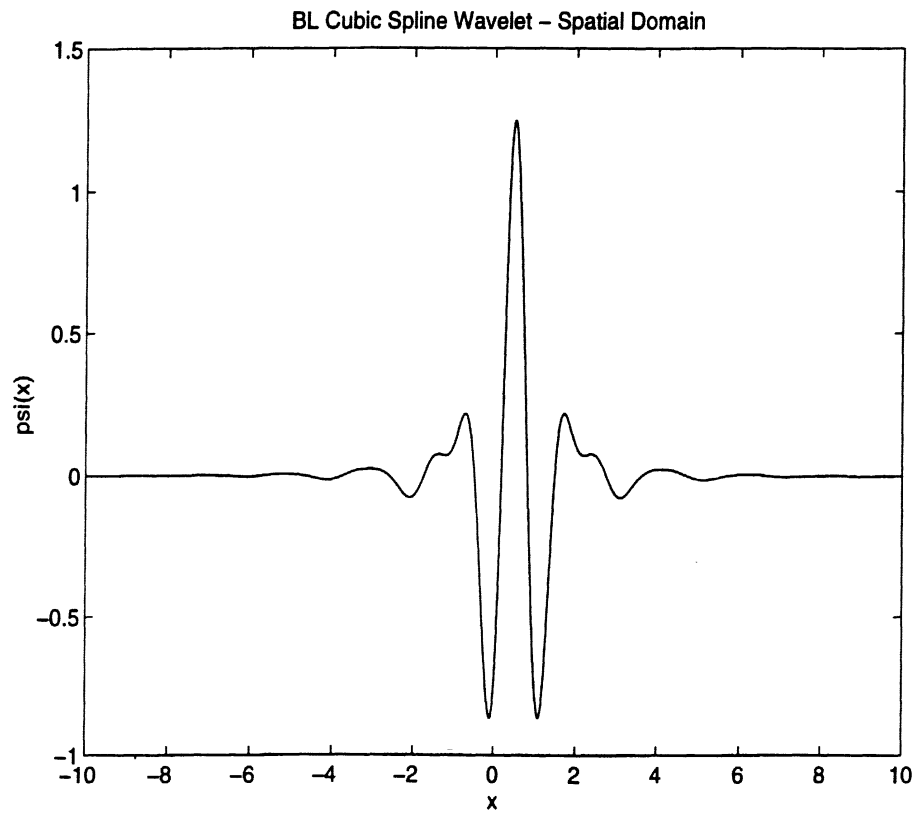


Figure 3.2: BL Cubic Spline Wavelet - Spatial Domain.

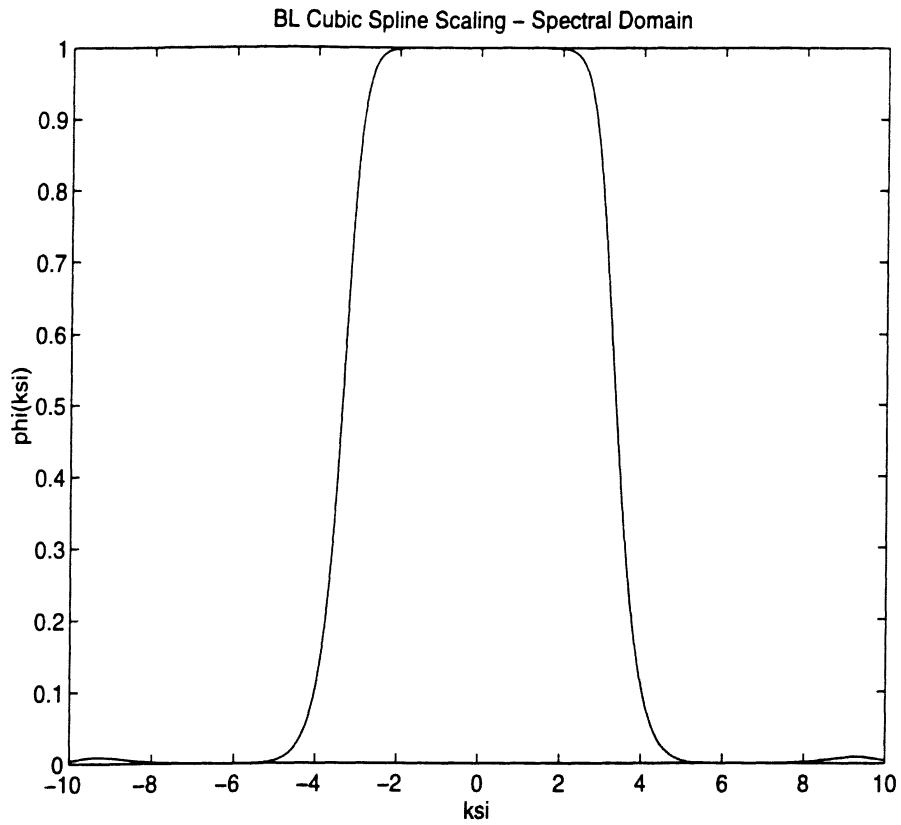


Figure 3.3: BL Cubic Spline Scaling - Spectral Domain.

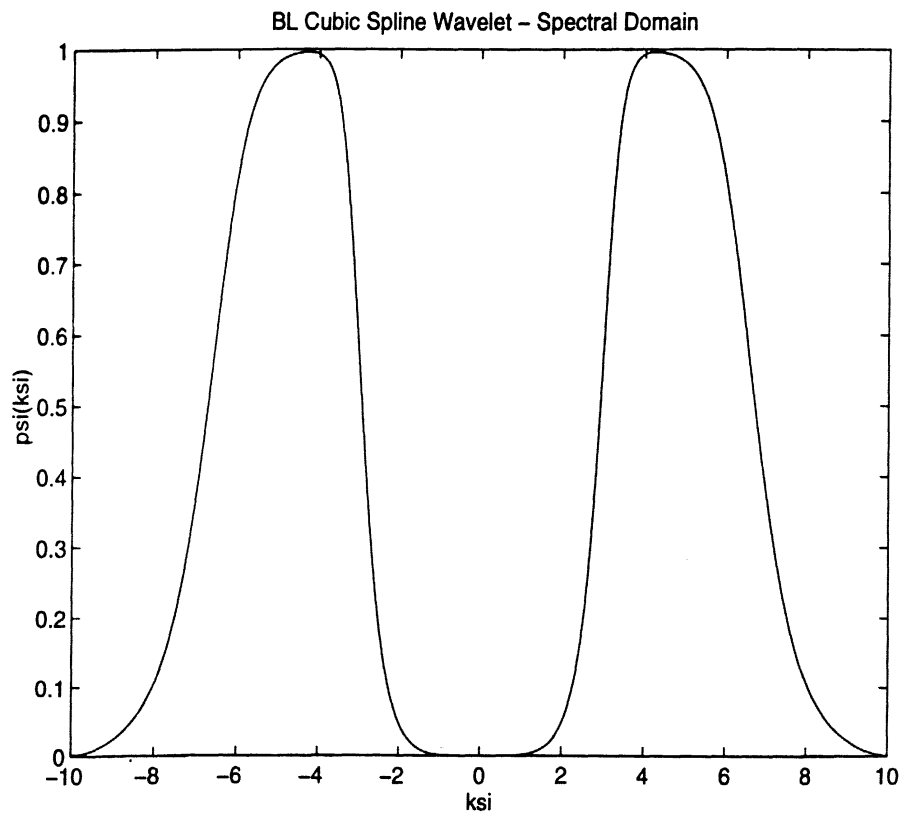


Figure 3.4: BL Cubic Spline Wavelet - Spectral Domain.

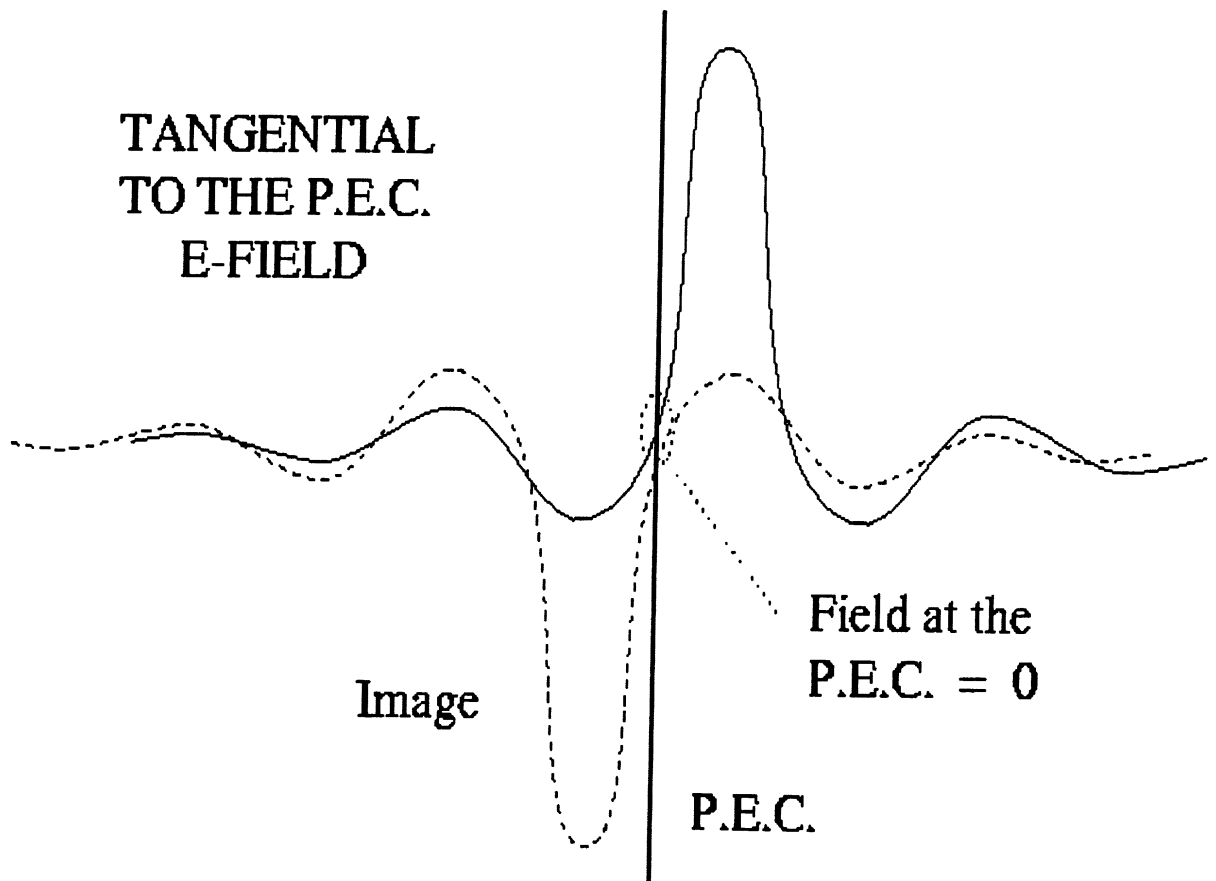


Figure 3.5: Image Theory Application for tangential-to-PEC E-field.

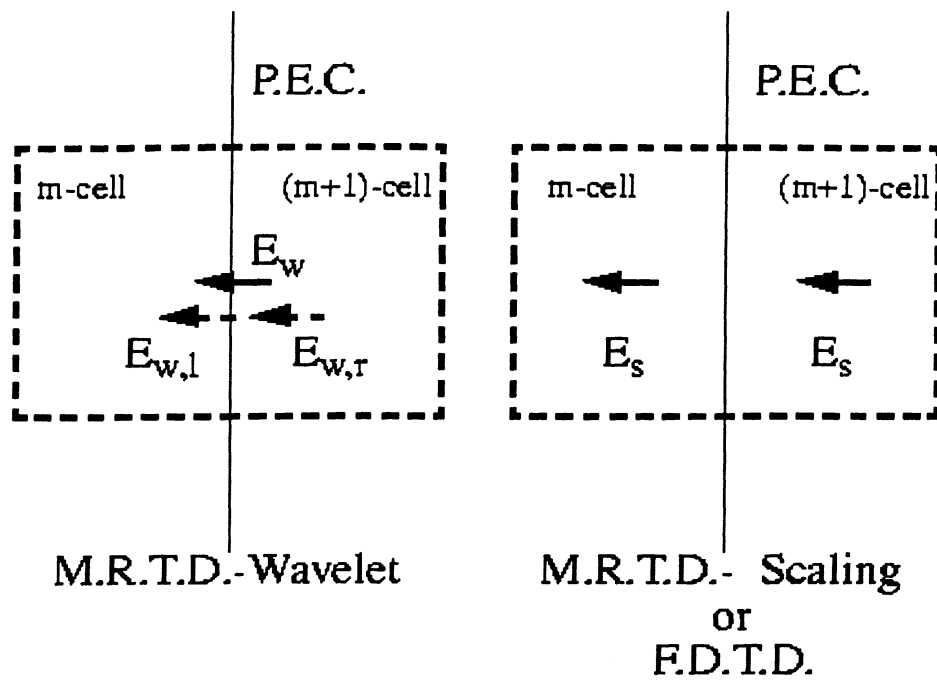


Figure 3.6: Treatment of Wavelet Components of normal-to-PEC E-field.

CHAPTER 4

Characterization of Microwave Circuit Components

Using the Multiresolution Time Domain Method (MRTD)

4.1 Introduction

Recently, the Battle-Lemarie based MRTD technique has been successfully applied [26, 53, 54] to a variety of microwave problems and has demonstrated unparalleled properties. When applied to linear as well as nonlinear propagation problems, it has exhibited MRTD schemes based on other entire-domain expansion basis can be developed in a similar way by calculating the appropriate summation coefficients. The use of Battle-Lemarie basis allows for a more simplified evaluation of the moment method integrals is simplified due to the existence of closed form expressions in spectral domain and simple representations in terms of cubic spline functions in space domain. The use of non-localized basis functions cannot accomodate localized boundary conditions. To overcome this difficulty, the image principle is used to model perfect electric and magnetic boundary conditions. Pulse functions are used as expansion and test functions in time-domain. In this Chapter, a 2.5D MRTD scheme is developed and applied to a variety of shielded and open of transmission line problems. Specifically, propagation constant, characteristic impedance and field patterns are derived

for shielded and open transmission line structures and compared to FDTD results. For the treatment of open boundaries, Berenger's PML principles [8] have been extended in split and non-split form, so as they can be used for entire-domain basis MRTD schemes.

4.2 The 2.5D-MRTD scheme

For simplicity, an overview of the 2.5D-MRTD scheme is presented for a homogeneous medium. The derivation is similar to that of the 2D-MRTD scheme in CH.3, which uses the method of moments with pulse functions as expansion and test functions. The magnetic field components are shifted by half a discretization interval in space and time-domain with respect to the electric field components.

Using the approach of [55], Maxwell's curl equations for a homogeneous medium with the permittivity ϵ and the permeability μ can be written in the following form

$$\epsilon \frac{\partial E_x}{\partial t} = \frac{\partial H_z}{\partial y} + \beta H_y \quad (4.1)$$

$$\epsilon \frac{\partial E_y}{\partial t} = -\beta H_x - \frac{\partial H_z}{\partial x} \quad (4.2)$$

$$\epsilon \frac{\partial E_z}{\partial t} = \frac{\partial H_y}{\partial x} - \frac{\partial H_x}{\partial y} \quad , \quad (4.3)$$

where β is the propagation constant and $j = \sqrt{-1}$. The electric and magnetic field components incorporated in these equations are expanded in a series of Battle-Lemarie scaling and wavelet functions in both x- and y-directions. For example, E_x can be represented as:

$$\begin{aligned} E_x(x, y, t) = & \sum_{k,l,m=-\infty}^{+\infty} k E_{l-1/2,m}^{x,\phi\phi} h_k(t) \phi_{l-1/2}(x) \phi_m(y) \\ & + \sum_{k,l,m=-\infty}^{+\infty} \sum_{r_y=0}^{+\infty} \sum_{p_y=0}^{2^{r_y}-1} k E_{l-1/2,m}^{x,\phi\psi_{r_y,p_y}} h_k(t) \phi_{l-1/2}(x) \psi_{m,p_y}^{r_y}(y) \\ & + \sum_{k,l,m=-\infty}^{+\infty} \sum_{r_x=0}^{+\infty} \text{sum}_{p_x=0}^{2^{r_x}-1} k E_{l-1/2,m}^{x,\psi_{r_x,p_x}\phi} h_k(t) \psi_{l-1/2,p_x}^{r_x}(x) \phi_m(y) \end{aligned}$$

CHAPTER 4

Characterization of Microwave Circuit Components Using the Multiresolution Time Domain Method (MRTD)

4.1 Introduction

Recently, the Battle-Lemarie based MRTD technique has been successfully applied [31, 58, 59] to a variety of microwave problems and has demonstrated unparalleled properties. When applied to linear as well as nonlinear propagation problems, it has exhibited MRTD schemes based on other entire-domain expansion basis can be developed in a similar way by calculating the appropriate summation coefficients. The use of Battle-Lemarie basis allows for a more simplified evaluation of the moment method integrals is simplified due to the existence of closed form expressions in spectral domain and simple representations in terms of cubic spline functions in space domain. The use of non-localized basis functions cannot accommodate localized boundary conditions. To overcome this difficulty, the image principle is used to model perfect electric and magnetic boundary conditions. Pulse functions are used as expansion and test functions in time-domain. In this Chapter, a 2.5D MRTD scheme is developed and applied to a variety of shielded and open of transmission line problems. Specifically, propagation constant, characteristic impedance and field patterns are derived

$t_o < (k + 1/2) \Delta t$, $\Delta x < x_o < i \Delta x$ and $(j - 1/2) \Delta y < y_o < (j + 1/2) \Delta y$ is calculated by

$$\begin{aligned}
E_x(x_o, y_o, t_o) &= \int \int \int E_x(x, y, t) \delta(x - x_o) \delta(y - y_o) \delta(t - t_o) dx dy dt \\
&= \sum_{i', j' = -\infty}^{\infty} {}_k E_{i+i'-1/2, j+j'}^{x, \phi\phi} \phi_{i+i'-1/2}(x_o) \phi_{j+j'}(y_o) \\
&\approx \sum_{i', j' = -l_1}^{l_1} {}_k E_{i+i'-1/2, j+j'}^{x, \phi\phi} \phi_{i+i'-1/2}(x_o) \phi_{j+j'}(y_o) \quad . \quad (4.6)
\end{aligned}$$

Extending the dispersion analysis from 2D to 2.5D space, the stability condition for the 2.5D S-MRTD scheme results in

$$\Delta t \leq \frac{1}{c \sqrt{\left(\left(\frac{1}{\Delta x}\right)^2 + \left(\frac{1}{\Delta y}\right)^2\right) \sum_{i=0}^{n_a-1} |a(i')|^2 + \left(\frac{\beta}{2}\right)^2}} \quad (4.7)$$

with the wave propagation velocity c . It is preferable to choose Δt at least 1.2-2.5 time less than the stability limit. In this way, much more linearity of the dispersion characteristics is achieved.

4.3 Applications of the 2.5D-MRTD scheme to Shielded Transmission Lines

First, the 2.5D-MRTD scheme is applied to the analysis of shielded stripline and microstrip lines to investigate propagation and coupling effects. Results for these shielded structures are presented and discussed separately below.

A shielded stripline is a simplified version of a membrane microstrip shown in (Fig.4.1a). The metallic shield has dimensions $47.6mm \times 22.0mm$ and the central strip has length $11.9mm$. The stripline is filled with air ($\epsilon_r = 1$). The analysis for the higher order propagating modes is straightforward. For the analysis using Yee's FDTD scheme, a 40×10 mesh was used resulting in a total number of 400 grid points. When the structure was analyzed with the 2.5D-MRTD scheme, a mesh 8×4 (32 grid points) was chosen reducing

Mode	TEM	Shield TE_{10}
Analytic values	1.4324 GHz	3.4615 GHz
8x2 MRTD	1.4325 GHz	3.4648 GHz
Rel.Error	0.007%	0.095%
8x4 MRTD	1.4325 GHz	3.4641 GHz
Rel.Error	0.007%	0.075%
16x4 MRTD	1.4325 GHz	3.4633 GHz
Rel.Error	0.007%	0.052%
40x10 FDTD	1.4322 GHz	3.4585 GHz
Rel.Error	-0.014%	-0.087%

Table 4.1: Mode frequencies for $\beta = 30$

the total number of grid points by a factor of 12.5. In addition, the execution time for the analysis was reduced by a factor of 3 to 4. The time discretization interval was chosen to be identical for both schemes and equal to the 0.8 of the 2.5D-MRTD maximum Δt . For the analysis $\beta = 30$ was used and 5,000 time-steps were considered.

From (Table 4.1) it can be observed that the calculated frequencies of the two first propagating modes for $\beta = 30$ by use of 2.5D-MRTD scheme are very close to the theoretical values, since the largest error is less than 0.1%. The relative error of the 2.5D-MRTD calculated frequencies is always positive, which corresponds to an overestimation of the resonant frequencies. This is exactly what has to be expected from the dispersion behavior of the MRTD schemes.

The non-localized character of the basis functions offers the opportunity to calculate the field values in any point of the discretization cells. The field values at the neighboring cells

can be combined appropriately by adjusting the scaling functions' values and by applying the image principle. For example, the total electric field $E_x(x_o, y_o, t_o)$ with $(k - 1/2) \Delta t < t_o < (k + 1/2) \Delta t$ is calculated by Eq.(4.6) by simply truncating the i', j' summation from $l_1 = -12, \dots, 12$ for each index. That means that the summation based only at the 12 neighboring cells from each side gives the total field component values with good accuracy. In (Fig.4.2-4.4), the value of the E_y field has been calculated and plotted for the 4 cells exactly below the strip by use of the 2.5D-MRTD scheme. The relative position of the strip is from 15 to 25 . For the TEM mode the pattern obtained by use of the conventional FDTD scheme is plotted for comparison. For the shield TE_{10} mode, the analytically calculated pattern has been added for reference. All results are normalized to the peak value. It can be observed that the agreement of the MRTD calculated field pattern with the reference data is very good for the shield TE_{10} mode, where the values are changing slowly (sinusoidally) (Fig.4.2). On the contrary, for the TEM mode where the edge effect is more prominent, the agreement is not good. In this case, wavelets of 0-Resolution are added in both directions to describe the higher spatial frequencies. It can be observed from (Fig.4.3) that the wavelet coefficients for the 8x4 grid have a significant contribution ($> 10\%$) close to the stripline. Increasing the grid size from 8 to 16 to the strip direction and/or from 4 to 8 to the normal to the strip direction improves more the accuracy of the field representation (Fig.4.4).

The characteristic impedance Z_o for the TEM mode of the stripline is computed from the equation:

$$Z_o = \frac{V}{I} = \frac{\int_{C_v} E_y dy}{\oint_{C_c} H dl} \quad , \quad (4.8)$$

where the integration paths C_v and C_c are shown in (Fig.4.1a). Since both of the schemes used in the analysis are discrete in space-domain, the above integrals are transformed to

Subpoints/cell	Z_o^{sc} (Ω)	Relative error	Z_o^{wa} (Ω)	Relative error
3	80.56	-15.71 %	84.04	-12.07 %
5	94.46	-1.17 %	92.55	-3.17 %
7	99.06	+3.64 %	94.59	-1.04 %
9	101.44	+6.13 %	94.96	-0.65 %
11	97.56	+2.07 %	95.01	-0.60 %

Table 4.2: Z_o for different number of subpoints/cell (8x4 Grid).

summations. For the FDTD summations, only one field value per cell is needed, due to the fact that pulse expansion functions which are constant for each cell are utilized. On the contrary, for the 2.5D-MRTD summation the field values for a number of subpoints along the integration path have to be calculated, since the expansion functions are not constant for each cell. It can be observed from (Table 4.2) that the accuracy of the calculation of the characteristic impedance is improved by increasing the number of subpoints per cell, at which the field values are calculated. An accuracy better than 1% is achieved if the field values are computed for more than 9 subpoints per cell along the integration path for the scheme including wavelets of 0-resolution to both directions. On the contrary, the value of Z_o that is calculated from the scheme based only on scaling functions is oscillating, thus indicating that a denser mesh is required. The analytical value of the Z_o is 95.58 Ω [56].

The modification of the dimensions of the MRTD mesh (Table 4.3) shows that the accuracy of the calculation of the Z_o by use of the MRTD is much better than that of the Yee's FDTD scheme with a 40x10 mesh (relative error -3.28%).

A similar procedure is used for the analysis of the shielded coupled-stripline geometry of (Fig.4.1b) for the first even and odd mode. Both strips have a length of 11.9mm, the

	Z_o (Ω)	Relative error
Analyt. Value	95.58	0.0%
8x4 MRTD	95.01	-0.60%
8x8 MRTD	95.19	-0.41%
16x4 MRTD	95.71	0.14%
40x10 FDTD	92.44	-3.28%

Table 4.3: Z_o for different mesh sizes (11 subpoints/cell).

distances between them is $11.9mm$, from the top and bottom PEC's are $11.0mm$ and from the left and right PEC's are $11.9mm$. The structure is filled with air ($\epsilon_r = 1$). For the analysis with the conventional FDTD scheme, a 70×20 mesh resulted in a total number of 1400 grid points. The same accuracy is achieved by an MRTD mesh 14×4 (56 grid points) resulting in an economy of memory by a factor of 25. The space distribution of the tangential-to-stripline E is plotted in logarithmic scale in (Fig.4.5) for the even mode.

The 2-D MRTD technique is also used for the analysis of a shielded microstrip (Fig.4.1c) with width $9.9mm$ on a dielectric substrate with $\epsilon_r = 10.65$ and thickness $11mm$. The microstrip is placed in the center of a rectangular shield $69.3mm \times 44mm$. The same accuracy for the characteristic impedance calculation (Theoretical $Z_o = 50$ Ohms) is achieved by an FDTD mesh 140×80 and an MRTD mesh 28×20 resulting in an economy in memory by a factor of 20.

4.4 Validation of the MRTD-PML Split and Non-split Algorithms

The extension of the popular PML absorber [8] principles for MRTD applications has been presented in CH.3. In this Section, the numerical performance of this absorber is investigated for 4-32 cells and for different cell sizes ($\lambda/10$ - $\lambda/2.5$). Specifically, propagation constant, characteristic impedance and field patterns are derived for open transmission lines and compared to 2D results.

A parallel-plate waveguide of width $d=48$ mm, terminated at both ends by PML, is used to validate the described algorithm. A TM^z line source with a Gabor time variation is excited close to the one side of the waveguide. The benchmark MRTD solution with no reflections is obtained by simulating the case of a much longer parallel-plate waveguide of the same width to provide a reflection-free observation area for the time interval of interest. A quadratic variation in PML conductivity is assumed for all cases, with maximum theoretical reflection coefficient of 10^{-5} at normal incidence. Two frequency ranges are investigated, $[0, 0.9f_c^{TM_1}]$ (TEM propagation) and $[0, 0.9f_c^{TM_2}]$ ($TEM + TM_1$ propagation), where $f_c^{TM_n} = \frac{nc}{2d} = 3.125 n$ (GHz) is the cutoff frequency of the TM_n mode. The time-step is chosen to be 0.637 of the Courant limit according to the stability analysis of Ch.5.

For the TEM propagation frequency range, it can be seen from Figs.(4.6)-(4.8) that for dense grids (Cell Size = $\lambda_{max}/10$) even 8 PML cells offer a numerical reflection close to -80 dB. Different values of theoretical maximum reflection ranging from 10^{-5} to 10^{-8} don't change significantly the numerical performance of the absorber (variation of 4-5 dB's). When 16 PML cells are used, the spurious reflection is below -100 dB for the whole frequency range. Similar conclusions can be drawn for the multimodal propagation ($TEM + TM_1$) in

Fig.(4.9). It can be observed that 8 and 16 PML cells cause a numerical reflection close to -70 dB and below -100 dB respectively. For coarse grids with cell sizes close to the Nyquist limit (Cell Size = $\lambda_{max}/2.5$), the behavior of the PML layer changes. The Large cell size causes retrospective reflections between the lossy cells and the numerical reflections from the absorber increase. Thus, a larger number of cells is required to obtain an acceptable reflection coefficient. Fig.(4.10)–(4.11) show that at least 32 cells are needed for reflection around -50 dB for the high frequencies. Again, the reflection at lower frequencies is negligible (below -100 dB's). It should be emphasized that the loss coefficients assigned to each cell must be given by Eq.(3.79); that implies that the conductivity profile must be sampled with the scaling and wavelet functions that have a significant value in the PML layer. For all simulations, scaling (and wavelet) functions located up to 6 cells away from the PML layer are used for the sampling. When this procedure is not applied and the loss coefficients get the point value of the loss distribution at each cell (FDTD approach), the PML performance gets worse as it is displayed at Fig.(4.12). It should be noted that the performances of the split and the non-split formulations are almost identical as it is displayed in Fig.(4.13).

4.5 Application of PML to the Analysis of Open Stripline Geometries

The PML non-split algorithm presented in Section 3.3.2 can be easily extended for the 2.5D and the 3D MRTD algorithms incorporating scaling and wavelet functions maintaining the same performance characteristics. For each resolution added to the scheme, the conductivity must be sampled with an appropriately positioned wavelet function. It was observed that S_{11} changes only by 1-1.6 dB after the enhancement of multiple resolutions.

In this section, the 2.5D MRTD scheme is applied to the analysis of open single and coupled striplines to investigate propagation and coupling effects. In all simulations only wavelets of the 0-resolution are used for both directions, since the value of the higher resolution fields is negligible (smaller than 1%).

First, the 2.5D MRTD scheme is applied to the analysis of the open stripline for the first (quasi-TEM) propagating mode. The analysis for the higher order propagating modes is straightforward. The central strip has a length of 23.8mm and the distances from the top and bottom are 5.5mm and 16.5mm respectively. The structure is filled with air ($\epsilon_r = 1$). The PML absorber is applied for 4 cells to the left and the right sides of the structure and the maximum theoretical reflection is $R_{max}=1e-7$. For the analysis using Yee's FDTD scheme, a 42×28 mesh is used resulting in a total number of 1176 grid points. Analyzing the structure with the 2D-MRTD scheme, a mesh 12×4 (48 grid points) is chosen to reduce the total number of grid points by a factor of 24.5. In addition, the execution time for the analysis is reduced by a factor of 4 to 5. The time discretization interval is chosen to be identical for both schemes and equal to $1/10$ of the 2D-MRTD maximum Δt . For the analysis $\beta = 30$ is used and 20,000 time-steps are considered. From (Table 4.4) it can be observed that the calculated frequencies of the dominant propagating mode for $\beta = 30$ by use of 2D-MRTD scheme is very close to the theoretical values, since the largest error is less than 0.1%, for mesh sizes much smaller than those used for the conventional FDTD simulations.

In (Fig.4.14), the pattern of the E_y field just below the strip has been calculated and plotted by use of the 2D-MRTD scheme. The pattern obtained by use of the conventional FDTD scheme is plotted for comparison. Since the edge effect is prominent, a mesh 12×8 (96 grid points) with scaling functions and wavelets of 0-resolution is used for the MRTD

Mode	TEM	Rel.Error
Analytic values	1.4324 GHz	0.000%
12x4 MRTD	1.4329 GHz	0.035%
12x8 MRTD	1.4325 GHz	0.007%
42x28 FDTD	1.4321 GHz	-0.021%

Table 4.4: Dominant mode frequency for $\beta = 30$

simulation. The characteristic impedance Z_o for the quasi-TEM mode of the stripline is computed from Eq.(4.8).

For the FDTD summations, only one field value per cell is needed, due to the fact that pulse expansion functions which are constant for each cell are utilized. On the contrary, for the 2D-MRTD summation the field values for a number of subpoints along the integration path have to be calculated, since the expansion functions are not constant for each cell. (Table 4.5) shows that the accuracy of the calculation of the characteristic impedance is improved by increasing the number of subpoints per cell, at which the field values are calculated. An accuracy better than 1% is achieved if the field values are computed for more than 9 subpoints per cell along the integration path. (Table 4.5) shows the calculated values of the characteristic impedance Z_o .

A similar procedure was used for the analysis of the open coupled-stripline geometry of (Fig.4.15) for the dominant even and odd modes. Both strips have a length of $23.8mm$, the distances between them is $23.8mm$, from the top PEC $16.5mm$ and from the bottom PEC $5.5mm$. The MRTD-PML layer has a thickness of 4 cells ($23.8mm$) with maximum reflection $R_{max}=1e-7$ and starts *exactly* at the edge of the striplines. The structure is filled with air ($\epsilon_r = 1.$). For the analysis with the conventional FDTD scheme, a 65×20 mesh

	Z_o (Ω)	Relative error
Analyt. Value	56.83	0.0%
12x4 MRTD	57.24	+0.72%
12x8 MRTD	57.09	+0.46%
42x28 FDTD	54.96	-3.29%

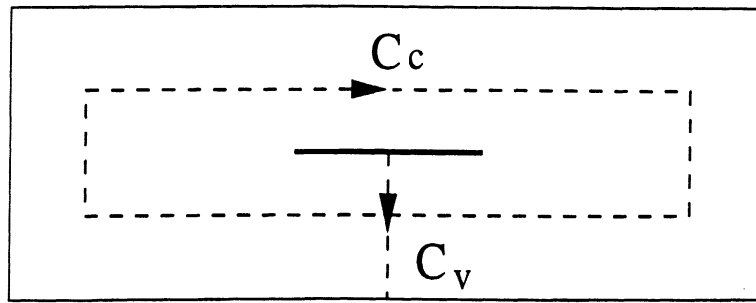
Table 4.5: Z_o for different mesh sizes.

resulted in a total number of 1300 grid points. The same accuracy is achieved by an MRTD mesh 20×4 (80 grid points) resulting in an economy of memory by a factor of 16.25. The space distribution of the tangential-to-stripline E is plotted in logarithmic scale in (Fig.4.16) for the even mode and in (Fig.4.17) for the odd mode.

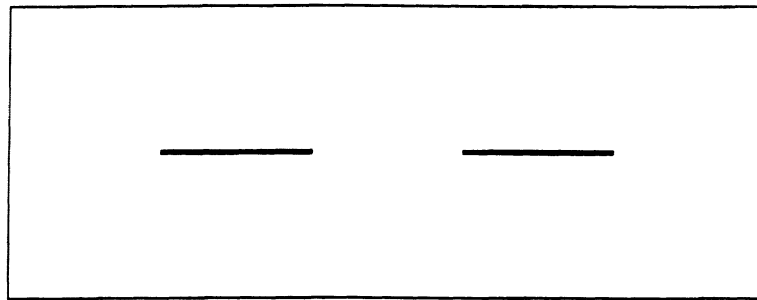
4.6 Conclusion

A multiresolution time-domain scheme in 2D has been applied to the numerical analysis of shielded and open striplines and microstrips. The field patterns and the characteristic impedance have been calculated and verified by comparison to reference data. In comparison to Yee's conventional FDTD scheme, the proposed 2.5D-MRTD scheme offer memory savings by a factor of 25 and execution time savings by a factor of about 4-5 maintaining a better accuracy for characteristic impedance calculations. This indicates memory savings of a factor 5 per dimension leading to two orders of memory savings in three dimensions. Compared to 2.5D-FDTD, 25 times less cells in MRTD require about 5 times less running time, thus the computation time per cell is increased by a factor of 5. This leads to computation time savings of more than one order for 3 dimensional structures. For structures, where the edge effect is prominent, additional wavelets have to be introduced to improve the accuracy

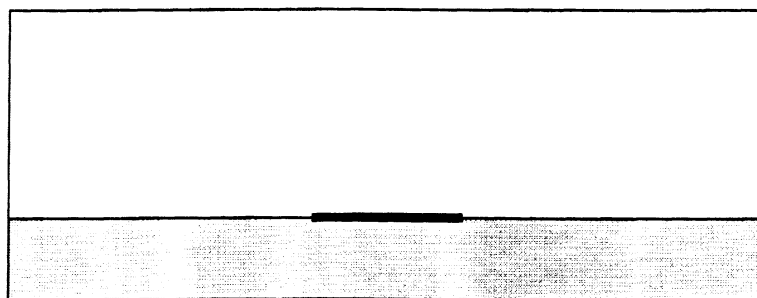
when using a coarse MRTD mesh. A non-split PML absorber has been evaluated and its performance is similar to that of the conventional FDTD Split PML absorber (reflections close to -100 dB).



(a)



(b)



(c)

Figure 4.1: Printed Lines Geometries.

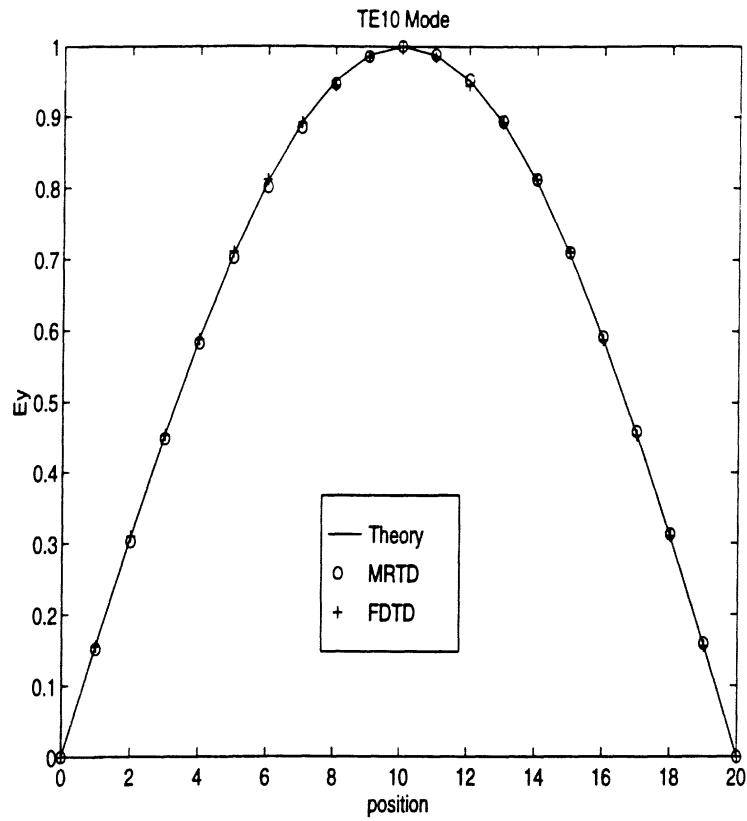


Figure 4.2: Shield TE_{10} E_y pattern.

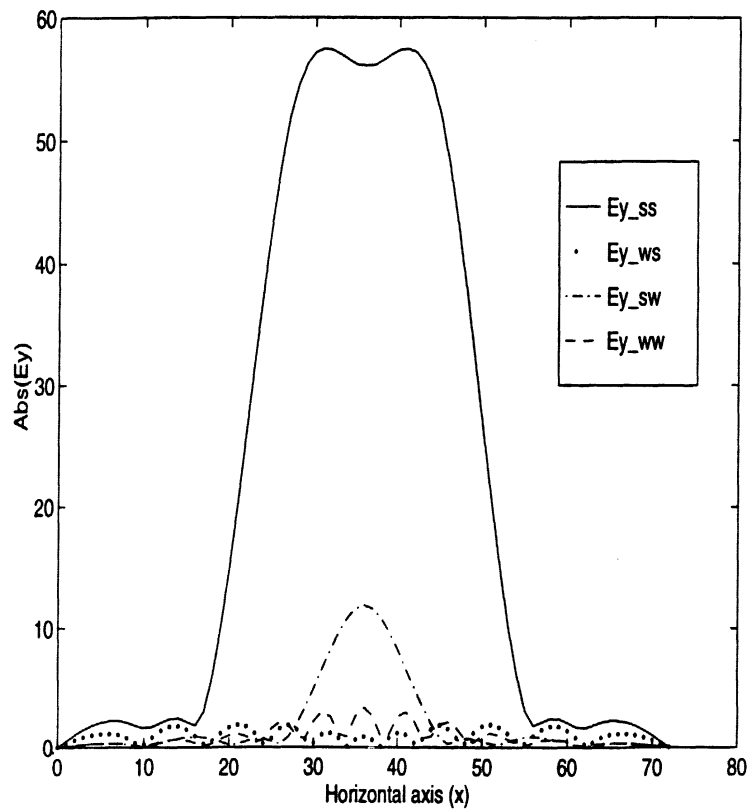


Figure 4.3: TEM E_y Pattern Components (8x8 Grid).

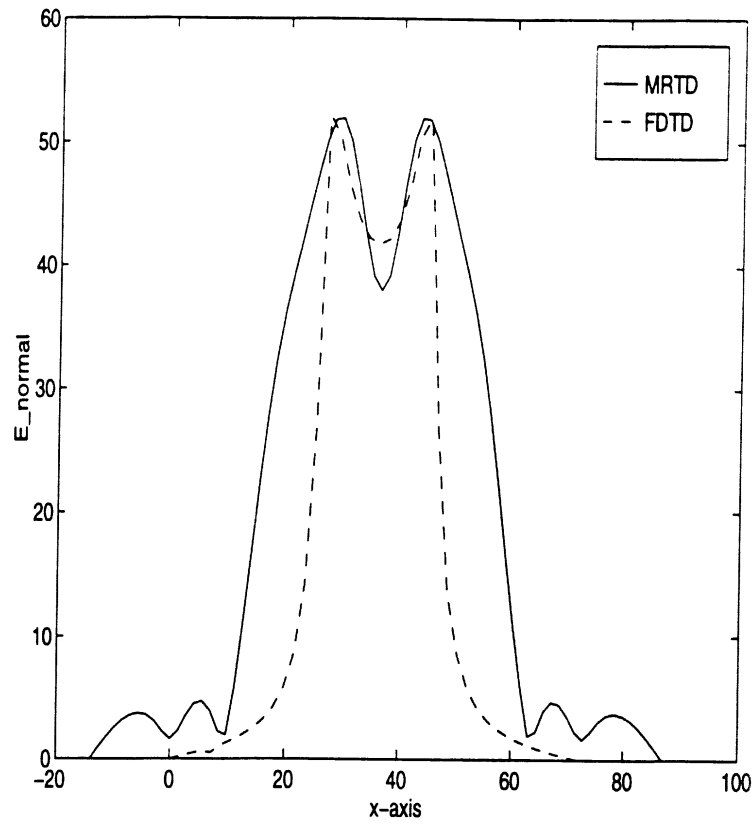


Figure 4.4: TEM E_y Pattern Comparison (8x8 Grid).

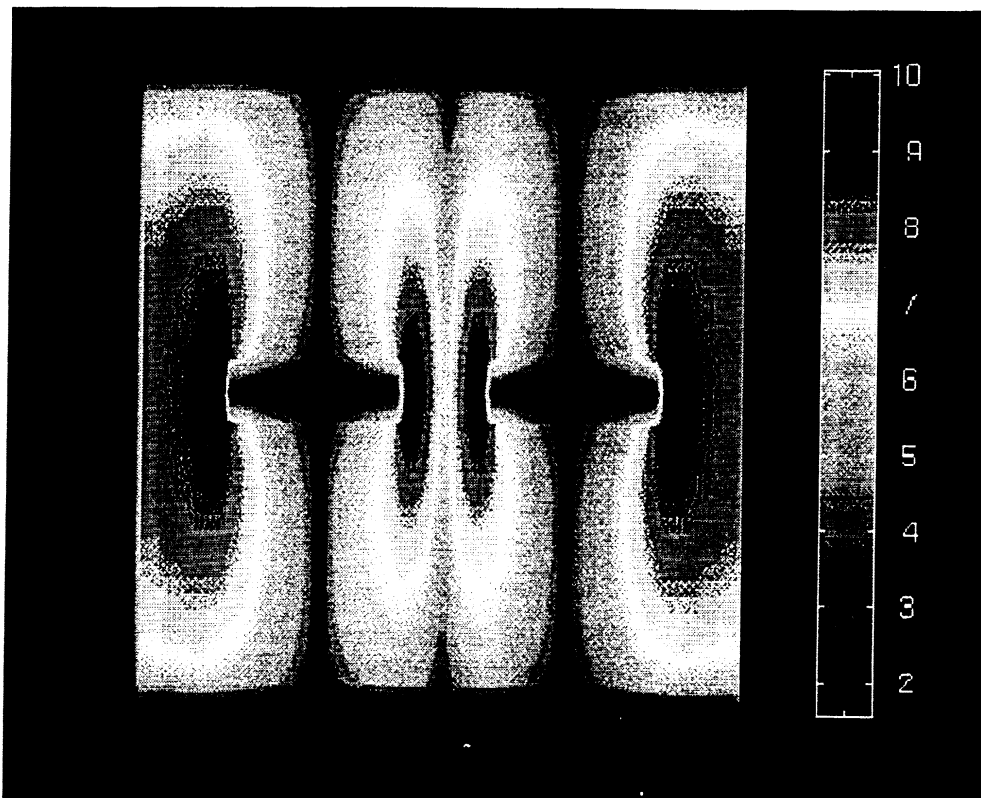


Figure 4.5: Tangential E-field Distribution (Shielded - Even Mode).

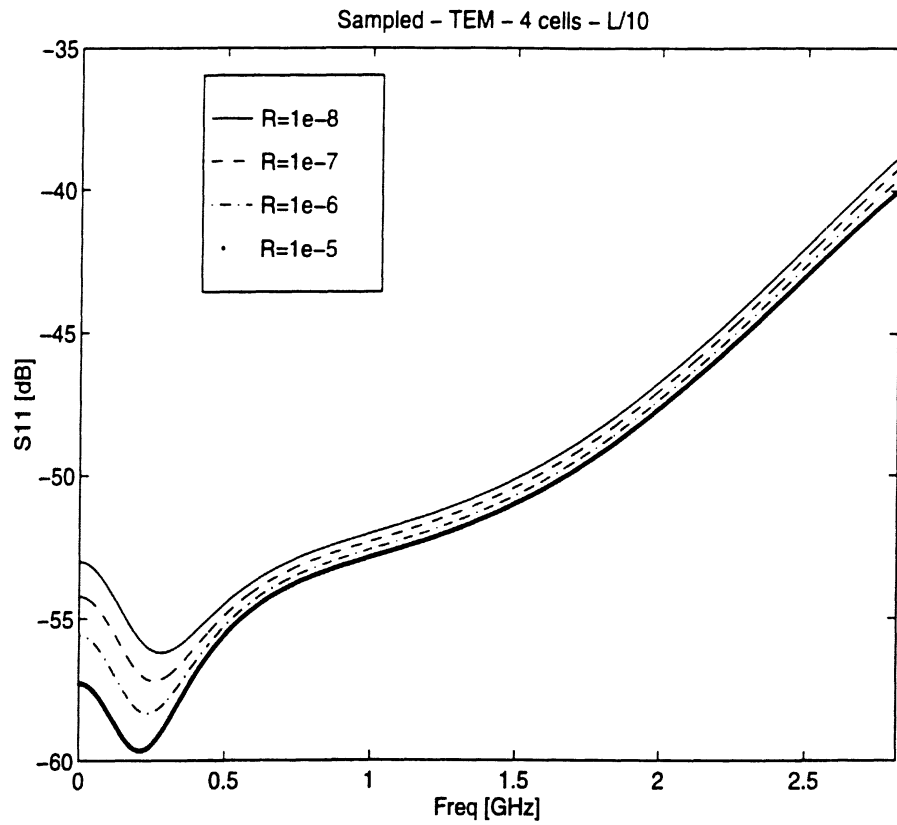


Figure 4.6: 4 PML cells - Non-split formulation - Dense Grid.

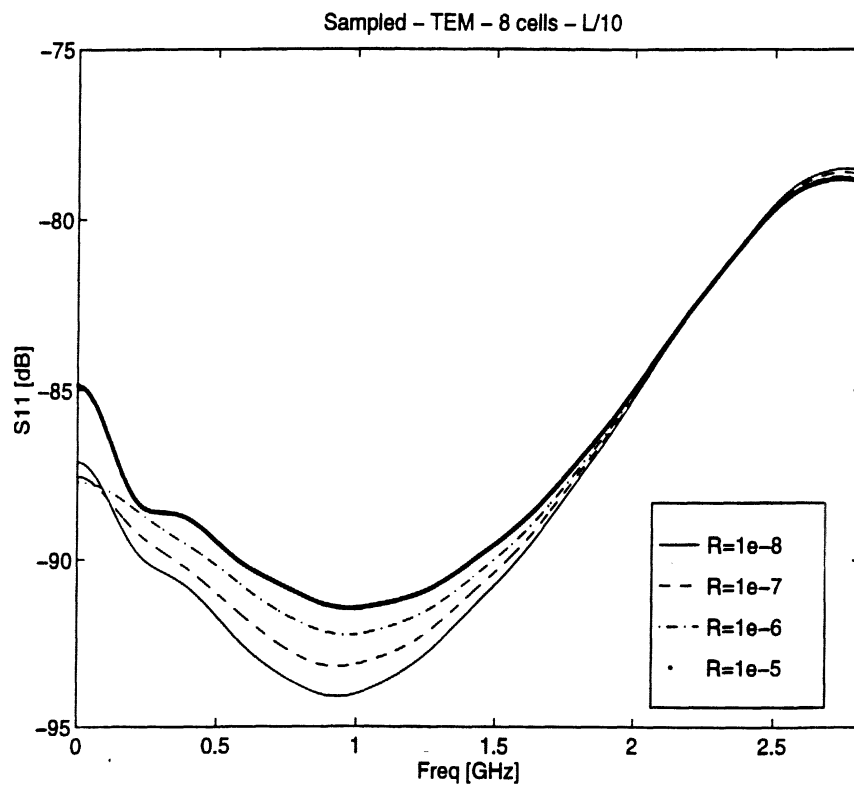


Figure 4.7: 8 PML cells - Non-split formulation - Dense Grid.

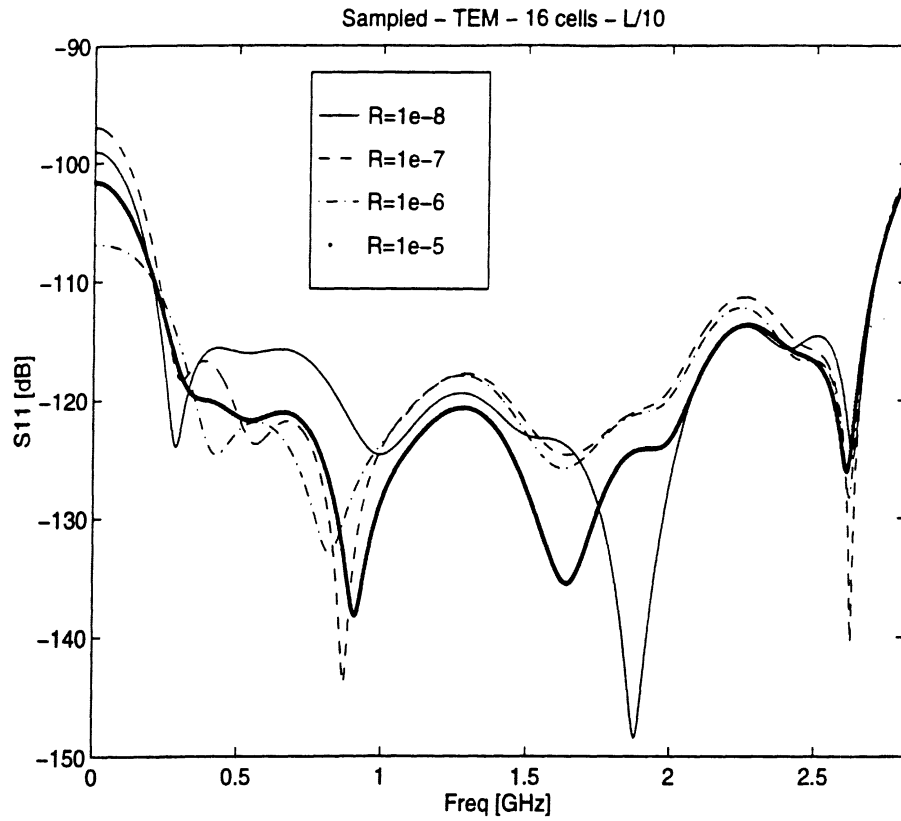


Figure 4.8: 16 PML cells - Non-split formulation - Dense Grid.

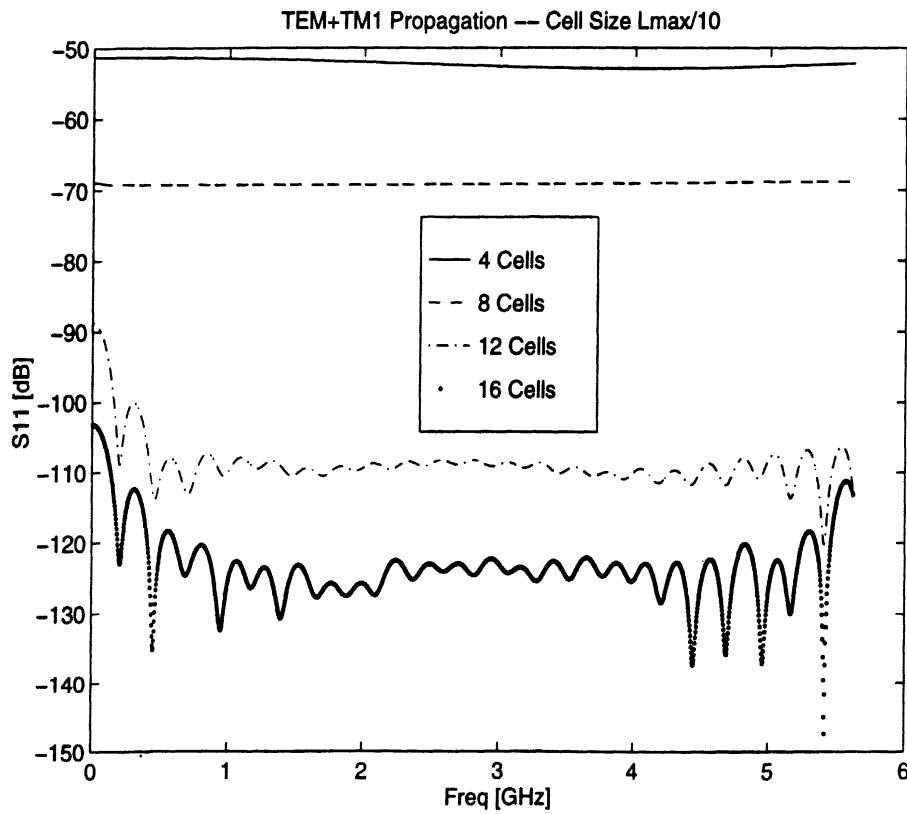


Figure 4.9: Multimodal Propagation - Dense Grid.

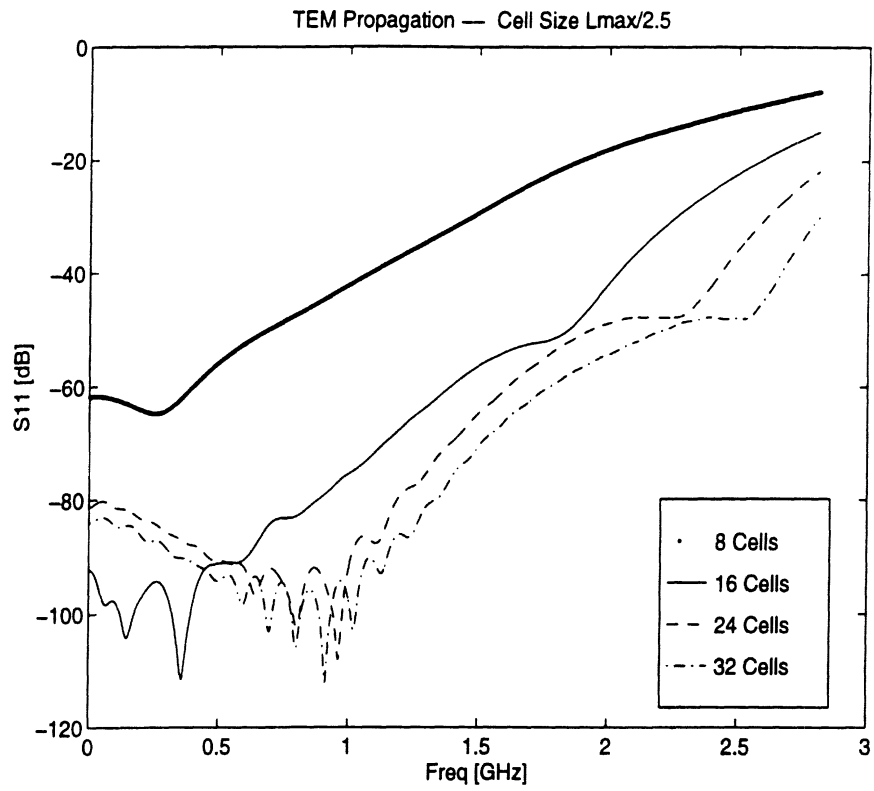


Figure 4.10: TEM Propagation - Coarse Grid.

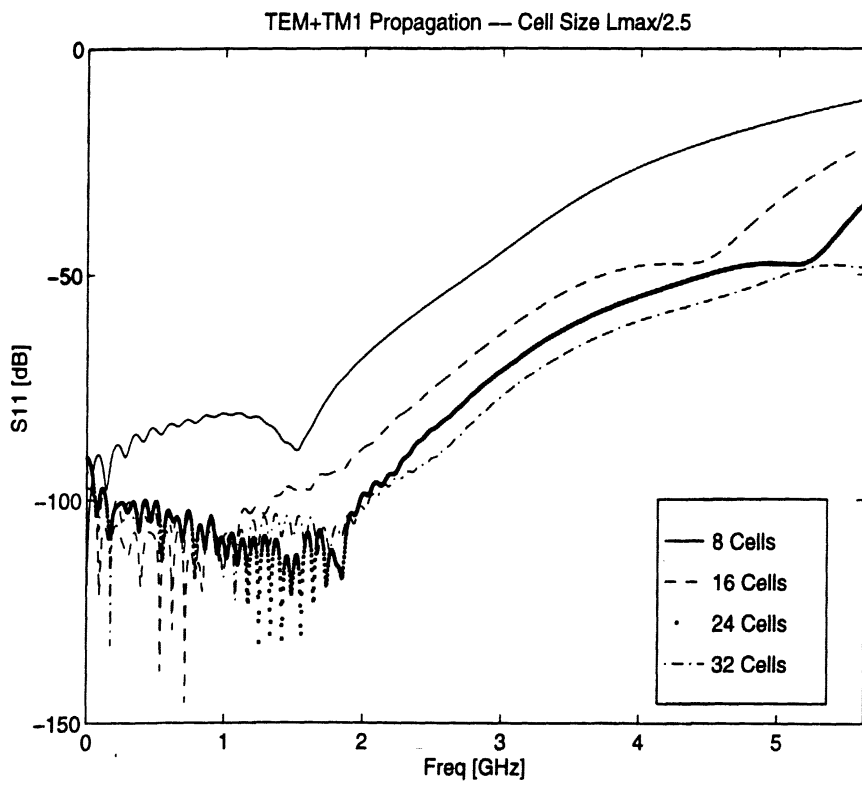


Figure 4.11: Multimodal Propagation - Coarse Grid.

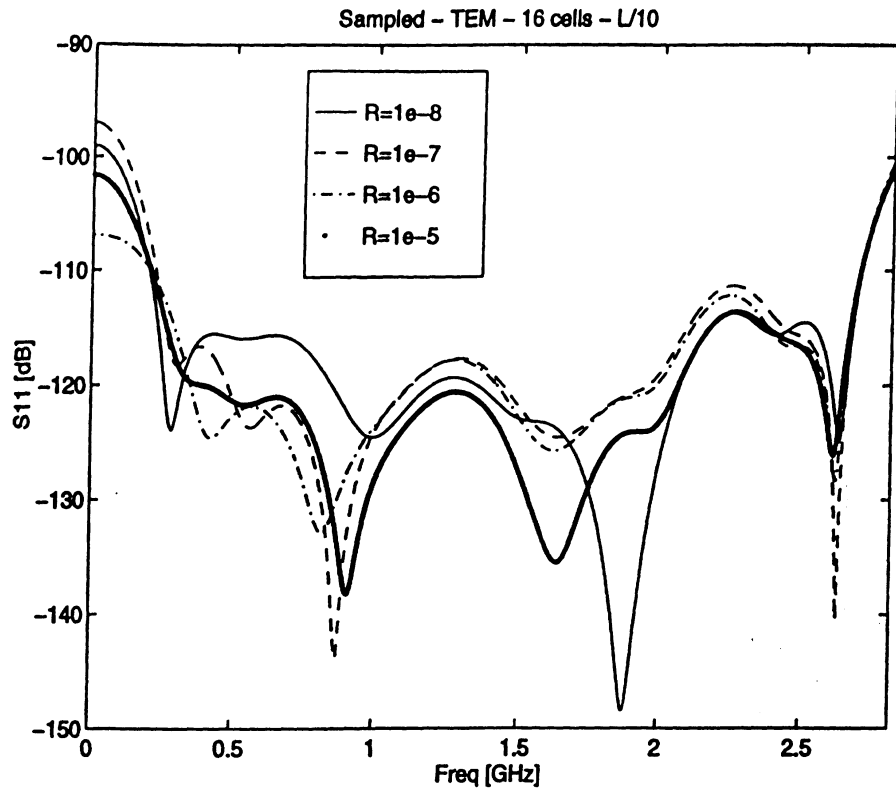


Figure 4.8: 16 PML cells - Non-split formulation - Dense Grid.

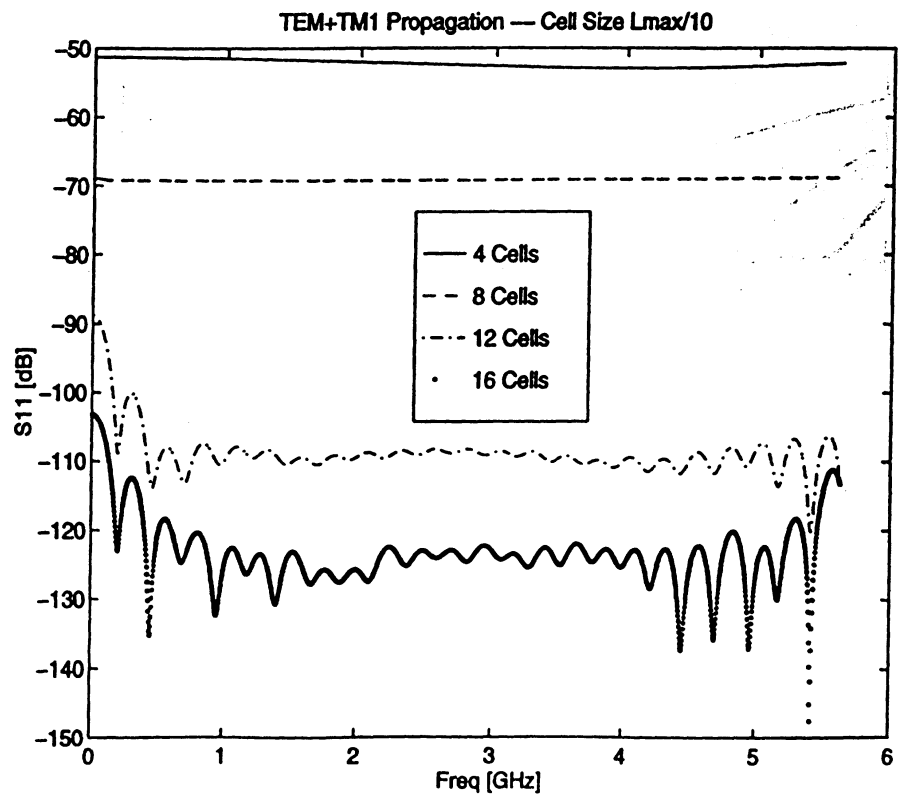


Figure 4.9: Multimodal Propagation - Dense Grid.

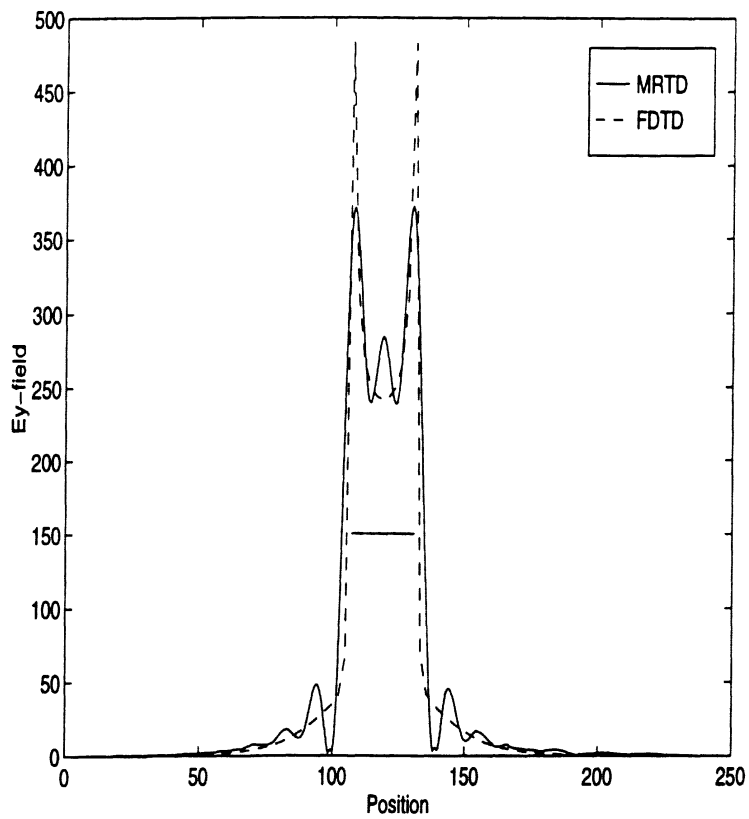


Figure 4.14: Open Single Stripline - E_y TEM Distribution.

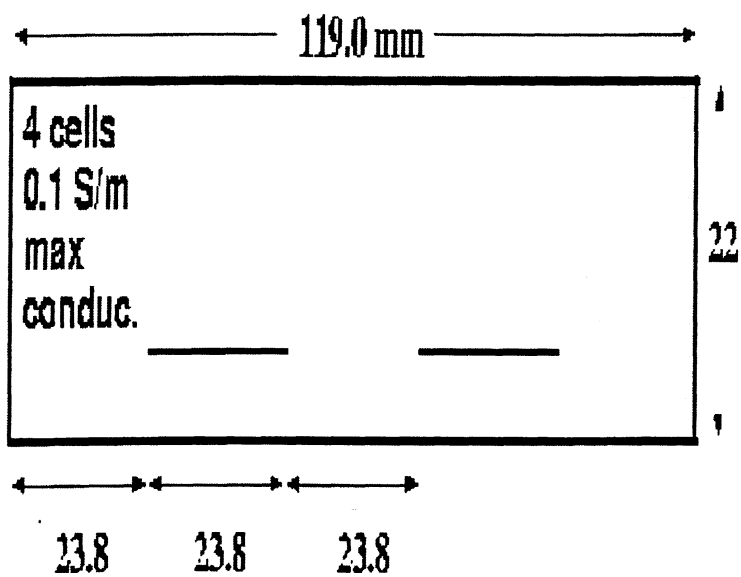


Figure 4.15: Open Coupled Stripline Geometry.

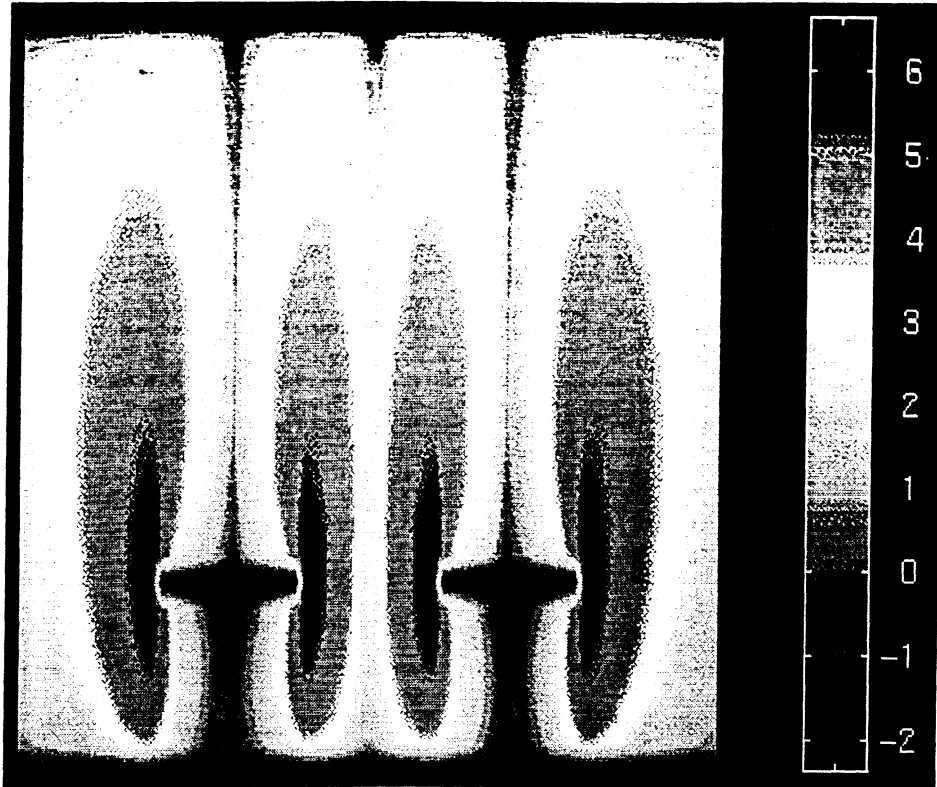


Figure 4.16: Tangential E-field Distribution (Open - Even Mode).

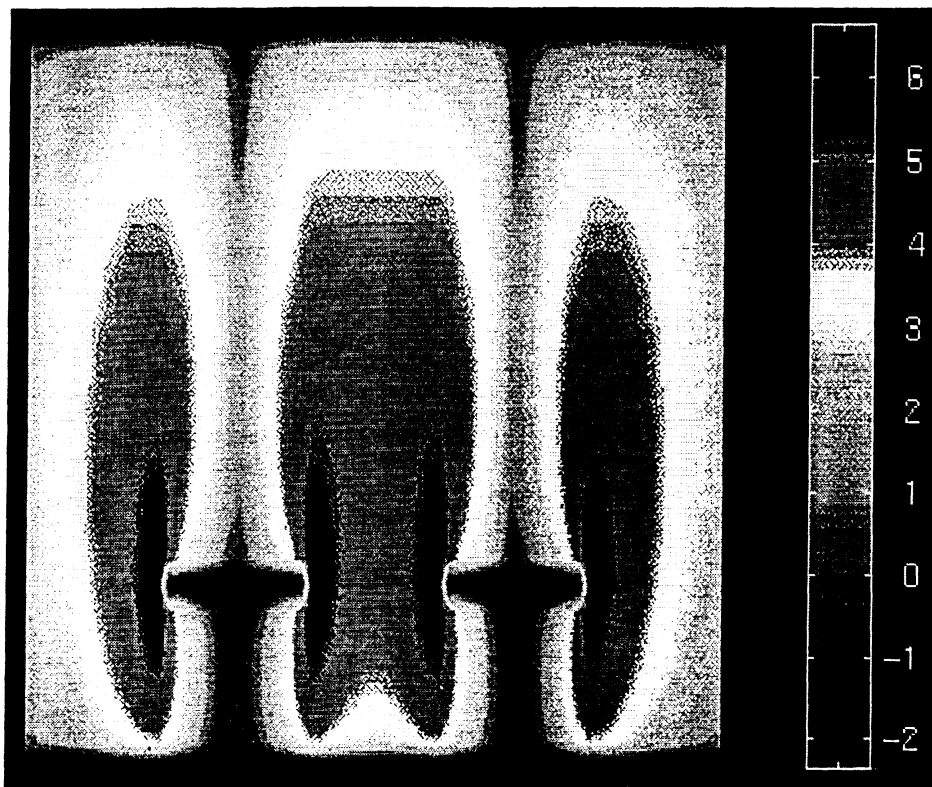


Figure 4.17: Tangential E-field Distribution (Open - Odd Mode).

CHAPTER 5

Stability and Dispersion Analysis of Multiresolution Time-Domain Schemes

5.1 Introduction

Discretized Time-Domain numerical techniques are very popular in the analysis of various microwave geometries and for the modelling of EM wave propagation. Though many of them are very simple to implement and can be easily applied to different topologies with remarkable accuracy, they cause a numerical phase error during the propagation along the discretized grid [57]. For example, the numerical phase velocity in the FDTD can be different than the velocity of light, depending on the cell size as a fraction of the smallest propagating wavelength and the direction of the grid propagation. Thus, a non-physical dispersion is introduced and affects the accuracy limits of FDTD simulations, especially of large structures.

In addition, it is well-known that the finite-difference schemes in time and space domain require that the used time step should take values within an interval that is a function of the cell size. If the time-step takes a value outside the bounds of this interval, the algorithm will be numerically unstable, leading to a spurious increase of the field values without limit

as the time increases.

Though the stability and the dispersion analysis for the conventional Yee's FDTD algorithm has been thoroughly investigated, only a few results have been presented concerning MRTD schemes based on cubic spline Battle-Lemarie scaling and wavelet functions [26]. The functions of this family do not have compact support, thus the finite approximations of the derivatives are finite-stencil summations instead of finite differences. In this paper, the effect of these stencils' size as well as of the enhancement of wavelets is investigated and a comparison with 2nd-order and higher-order FDTD schemes exhibits the differences in their respective behaviors.

5.2 Stability Analysis

Following the stability analysis described in [57], the MRTD [26] equations are decomposed into separate time and space eigenvalue problems. Assuming a 2D expansion only to scaling functions (S-MRTD) similar to Eqs.(3.36)-(3.38) of CH.3, the left-hand side time-differentiation parts can be written as an eigenvalue problem

$$\frac{{}^{k+1/2}H_{i,j-1/2}^x - {}^{k-1/2}H_{i,j-1/2}^x}{\Delta t} = \Lambda {}^k H_{i,j-1/2}^x \quad (5.1)$$

$$\frac{{}^{k+1/2}H_{i-1/2,j}^y - {}^{k-1/2}H_{i-1/2,j}^y}{\Delta t} = \Lambda {}^k H_{i,j-1/2}^y \quad (5.2)$$

$$\frac{{}^{k+1}E_{i,j}^z - {}^k E_{i,j}^z}{\Delta t} = \Lambda {}^{k+1/2} E_{i,j}^z \quad (5.3)$$

In order to avoid having any spatial mode increasing without limit during normal time-stepping, the imaginary part of Λ , $Imag(\Lambda)$, must satisfy the equation

$$-\frac{2}{\Delta t} \leq Imag(\Lambda) \leq \frac{2}{\Delta t} \quad (5.4)$$

For each time step k , the instantaneous values of the electric and magnetic fields distributed in space across the grid can be Fourier-transformed with respect to the i - and j - coordinates

to provide a spectrum of sinusoidal modes (plane wave eigenmodes of the grid). Assuming an eigenmode of the spatial-frequency domain with k_x and k_y being the x- and y- components of the numerical eigenvector, the field components can be written

$$\begin{aligned} E_{I,J}^z &= E_{z_0} e^{j(k_x I \Delta x + k_y J \Delta y)} \\ H_{I,J-1/2}^x &= H_{x_0} e^{j(k_x I \Delta x + k_y (J-1/2) \Delta y)} \\ H_{I-1/2,J}^y &= H_{y_0} e^{j(k_x (I-1/2) \Delta x + k_y J \Delta y)} \end{aligned}$$

Substituting these expressions to (5.1)–(5.3) and applying Euler's identity, we get

$$\Lambda^2 = -\frac{4}{\mu\epsilon} \left[\frac{1}{(\Delta x)^2} \left(\sum_{i'=0}^{n_a-1} a(i') \sin(k_x(i+1/2)\Delta x) \right)^2 + \frac{1}{(\Delta y)^2} \left(\sum_{j'=0}^{n_a-1} a(j') \sin(k_y(j+1/2)\Delta y) \right)^2 \right]$$

Thus, Λ is a pure imaginary, which can be bounded for any wavevector $k = (k_x, k_y)$:

$$\begin{aligned} &- 2c \left(\sum_{i'=0}^{n_a-1} |a(i')| \right) \sqrt{\frac{1}{(\Delta x)^2} + \frac{1}{(\Delta y)^2}} \leq \text{Imag}(\Lambda) \\ &\leq 2c \left(\sum_{i'=0}^{n_a-1} |a(i')| \right) \sqrt{\frac{1}{(\Delta x)^2} + \frac{1}{(\Delta y)^2}} \quad , \end{aligned} \quad (5.5)$$

where $c = \frac{1}{\sqrt{\mu\epsilon}}$ is the velocity of the light in the modeled medium.

Numerical stability is maintained for every spatial mode only when the range of eigenvalues given by (5.5) is contained entirely within the stable range of time-differentiation eigenvalues given by (5.4). Since both ranges are symmetrical around zero, it is adequate to set the upper bound of (5.5) to be smaller or equal to (5.4), giving:

$$\Delta t \leq \frac{1}{c \left(\sum_{i'=0}^{n_a-1} |a(i')| \right) \sqrt{\frac{1}{(\Delta x)^2} + \frac{1}{(\Delta y)^2}}} \quad . \quad (5.6)$$

For $\Delta x = \Delta y = \Delta$, the above stability criterion gives

$$\Delta t_{S-MRTD} \leq \frac{\Delta}{c\sqrt{2} \sum_{i'=0}^{n_a-1} |a(i')|} = s_{SS} \frac{\Delta}{c\sqrt{2}} \quad . \quad (5.7)$$

It is known [5] that

$$\Delta t_{FDTD} \leq \frac{1}{c\sqrt{\frac{1}{(\Delta x)^2} + \frac{1}{(\Delta y)^2}}} \quad , \quad (5.8)$$

which gives for $\Delta x = \Delta y = \Delta$

$$\Delta t_{FDTD} \leq \frac{\Delta}{c\sqrt{2}} \quad (5.9)$$

Equations (5.7)–(5.9) show that for same discretization size, the upper bounds of the time-steps of FDTD and S-MRTD are comparable and related through the factor s . The stability analysis can be generalized easily to 3D. The new stability criteria can be derived by the equations (5.7) and (5.9) by substituting the term $\sqrt{2}$ with $\sqrt{3}$.

More complicated expressions can be derived for the maximum allowable time-step for schemes containing scaling and wavelet functions. For simplicity and without loss of generality, it is assumed that the stencil size is equal for all three summations ($n_a = n_b = n_c = n$). The upper bound of the time-step for the 2D MRTD scheme with 0-resolution wavelets to the one (x-direction) or two directions (x- and y-directions) for $\Delta x = \Delta y = \Delta$ is given by

$$\Delta t_{W_0 S-MRTD, max} \approx s_{W_0 S} \frac{\Delta}{c\sqrt{2}}$$

with

$$s_{W_0 S} = \frac{2}{\sqrt{3(\sum_{i'} |a|)^2 + (\sum_{i'} |b_0|)^2 + 2(\sum_{i'} |c_0|)^2 + (\sum_{i'} |a + b_0|)\sqrt{(\sum_{i'} |a - b_0|)^2 + 4(\sum_{i'} |c_0|)^2}}}$$

and

$$\Delta t_{W_0 W_0-MRTD, max} \approx s_{W_0 W_0} \frac{\Delta}{c\sqrt{2}}$$

with

$$s_{W_0 W_0} = \frac{2}{\sqrt{2(\sum_{i'} |a|)^2 + 2(\sum_{i'} |b_0|)^2 + 4(\sum_{i'} |c_0|)^2 + 2(\sum_{i'} |a + b_0|)\sqrt{(\sum_{i'} |a - b_0|)^2 + 4(\sum_{i'} |c_0|)^2}}}$$

where the notation

$$\sum_{k'} |x| = \sum_{k'=0}^{n-1} |x(k')|$$

has been used.

It can be observed that the upper bound of the time step depends on the stencil size n_a, n_b, n_c . This dependence is expressed through the coefficients $s_{SS}, s_{W_0S}, s_{W_0W_0}$, which decrease as the stencil size increases. (Figure 5.1) shows that s_{SS} practically converges to the value 0.6371 after $n_a \geq 10$ and $s_{W_0S} \approx 0.3433$ and $s_{W_0W_0} \approx 0.2625$ for $n_a = n_b = n_c \geq 10$. The expression of s_{SS} can be easily derived by the expressions of s_{W_0S} and $s_{W_0W_0}$ by zeroing out the effect of b_0, c_0 .

5.3 Dispersion Analysis

To calculate the numerical dispersion of the S-MRTD scheme, plane monochromatic traveling-wave trial solutions are substituted in the discretized Maxwell's equations. For example, the E_z component for the TM^z mode has the form

$${}_k E_{I,J}^z = E_{z_0} e^{j(k_x I \Delta x + k_y J \Delta y - \omega k \Delta t)} \quad ,$$

where k_x and k_y are the x- and y- components of the numerical wavevector and ω is the wave angular frequency. Substituting the above expressions into Eqs.(3.36)-(3.38), the following numerical dispersion relation is obtained for the TM^z mode for the S-MRTD Scheme after algebraic manipulation

$$\begin{aligned} \left[\frac{1}{c\Delta t} \sin\left(\frac{\omega\Delta t}{2}\right) \right]^2 &= \left[\frac{1}{\Delta x} \left(\sum_{i'=0}^{n_a-1} a(i') \sin(k_x(i+1/2)\Delta x) \right) \right]^2 \\ &+ \left[\frac{1}{\Delta y} \left(\sum_{j'=0}^{n_a-1} a(j') \sin(k_y(j+1/2)\Delta y) \right) \right]^2 \end{aligned} \quad (5.10)$$

For square unit cells ($\Delta x = \Delta y = \Delta$) and wave propagating at an angle ϕ with respect to x-axis ($k_x = k \cos\phi$ and $k_y = k \sin\phi$), the above expression is simplified to

$$\begin{aligned}
\left[\frac{\Delta}{c\Delta t} \sin\left(\frac{\omega \Delta t}{2}\right)\right]^2 &= \left(\sum_{i'=0}^{n_a-1} a(i') \sin(k \cos\phi (i' + 1/2) \Delta)\right)^2 \\
&+ \left(\sum_{j'=0}^{n_a-1} a(j') \sin(k \sin\phi (j' + 1/2) \Delta)\right)^2 \quad (5.11)
\end{aligned}$$

This equation relates the numerical wavevector, the wave frequency, the cell size and the time-step. Solving this numerically for different angles, time-step sizes and frequencies, the dispersion characteristics can be quantified.

Defining the Courant number $q = (c\Delta t)/\Delta$ and the number of cells per wavelength $n_l = \lambda_{REAL}/\Delta$ and using the definition of the wavevector $k = (2\pi)/\lambda_{NUM}$ the dispersion relationship can be written as

$$\begin{aligned}
\left[\frac{1}{q} \sin(\pi q / n_l)\right]^2 &= \left[\sum_{i'=0}^{n_a-1} a(i') \sin(\pi u (2i' + 1) \cos\phi / n_l)\right]^2 \\
&+ \left[\sum_{j'=0}^{n_a-1} a(j') \sin(\pi u (2j' + 1) \sin\phi / n_l)\right]^2 \quad (5.12)
\end{aligned}$$

where $u = \lambda_{REAL}/\lambda_{NUM}$ is the ratio of the theoretically given to the numerical value of the propagating wavelength and expresses the phase error introduced by the S-MRTD algorithm. To satisfy the stability requirements, q has to be smaller than 0.45 ($= 0.6371/\sqrt{2}$) for the 2D simulations.

The above analysis can be extended to cover the expansion in scaling and 0-resolution wavelet functions in x-, y- or both directions.

The general dispersion relationship is

$$\begin{aligned}
\frac{\mu}{\epsilon} (C_1 C_1 + C_2 C_2 + C_4 C_4 + C_5 C_5) + \left(\frac{\mu}{\epsilon}\right)^2 \left[\frac{(C_4 C_5 + C_5 C_6)^2}{A} + \frac{(C_1 C_2 + C_2 C_3)^2}{B}\right] \\
+ \left(\frac{\mu}{\epsilon}\right)^4 (C_1 C_2 + C_2 C_3)^2 (C_4 C_5 + C_5 C_6)^2 \left(\frac{1}{A} + \frac{1}{B}\right)^2 \frac{1}{F} = 1 \quad (5.13)
\end{aligned}$$

with

$$F = 1 - \left[\frac{\mu}{\epsilon} (C_1 C_2 + C_2 C_3)\right]^2 \frac{1}{A} - \left[\frac{\mu}{\epsilon} (C_4 C_5 + C_5 C_6)\right]^2 \frac{1}{B}$$

Scheme	C_1	C_2	C_3	C_4	C_5	C_6
SS	$\neq 0$	0	0	$\neq 0$	0	0
W_0S	$\neq 0$	0	0	$\neq 0$	$\neq 0$	$\neq 0$
SW_0	$\neq 0$	$\neq 0$	$\neq 0$	$\neq 0$	0	0
W_0W_0	$\neq 0$	$\neq 0$	$\neq 0$	$\neq 0$	$\neq 0$	$\neq 0$

Table 5.1: Coefficients C_i for Different MRTD Schemes

$$- \left[\frac{\mu}{\epsilon} (C_2C_2 + C_3C_3 + C_5C_5 + C_6C_6) \right] \quad (5.14)$$

$$A = 1 - \frac{\mu}{\epsilon} (C_1C_1 + C_2C_2 + C_5C_5 + C_6C_6)$$

$$B = 1 - \frac{\mu}{\epsilon} (C_2C_2 + C_3C_3 + C_4C_4 + C_5C_5) \quad (5.15)$$

. The C_i are defined by

$$\begin{aligned}
C_1 &= -\frac{\Delta t}{\mu \Delta \sin(\omega \Delta t / 2)} \sum_{j'=0}^{n_a} a(j') \sin(k_y(j' + 1/2)\Delta) \\
C_2 &= -\frac{\Delta t}{\mu \Delta \sin(\omega \Delta t / 2)} \sum_{j'=0}^{n_c} c_0(j') \sin(k_y j' \Delta) \\
C_3 &= -\frac{\Delta t}{\mu \Delta \sin(\omega \Delta t / 2)} \sum_{j'=0}^{n_b} b_0(j') \sin(k_y(j' + 1/2)\Delta) \\
C_4 &= -\frac{\Delta t}{\mu \Delta \sin(\omega \Delta t / 2)} \sum_{i'=0}^{n_a} a(i') \sin(k_x(i' + 1/2)\Delta) \\
C_5 &= -\frac{\Delta t}{\mu \Delta \sin(\omega \Delta t / 2)} \sum_{i'=0}^{n_c} c_0(i') \sin(k_x i' \Delta) \\
C_6 &= -\frac{\Delta t}{\mu \Delta \sin(\omega \Delta t / 2)} \sum_{i'=0}^{n_b} b_0(i') \sin(k_x(i' + 1/2)\Delta) \quad (5.16)
\end{aligned}$$

Eq.(5.13) can be applied to the dispersion analysis of SS (only scaling functions), W_0S (0-resolution wavelets only to x-direction), SW_0 (0-resolution wavelets only to y-direction) and W_0W_0 (0-resolution wavelets to both x - and y- directions) following Table (5.1). In case the $C_i \neq 0$, it can be calculated by Eq.(5.16).

The above equation is solved numerically by use of Bisection-Newton-Raphson Hybrid

Technique for different values of n_a , n_b , n_c , n_l , ϕ and q . (Figs.5.2–5.5) show the variation of the numerical phase velocity as a function of the inverse of the Courant number $1/s=1/q$ for stencil sizes $n_a = n_b = n_c = 8, 10, 12, 14$. For each figure, three different discretization sizes are used: 10 cells/wavelength (coarse), 20 cells/wavelength (normal) and 40 cells/wavelength (dense). The results are compared to the respective values of conventional FDTD. It can be observed that the phase error for F.D.T.D. decreases quadratically. The variation of the phase error in M.R.T.D. exhibits some unique features. Though for any stencil size the numerical phase error for M.R.T.D. discretization of $10\text{cells}/\lambda$ is smaller than that of the F.D.T.D. discretization of $40\text{cells}/\lambda$, the M.R.T.D. error doesn't behave monotonically [58]. It decreases up to a certain discretization value and then it starts increasing. This value depends on the stencil size and takes larger values for larger stencils. For example, this value is between 10 and 20 cells/λ for stencil equal to 10, between 20 and 40 cells/λ for stencil=12 and very close to 40 cells/λ for stencil=14 and can be used as a criterion to characterize the discretization range that the M.R.T.D. offers significantly better numerical phase performance than the F.D.T.D.

The phase error caused by the dispersion is cumulative and it represents a limitation of the conventional FDTD Yee algorithm for the simulation of electrically large structures. It can be observed that the error of S-MRTD is significantly lower, allowing the modeling of larger structures. FDTD is derived by expanding the fields in pulse basis. As it is well known the Fourier transform of the pulse is a highly oscillating $\text{Si}(x)$. On the contrary, the Fourier transform of the Battle-Lemarie Cubic spline is similar to a low-pass filter. That "smooth" spectral characteristic offers a much lower phase error even for very coarse (close to 3-4 cells/λ) cells.

By using a larger stencil n_a , the entire-domain oscillating nature of the scaling functions

is better represented. Thus, smoother performance for low discretizations (Fig.5.6) and lower phase error for higher discretizations (Fig.5.7) is achieved as n_a increases from 8 to 12. Wavelets contribute to the improvement of the dispersion characteristics for even coarser cells (close to 2.2-2.4 cells/ λ) as it is demonstrated in (Figs.5.8–5.13). For discretizations above 4 cells/ λ the effect of the wavelets is negligible. (Fig.5.11) and (Fig.5.13) show clearly that the phase error has a minimum for a specific discretization (17 for $n_a = 10$ and 25 for $n_a = 12$).

(Figs.5.14-5.17) show that for discretizations smaller than 30cells/ λ the choice of the Courant number affects significantly the dispersion performance which starts converging to the minimum numerical phase error (0.8 deg/ λ for $n_a = n_b = n_c = 10$ and 0.2 deg/ λ for $n_a = n_b = n_c = 12$) for $1/q$ close to 10. On the contrary, the F.D.T.D. dispersion is almost independent of the Courant number (Figs.5.18–5.19).

It has been claimed in [59] that the S-MRTD Scheme is slightly oscillating and its performance is only comparable with the 14th order accuracy Yee's scheme. Though this is true for the S-MRTD schemes with stencil size of 8, the comparison of the dispersion diagrams of Yee's FDTD scheme, Yee's 16th order (H.F.D.-16) and 22th order (H.F.D.-22) and S-MRTD and Wo-MRTD schemes with different stencils leads to interesting results. For comparison purposes, the values of $\Delta t = \Delta t_{max}/5$ and $\Delta t_{max} = 0.368112\Delta l/c$ have been used and all the dispersion curves are subtracted by the linear dispersion relation for 1D simulations. (Fig.5.20) shows that the S-MRTD scheme with stencil 10 has a comparable performance to the 16th order Yee's scheme. The enhancement of the wavelets for the same stencil improves significantly the dispersion characteristics of the MRTD scheme increasing the dynamic range of ω by approximately 90% and comparing favorable even to the 22th order Yee's scheme. This is expected due to the fact that the scaling+wavelet basis spans

a larger ("more complete") subspace of \mathbb{R} than the scaling functions alone. Both S-MRTD and Wo-MRTD schemes have identical numerical phase errors up to the point that the S-MRTD scheme starts diverging (Fig.5.21). As the stencil size of the Wo-MRTD scheme is increasing from 6 to 12 (Figs.5.22–5.23), the oscillatory variation of the phase error is diminishing to a negligible level generating an almost flat algorithm similar to the higher order Yee's ones.

As a conclusion, due to the poor dispersion performance of the FDTD technique even for 10 cells/wavelength a normal to coarse grid is always required to avoid significant pulse distortions especially for the higher-spatial-frequency components. MRTD offers low dispersion even for sparse grids very close to the Nyquist limit.

5.4 Conclusion

The stability and the dispersion performance of the recently developed Battle-Lemarie MRTD schemes has been investigated for different stencil sizes and for 0-resolution wavelets. Analytical expressions for the maximum stable time-step have been derived. Larger stencils decrease the numerical phase error making it significantly lower than FDTD for low and medium discretizations. Stencil sizes greater than 10 offer a smaller phase error than FDTD even for discretizations close to 40 cells/ λ . The enhancement of wavelets further improves the dispersion performance for discretizations close to the Nyquist limit (2-3 cells/wavelength) making it comparable to that of much denser grids, though it decreases the value of the maximum time-step guaranteeing the stability of the scheme.

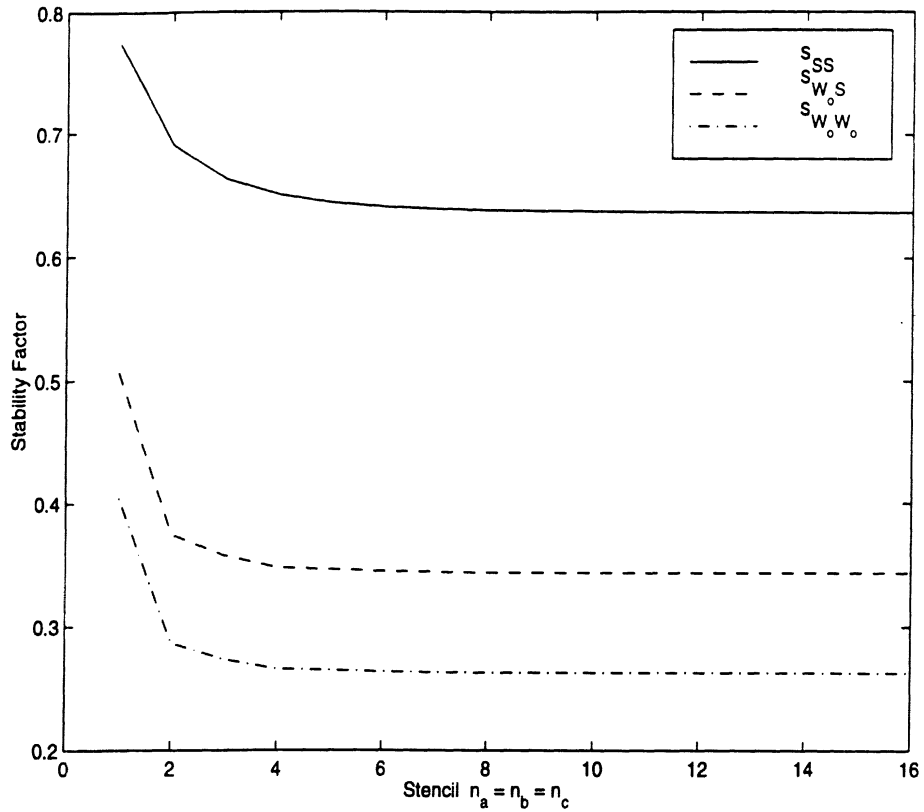


Figure 5.1: Stability Parameter s for MRTD.

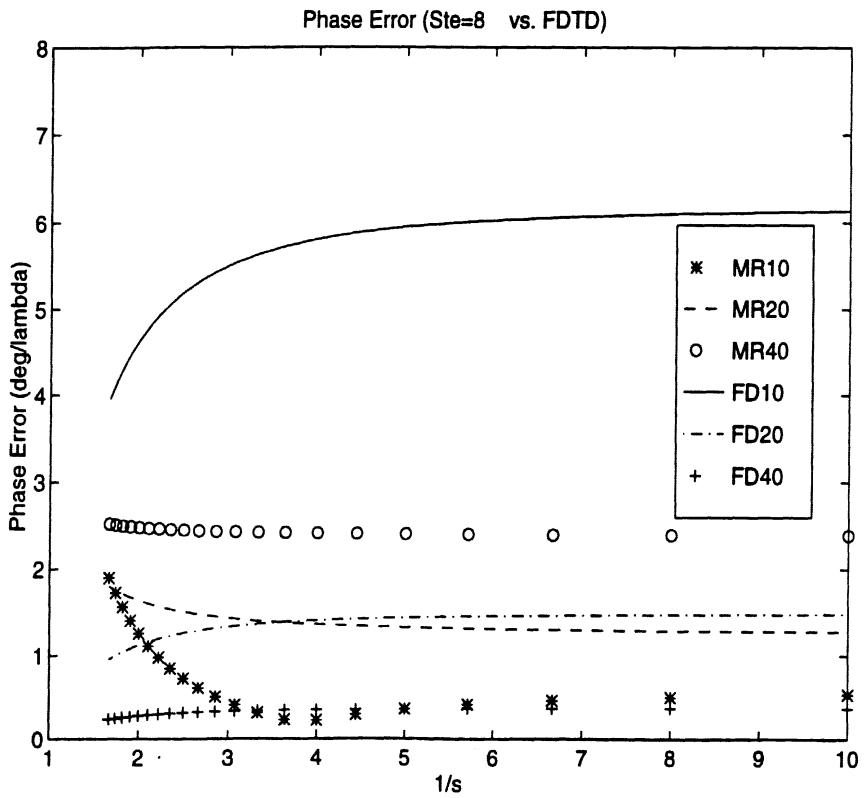


Figure 5.2: Dispersion Characteristics of S-MRTD for $n_a=8$.

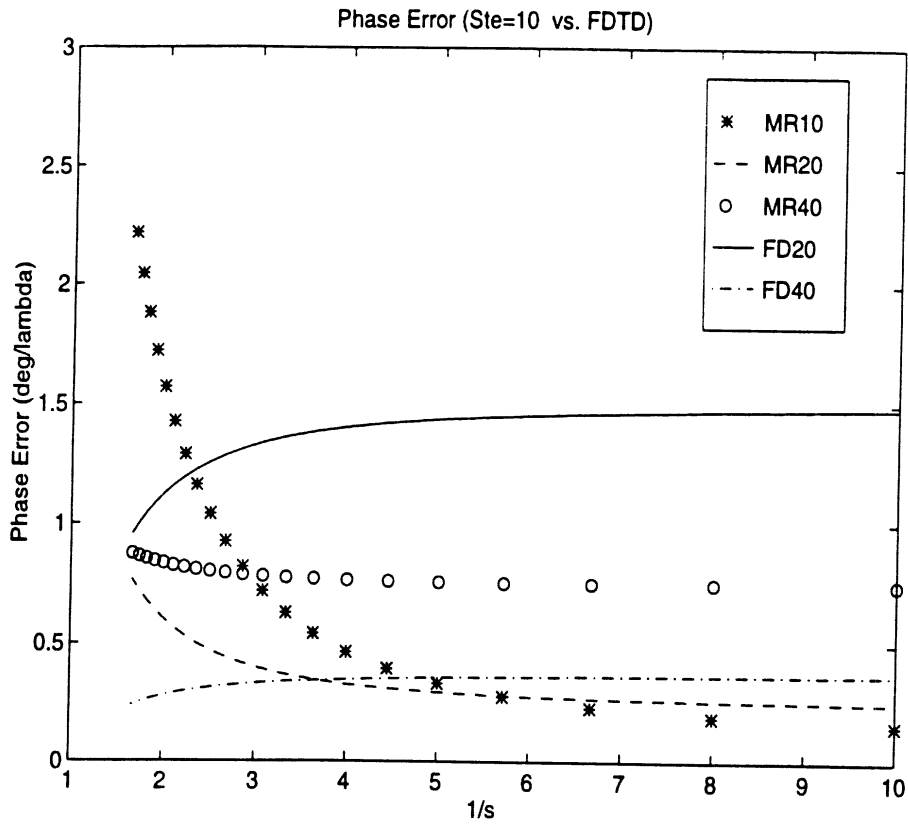


Figure 5.3: Dispersion Characteristics of S-MRTD for $n_a=10$.

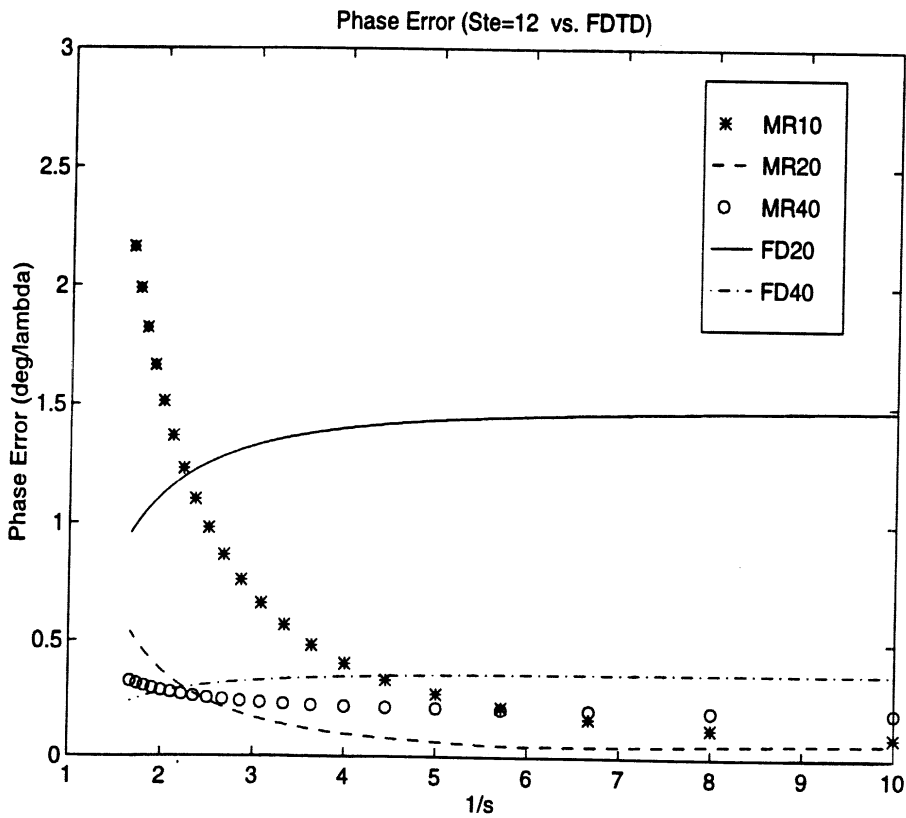


Figure 5.4: Dispersion Characteristics of S-MRTD for $n_a=12$.

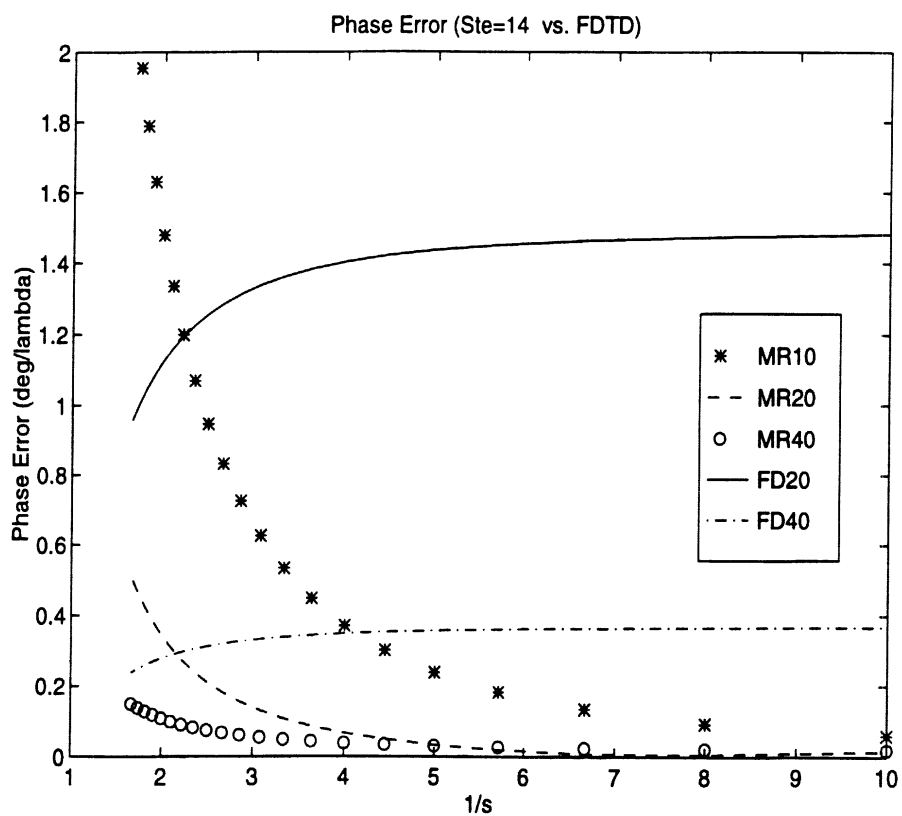


Figure 5.5: Dispersion Characteristics of S-MRTD for $n_a=14$.

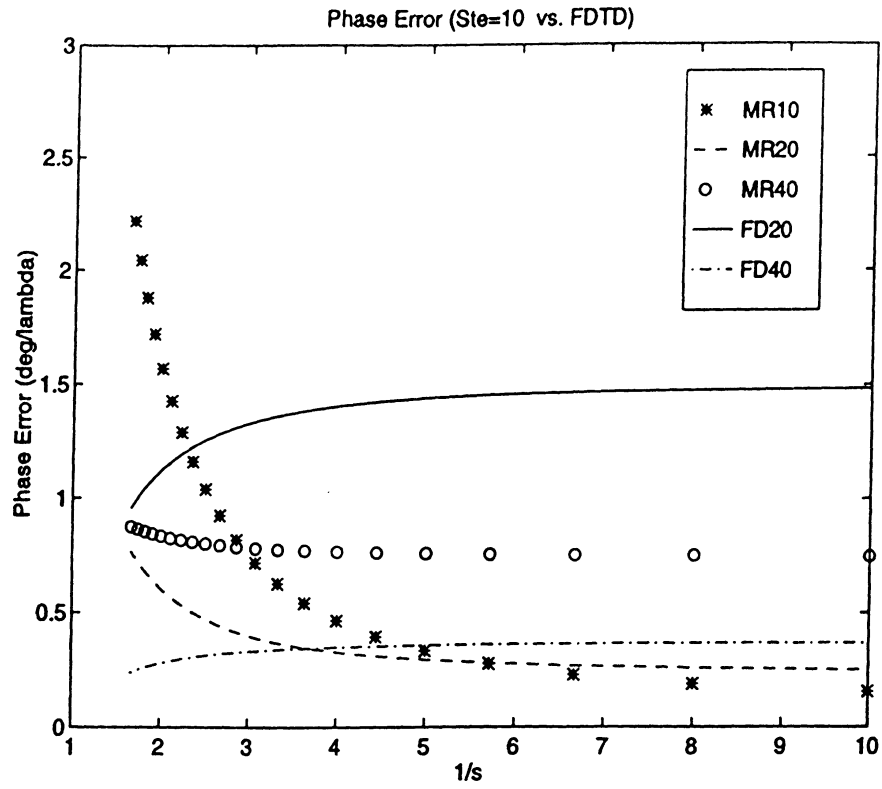


Figure 5.3: Dispersion Characteristics of S-MRTD for $n_a=10$.

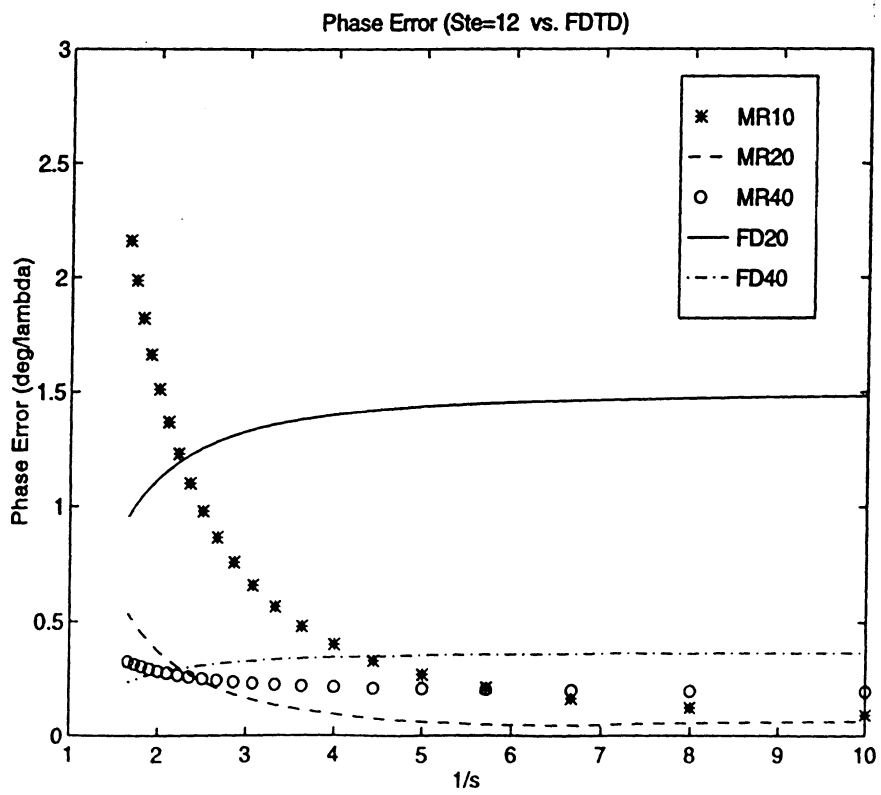


Figure 5.4: Dispersion Characteristics of S-MRTD for $n_a=12$.

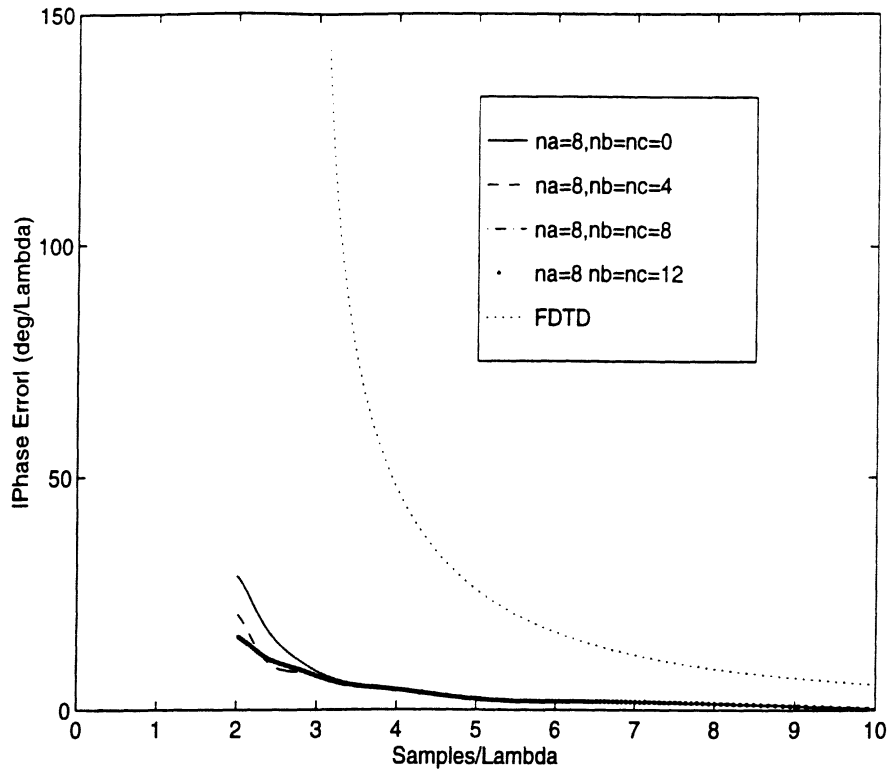


Figure 5.8: Wavelets Effect on the Dispersion Characteristics of MRTD for $n_a=8$ (Coarse Grid).

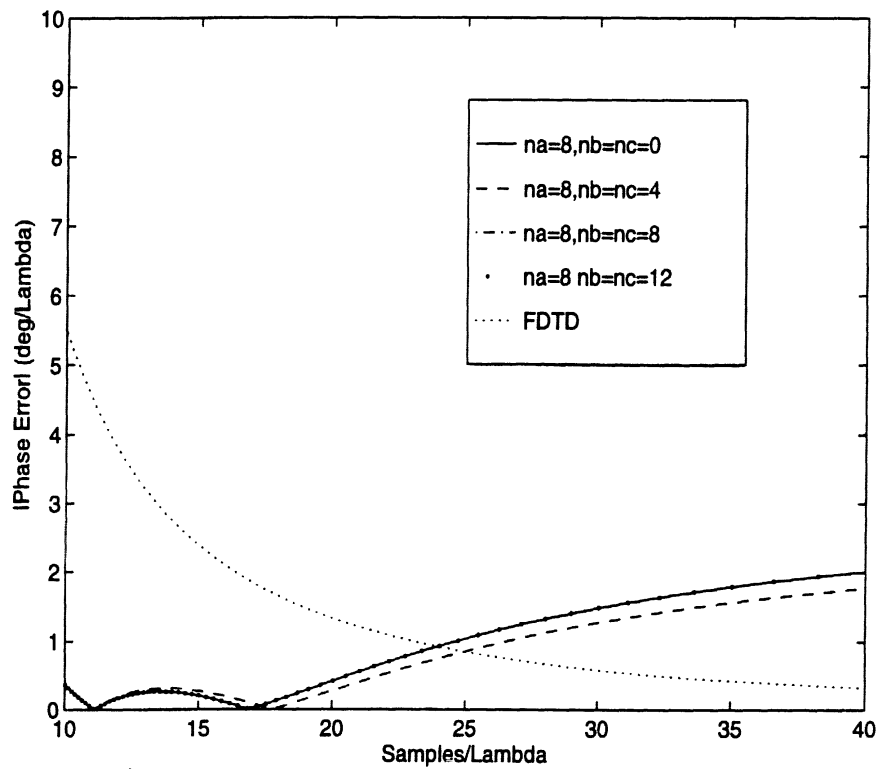


Figure 5.9: Wavelets Effect on the Dispersion Characteristics of MRTD for $n_a=8$ (Denser Grid).

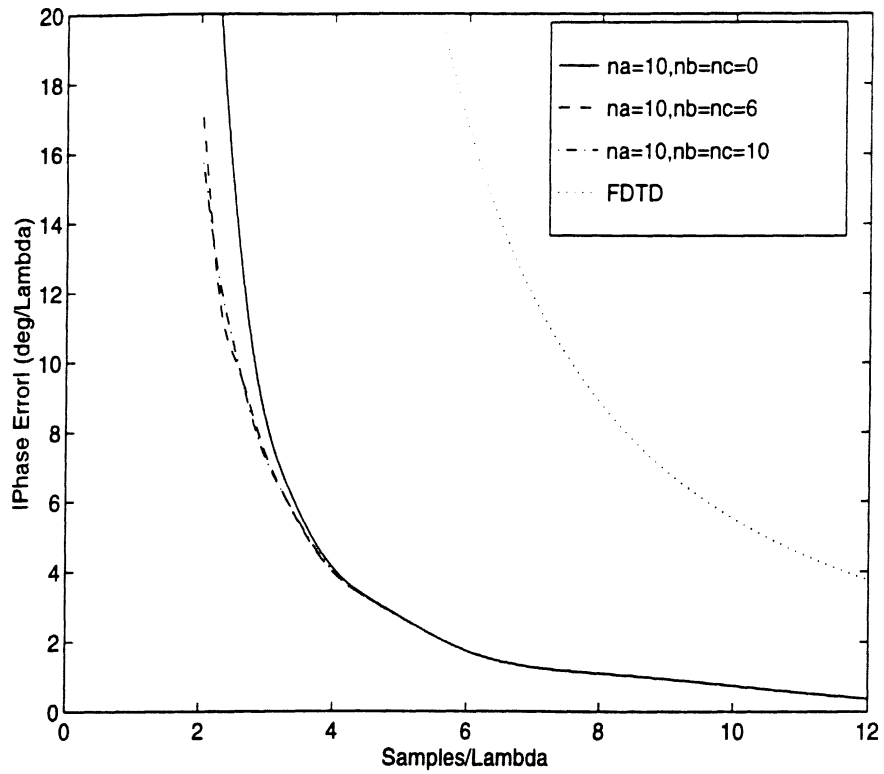


Figure 5.10: Wavelets Effect on the Dispersion Characteristics of MRTD for $n_a=10$ (Coarse Grid).

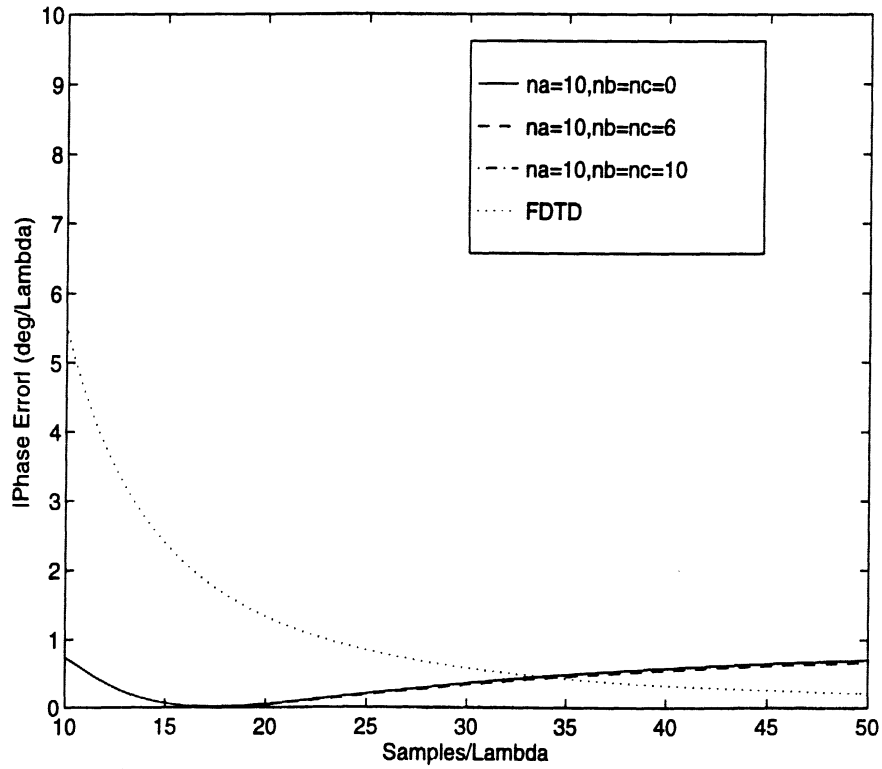


Figure 5.11: Wavelets Effect on the Dispersion Characteristics of MRTD for $n_a=10$ (Denser Grid).

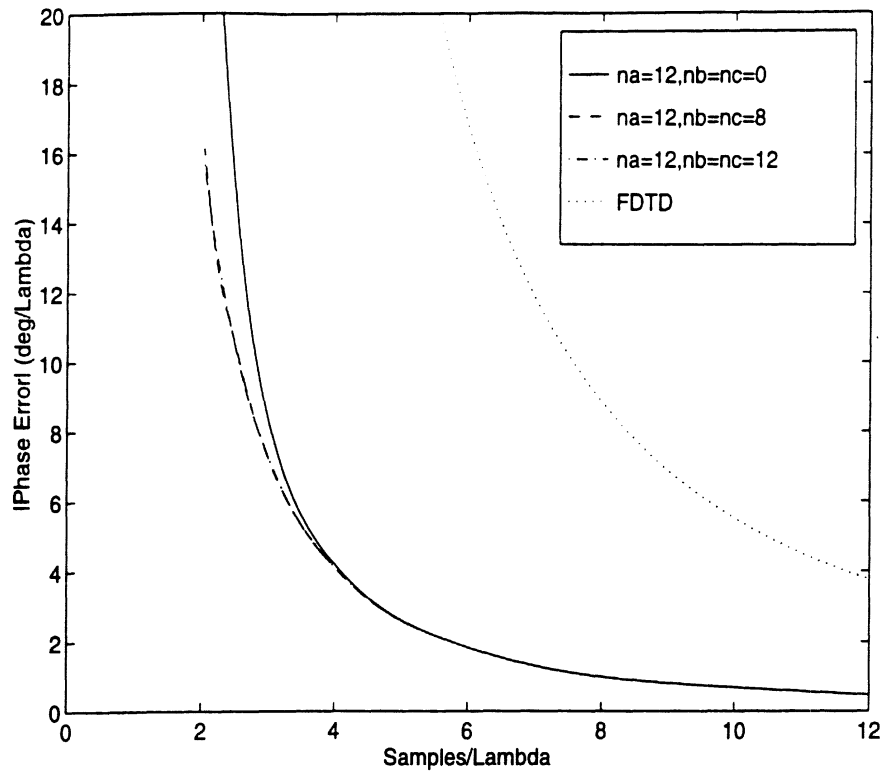


Figure 5.12: Wavelets Effect on the Dispersion Characteristics of MRTD for $n_a=12$ (Coarse Grid).

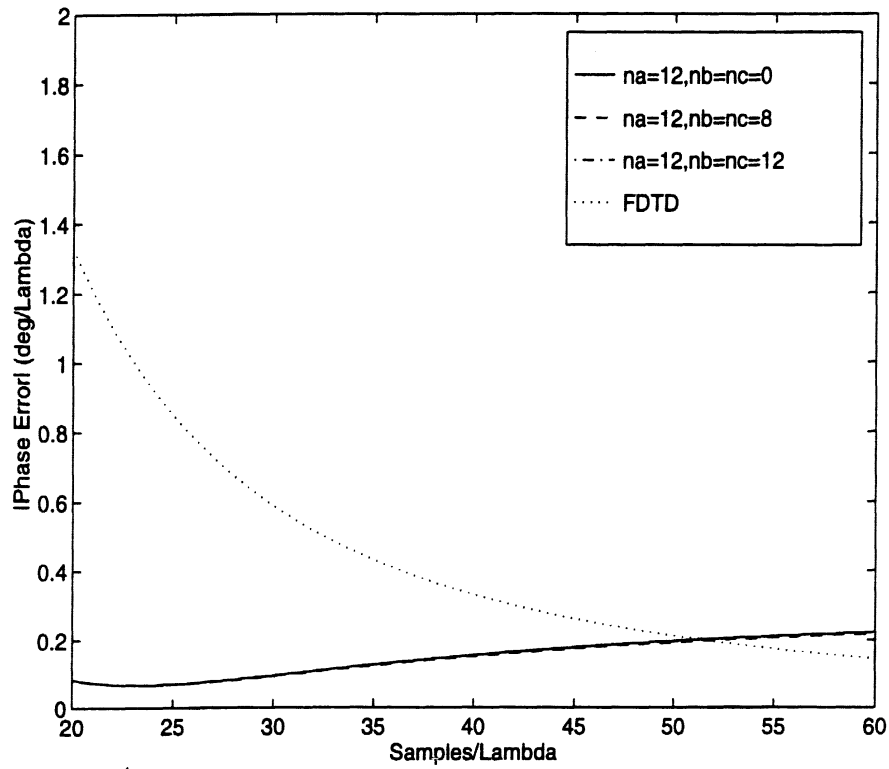


Figure 5.13: Wavelets Effect on the Dispersion Characteristics of MRTD for $n_a=12$ (Denser Grid).

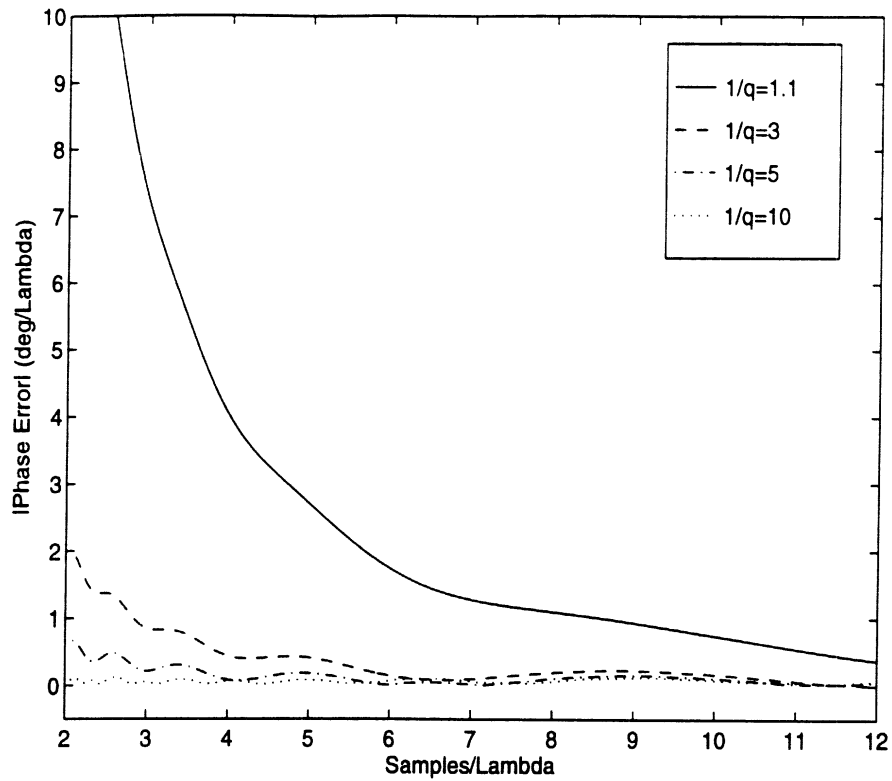


Figure 5.14: Effect of the Courant Number on the Dispersion Characteristics of $W_0 - MRTD$ for $n_a = n_b = n_c = 10$ (Coarse Grid).

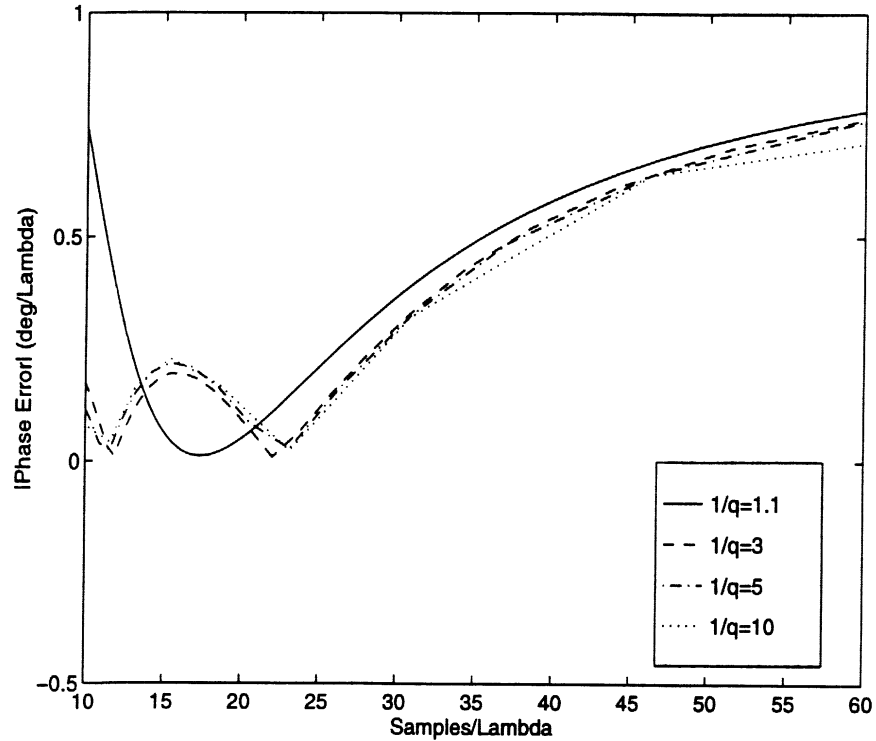


Figure 5.15: Effect of the Courant Number on the Dispersion Characteristics of $W_0 - MRTD$ for $n_a = n_b = n_c = 10$ (Denser Grid).

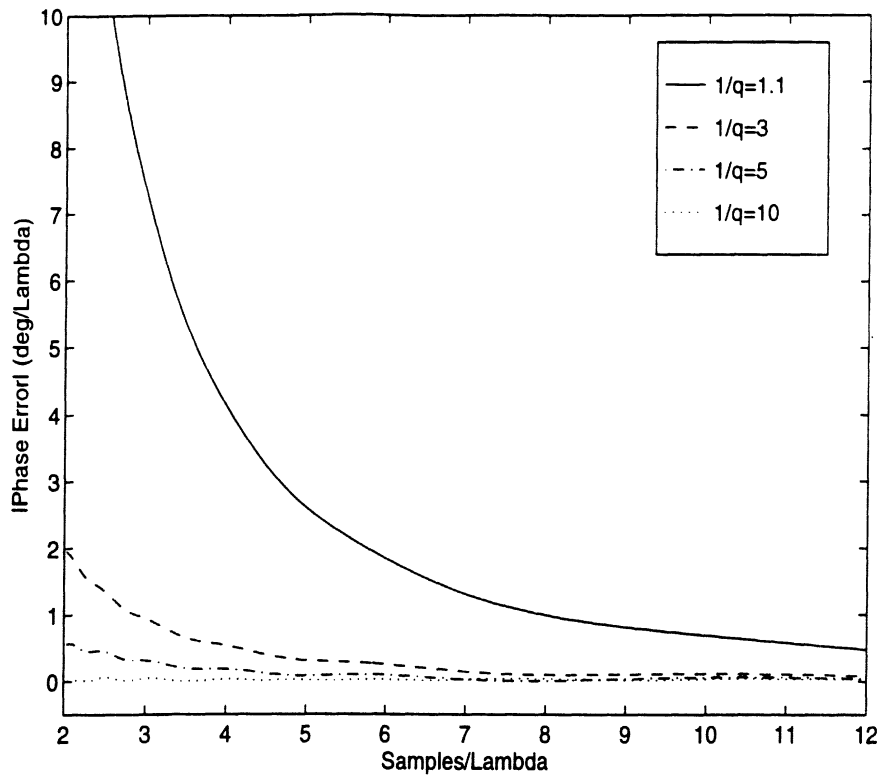


Figure 5.16: Effect of the Courant Number on the Dispersion Characteristics of $W_0 - MRTD$ for $n_a = n_b = n_c = 12$ (Coarse Grid).

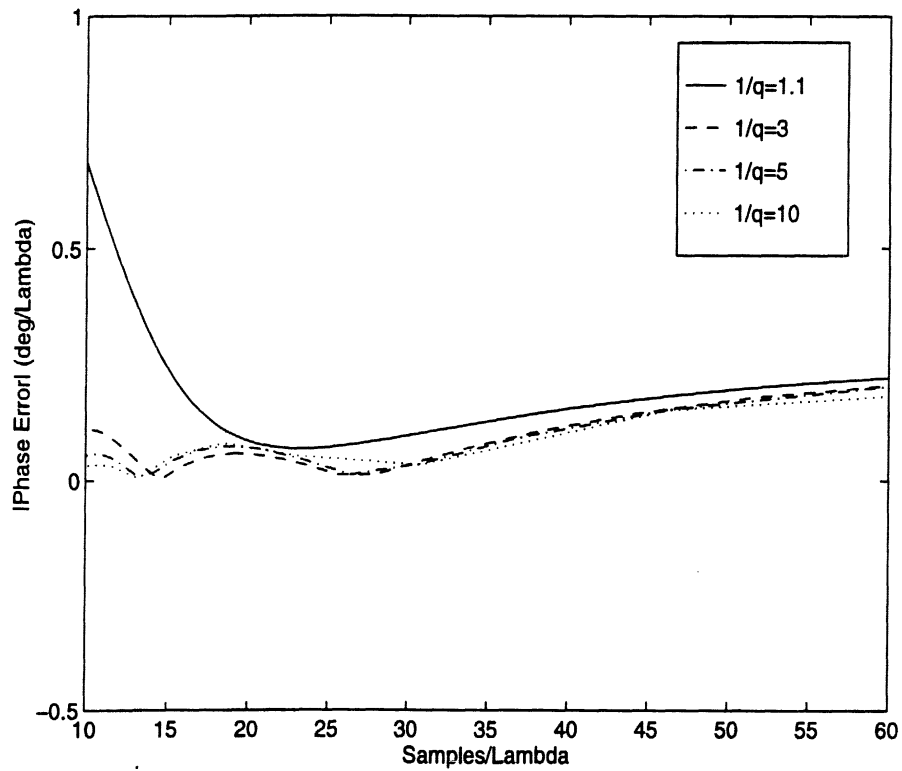


Figure 5.17: Effect of the Courant Number on the Dispersion Characteristics of $W_0 - MRTD$ for $n_a = n_b = n_c = 12$ (Denser Grid).

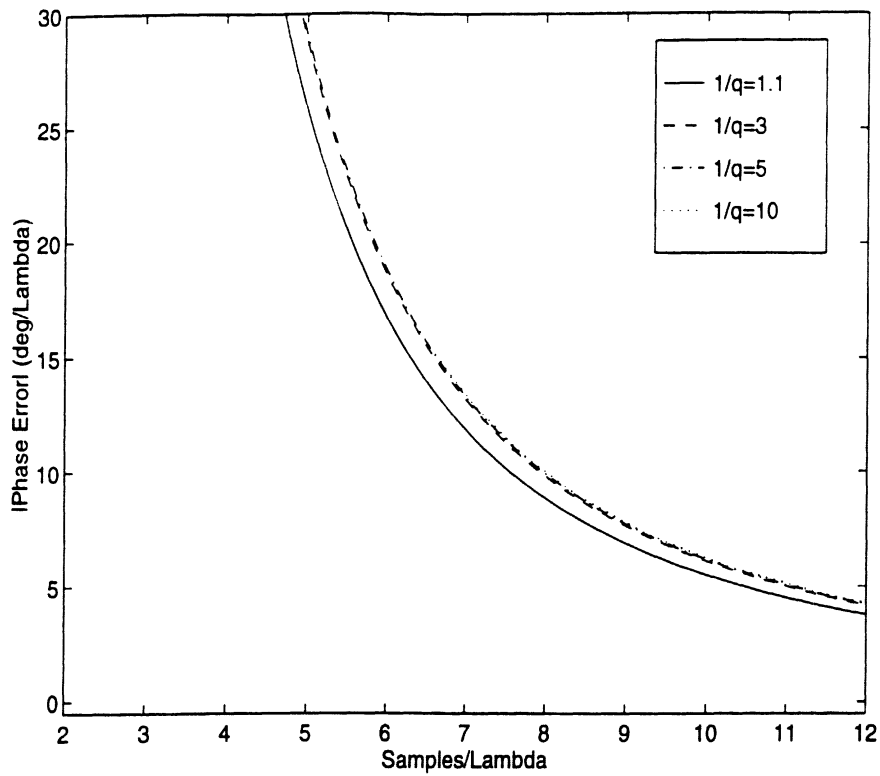


Figure 5.18: Effect of the Courant Number on the Dispersion Characteristics of FDTD (Coarse Grid).

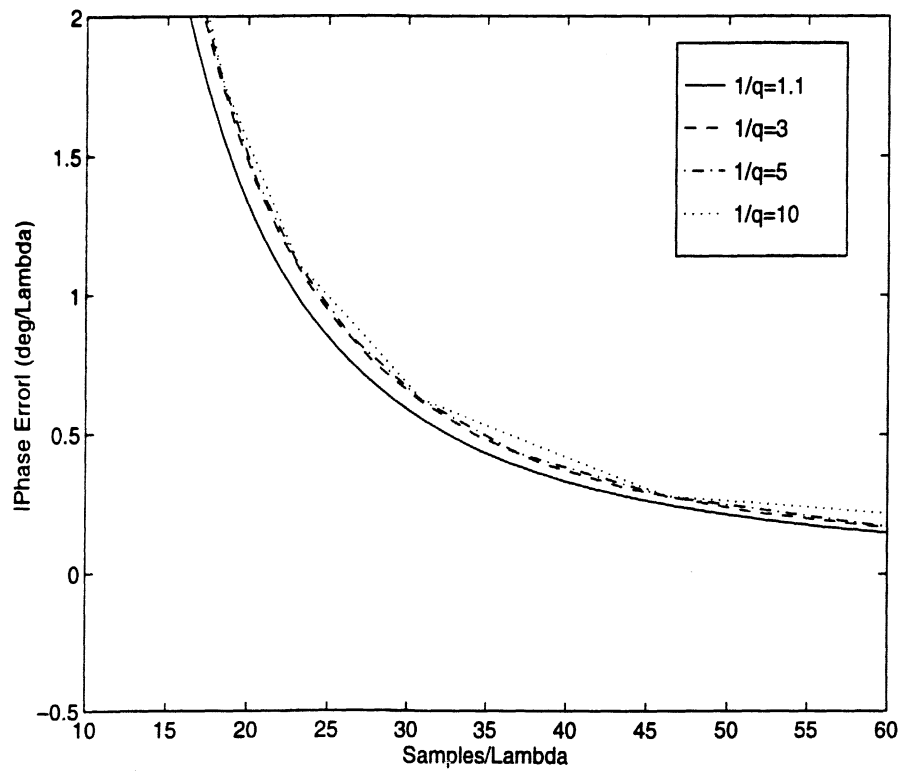


Figure 5.19: Effect of the Courant Number on the Dispersion Characteristics of FDTD (Denser Grid).

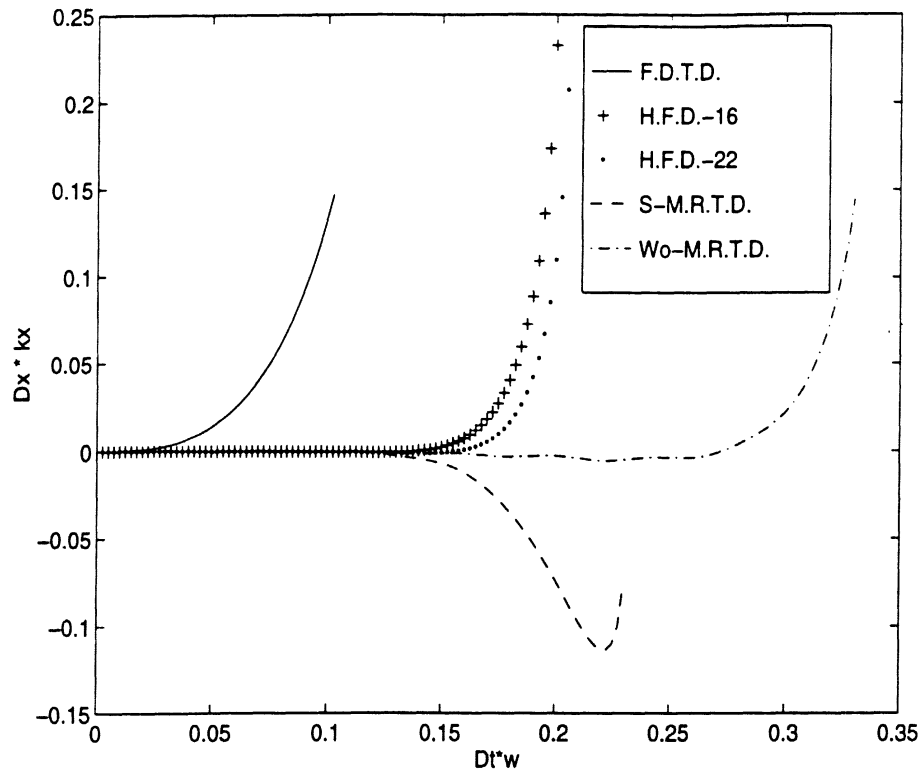


Figure 5.20: Comparison of the Dispersion Performance of S-MRTD and Wo-MRTD with Different Higher Order Yee's Schemes.

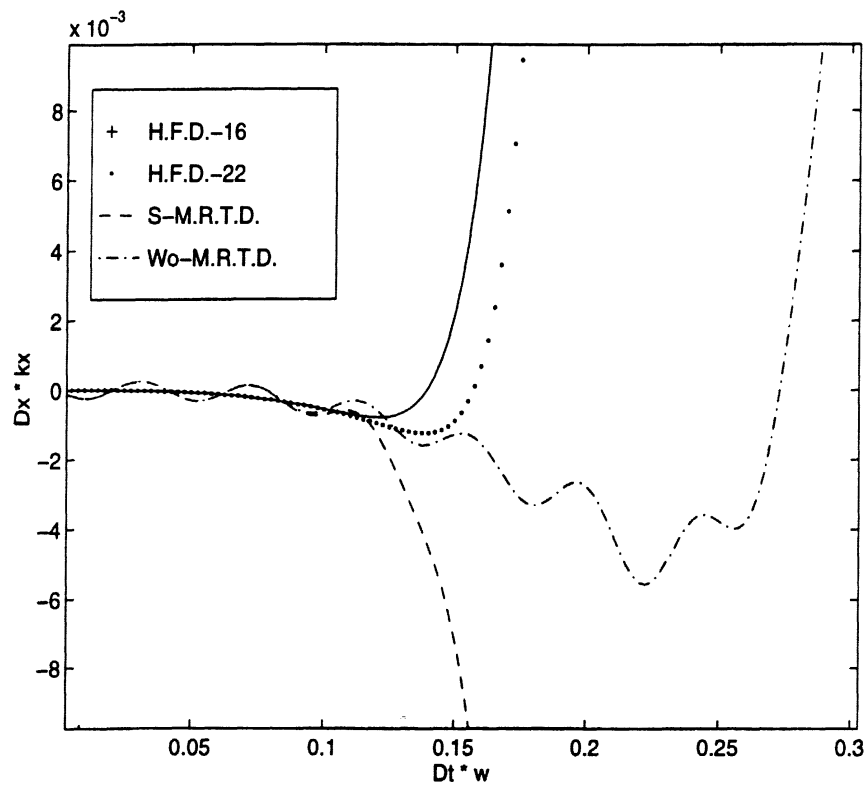


Figure 5.21: Details of Fig.(5.20).

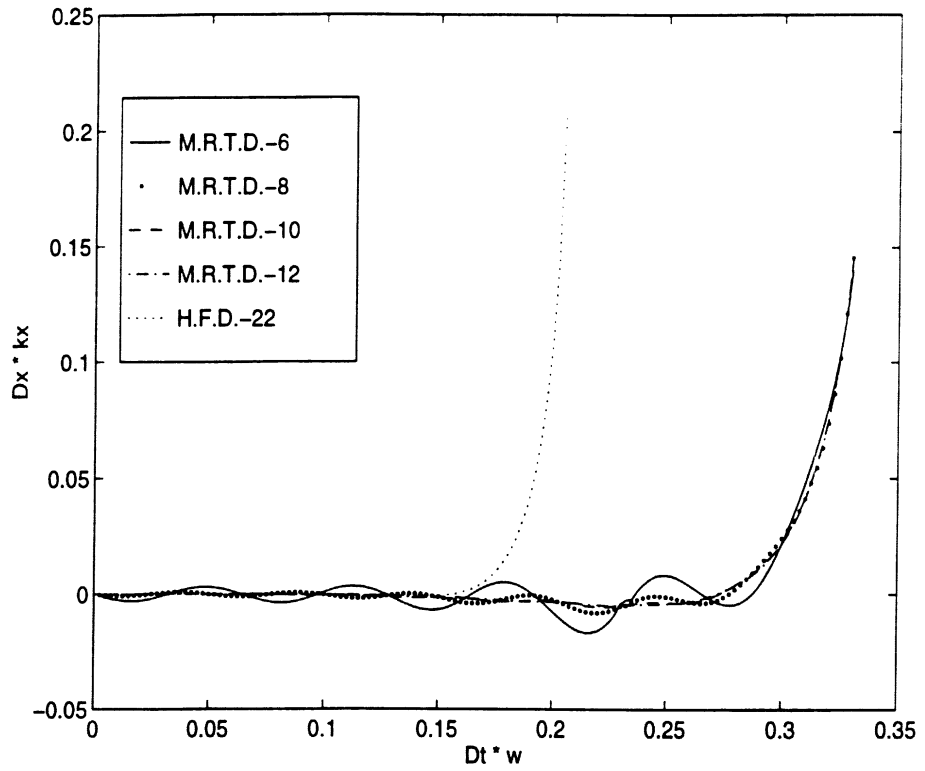


Figure 5.22: Comparison of the Oscillations of Wo-MRTD Scheme for Different Stencil Size.

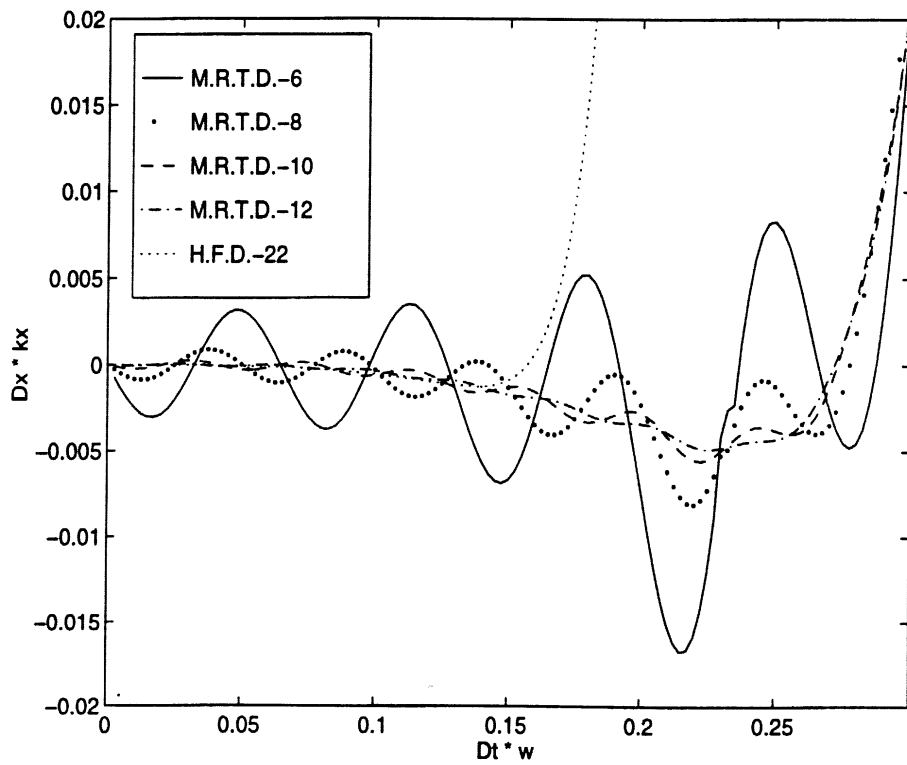


Figure 5.23: Details of Fig.(5.22).

CHAPTER 6

Development of a Space- and Time-Adaptive MRTD Gridding Algorithm for the Analysis of 2D Microwave Dielectric Geometries

6.1 Introduction

In CH.4, the MRTD Technique has been applied to a variety of homogeneous microwave problems and has exhibited significant savings in memory and execution time. Nevertheless the most important advantage of this new technique is its capability to provide space and time adaptive gridding without the problems that the conventional FDTD is encountering. This is due to the use of two separate sets of basis functions, the scaling and wavelets and the capability to threshold the field coefficients due to the excellent conditioning of the formulated mathematical problem. In this Chapter, a space/time adaptive gridding algorithm based on the MRTD scheme is proposed and applied to nonhomogeneous waveguide problems. As an example, the propagation of a Gabor pulse in a partially-filled parallel-plate waveguide is simulated and the S-parameters are evaluated. Wavelets are placed only at locations where the EM fields have significant values, creating a space- and time- adaptive

dense mesh in regions of strong field variations, while maintaining a much coarser mesh elsewhere. The modification of the 2D MRTD algorithm to include dielectric variation is presented and wavelet thresholding approaches are compared and evaluated.

6.2 The 2D-MRTD Nonhomogeneous scheme

6.2.1 The 2D-MRTD scaling and wavelets scheme

For simplicity the 2D-MRTD scheme for the TM_z modes will be used herein. To derive the 2D-MRTD scheme, the field components are represented by a series of cubic spline Battle-Lemarie [25] scaling and wavelet functions up to the r_{max} -resolution to the longitudinal direction in space and pulse functions in time in a similar way to CH3. Due to the entire domain basis functions, D of one cell is related to E values all over the neighboring cells. To circumvent this problem, the CurlD equations have to replace the CurlE equations and then the E-coefficients have to be calculated from the D-coefficients in a mathematically correct way. After inserting the field expansions in Maxwell's equations, we sample them using pulse functions in time and scaling/wavelet functions in space domain.

As an example, sampling $\partial D_x/\partial t, = -\partial H_y/\partial z$ in space and time, the following equations are obtained

$$\begin{aligned} \frac{1}{\Delta t} ({}_{k+1}D_{l+1/2,m}^{\phi x} - {}_kD_{l+1/2,m}^{\phi x}) = & -\frac{1}{\Delta y} \left(\sum_{i=-m_\phi}^{m_\phi} a_\phi^\phi(i)_{k+1/2} H_{l+1/2,m+i+1/2}^{\phi y} \right. \\ & \left. + \sum_{r=0}^{r_{max}} \sum_{p=0}^{2^r-1} \sum_{i=-m_{\psi_{r,p}}^\phi}^{m_{\psi_{r,p}}^\phi} a_{\psi_{r,p}}^\phi(i)_{k+1/2} H_{l+1/2,m+i+(2p+1)/2^{r+1}}^{\psi_{r,p}y} \right) \quad , \quad (6.1) \end{aligned}$$

$$\begin{aligned} \frac{1}{\Delta t} \left({}_{k+1}D_{l+1/2,m+(2p+1)/2^{r+1}}^{\psi_{r,p'}x} - {}_kD_{l+1/2,m+(2p+1)/2^{r+1}}^{\psi_{r,p'}x} \right) = \\ - \frac{1}{\Delta y} \left(\sum_{i=-m_{\psi_{r,p'}}^\phi}^{m_{\psi_{r,p'}}^\phi} a_{\psi_{r,p'}}^{\psi_{r,p'}}(i)_{k+1/2} H_{l+1/2,m+i+1/2}^{\phi y} \right) \end{aligned}$$

$$+ \sum_{r=0}^{r_{max}} \sum_{p=0}^{2^r-1} \sum_{i=-m_{\psi_{r,p}}^{\psi_{r,p'}}}^{m_{\psi_{r,p}}^{\psi_{r,p'}}} a_{\psi_{r,p}}^{\psi_{r,p'}}(i)_{k+1/2} H_{l+1/2, m+i+(2p+1)/2^{r+1}}^{\psi_{r,p}y} \quad , \quad (6.2)$$

where ${}_k D_{l,m}^{\xi x}$ and ${}_k H_{l,m}^{\xi y}$ with $\xi = \phi$ (scaling), $\psi_{r,p}$ (wavelets of r-resolution at the p-position of the cell) are the coefficients for the electric and magnetic field expansions . The indices l, m and k are the discrete space and time indices, which are related to the space and time coordinates via $x = l\Delta x, z = m\Delta z$ and $t = k\Delta t$, where $\Delta x, \Delta z$ are the space discretization intervals in x- and z-direction and Δt is the time discretization interval. The coefficients $a_{\phi}^{\phi}(i), a_{\phi}^{\psi_{0,0}}(i), a_{\psi_{0,0}}^{\phi}(i), a_{\psi_{0,0}}^{\psi_{0,0}}(i)$ are derived in a similar way to CH.3. For an accuracy of 0.1% the values $m_{\phi}^{\phi} = 10 - 12$ and $m_{\phi}^{\psi_{0,0}} = m_{\psi_{0,0}}^{\phi} = m_{\psi_{0,0}}^{\psi_{0,0}} = 8 - 12$ have been used when only the 0-resolution of the wavelets was applied.

6.2.2 The PML numerical absorber

For open structures, the perfectly matched layer (PML) technique can be applied by assuming that the conductivity is given in terms of scaling and wavelet functions instead of pulse functions with respect to space [61]. The PML is characterized by artificial electric and magnetic conductivities σ^E and σ^H , which satisfy the relationship

$$\frac{\sigma_H}{\mu_o} = \frac{\sigma_E}{\epsilon} = \frac{\sigma_D}{\epsilon_o} \quad (6.3)$$

for each cell with constitutive parameters (ϵ, μ_o) . The spatial distribution of the magnetic conductivity for the absorbing layers is modelled by assuming that the amplitudes of the scaling and the wavelet functions have a polynomial distribution (linear, parabolic, ...) and by sampling this distribution with scaling and wavelet functions (Eq.(3.79)). It has been observed that the parabolic distribution is the most computationally efficient. For multidielectric non-magnetic structures, the electric conductivity is given from the above relationship assigning the appropriate ϵ . The MRTD mesh is terminated by a perfect electric

conductor (PEC) at the end of the PML region. Following a procedure similar to (3.4.3) the equations for the D_x scaling components in the PML region are given by

$${}_{k+1}D_{i-1/2,j}^{x,\phi\phi} = e^{-\sigma_D^j \Delta t / \epsilon_o} {}_kD_{i-1/2,j}^{x\phi\phi} - \epsilon^{-0.5\sigma_D^j \Delta t / \epsilon_o} \frac{\Delta t}{\epsilon_o \Delta y} \left(\sum_{j'=-n_a}^{n_a-1} a(j')_{k+1/2} H_{i-1/2,j+j'+1/2}^{y,\phi\phi} \right. \\ \left. + \sum_{r=0}^{r_{max}} \sum_{p=0}^{2^r-1} \sum_{j'=-m_{\psi_{r,p}}^{\phi}}^{m_{\psi_{r,p}}^{\phi}} a_{\psi_{r,p}}^{\phi}(i)_{k+1/2} H_{i-1/2,j+j'+(2p+1)/2^{r+1}}^{y,\phi\psi_{r,p}} \right) \quad (6.4)$$

Similar equations can be obtained for the wavelet equations. For the simulations presented in this paper, there are used 24 cells of PML medium with σ_H for designated $R_{max}=1.e-6$ for MRTD (coarser mesh) and for $R_{max}=1.e-7$ for FDTD (4 times/dimension finer mesh) which provide reflection coefficients in the region of -80 to -90 dB.

6.2.3 The Excitation Implementation

In order to implement an excitation $E_F(t)$ at $z = m\Delta z$ and to obtain an excitation identical to an FDTD excitation (pulse excitation with respect to space), the space pulse is decomposed in terms of scaling and wavelet functions.

$${}_kE_m^{exc} \approx E_F(k\Delta t) \left(\sum_{i=-\zeta_{\phi}}^{\zeta_{\phi}} c_{\phi}(i) \phi_{m+i} + \sum_{r=0}^{r_{max}} \sum_{p=0}^{2^r-1} \sum_{i=-\zeta_{\psi_{r,p}}}^{\zeta_{\psi_{r,p}}} c_{\psi_{r,p}}(i) \psi_{m+i}^{r,p} \right) \quad (6.5)$$

where the coefficients $c_{\phi}(i), c_{\psi_{0,1}}(i), c_{\psi_{1,1}}(i), c_{\psi_{1,2}}(i)$ (wavelets of 0- and 1-resolutions) are given in Chapter 3. For $i < 0$ it is $c_{\phi}(-i) = c_{\phi}(i)$, $c_{\psi_{0,1}}(i) = c_{\psi_{0,1}}(-1-i)$, $c_{\psi_{1,1}}(i) = c_{\psi_{1,2}}(-1-i)$ and $c_{\psi_{1,2}}(i) = c_{\psi_{1,1}}(-1-i)$. The above excitation components are superimposed to the field values obtained by the MRTD algorithm for the same time step. For example, the total ${}_kE_{m+i}^{\phi}$ will be given by

$${}_kE_{m+i}^{\phi} \Big|_{total} = E_F(k\Delta t) c_{\phi}(i) + E_{k,m+i}^{\phi} \quad (6.6)$$

It has been observed that the minimum limits of the summations for an accuracy of 0.1% are $\zeta_{\phi} = \zeta_{\psi_{0,0}}=4$ and $\zeta_{\psi_{1,0}} = \zeta_{\psi_{1,1}}=3$ for the first 2 resolutions of the wavelets ($r_{max}=1$).

Similar accuracy can be observed when the scaling function at the excitation cell is set equal to the value of the excitation function $E_F(t)$. No superposition is used and the field scaling and wavelet values elsewhere are given by the MRTD equations. The wavelet coefficients are excited through the coupling of the discretized MRTD equations. In the following numerical simulations the latter excitation technique was employed since it adds significantly smaller computational overhead.

6.2.4 The Modelling of Dielectrics

Starting from the constitutive relationship $D = \epsilon E$ for the total electric field at one mesh point and sampling the scaling and wavelet components with a similar way to (A) we reach the following equations for D_x

$${}_k D_{i,j}^\phi = \sum_{j'=-l_\phi}^{l_\phi} c_{\phi d}^\phi(j') {}_k E_{i,j+j'}^\phi + \sum_{r=0}^{r_{max}} \sum_{p=0}^{2^r-1} \sum_{j'=-l_{\psi_{r,p}}}^{l_{\psi_{r,p}}} c_{\psi_{r,p}d}^\phi(j') {}_k E_{i,j+j'}^{\psi_{r,p}} \quad (6.7)$$

and

$${}_k D_{i,j}^{\psi_{r',p'}} = \sum_{j'=-\xi_\phi}^{\xi_\phi} c_{\phi d}^{\psi_{r',p'}}(j') {}_k E_{i,j+j'}^\phi + \sum_{r=0}^{r_{max}} \sum_{p=0}^{2^r-1} \sum_{j'=-\xi_{\psi_{r,p}}}^{\xi_{\psi_{r,p}}} c_{\psi_{r,p}d}^{\psi_{r',p'}}(j') {}_k E_{i,j+j'}^{\psi_{r,p}} \quad (6.8)$$

where

$$c_{\phi d}^\phi(j') = \int_{-\infty}^{\infty} \epsilon \phi_k(z) \phi_{k+j'}(z) dz \quad (6.9)$$

$$c_{\phi d}^{\psi_{r,p}}(j') = \int_{-\infty}^{\infty} \epsilon \phi_k(z) \psi_{k+j'}^{r,p}(z) dz \quad (6.10)$$

$$c_{\psi_{r',p'}d}^\phi(j') = \int_{-\infty}^{\infty} \epsilon \psi_k^{r',p'}(z) \phi_{k+j'}(z) dz \quad (6.11)$$

$$c_{\psi_{r',p'}d}^{\psi_{r,p}}(j') = \int_{-\infty}^{\infty} \epsilon \psi_k^{r',p'}(z) \psi_{k+j'}^{r,p}(z) dz \quad (6.12)$$

Equations (6.7) and (6.8) can be written in a compact form

$$[\bar{D}] = [\bar{\epsilon}][\bar{E}] \quad (6.13)$$

For geometries with dielectrics varying from air ($\epsilon_r=1$) to Si ($\epsilon_r=2.56$), it was observed that the above summations can be truncated for $l_\phi=l_{\psi_{0,0}}=\xi_\phi=\xi_{\psi_{0,0}}=6$ when only one resolution of wavelets ($r_{max}=0$) was used. Also, the integrals can be approximated by finite summations of 10 cells on each side of the central cell (k-cell).

Due to the orthogonality relationship between the scaling and the wavelet functions, for uniform dielectrics (constant ϵ throughout the integration domain) these integrals are simplified to $c_{\phi d}^\phi = \epsilon \delta_{i,0}$, $c_{\phi d}^{\psi_{r,p}} = c_{\psi_{r',p'}}^\phi = 0$ and $c_{\psi_{r',p'} d}^{\psi_{r,p}}(i) = \epsilon \delta_{r',r} \delta_{p',p} \delta_{i,0}$ and $[\bar{\epsilon}]$ becomes a diagonal matrix. For structures containing dielectric discontinuities, none of these integrals have a zero value. In this case, the whole geometry has to be preprocessed before the initialization of the time loop and coefficients $c_{\phi d}^\phi, c_{\phi d}^{\psi_{r,p}}, c_{\psi_{r',p'} d}^\phi, c_{\psi_{r',p'} d}^{\psi_{r,p}}$ have to be assigned to any cell (m,n) and included in the matrix $[\bar{\epsilon}]$. For each cell the amplitude of these coefficients is compared to the amplitude of the self-term $c_{\phi d}^\phi(i)$. If all coefficients are below a threshold (usually $\leq 0.1\%$), they are set to zero and this cell is exempted from the following inversion, otherwise it is included in a new submatrix. This submatrix has significantly smaller dimensions than $[\bar{\epsilon}]$ (usually $\leq 10\%$) and contains only cells close to dielectric discontinuities. The inverse of this matrix is used for the calculation of the E from the D values for each time step. The inversion takes place only once, thus it adds only negligible computational overhead to the algorithm.

6.2.5 Total Field Calculation

Due to the nature of the Battle-Lemarie expansion functions, the total field is a summation of the contributions from the non-localized scaling and wavelet functions. For example, the total electric field $E_x(x_o, z_o, t_o)$ with $(i-1)\Delta x < x_o < i\Delta x$, $(j-1/2)\Delta z < z_o < (j+1/2)\Delta z$ and $(k-1/2)\Delta t < t_o < (k+1/2)\Delta t$ is calculated in the same way with

Similar accuracy can be observed when the scaling function at the excitation cell is set equal to the value of the excitation function $E_F(t)$. No superposition is used and the field scaling and wavelet values elsewhere are given by the MRTD equations. The wavelet coefficients are excited through the coupling of the discretized MRTD equations. In the following numerical simulations the latter excitation technique was employed since it adds significantly smaller computational overhead.

6.2.4 The Modelling of Dielectrics

Starting from the constitutive relationship $D = \epsilon E$ for the total electric field at one mesh point and sampling the scaling and wavelet components with a similar way to (A) we reach the following equations for D_x

$${}_k D_{i,j}^\phi = \sum_{j'=-l_\phi}^{l_\phi} c_{\phi_d}^\phi(j') {}_k E_{i,j+j'}^\phi + \sum_{r=0}^{r_{\max}} \sum_{p=0}^{2^r-1} \sum_{j'=-l_{\psi_{r,p}}}^{l_{\psi_{r,p}}} c_{\psi_{r,p,d}}^\phi(j') {}_k E_{i,j+j'}^{\psi_{r,p}} \quad (6.7)$$

and

$${}_k D_{i,j}^{\psi_{r',p'}} = \sum_{j'=-\xi_\phi}^{\xi_\phi} c_{\phi_d}^{\psi_{r',p'}}(j') {}_k E_{i,j+j'}^\phi + \sum_{r=0}^{r_{\max}} \sum_{p=0}^{2^r-1} \sum_{j'=-\xi_{\psi_{r,p}}}^{\xi_{\psi_{r,p}}} c_{\psi_{r,p,d}}^{\psi_{r',p'}}(j') {}_k E_{i,j+j'}^{\psi_{r,p}} \quad (6.8)$$

where

$$c_{\phi_d}^\phi(j') = \int_{-\infty}^{\infty} \epsilon \phi_k(z) \phi_{k+j'}(z) dz \quad (6.9)$$

$$c_{\phi_d}^{\psi_{r,p}}(j') = \int_{-\infty}^{\infty} \epsilon \phi_k(z) \psi_{k+j'}^{r,p}(z) dz \quad (6.10)$$

$$c_{\psi_{r',p',d}}^\phi(j') = \int_{-\infty}^{\infty} \epsilon \psi_k^{r',p'}(z) \phi_{k+j'}(z) dz \quad (6.11)$$

$$c_{\psi_{r',p',d}}^{\psi_{r,p}}(j') = \int_{-\infty}^{\infty} \epsilon \psi_k^{r',p'}(z) \psi_{k+j'}^{r,p}(z) dz \quad (6.12)$$

Equations (6.7) and (6.8) can be written in a compact form

$$[\bar{D}] = [\bar{\epsilon}][\bar{E}] \quad (6.13)$$

1/10000 of the peak of the excitation time-domain function). This comparison is repeated for each time-step (time adaptiveness). All components below this threshold are eliminated from the subsequent calculations. This is the simplest thresholding algorithm. It doesn't add any significant overhead in execution time (usually $\leq 10\%$), but it offers only a moderate (pessimistic) economy in memory (factor close to 2). Also, this algorithm allows for the dynamic memory allocation in its programming implementation by using the appropriate programming languages (e.g. C).

The principles of the dynamically changing time- and space-adaptive grid are demonstrated in (Fig.6.1). A pulse is propagating from the left to the right in a partially filled parallel plate waveguide. For $t=0$, the wavelets are localized at the excitation area. They follow the propagating pulse (t before the incidence to the dielectric interface) creating a moving dense subgrid. After the pulse has been split in reflected and transmitted pulses, the wavelets increase the grid resolution only around these pulses. Elsewhere the wavelet components have negligible values and are ignored.

6.3 Applications of 2D-MRTD

6.3.1 Air-Filled Parallel Plate Waveguide

The 2D-MRTD scheme is applied to the analysis of an air-filled parallel-plate waveguide with width 4.8 mm. The front and back open planes are terminated with a PML region of 22 cells and σ_E^{max} calculated for designated $R_{max}=1.e-7$. The waveguide is excited with a Gabor function 0-30GHz along a vertical line next to the PML region. A Gabor excitation is propagating for a distance of 2,000 mm. For the analysis based on Yee's FDTD scheme, a 4×1120 mesh is used resulting in a total number of 4480 grid points. When the structure is analyzed with the 2D-MRTD scheme, a mesh 2×160 (320 grid points) is

chosen ($dx = 0.24\lambda_o$, $dz = 0.42\lambda_o$ for $f = 30GHz$). This size is based on the number of the scaling functions, since the wavelets are used only when and where necessary. The time discretization interval is selected to be identical for both schemes and equal to the 1/4 of the 2D-MRTD maximum Δt . For the analysis we use 3,000 time-steps. The longitudinal distance is chosen such that no reflections would appear before the Gabor function is complete and the schemes dispersion performance can be evaluated. The normal electric field E_x is probed at three different locations and the results are plotted in (Fig.6.2) showing only minimal dispersion.

The capability of the MRTD technique to provide space and time adaptive gridding is verified by thresholding the wavelet components to the maximum of the 0.01% of the value of the scaling function at the same cell for each time-step and the absolute threshold of 10^{-5} . The use of the absolute threshold enhances the efficiency of the algorithm for very small field values. It has been observed that the accuracy by using only a small number of wavelets is equal to what would be achieved if wavelets were used everywhere. Though this number is varying in time, its maximum value is 122 out of a total of 320 to the z-direction (economy in memory by a factor of 5.1 to the z-direction) as it can be observed from (Fig.6.3). In addition, execution time is reduced by a factor 3-4. The principle of the space-adaptive grid is exhibited at (Fig.6.4) which represents the E_x field distribution at $t=1000$ time steps. The wavelets have a significant value only at the region of the propagating pulse, thus creating a locally dense grid.

6.3.2 Parallel-Plate Partially Filled Waveguide

The second structure analyzed with the MRTD algorithm was the geometry of (Fig.6.5). A Gabor pulse 0-30 GHz is propagating from the left (air region) to the right (region

with $\epsilon_r = 2.56$). PML regions of 16 cells with σ_E^{max} calculated for designated $R_{max}=1.e-7$ terminate the grid and wavelets of 0-resolution are used in the longitudinal direction. The reflection coefficient S_{11} is calculated by separating the incident and the reflected part of the probed field and taking the Fourier transform of their ratio (Fig.6.6). Similar accuracy can be obtained for a 4x640 FDTD grid and a 2x80 MRTD grid with relative threshold 0.01% and absolute threshold 10^{-3} . The maximum number of wavelets used is 36 (Fig.6.7) offering an economy in memory by a factor of 6.53 in comparison to the FDTD simulations for the longitudinal (z) direction. The results for 5 GHz (TEM propagation) are validated by comparison to the theoretical value obtained applying ideal transmission line theory [62] and are plotted at Table (6.1).

The time- and space-adaptive character of the gridding is exploited in (Fig.6.8) which show that the wavelets follow the reflected and the transmitted pulses after the incidence to the dielectric interface and have negligible values elsewhere. The location and the number of the wavelet coefficients with significant values are different for each time-step, something that creates a dense mesh in regions of strong field variations, while maintaining a much coarser mesh for the other cells.

6.3.3 Parallel-Plate Five-Stage Filter

The last structure analyzed with the variable grid is the 5-stage filter of (Fig.6.9). A gabor function 0-4GHz is propagating from the left to the right. The input and output stages have $\epsilon_r = 12.5$ and the intermediate stages have $\epsilon_r = 50.5$ (stages with $d_1 = d_5 = 0.5mm$ and $d_3 = 2mm$) and $\epsilon_r = 1$. (stages with $d_2 = d_4 = 14.mm$). The total length to the longitudinal direction is 600 mm and to the vertical 4.8 mm. PML regions of 16 cells with σ_E^{max} calculated for designated $R_{max} = 1.e-7$ terminate the grid and wavelets of 0-resolution

are used to the longitudinal direction. The structure is analyzed by using an FDTD grid of 8×1600 cells, a scaling only MRTD grid of 2×400 cells and an adaptive (scaling+wavelets) MRTD grid of 2×200 cells. The relative threshold has the value of 0.01% and the absolute threshold equals to 10^{-4} . The maximum number of wavelets required during the 3,000 time steps of the simulation is 102 (Fig.6.10) , offering an economy by 37.25% in comparison to the scaling only grid and by a factor of 6.37 in comparison to the FDTD scheme for the direction of wavelet expansion (z-direction). The accuracy in the calculation of the S-parameters is similar for all three schemes as it can be observed from (Fig.6.11). Again, the time- and space- adaptive character of the proposed gridding is demonstrated in (Fig.6.12) with the E_x field space distribution for $t=1000$ time steps.

6.4 Conclusion

A dynamically changing space- and time- adaptive meshing algorithm based on a multiresolution time-domain scheme in two dimensions and on absolute and relative thresholding of the wavelet values has been proposed and has been applied to the numerical analysis of various nonhomogeneous waveguide geometries. A mathematically correct way of dielectric modeling has been presented and evaluated. The field distributions and the S parameters have been calculated and verified by comparison to reference data. In comparison to Yee's conventional FDTD scheme, the proposed scheme offers memory savings by a factor of 5-6 per dimension maintaining a similar accuracy. The above algorithm can be effectively extended to three-dimension problems.

	S_{11} (Ω)	Relative error
Analyt. Value [62]	0.4298	0.0%
4x640 FDTD	0.4283	-0.3%
2x80 MRTD	0.4360	+1.4%

Table 6.1: S_{11} calculated by 2D-MRTD

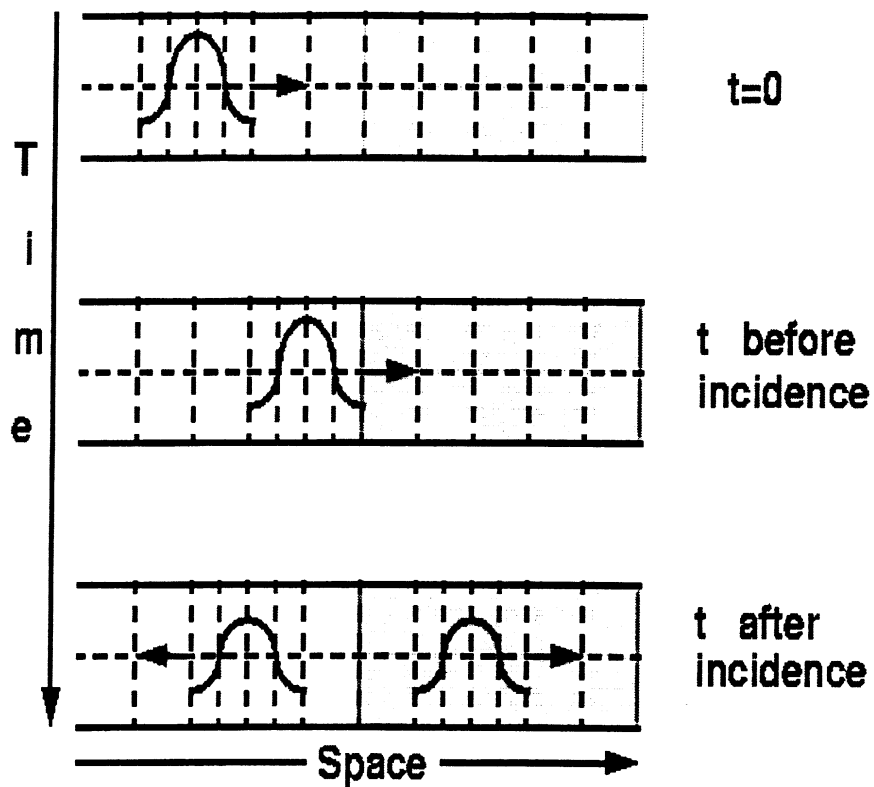


Figure 6.1: Time- and Space- adaptive grid.

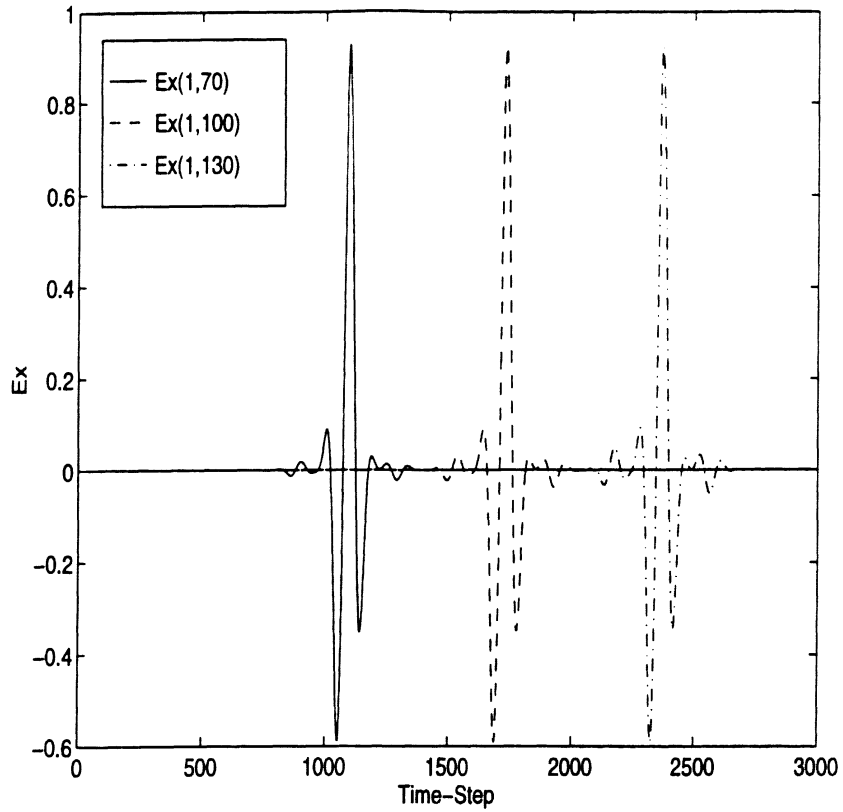


Figure 6.2: Normal E-field (Time-Domain).

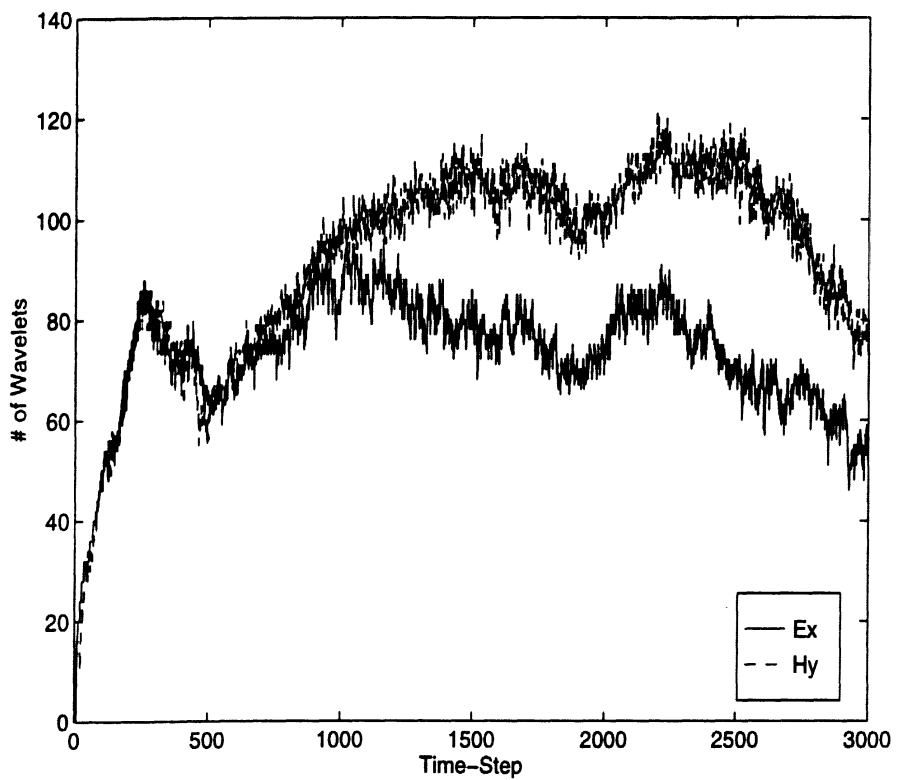


Figure 6.3: Non-zero Wavelets' Number

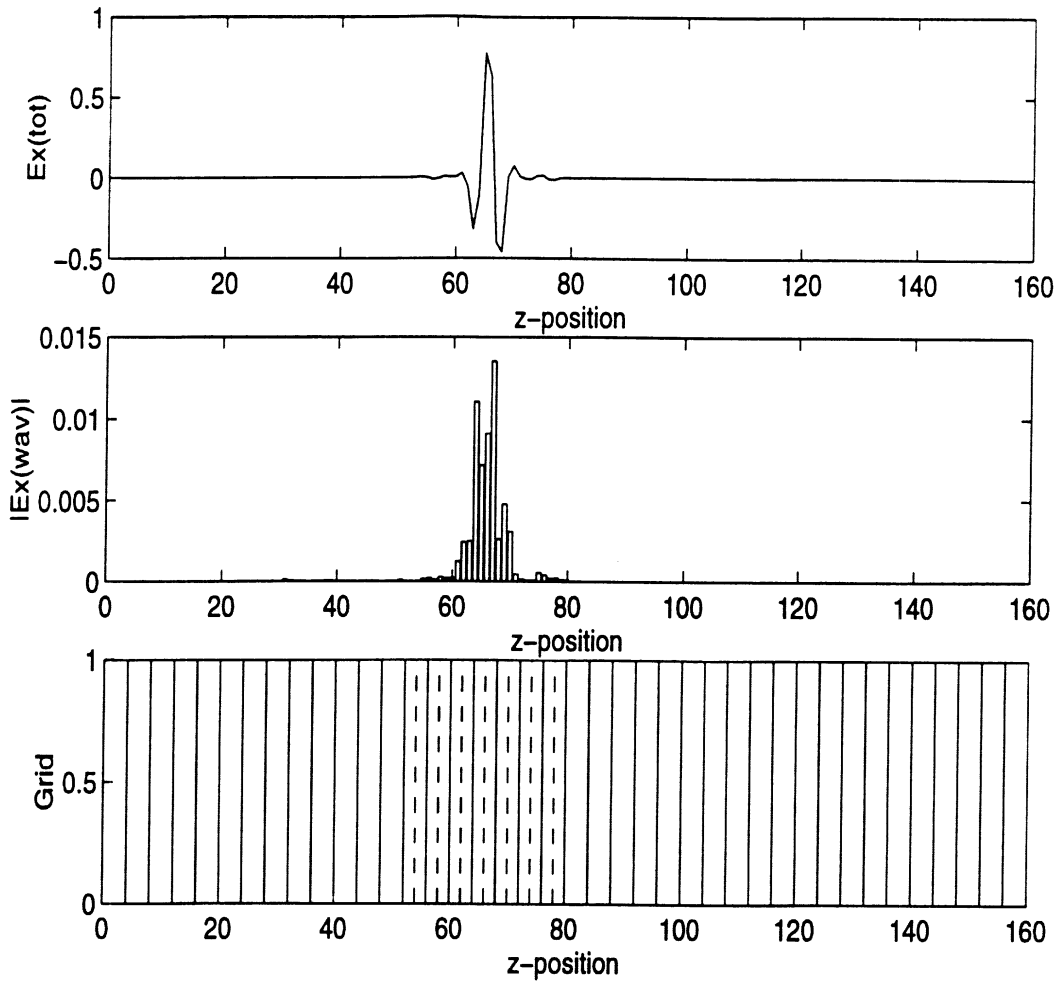


Figure 6.4: Adaptive Grid Demonstration ($t=1000$ steps).

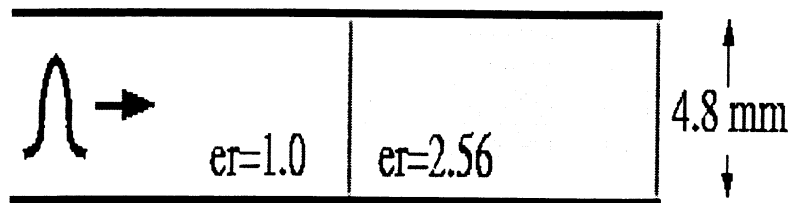


Figure 6.5: Parallel-Plate Partially Filled Waveguide.

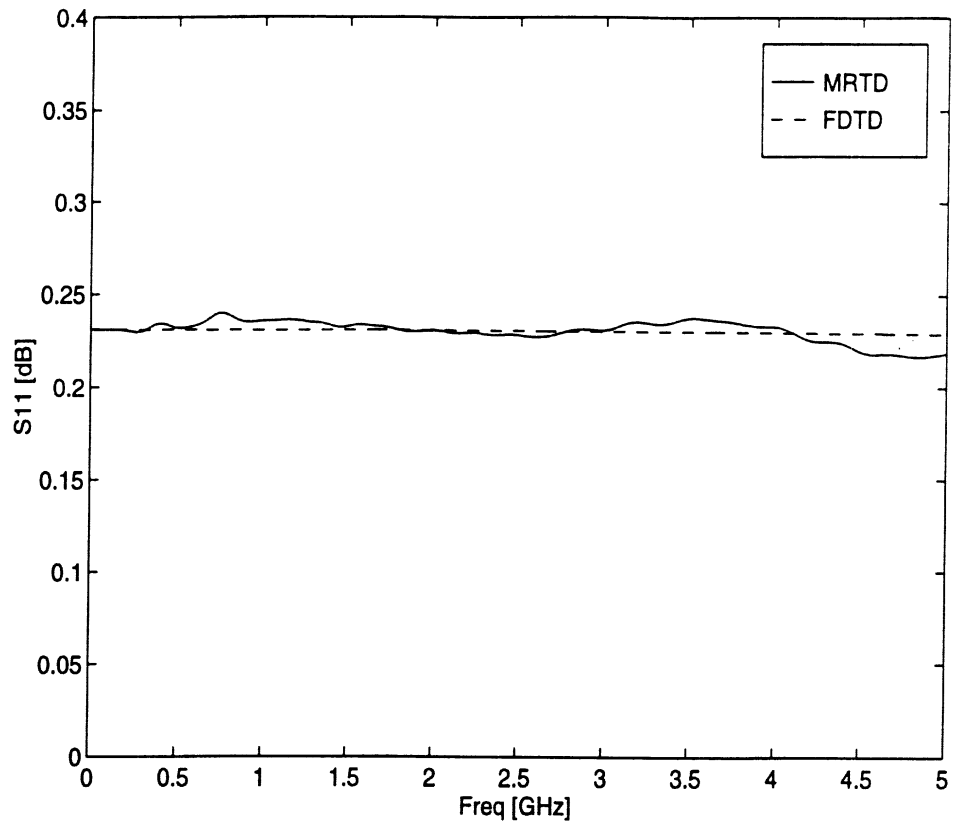


Figure 6.6: S-Parameters of the Waveguide.

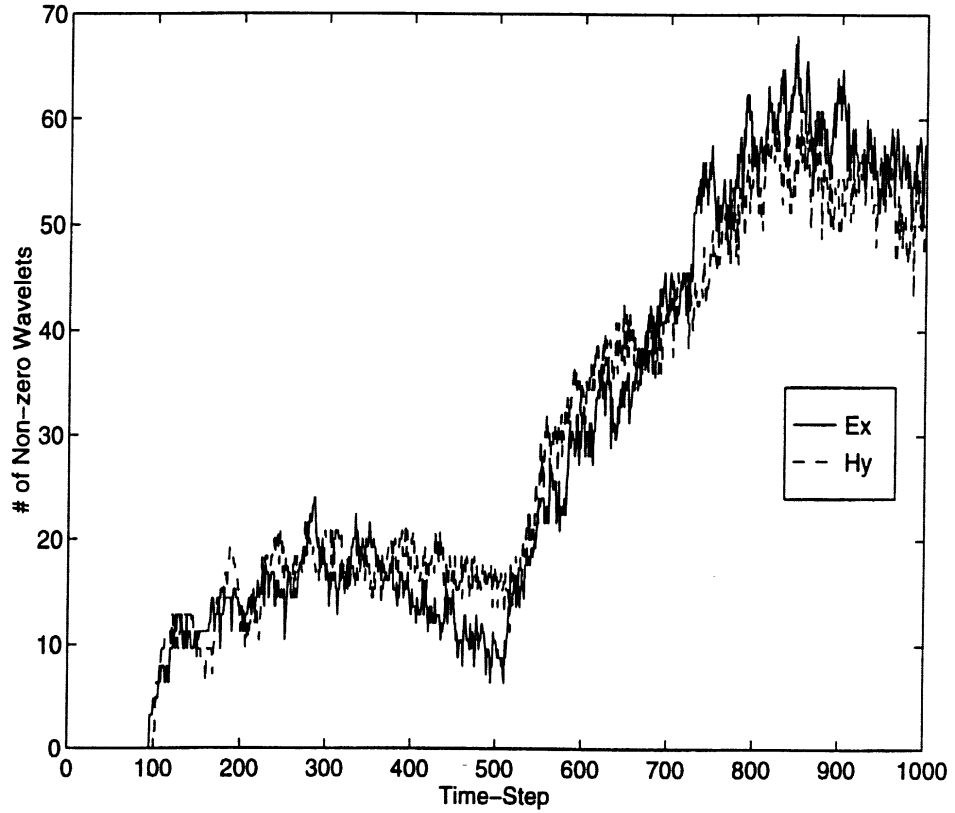


Figure 6.7: Non-zero Wavelets' Number.

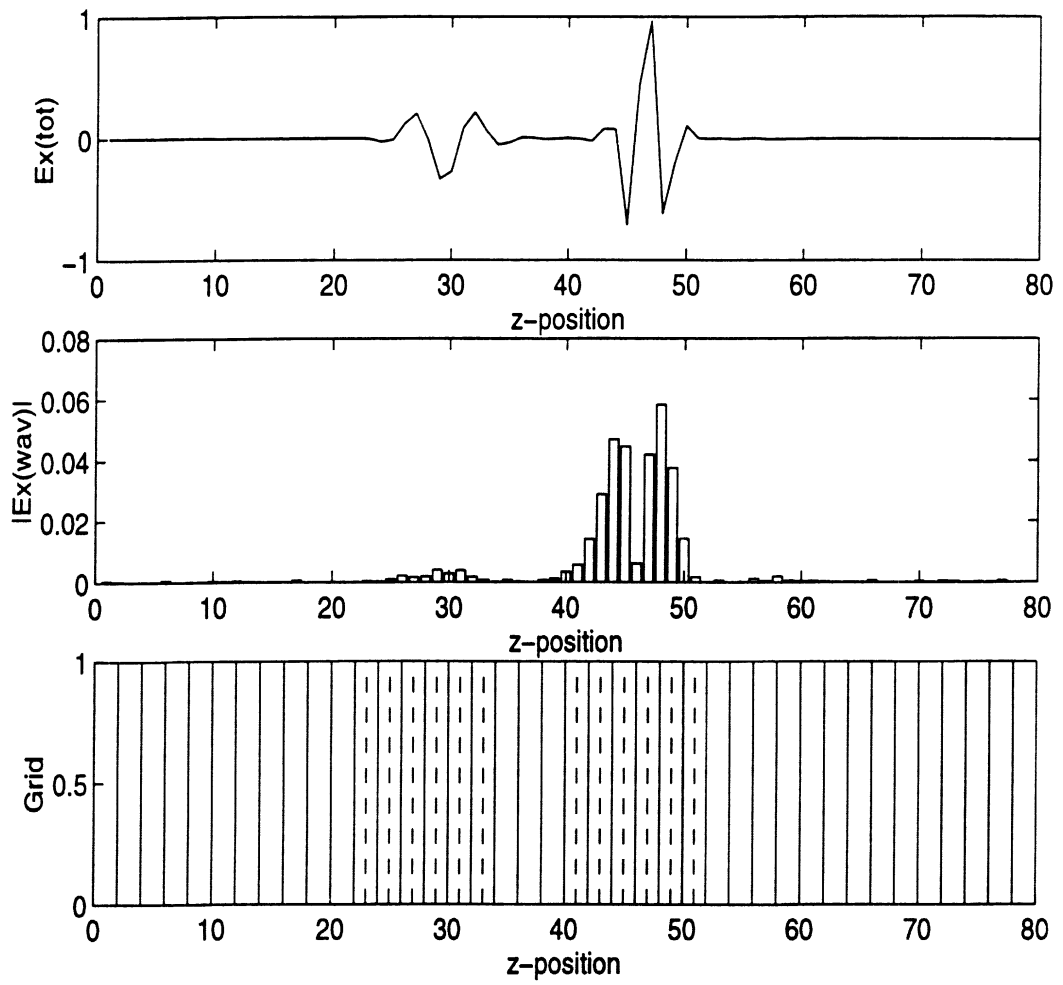


Figure 6.8: Adaptive Grid Demonstration ($t=1000$ steps).

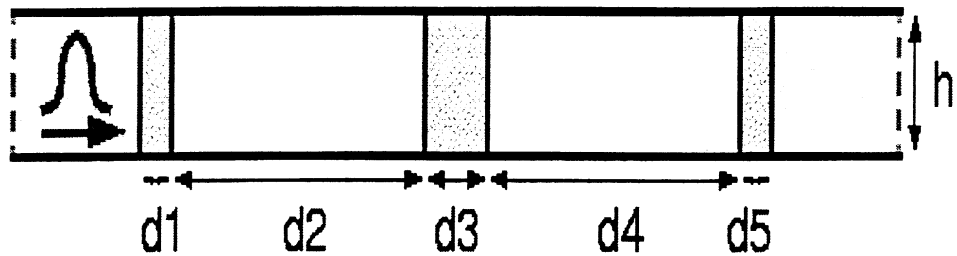


Figure 6.9: Parallel-Plate Five-Stage Filter.

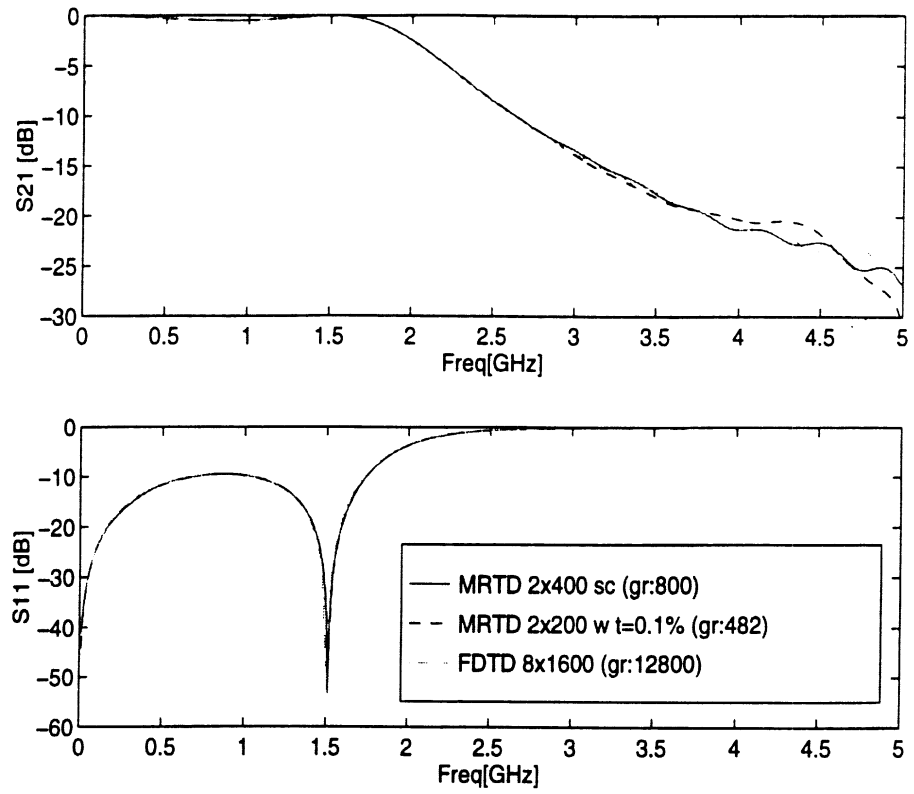


Figure 6.10: S-Parameters of the Filter.

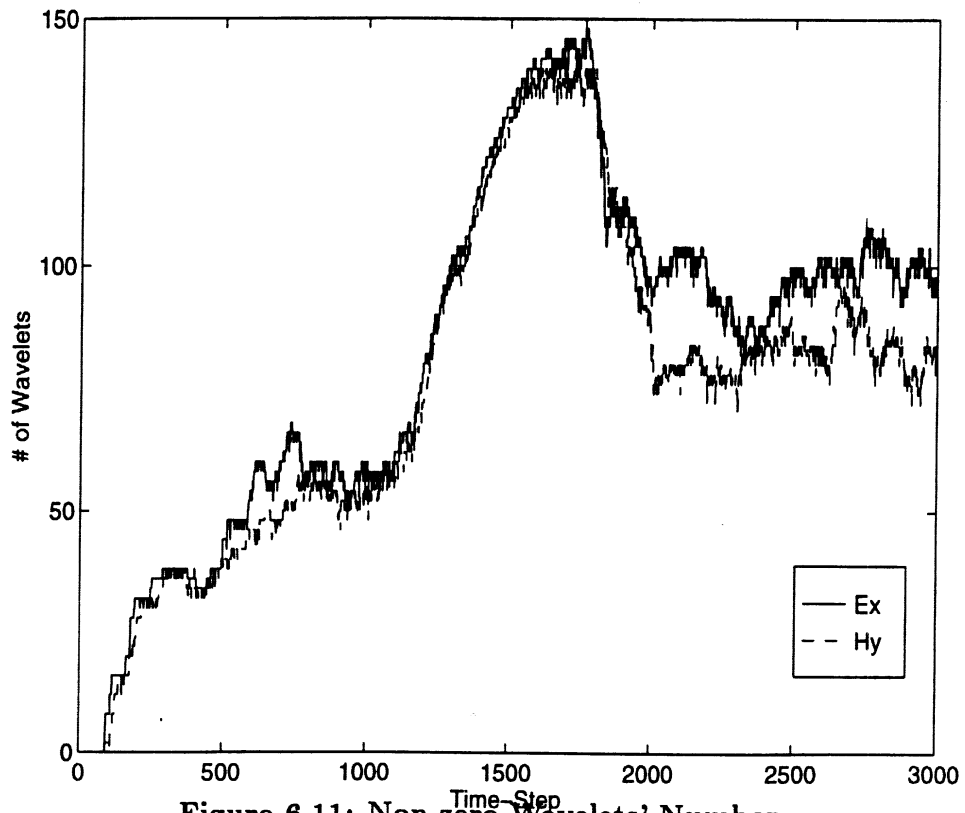


Figure 6.11: Non-zero Wavelets' Number.

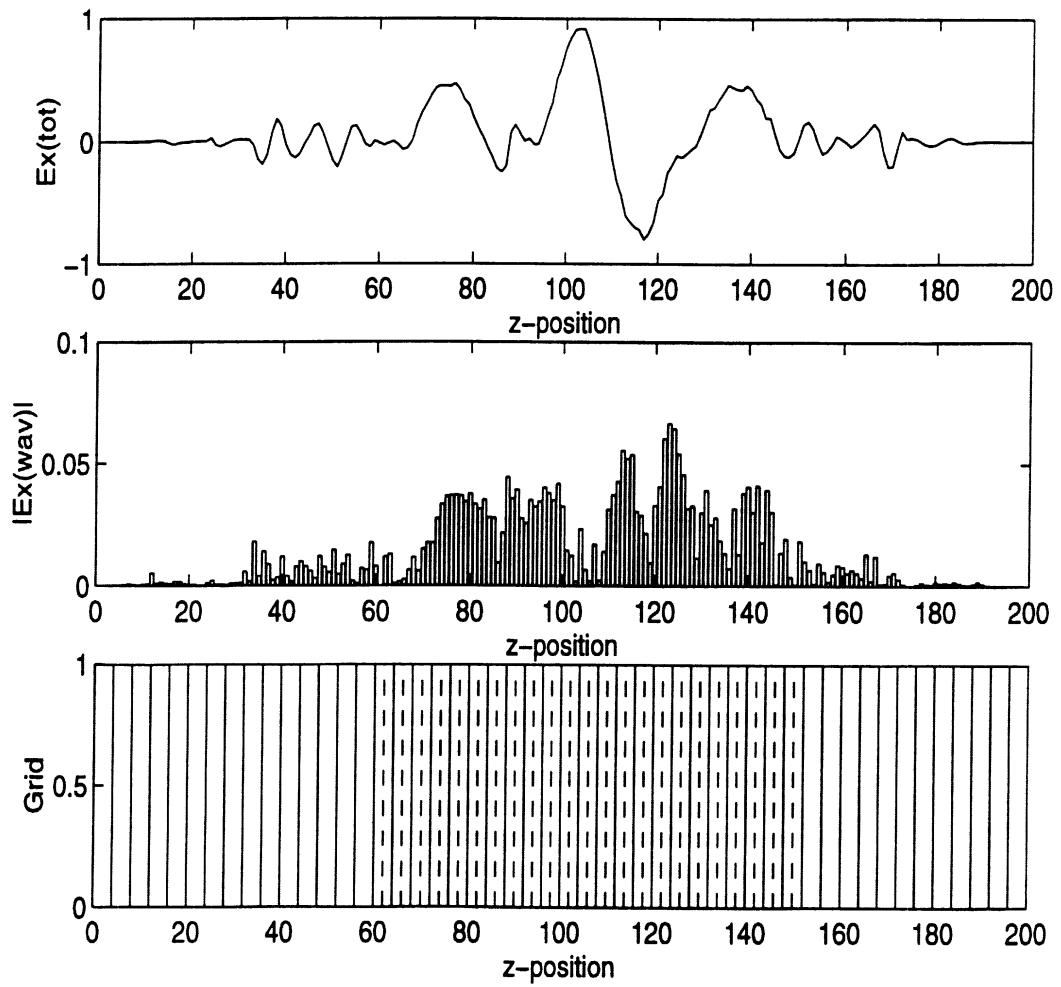


Figure 6.12: Adaptive Grid Demonstration (t=1000 steps).

CHAPTER 7

Time Adaptive Time-Domain Techniques for the Design of Microwave Circuits

7.1 Introduction

In the previous Chapters, MRTD schemes based on cubic spline Battle-Lemarie scaling and wavelet functions have been successfully applied to the simulation of 2D and 3D open and shielded problems [26, 53, 65, 61]. The functions of this family do not have compact support, thus the MRTD schemes have to be truncated with respect to space. Localized boundary conditions (PECs, PMCs etc.) and material properties are modelled by use of the image principle and of matrix equations respectively. However, this disadvantage is offset by the low-pass (scaling) and band-pass (wavelets) characteristics in spectral domain, allowing for an a priori estimate of the number of resolution levels necessary for a correct field modelling. In addition, the evaluation of the moment method integrals during the discretization of Maxwell's PDEs is simplified due to the existence of closed form expressions in spectral domain and simple representations in space domain. Dispersion analysis of this MRTD scheme shows the capability of excellent accuracy with up to 2 points/wavelength (Nyquist Limit). However, specific circuit problems may require the use of functions with

compact support. Especially in the approximation of time derivatives, the use of entire domain expansion basis would require very high memory resources for the storage of the field values everywhere on the grid for the whole or a large fraction of the simulation time. This problem does not exist in the approximation of the spatial derivatives since the field values on the neighboring spatial grid points have to be calculated and stored no matter what expansion basis are used. For that reason, Haar basis functions have been utilized and have led to [66]. As an extension to this approach, intervalic wavelets (Fig.7.1) may be incorporated into the solution of SPICE-type circuits, especially those containing active elements (PN Diodes, ...). Results from this new finite-domain expansion basis will be presented in this Chapter.

7.2 Time Adaptive MRTD Scheme

The major advantage of the use of Multiresolution analysis to time domain is the capability to develop time and space adaptive schemes. This is due to the property of the wavelet expansion functions to interact weakly and allow for a spatial sparsity that may vary with time through a thresholding process. The adaptive character of this technique is extremely important for the accurate modelling of sharp field variations of the type encountered in beam focusing in nonlinear optics, etc. The use of the principles of the multiresolution analysis for adaptive grid computations for PDEs has been suggested by Perrier and Basdevant [67]. To understand the fundamental steps of such an adaptive scheme for Maxwell's hyperbolic system, let's consider Maxwell's equations in 2D (1 for space and 1 for time):

$$\frac{\partial \hat{u}}{\partial t} = A \hat{u} = \begin{bmatrix} 0 & -\epsilon(z)^{-1} \frac{\partial}{\partial z} \\ -\mu(z)^{-1} \frac{\partial}{\partial z} & 0 \end{bmatrix} \hat{u}, \quad \hat{u} = (E(z, t), H(z, t))^T, \quad (7.1)$$

After manipulation, the above equation can be written as

$$\mathbf{M}\hat{u} = \begin{bmatrix} \epsilon T_h^\dagger D_t & T_h^\dagger D_z \\ Z_h^\dagger D_z & \mu Z_h^\dagger D_t \end{bmatrix} \hat{u} = 0$$

where Z_h, T_h are half shift operators for space and time coordinates z, t and Z_h^\dagger, T_h^\dagger are their Hermitian conjugates. D_t, D_z are difference operators given by:

$$D_t = \frac{1}{\Delta t} \left(\sum_{i=-9}^8 a_{\phi t}(i) T^{-i} + \sum_{i=-9}^9 a_{\psi t}(i) T^{-i} \right), \quad D_z = \frac{1}{\Delta z} \left(\sum_{i=-9}^8 a_{\phi z}(i) Z^{-i} + \sum_{i=-9}^9 a_{\psi z}(i) Z^{-i} \right), \quad (7.2)$$

where a_ϕ, a_ψ are the coefficients associated with the scalar and the wavelet functions respectively. At each time step we keep both the wavelet field values that are larger than a given threshold as well as the adjacent values. An adjacent wavelet field value is defined on the basis of the wavelet resolution level(s) incorporated in the solution. Recently, an efficient space/time adaptive meshing procedure was proposed [68] for Battle-Lemarie expansion functions. In this chapter, intervalic 0-order wavelets are used for the expansion of the fields and a simple thresholding procedure is employed. The adaptive mesh is applied to a variety of circuit problems and results are discussed in the next section.

7.3 Applications in SPICE problems

For simplicity, the 1D MRTD scheme will be derived. It can be extended to 2D and 3D in a straightforward way. In addition, only the 0-resolution of wavelets is enhanced. The Voltage and the Current are displaced by half step in both time- and space-domains (Yee cell formulation) and are expanded in a summation of scaling functions in space and scaling (ϕ) and wavelet (ψ_0) components in time

$$\begin{aligned} V(z, t) &= \sum_{m=-\infty}^{\infty} \sum_{i=-\infty}^{\infty} (i V_m^\phi \phi_i(t) + i V_m^{\psi_0} \psi_{0,i}(t)) \phi_m(z) \\ I(z, t) &= \sum_{m=-\infty}^{\infty} \sum_{i=-\infty}^{\infty} (i_{-0.5} I_m^\phi \phi_{i-0.5}(t) + i_{-0.5} I_m^{\psi_0} \psi_{0,i-0.5}(t)) \phi_{m-0.5}(z) \quad (7.3) \end{aligned}$$

where $\phi_i(t) = \phi(t/\Delta t - i)$ and $\psi_{0,i}(t) = \psi_0(t/\Delta t - i)$ represent the 0-order intervalic scaling and 0-resolution wavelet functions. The conventional notation ${}_k V_m$ is used for the voltage component at time $t = k\Delta t$ and $z = m\Delta z$, where Δt and Δz are the time-step and the spatial cell size respectively. The notation for the current I is similar.

Due to the finite-domain nature of the expansion basis, the Hard Boundary conditions (Open/Short Circuit) can be easily modeled. If a Short Circuit exists at the $z = m\Delta z$, then both scaling and wavelet voltage coefficients for the m - cell must be set to zero for each time-step k .

$${}_k V_m^\phi = {}_k V_m^{\psi_0} = 0, \quad k = 0, 1, 2, \dots \quad (7.4)$$

Similarly, an Open Circuit at $z = (m - 0.5)\Delta z$ can be modeled by applying the conditions

$${}_{k-0.5} I_{m-0.5}^\phi = {}_{k-0.5} I_{m-0.5}^{\psi_0} = 0, \quad k = 0, 1, 2, \dots \quad (7.5)$$

The alternating nature of the 0-resolution wavelet function guarantees the double time-domain resolution of the MRTD scheme. Assuming that the voltage scaling and wavelet coefficients at $m = \Delta z$ for a specific time-step k , two values can be defined for the time span $[(k - 0.5)\Delta t, (k + 0.5)\Delta t]$ of this time-step

$${}_k V_m^{total,1} = {}_k V_m^\phi + {}_k V_m^{\psi_0}, \quad t \in [(k - 0.5)\Delta t, k\Delta t] \quad (7.6)$$

$${}_k V_m^{total,2} = {}_k V_m^\phi - {}_k V_m^{\psi_0}, \quad t \in [k\Delta t, (k + 0.5)\Delta t] \quad (7.7)$$

7.3.1 Distributed Elements

Lossless Line

The ideal transmission line (Fig.7.2) equations are given by

$$\begin{aligned} \frac{dV}{dz} &= -L_{dis} \frac{dI}{dt} \\ \frac{dI}{dz} &= -C_{dis} \frac{dV}{dt} \end{aligned}, \quad (7.8)$$

where L_{dis}, C_{dis} are the distributed inductance and capacitance of the line. Inserting the expansions of Eq.(7.3) and applying the Method of Moments, the following MRTD equations are derived

$$\frac{C_{dis}}{\Delta t} ({}_{k+1}V_m^\phi - {}_kV_m^\phi) = -\frac{1}{\Delta z} ({}_{k+0.5}I_{m+0.5}^\phi - {}_{k+0.5}I_{m-0.5}^\phi) \quad (7.9)$$

$$\frac{C_{dis}}{\Delta t} ({}_{k+1}V_m^{\psi_0} - {}_kV_m^{\psi_0}) = -\frac{1}{\Delta z} ({}_{k+0.5}I_{m+0.5}^{\psi_0} - {}_{k+0.5}I_{m-0.5}^{\psi_0}) \quad (7.10)$$

$$\frac{L_{dis}}{\Delta t} ({}_{k+0.5}I_{m-0.5}^\phi - {}_{k-0.5}I_{m-0.5}^\phi) = -\frac{1}{\Delta z} ({}_kV_m^\phi - {}_kV_{m-1}^\phi) \quad (7.11)$$

$$\frac{L_{dis}}{\Delta t} ({}_{k+0.5}I_{m-0.5}^{\psi_0} - {}_{k-0.5}I_{m-0.5}^{\psi_0}) = -\frac{1}{\Delta z} ({}_kV_m^{\psi_0} - {}_kV_{m-1}^{\psi_0}) \quad (7.12)$$

It can be observed that Eqs.(7.9) and (7.11) updating the scaling coefficients only are independent of the Eqs.(7.10) and (7.12) updating the wavelet coefficients. To create an efficient time adaptive algorithm, all four equations must be coupled. An efficient way is to apply the excitation in a physically correct manner. If the excitation has the time-dependence $g(t)$ at the location $z = m_e \Delta z$, then the scaling and wavelet coefficients for this cell have to take the values

$$\begin{aligned} {}_kV_{m_e}^\phi &= \int_{(k-0.5)\Delta t}^{(k+0.5)\Delta t} g(t) \phi_k(t) dt \\ {}_kV_{m_e}^{\psi_0} &= \int_{(k-0.5)\Delta t}^{(k+0.5)\Delta t} g(t) \psi_{0,k}(t) dt \end{aligned} \quad (7.13)$$

To validate this approach, the MRTD algorithm was applied to the simulation of a lossless transmission line with $(L_{dis}, C_{dis}) = (20nH/m, 3nF/m)$ for a Gabor excitation and time-step $dt = dt_{max}/1.01$. (Fig.7.3) which displays the Voltage Scaling and Wavelet Coefficients evolution at $z = 200\Delta z$ for the first 800 time-steps of the simulation, shows that the wavelet coefficients have the correct shape (significant values only at areas with significant scaling function values) and are close to the 12% of the respective scaling functions. (Fig.7.4) which compares the total voltage value at $z = 200\Delta z$ calculated by FDTD (Sc.ONLY) and MRTD (Sc.+Wav.) for the time-steps 357–362 demonstrates the ability of this MRTD

scheme to double the conventional FDTD resolution in the time-domain by providing two values for each time-step. The fact that the wavelet coefficients take significant values only for a small number of time-steps allows for their thresholding by comparing them to a combination of relative to the respective value of the scaling coefficient (5.e-4) and absolute (1.e-6) thresholds. (Fig.7.5) proves that up to 60% of the maximum number of wavelet coefficients are necessary for an accurate simulation, offering an extra economy in memory by a factor of 20%.

Lossy Line

The lossy transmission line (Fig.7.6) equations are derived by the ideal transmission line equations (Eq.(7.8)) adding the Conductor Loss R_{dis} and the Dielectric Loss G_{dis}

$$\begin{aligned}\frac{dV}{dz} &= -R_{dis}I - L_{dis}\frac{dI}{dt} \\ \frac{dI}{dz} &= -G_{dis}V - C_{dis}\frac{dV}{dt} \quad .\end{aligned}\quad (7.14)$$

Following a procedure similar to the previous section, the following MRTD equations are derived

$$\begin{aligned}{}_{k+1}V_m^\phi &= -\frac{(C_1 - C_2)}{C_1^2} \Delta t ({}_{k+0.5}I_{m+0.5}^\phi - {}_{k-0.5}I_{m-0.5}^\phi) + \frac{C_2}{C_1^2} \Delta t ({}_{k+0.5}I_{m+0.5}^{\psi_0} - {}_{k-0.5}I_{m-0.5}^{\psi_0}) \\ &+ \frac{(C_1 - C_2)^2 + C_2^2}{C_1^2} {}_kV_m^\phi - 2\frac{C_2^2}{C_1^2} {}_kV_m^{\psi_0}\end{aligned}\quad (7.15)$$

$$\begin{aligned}{}_{k+1}V_m^{\psi_0} &= -\frac{C_2}{C_1^2} \Delta t ({}_{k+0.5}I_{m+0.5}^\phi - {}_{k-0.5}I_{m-0.5}^\phi) - \frac{(C_1 + C_2)}{C_1^2} \Delta t ({}_{k+0.5}I_{m+0.5}^{\psi_0} - {}_{k-0.5}I_{m-0.5}^{\psi_0}) \\ &- 2\frac{C_2^2}{C_1^2} {}_kV_m^\phi + \frac{(C_1 - C_2)^2 + C_2^2}{C_1^2} {}_kV_m^{\psi_0}\end{aligned}\quad (7.16)$$

$$\begin{aligned}{}_{k+0.5}I_{m-0.5}^\phi &= -\frac{(C_3 - C_4)}{C_3^2} \Delta t ({}_kV_m^\phi - {}_kV_{m-1}^\phi) + \frac{C_4}{C_3^2} \Delta t ({}_kV_m^{\psi_0} - {}_kV_{m-1}^{\psi_0}) \\ &+ \frac{(C_3 - C_4)^2 + C_4^2}{C_3^2} {}_{k-0.5}I_{m-0.5}^\phi - 2\frac{C_4^2}{C_3^2} {}_{k-0.5}I_{m-0.5}^{\psi_0}\end{aligned}\quad (7.17)$$

$$\begin{aligned}{}_{k+0.5}I_{m-0.5}^{\psi_0} &= -\frac{C_4}{C_3^2} \Delta t ({}_kV_m^\phi - {}_kV_{m-1}^\phi) - \frac{(C_3 + C_4)}{C_3^2} \Delta t ({}_kV_m^{\psi_0} - {}_kV_{m-1}^{\psi_0}) \\ &- 2\frac{C_4^2}{C_3^2} {}_{k-0.5}I_{m-0.5}^\phi + \frac{(C_3 - C_4)^2 + C_4^2}{C_3^2} {}_{k-0.5}I_{m-0.5}^{\psi_0} \quad ,\end{aligned}\quad (7.18)$$

with

$$C_1 = C_{dis}\Delta z \quad , \quad C_2 = 0.5 G_{dis}\Delta z \Delta t,$$

$$C_3 = L_{dis}\Delta z \quad , \quad C_4 = 0.5 R_{dis}\Delta z \Delta t, \quad .$$

For this type of transmission line, the equations giving the scaling and wavelet coefficients for voltage and current are coupled. Nevertheless, the condition (7.13) has to be applied in order to satisfy the physical boundary condition at the excitation cell(s). It has to be noted, that Eqs.(7.15)–(7.18) can be used only for lossy lines with low to medium Loss Coefficients. The threshold $C_2 \leq 4C_1$ for G_{dis} ($C_4 \leq 4C_3$ for R_{dis}) gave satisfactory results for all simulations. For higher loss coefficients, the Loss can be modeled in an exponential way similar to [61]. For example, for large values of R_{dis} ($C_4 > C_3$), Eqs.(7.17)–(7.18) have to be replaced by the following uncoupled expressions

$${}_{k+0.5}I_{m-0.5}^\phi = e^{\frac{-R_{dis}\Delta t}{L_{dis}}} {}_{k-0.5}I_{m-0.5}^\phi - e^{\frac{-0.5R_{dis}\Delta t}{L_{dis}}} \frac{\Delta t}{C_3} ({}_kV_m^\phi - {}_kV_{m-1}^\phi) \quad (7.19)$$

$${}_{k+0.5}I_{m-0.5}^{\psi_0} = e^{\frac{-R_{dis}\Delta t}{L_{dis}}} {}_{k-0.5}I_{m-0.5}^{\psi_0} - e^{\frac{-0.5R_{dis}\Delta t}{L_{dis}}} \frac{\Delta t}{C_3} ({}_kV_m^{\psi_0} - {}_kV_{m-1}^{\psi_0}) \quad (7.20)$$

Using this procedure, a termination layer similar to the FDTD widely used PML layer can be easily modeled. The R_{dis}, G_{dis} should have a spatial parabolic distribution with very high maximum value and they should satisfy the condition $G_{dis} = R_{dis}L_{dis}/C_{dis}$ for each cell of the layer. In this way, one matched transmission line can be simulated by choosing the appropriate R_{dis}, G_{dis} that satisfy the specified numerical reflection coefficient (usually smaller than -80dB).

For validation purposes, the propagation of a Gabor pulse along a lossy line with $R_{dis} = 5\Omega/m$ has been simulated and the scaling and wavelet voltage coefficients have been probed at the positions $z = 140\Delta z$ and $z = 160\Delta z$. Data for the first 200 time-steps ($\Delta t = 2\Delta t/3$) have been plotted in (Fig.7.7). The maximum value of the wavelet coefficients

(approximately 7% of the respective scaling coefficient) is smaller than that of the lossless line. By applying a thresholding procedure using an absolute threshold of 10^{-6} and a relative threshold of $5e - 4$, an extra economy of 29% is achieved. since only 60% of the voltage and 25% of the current wavelet coefficients take values above the thresholds throughout the simulation time (Fig.7.8).

7.3.2 Lumped Elements

Passive Elements

Lumped Passive Elements such as Capacitors, Inductors and Resistors can be modeled in a similar way with the Distributed ones by numerically distributing them along one cell. For example, if one lumped Capacitor C_{lum} is located at $z = m\Delta z$ along a lossy line with $(R_{dis}, G_{dis}, L_{dis}, C_{dis})$, the voltage coefficients ${}_{k+1}V_m^\phi, {}_{k+1}V_m^{\psi_0}$ will still be given by Eqs.(7.15)–(7.16). The only difference is that the constant C_1 will have the new value $C_1 = C_{tot}\Delta z$ with

$$C_{tot} = C_{dist} + \frac{C_{lum}}{\Delta z} \quad . \quad (7.21)$$

PN-Diode

To model lumped active elements such as a PN-diode, their nonlinear equation has to be discretized after inserting the voltage and current expansions. The MRTD equations are not linear and require the use of numerical solvers for nonlinear systems. The combined Newton-Raphson/Bisection solver has provided stable solutions for PN-diode simulations with $I_0 \leq 1.e - 10A$, though sometimes diverges for larger values. The voltage scaling and wavelet coefficients for the diode cell are updated by inserting the voltage and current

expansion in the equation

$$I_{DIODE}(V) = I_0 (e^{qV/kT} - 1) \quad (7.22)$$

adding the diode capacitance C_j to the C_{dis} and applying the moments method, thus giving the nonlinear system for a diode positioned in parallel

$$\begin{aligned} (C_5 + C_{dis}) {}_k V_m^\phi &+ C_5 {}_k V_m^{\psi_0} + (C_5 - C_{dis}) {}_{k-1} V_m^\phi \\ &- C_5 {}_{k-1} V_m^{\psi_0} + \frac{\Delta t}{\Delta z} ({}_{k-0.5} I_{m+0.5}^\phi - {}_{k-0.5} I_{m-0.5}^\phi) \\ &+ 0.5 \Delta t C_j (e^{kT/q} I_0 ({}_{k-1} V_m^\phi - {}_{k-1} V_m^{\psi_0}) + e^{kT/q} I_0 ({}_k V_m^\phi + {}_k V_m^{\psi_0})) = 0 \end{aligned} \quad (7.23)$$

$$\begin{aligned} -C_5 {}_k V_m^\phi &- (C_5 - C_{dis}) {}_k V_m^{\psi_0} + C_5 {}_{k-1} V_m^\phi \\ &- (C_5 + C_{lum}) {}_{k-1} V_m^{\psi_0} + \frac{\Delta t}{\Delta z} ({}_{k-0.5} I_{m+0.5}^{\psi_0} - {}_{k-0.5} I_{m-0.5}^{\psi_0}) \\ &+ 0.5 \Delta t C_j (e^{kT/q} I_0 ({}_{k-1} V_m^{phi} - {}_{k-1} V_m^{\psi_0}) - e^{kT/q} I_0 ({}_k V_m^\phi + {}_k V_m^{\psi_0})) = 0 \end{aligned} \quad (7.24)$$

with

$$C_5 = 0.5 \Delta t G_{lum} \quad . \quad (7.25)$$

To validate the algorithm, the rectifier topology of (Fig.7.9) is analyzed using FDTD (Scaling Only) with $\Delta t = \Delta t_{max}/4.4$ and MRTD (Scaling+wavelets) with double time-step $\Delta t = \Delta t_{max}/2.2$. A lossless line with $(L_{dis}, C_{dis}) = (20nH/m, 3nF/m)$ and a PN-Diode with $I_0 = 3pA$ are used in the simulation. The probed total voltage is plotted in Fig.(10) and the agreement is very good. The use of an absolute threshold of 10^{-6} and a relative threshold of $5e - 4$ offers an extra economy of 35% for the MRTD algorithm.

7.4 Conclusion

A Time Adaptive Time-Domain Technique based on intervalic wavelets has been proposed and applied to various types of circuits problems with active and passive lumped and distributed elements. This scheme exhibits significant savings in execution time and memory requirements while maintaining a similar accuracy with the conventional FDTD technique.

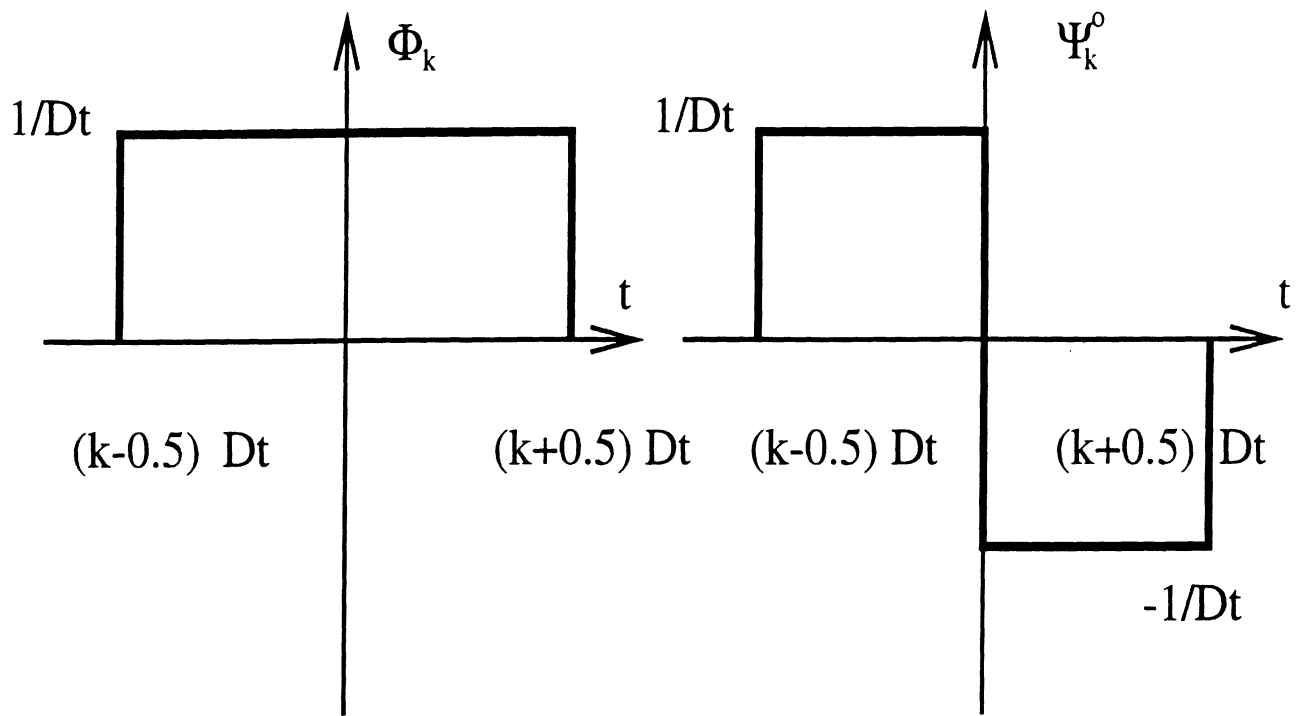


Figure 7.1: 0-Order Intervalic Function Basis.

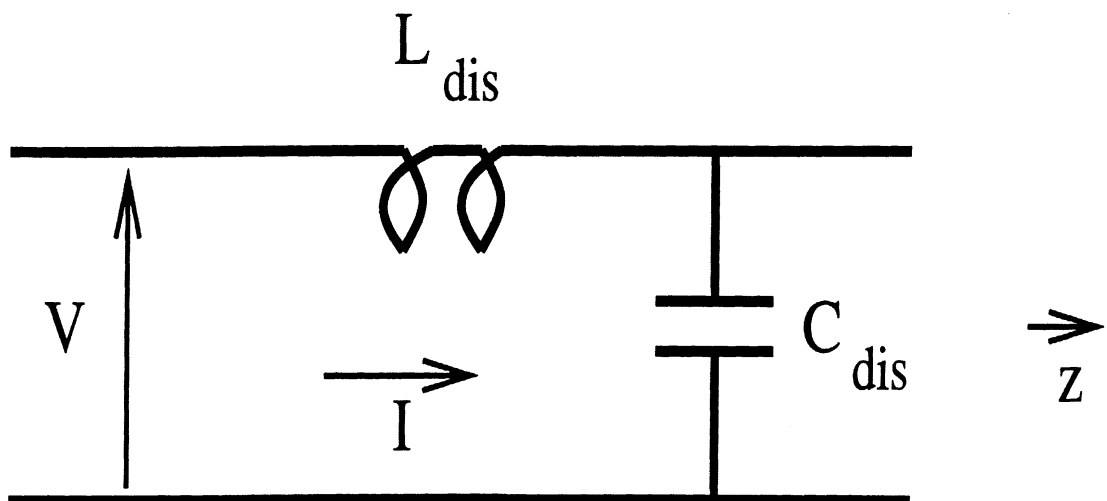


Figure 7.2: Ideal (Lossless) Transmission Line.

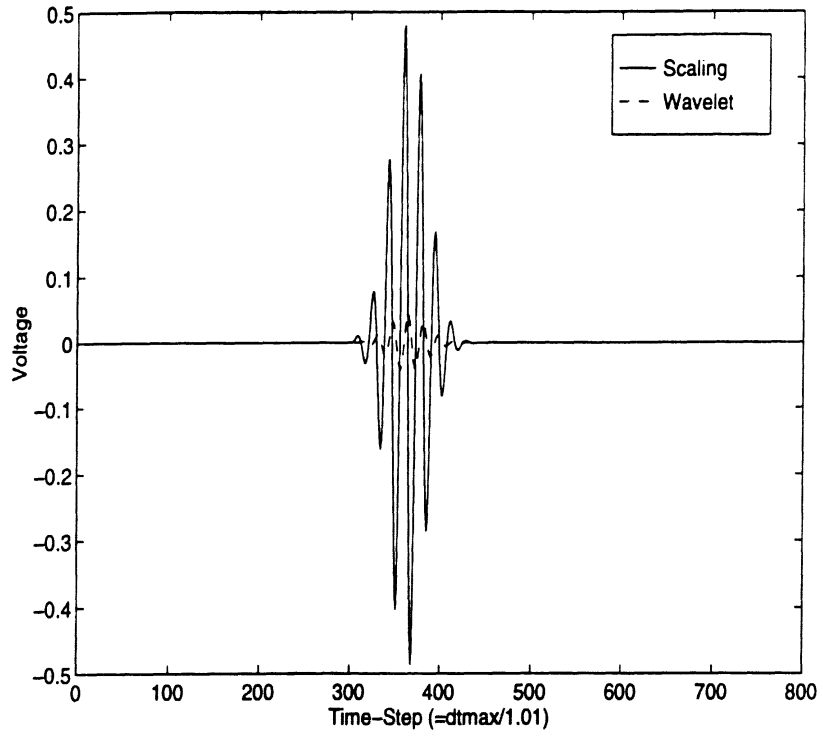


Figure 7.3: Voltage Coefficients.

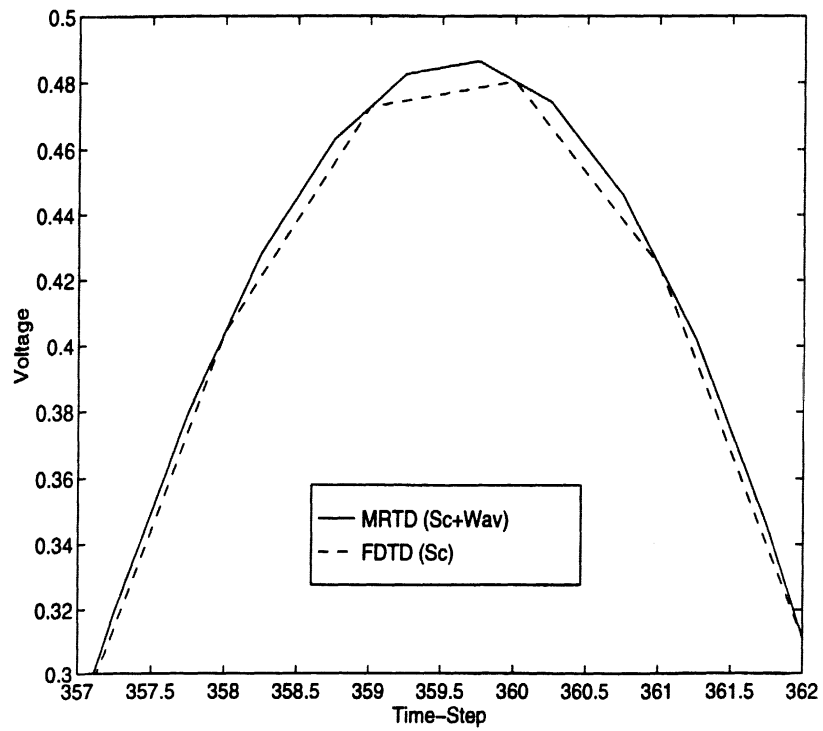


Figure 7.4: Comparison MRTD-FDTD.

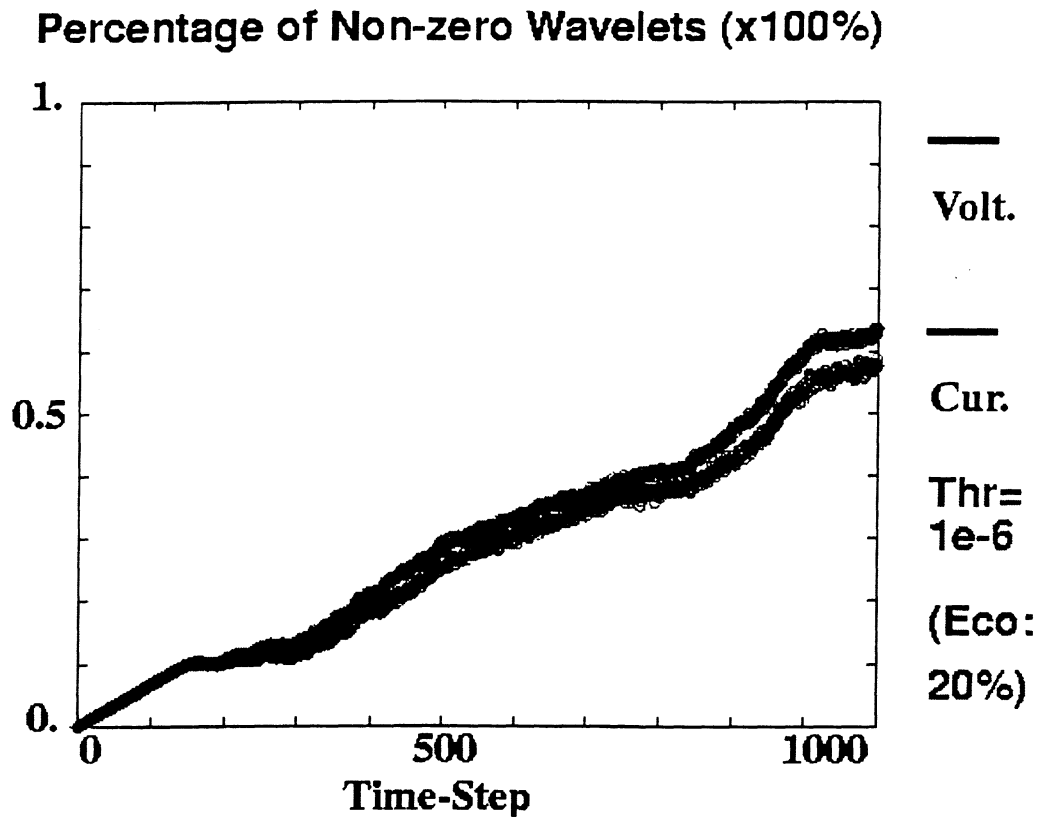


Figure 7.5: Fraction of Wavelets above Threshold.

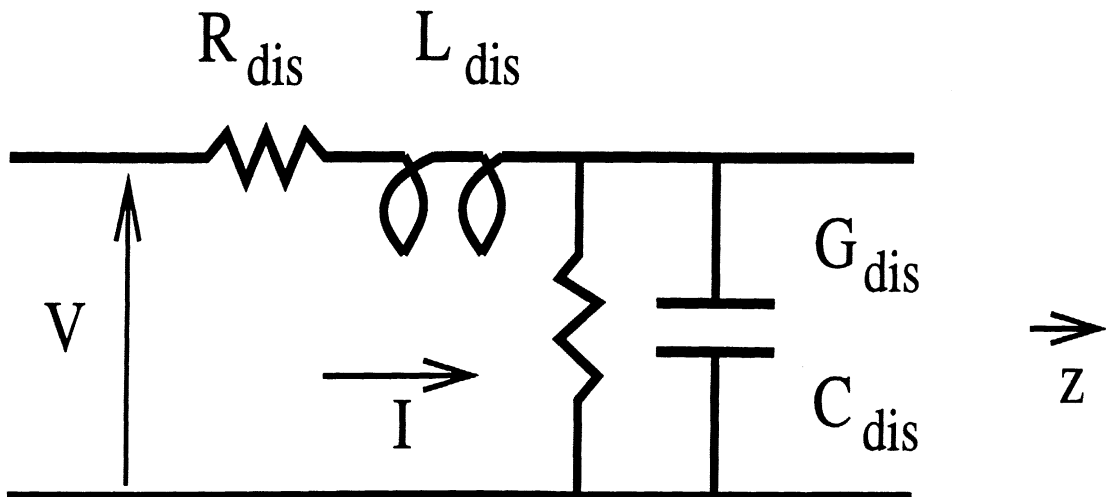


Figure 7.6: Lossy Transmission Line.

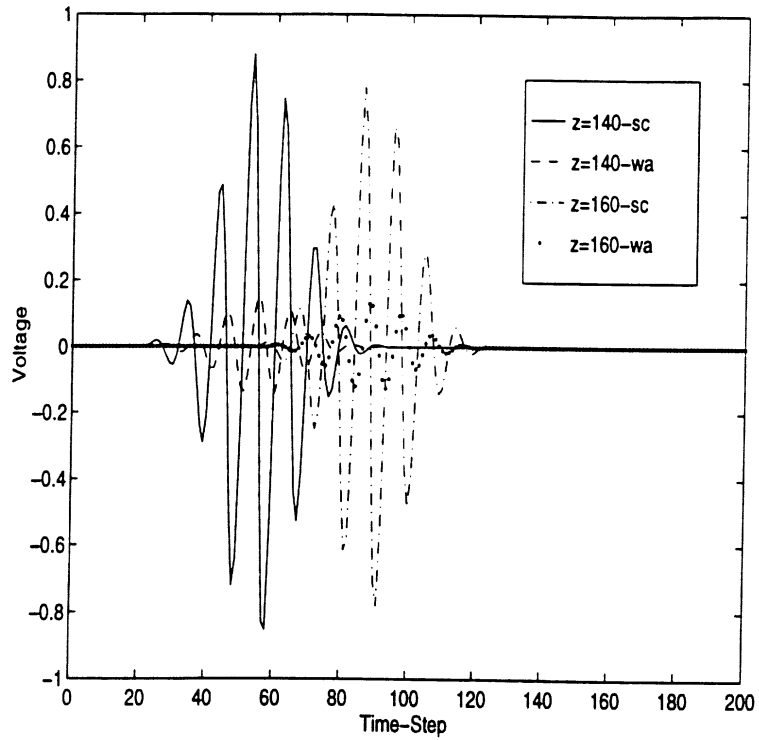


Figure 7.7: Voltage Coefficients.

Percentage of Non-zero Wavelets (x100%)

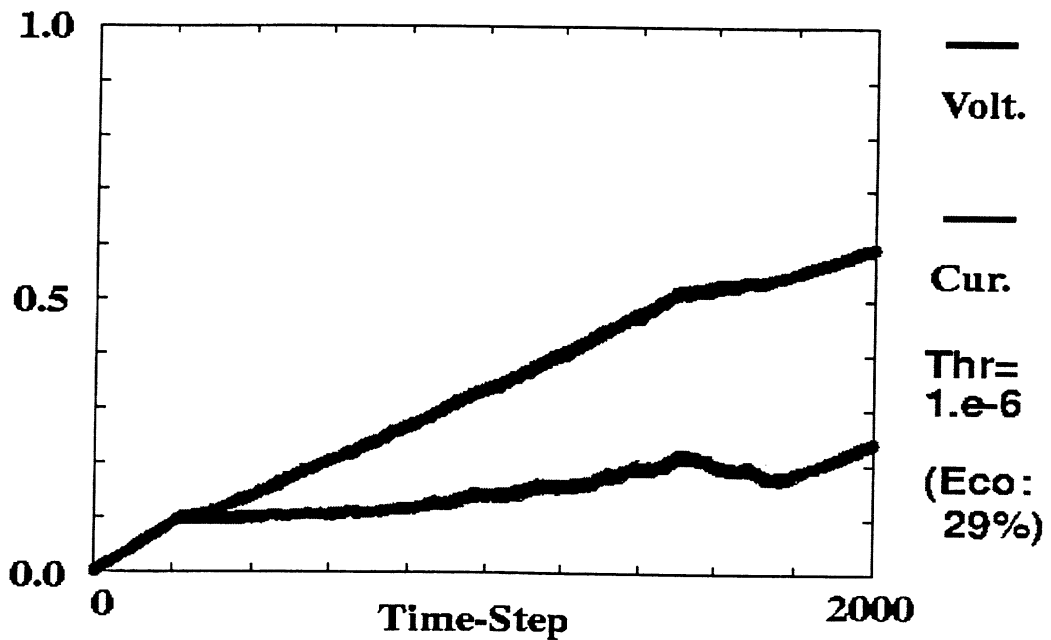


Figure 7.8: Fraction of Wavelets above Threshold.

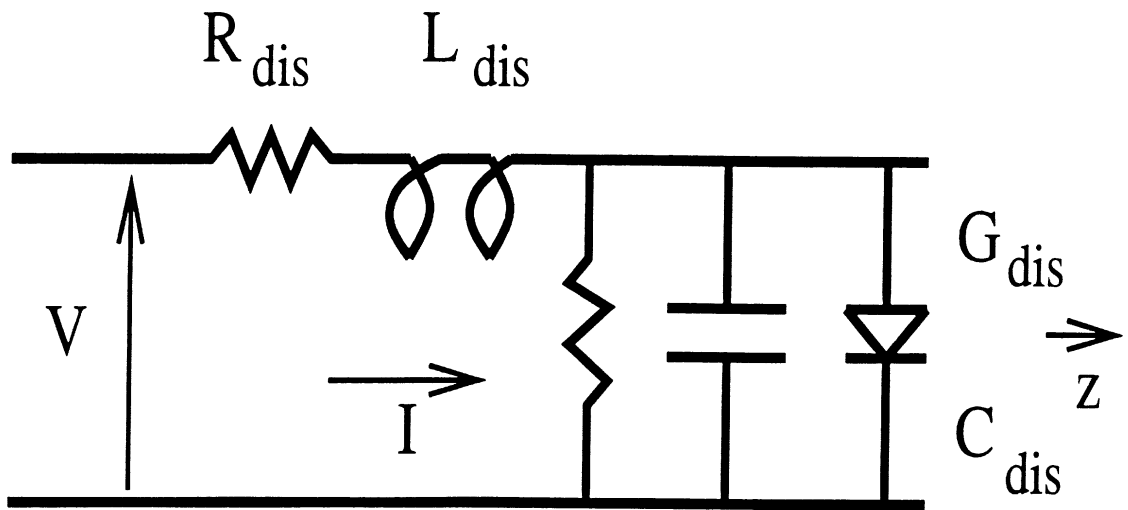


Figure 7.9: Rectifier Geometry.

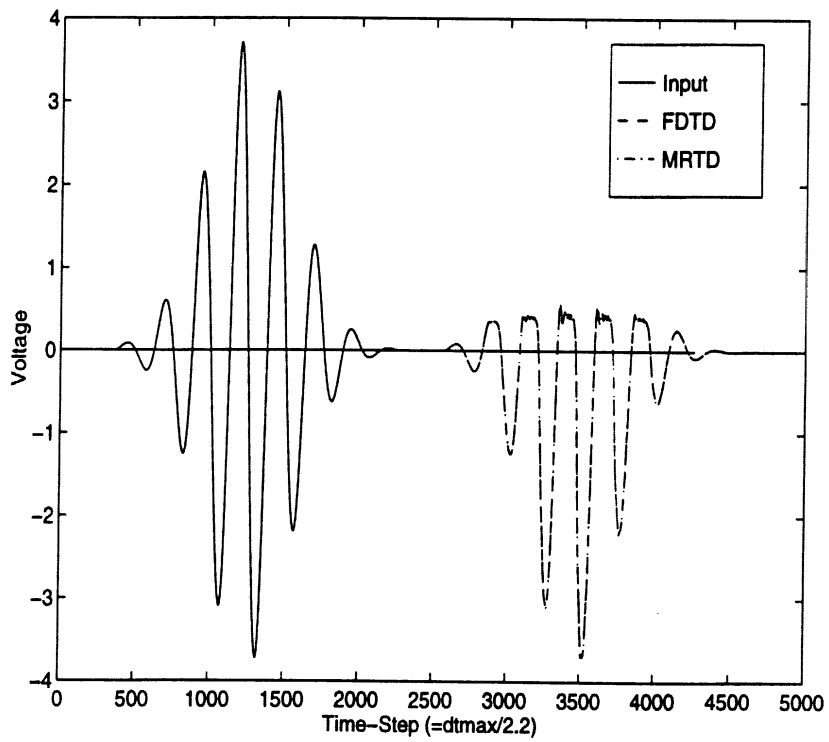


Figure 7.10: Comparison MRTD-FDTD.

CHAPTER 8

Summary of Achievements-Future Work

The goal of this dissertation was to develop efficient time-domain numerical techniques for the analysis and design of microwave circuits. To achieve it, the principles of Multiresolution Analysis were employed and novel time-domain schemes based on field expansions in scaling and wavelet functions were derived (MRTD). These new schemes offer memory savings by a factor of 5 per dimension and execution time savings by a factor of 4-5 while maintaining a similar accuracy to the conventional FDTD technique. They also feature an inherent capability of a dynamically changing space- and time- adaptive gridding algorithm by thresholding the wavelet values in a mathematically correct way. In addition, they offer the unique opportunity of a multi-point field representation per cell. Results from 2D and 2.5D simulations prove the validity and the versatility of the MRTD schemes.

Nevertheless, future work on the MRTD schemes should include the study of the effects of the enhancement of arbitrary wavelet resolutions for schemes based on entire-domain and finite-domain expansion basis. In addition, different functions should be tested and their performance for different geometries should be evaluated. As it was displayed in CH.6,7 dynamic gridding is achieved by a simple thresholding algorithm. It might be useful to perform a systematic study on the relationship between different thresholding schemes and

the error of calculations in order to guarantee a predefined accuracy and justify an a-priori choice of a relative and an absolute threshold.

BIBLIOGRAPHY

BIBLIOGRAPHY

- [1] J.B.Keller, "Geometrical Theory of Diffraction", J.Optical Society of America, vol.52, 1962, pp.116-130.
- [2] R.G.Kouyoumjian and P.H.Pathak, "A Uniform Geometrical Theory of Diffraction for an Edge in a Perfectly Conducting Surface", Proc.IEEE, vol.62, 1974, pp.1448-1461.
- [3] R.F.Harrington, "Field Computation by Moment Methods", New York, Macmillan, 1968.
- [4] K.R.Umashankar, "Numerical Analysis of Electromagnetic Wave Scattering and Interaction Based on Frequency-Domain Integral Equation and Method of Moments Techniques", Wave Motion, vol.10, 1988, pp.493-525.
- [5] K.S.Yee, "Numerical Solution of Initial Bounday Value Problems Involving Maxwell's Equations in Isotropic Media", IEEE Trans. Antennas and Propagation, vol.14, 1966, pp.302-307.
- [6] A.Taflove and M.E.Brodwin, "Numerical Solution of Steady-State Electromagnetic Scattering Problems Using the Time-Dependent Maxwell's Equations", IEEE Trans. Microwave Theory and Techniques, vol.23, 1975, pp.623-630.
- [7] G.Mur, "Absorbing Boundary Conditions for the Finite-Difference Approximation of the Time-Domain Electromagnetic Field Equations", IEEE Trans. Electromagnetic Compatibility, vol.23, 1981, pp.377-382.
- [8] J.-P.Berenger, "A Perfectly Matched Layer for the Absorption of Electromagnetic Waves", Computational Physics, vol.114, 1994, pp.185-200.
- [9] D.S.Katz, E.T.Thiele and A.Taflove, "Validation and Extension to Three Dimensions of the Berenger PML Absorbing Boundary Condition for FDTD Meshes", IEEE Microwave and Guided Wave Letters, vol.4, 1994, pp.344-346.
- [10] A.Taflove and K.R.Umashankar, "Radar Cross Section of Geneneral Three-dimensional Scatterers", IEEE Trans. Electromagnetic Compatibility, vol.25, 1983, pp.433-440.
- [11] K.R.Umashankar and A.Taflove, "A Novel Method to Analyze Electromagnetic Scattering of Complex Objects", IEEE Trans. Electromagnetic Compatibility, vol.24, 1982, pp.397-405.
- [12] D.H.Choi and W.J.Hoefer, "The Finite-difference Time-domain Method and its Application to Eigenvalue Problems", IEEE Trans. Microwave Theory and Techniques, vol.34, 1986, pp.1464-1470.
- [13] X.Zhang, J.Fang, K.K.Mei and Y.Liu, "Calculation of the Dispersive Characteristics of Microstrips by the Time-domain Finite-difference Method", IEEE Trans. Microwave Theory and Techniques, vol.36, 1988, pp.263-267.
- [14] J.G.Maloney, G.S.Smith and W.R.Scott, Jr., "Accurate Computation of the Radiation from Simple Antennas using the Finite-difference Time-domain Method", IEEE Trans. Antennas and Propagation, vol.38, 1990, pp.1059-1065.
- [15] S.M.El-Ghazaly, R.P.Joshi and R.O.Gronidin, "Electromagnetic and Transport Considerations in Sub-picosecond Photoconductive Switch Modeling", IEEE Trans. Microwave Theory and Techniques, vol.38,1990, pp.629-637.
- [16] B.Toland, B.Housmand and T.Itoh, "Modeling of Nonlinear Active Regions with the FDTD Method", IEEE Microwave and Guided Wave Letters, vol.3, 1993, pp.333-335.
- [17] W.Sui, D.A.Christensen and C.H.Durney, "Extending the two-dimensional FDTD Method to Hybrid Electromagnetic Systems with Active and Passive Lumped Elements", IEEE Trans. Microwave Theory and Techniques, vol.40, 1992, pp.724-730.

- [18] S.Mallat, "Multiresolution Representation and Wavelets", Ph.D. Thesis, University of Pennsylvania, Philadelphia, 1988.
- [19] Y.Meyer, "Ondelettes et Fonctions Splines", Seminaire EDP, Ecole Polytechnique. Paris, December 1986.
- [20] L.L.Schumaker, "Spline Functions: Basic Theory", Wiley-Interscience, New York, 1981.
- [21] H.C.Schweimler and E.P.Wigner, "Orthogonalization Methods", J.Math.Phys., 11 (1970), pp.1693-1694.
- [22] G.Battle, "A Block Spin Construction of Ondelettes, Part I:Lemarie functions", Comm. Math. Phys., 110 (1987), pp.601-615.
- [23] P.G.Lemarie, "Ondelettes a Localization Exponentielles", J.Math. Pures Appl., 67 (1988), pp.227-236.
- [24] , A.Haar, "Zur Theorie der Orthogonalen Funktionsysteme", Math.Ann., 69 (1910), pp.331-371.
- [25] I.Daubechies, "Orthonormal Bases of Compactly Supported Wavelets", Comm. Pure Appl. Math., 41 (1988), pp.909-996.
- [26] M.Krumpholz, L.P.B.Katehi, "MRTD: New Time Domain Schemes Based on Multiresolution Analysis", IEEE Trans. Microwave Theory and Techniques, vol. 44, no. 4, pp. 555-561, April 1996.
- [27] R. Holland, "Finite-difference time-domain (FDTD) analysis of magnetic diffusion", IEEE Transactions on Electromagnetic Compatibility, vol. 36, pp. 32-39, Feb.1994.
- [28] A.Bayliss and E.Turkel, "Radiation Boundary Conditions for wave-like equations", Comm. Pure Appl. Math., vol. 23, pp. 707-725, 1980.
- [29] B.Engquist and A.Majda, "Absorbing Boundary Conditions for the numerical simulation of waves", Mathematics of Computation, vol. 31, pp. 629-651, 1977.
- [30] R.L.Higdon, "Absorbing Boundary Conditions for difference approximations to the multidimensional wave equation", Mathematics of Computation, vol. 47, pp. 437-459, 1986.
- [31] Z.P.Liao et al., "A transmitting boundary for transient wave analyses", Scientia Sinica (Series A), vol. XXVII, pp. 1063-1076, 1984.
- [32] K.K.Mei and J.Fang, "Superabsorption-a method to improve absorbing boundary conditions", IEEE Trans. Antennas Propagation, vol. 40, pp.1001-1010, Sept.1992.
- [33] A.Taflove, "Computation of the Electromagnetic Fields and Induced Temperatures within a Model of the Microwave-Irradiated Human Eye", Ph.D. Dissertation, Department of Electrical Engineering, Northwestern University, Evanston, IL, June 1975.
- [34] S.M.Kay, "Modern Spectral Estimation", Englewood Cliffs, NJ: Prentice-Hall, 1988.
- [35] L.Marple, "A new autoregressive spectrum analysis algorithm", IEEE Trans. Acoustics, Speech and Signal Processing, vol. 28, pp. 441-454, 1980.
- [36] J.M.Rollins and J.M.Jarem, "The input impedance of a hollow-probe-fed, semi-infinite rectangular waveguide", IEEE Transactions on Microwave Theory and Techniques, vol. 37, pp. 1144-1146, Jul.1989.
- [37] A.G.Williamson, "Coaxially fed hollow probe in a rectangular waveguide", Proc. Inst. Elec. Eng., vol. 132, part H, pp. 273-285, 1985.
- [38] W.W.S. Lee and E.K.N. Yung, "The Input Impedance of a Coaxial Line Fed Probe in a Cylindrical Waveguide", IEEE Transactions on Microwave Theory and Techniques, vol. 42, pp. 1468-1473, Aug.1994.
- [39] E.Tentzeris, N.Dib, L.Katehi, J.Oswald and P.Siegel, "Time-Domain Characterization of Diode-Mounting structures", Nasa Terahertz Symposium Digest, March 1994.
- [40] P.B.Johns, K.Akthar zad "The Use of Time Domain Diakoptics in Time Discrete Models of Fields", Int.J.Num.Methods Eng., vol. 17, pp. 1-14, 1981.
- [41] W.J.R.Hoefler "The Discrete Time Domain Green's Function or Johns' Matrix - A new powerful Concept in Transmission Line Modelling (TLM)", Int.Journal of Num.Modeling, vol. 2, pp. 215-225, 1989.
- [42] T.W.Huang, B.Housmand, T.Itoh "The Implementation of Time-Domain Diakoptics in the FDTD Method", IEEE Transactions on Microwave Theory and Techniques, vol. 42, pp. 2149-2155, Nov.1994.
- [43] C.Eswarappa, W.J.R.Hoefler "Diakoptics and Wideband Dispersive Absorbing Boundaries in the 3-D TLM Method with Symmetrical Condensed Node", IECE Transactions, vol. E74, no. 5, pp.1242-1250, May 1991.

- [44] M.Righi, W.J.R.Hoefer "Efficient 3D-SCN-TLM Diakoptics for Waveguide Components", IEEE Transactions on Microwave Theory and Techniques, vol. 42, pp. 2381-2385, Dec.1994.
- [45] M.Righi, W.J.R.Hoefer, M.Mongiardo and R.Sorrentino "Efficient TLM Diakoptics for Separable Structures", IEEE Transactions on Microwave Theory and Techniques, vol. 43, pp. 854-859. Apr.1995.
- [46] M.Werthen, M.Rittweger, I.Wolff " FDTD-Simulation of Waveguide Junctions using a new Boundary Condition for Rectangular Waveguides", Proc. 24th European Microwave Conference, pp.1715-1719, 1994.
- [47] F.Moglie, T.Rozzi, P.Marcozzi and A.Schiavoni "A New Termination Condition for the Application of FDTD Techniques to Discontinuity Problems in Close Homogeneous Waveguide", IEEE Microwave and Guided Wave Letters, vol. 2, no. 12, pp. 475-477, Dec.1992.
- [48] M.Krumpholz, B.Bader and P.Russer "On the theory of Discrete TLM Green's functions in Three-dimensional TLM", IEEE Transactions on Microwave Theory and Techniques, vol. 43, pp. 1472-1483, Jul.1995.
- [49] M.Werthen, M.Rittweger and I.Wolff "Multi-mode Simulation of Homogeneous Waveguide Components Using a Combination of the FDTD and FD^2 Method", Proc. 25th European Microwave Conference, pp.234-237, 1995.
- [50] M.Schwarz "Information, Transmission, Modulation and Noise", McGraw-Hill International Editions, pp. 72-76, 7th Ed., 1987.
- [51] M.Krumpholz, C.Huber and P.Russer "A field theoretical comparison of FDTD and TLM", IEEE Transactions on Microwave Theory and Techniques, vol. 43, pp. 1935-1950, Aug.1995.
- [52] C-Y.Chi, G.M.Rebeiz, "Planar Microwave and Millimeter-Wave Lumped Elements and Couple-line Filters Using Micro-Machining Techniques", IEEE Trans. Microwave Theory and Techniques, pp. 730-738, April 1995.
- [53] E.M.Tentzeris, R.L.Robertson, M.Krumpholz, L.P.B.Katehi, "Application of MRTD to Printed Transmission Lines", Proc. MTT-S 1996, pp. 573-576.
- [54] M.Krumpholz, L.P.B.Katehi, "MRTD Modeling of Nonlinear Pulse Propagation", to be published at the IEEE Trans. Microwave Theory and Techniques.
- [55] S.Xiao, R.Vahldieck, "An Improved 2D-FDTD Algorithm for Hybrid Mode Analysis of Quasi-planar Transmission Lines", MWSYM 93, vol. 1, pp.421-424.
- [56] B.C.Wadell, "Transmission Line Design Handbook", pp. 136-137, Artech House, 1991.
- [57] A.Taflove, "Computational Electrodynamics", Artech House, 1995.
- [58] K.L.Shlager and J.B.Schneider, "Analysis of the Dispersion Properties of the Multiresolution Time-Domain Method", IEEE AP-S 1997 Proceedings, vol. 4, pp. 2144-2147, 1997.
- [59] W.Y.Tam, "Comments on "New Prospects for Time Domain Analysis"", IEEE Microwave and Guided Wave Letters, vol. 6, pp. 422-423, 1996.
- [60] M.Krumpholz, L.P.B.Katehi, "New Prospects for Time Domain Analysis", IEEE Microwave and Guided Wave Letters, pp. 382-384, November 1995.
- [61] E.Tentzeris, R.Robertson, M.Krumpholz and L.P.B. Katehi, "Application of the PML Absorber to the MRTD Technique", Proc. AP-S 1996, pp. 634-637.
- [62] D.M.Pozar, "Microwave Engineering", pp. 94-96, Addison-Wesley, 1990.
- [63] M.Krumpholz, P.Russer, "Two-Dimensional FDTD and TLM", Int.Journal of Num. Modelling, vol. 7, no. 2, pp. 141-153, February 1993.
- [64] P.Russer, M.Krumpholz, "The Hilbert Space Formulation of the TLM Method", International Journal of Numerical Modelling: Electronic Networks, Devices and Fields, vol. 6, no. 1, pp. 29-45, February 1993.
- [65] R. Robertson, E. Tentzeris, M. Krumpholz, L.P.B. Katehi, "Application of MRTD Analysis to Dielectric Cavity Structures", Proc. MTT-S 1996, pp. 1861-1864.
- [66] K.Goverdhanam, E.Tentzeris, M.Krumpholz and L.P.B. Katehi, "An FDTD Multigrid based on Multiresolution Analysis", Proc. AP-S 1996, pp.352-355.
- [67] V.Perrier and C.Bàsdevant, "La decomposition en ondelettes periodiques: un outil pour l'analyse des champs inhomogenes. Theorie et algorithmes", La Recherche Aerospatiale, no.3, pp.53-67, 1989.
- [68] E.Tentzeris, R.Robertson, A.Cangellaris and L.P.B. Katehi, "Space- and Time- Adaptive Gridding Using MRTD", Proc. MTT-S 1997, pp. 337-340.

REPORT DOCUMENTATION PAGE

Form Approved
OMB NO. 0704-0188

Public reporting burden for this collection of information is estimated to average 1 hour per response, including the time for reviewing instructions, searching existing data sources, gathering and maintaining the data needed, and completing and reviewing the collection of information. Send comment regarding this burden estimates or any other aspect of this collection of information, including suggestions for reducing this burden to Washington Headquarters Services, Directorate for Information Operations and Reports, 1215 Jefferson Davis Highway, Suite 1204, Arlington, VA 22202-4302, and to the Office of Management and Budget, Paperwork Reduction Project (0704-0188), Washington, DC 20503.

1. AGENCY USE ONLY (Leave blank)		2. REPORT DATE 5/1/98	3. REPORT TYPE AND DATES COVERED Final Report, May 1995-April 1998	
4. TITLE AND SUBTITLE Micropackaging for Mm-Wave Circuits			5. FUNDING NUMBERS DAAH04-95-1-0321 P-33939-EL	
6. AUTHOR(S) Linda P.B. Katehi				
7. PERFORMING ORGANIZATION NAME(S) AND ADDRESS(ES) University of Michigan Dept. of Electrical Engineering and Computer Science 1301 Beal Avenue Ann Arbor, Michigan 48109-2122			8. PERFORMING ORGANIZATION REPORT NUMBER 033259-1-F	
9. SPONSORING / MONITORING AGENCY NAMES(S) AND ADDRESS(ES) U.S. Army Research Office ATTN: Dr. James F. Harvey Electronics Division P.O. Box 12211 Research Triangle Park, NC 27709-2211			10. SPONSORING / MONITORING AGENCY REPORT NUMBER	
11. SUPPLEMENTARY NOTES The views, opinions and/or findings contained in this report are those of the author(s) and should not be construed as an official Department of the Army position, policy or decision, unless so designated by other documentation.				
12a. DISTRIBUTION / AVAILABILITY STATEMENT Approved for public release; distribution unlimited.			12b. DISTRIBUTION CODE	
13. ABSTRACT (Maximum 200 words) Complex antenna and circuit problems including their package on wafer require very intensive calculations due to the need to accurately simulate the underlying high-frequency effects and account for all the parasitic mechanisms. As part of this project, we have successfully applied a novel frequency domain scheme recently developed at the University of Michigan that allows for the very successful and computationally efficient solution of complex antenna problems. This technique has been applied to a variety of circuit and antenna problems and has demonstrated the capability to provide accurate solutions in much more efficient ways than in the conventional techniques. The whole idea in this approach is the use of wavelets in the expansion of the unknown functions. The use of wavelets allows for the computation of the values of the derivatives of the unknown field quantities in addition to the average values of the field. This allows for the development of novel space-adaptive schemes with unique capabilities.				
14. SUBJECT TERMS			15. NUMBER OF PAGES	
			16. PRICE CODE	
17. SECURITY CLASSIFICATION OR REPORT UNCLASSIFIED	18. SECURITY CLASSIFICATION OF THIS PAGE UNCLASSIFIED	19. SECURITY CLASSIFICATION OF ABSTRACT UNCLASSIFIED	20. LIMITATION OF ABSTRACT UL	